Extreme Design Events due to Combined, Non-Gaussian Loading

by

Harleigh C. Seyffert

A dissertation submitted in partial fulfillment
of the requirements for the degree of
Doctor of Philosophy
(Naval Architecture and Marine Engineering)
in The University of Michigan
2018

Doctoral Committee:

Professor Armin W. Troesch, Chair
Associate Professor Matthew D. Collette
Professor Charles R. Doering
Associate Professor Kevin J. Maki
Associate Professor David J. Singer

Harleigh C. Seyffert
harleigh@umich.edu
ORCID id: 0000-0003-0323-2096

For my family, and their unwavering support and belief

ACKNOWLEDGEMENTS

Whenever I talked with someone, and told them I was working on my PhD, I always seemed to get a different version of the same response: "That must be awful! You must be miserable!" But that description of PhD life could not have been further from the truth for me. Honestly, my time in graduate school has included some of the most fulfilling, enjoyable, and happy times of my life. That is mainly due to a whole lot of luck, the favor of the Lord, and the help and encouragement of others.

Before anything, I am grateful for my parents. They sacrificed for me to have the best education and supported me when I decided to make my education a never-ending pursuit. I always heard from them that I could, and that I would, succeed. Those messages popped up as timely reminders when it seemed like I couldn't or wouldn't make it. They nourished my desire to read, try, and learn, through years of trips to the library, and countless nights spent building projects for Destination Imagination. Thank you for allowing me to pursue this dream.

My sister Morgan has constantly been my role model for how to do things well and dream extravagantly, and how to have a really great time along the way. Morgan's thirst for life and willingness for risk has made me believe big things about my own life. If I end up with half of the adventures and stories she's already experienced, I'll consider that a success.

My friends have made this whole process worthwhile and fun. Thank you, Natalie & Vittorio, for housing me countless times on work trips back to Ann Arbor, and all of my friends at the office made every day enjoyable, even if we did waste a lot of time "talking about research."

I'm grateful to the staff in the NAME department, who were unfailingly helpful throughout every crisis and question. From the constant cheerleading and advice from Warren & Nathalie, every administrative nuance that Lisa helped with, the countless travel reimbursement sheets to Sallie- their support when I moved to Washington D.C. to work remotely made it possible for me to finish this degree.

I am grateful to my committee members for their flexibility, input, and support. I gratefully acknowledge the support by the Office of Naval Research (ONR) through the Probabilistic Assessment of Design Events for Complex Systems Subject to Stochastic Input project (program manager Kelly Cooper) and the National Defense Science and Engineering Graduate (NDSEG) Fellowship. I also gratefully acknowledge the help of Navatek for running Aegir to produce the trimaran transfer functions used in Chapter VIII, and for supplying the trimaran hull form.

I cannot imagine having gone through the PhD process without the encouragement, mentorship, and support of my advisor, Professor Troesch. That he saw something in me made me see something in myself. Through Professor Troesch's patience, inexhaustible supply of knowledge, sense of humor, and willingness to spend hours and hours advising, I flourished. He is truly the best teacher I have ever known. I cannot believe my good luck that he chose me as his student. Professor Troesch, I hope that this dissertation has made you proud, and has done justice to your ideas that started it all.

I would never have finished this degree without the support of my husband. Phil, your willingness to uproot your life, risk your job, and be a constant source of support has made this effort possible. I am humbled by your sacrifices for me. In a world of people telling strong women to be less- be less challenging, be less ambitious, be less opinionated, be less assertive- you love me because I am more. Thank you for always encouraging me to be more, and for helping with the logistics while I took this all on. I am ready for any adventure with you.

Above all, Praise the Lord. Praise God for this opportunity. Praise God for His provision. Praise God for every day.

Praise God, from whom all blessings flow;
Praise Him, all creatures here below;
Praise Him, above, ye heavenly host;
Praise Father, Son, and Holy Ghost. Amen.

TABLE OF CONTENTS

LIST OF FIGURES

Figure

LIST OF TABLES

Table

ABSTRACT

A major design driver for marine systems is lifetime performance. How a vessel responds in harsh environments has stark consequences for safety and operability, necessitating the consideration of lifetime performance analysis during the design stage. However, extreme events associated with marine dynamic systems may not be caused by the most extreme ocean environments, like the largest wave. Some severe vessel responses may be due to simultaneous combinations of potentially correlated, non-Gaussian loading, which may be excited by any number of wave profiles.

Different analytical methods based on extrapolation or solving for threshold exceedances can examine certain aspects of this problem: extreme system responses, combined loading, and long exposures to harsh excitation. But these methods, in general, do not retain the wave profiles which lead to extreme responses. These waves profiles can drive high-fidelity codes, like Computational Fluid Dynamics or Finite Element Analysis time-domain simulations, to give pressure and loading distributions. Such analyses can give an overall account of a system during lifetime events and refine estimates of system performance due to lifetime loading.

The Design Loads Generator (DLG) was developed to construct wave profiles that lead to a distribution of linear extreme responses, given an operational profile and exposure period. However, there are some limitations when applying the DLG method to non-linear problems. Some marine systems may experience extreme responses due to varying combinations of non-linear loading. If those loads are strongly correlated, or have an unknown correlation, it is unclear how the capability of the DLG, which considers a single linear load, can be utilized. It may also be desirable to consider lifetime system performance, and not performance conditioned on a specific excitation input, as is estimated by the DLG framework.

This dissertation addresses those concerns by expanding the DLG method to what is called the non-linear Design Loads Generator (NL-DLG) process. Given a complex system, operational profile, and exposure, the NL-DLG process uses the DLG capability to determine an ensemble of excitation inputs which lead to lifetime extreme events. Unlike the DLG, which is developed for a single response, the NL-DLG pro-

cess considers the interaction of multiple stochastic processes which excite the system. These processes, which may be non-Gaussian, are examined so that the resulting ensemble of excitation inputs are demonstrably exhaustive in generating possible defined responses. Short excitation inputs are constructed that estimate the same distribution of responses as would full Monte Carlo Simulations (MCS). Instead of conducting the necessary large number of full-exposure MCS for converged statistics of joint responses, the ensemble of short excitation inputs assembled by the NL-DLG process approximates that same distribution. Various examples are given in this dissertation where comparisons between MCS and NL-DLG extreme value probabilities validate the method.

For a complex system with a threshold of allowable responses, the ensemble of NL-DLG generated inputs can estimate an exceedance probability, given the exposure and operational profile. This threshold may be multi-dimensional and a non-linear function of multiple loads. The NL-DLG process examines complex system responses due to combined loading, and maintains links back to the excitation environment, without the computational cost associated with brute-force MCS. These capabilities give deeper insights into system responses, and aid in the design of safer, better operating systems.

CHAPTER I

Introduction

1.1 Performance Analysis of Marine Systems

Performance analysis is complex and time-consuming, resulting in design decisions driven by factors like cost (i.e. the cheapest option) and ease of production, but not necessarily design reliability. However, with harshening ocean environments and the push to extend the service life of marine systems, it is desirable to consider earlier in the design cycle a design's performance over the intended lifetime. Rationally defined metrics on the performance of basic design options allow for more informed decisions, and better understanding of lifetime extreme responses.

For a system excited by multiple potentially correlated and non-Gaussian loads, it may be difficult to analytically examine how those loads interact toward extreme design events. The problem is further complicated if varying combinations of those loads can lead to an extreme system response. This is a similar problem to determining the probability that a vector of non-Gaussian loads with an unknown correlation structure exceeds a multi-dimension complex threshold surface during a long exposure. A threshold surface of a system or specific design feature may represent an allowable level of experienced loading. Or, this threshold may represent combinations of loads that lead to a physical failure or collapse when exceeded. To accurately determine the probability of threshold exceedance by a vector of random processes given an operational profile over a set exposure, while preserving the excitation inputs which lead to extreme responses, suggests a time-domain simulation-based approach. Without these excitation inputs, there is no connection to the underlying physics relevant to the extreme response, which can link hydrodynamic and structural analyses of a vessel during lifetime events.

Conducting many simulations is necessary to ensure converged statistics, but may prove computationally expensive for long exposure periods, or for high-fidelity Computational Fluid Dynamics (CFD) or Finite Element Analysis (FEA) time-domain simulations. For such analyses to be feasible at an early design stage, simulations should be directed, meaning that the simulated excitation inputs are representative of the exposure period and operating environment, but focused on the small subset of times when threshold exceedances actually occur. In a sense, the desire is to simulate only the excitation inputs which lead to threshold exceedances, while still maintaining the overall operating profile.

This directed simulation capability requires information about the system input: namely, what kind of excitation inputs lead to extreme responses. Information about the system and response is also required: how combinations of the random processes may lead to threshold exceedances. For physical loading on marine systems, it may be necessary to consider different extreme wave profiles, based on the system in question. An extreme dynamic event may be due to a single extreme (i.e. rogue) wave, or a specific pattern of waves, potentially represented by a wave group. To evaluate lifetime responses without resorting to brute-force Monte Carlo Simulations (MCS), it is desirable to simulate only the wave forms that are expected to lead to threshold exceedances.

However, wave profiles associated with extreme responses cannot be separated from the system dynamics. Additionally, for systems whose extreme responses are due to varying levels of loads acting on the system, meaning the allowable threshold is multi-dimensional, there may be many excitation input profiles that lead to threshold exceedances. Such exceedances may be due to a single load extreme, or simultaneous moderate values of multiple loads. To examine such scenarios within the global context of the probability of a threshold exceedance implies that extreme wave profiles, and how such profiles lead to various extreme events, must be considered. Therefore, this dissertation considers both problems: extreme wave profiles, and threshold-crossings of a surface by combined stochastic excitation. Some major findings and methods associated with both problems are reviewed here.

1.2 Literature Review: Extreme Wave Profiles

Different types of extreme wave profiles, or wave elevation time histories, can be associated with severe vessel responses. Impact due to a single large-amplitude wave

may lead to extreme bottom slamming pressure. A different extreme, or rare, wave profile may be a sequence of multiple waves that excite a resonant or near-resonant response, potentially leading to parametric roll. While both types of wave profiles are of interest, they are fundamentally different in that rare wave groups may not appear to be severe, even though they can excite design responses. This section examines some canonical research relating to single extreme wave profiles and to wave groups.

1.2.1 New Wave Method

The expected wave surface around a wave maximum in a Gaussian seaway has been developed by multiple authors. *Lindgren* (1970) showed that this maximum is a scaled autocorrelation function of the seaway, approximated as:

$$E[\zeta(t)|\zeta(0) = a, \dot{\zeta}(0) = 0] = a\rho(t) \tag{1.1}$$

where

$\zeta(t)$ = random time-varying process of the sea surface (assumed Gaussian)

$\rho(t)$ = normalized autocorrelation function of $\zeta(t)$

Boccotti (2015) showed that the condition the wave maximum be a crest (i.e. $\dot{\zeta}(0) = 0$) can be relaxed as a goes to infinity.

1.2.2 Wave Groups Defined by a Threshold-Crossing Criteria

Traditional descriptions of wave groups are typically formulated as an envelope peaks over a threshold (EPOT) problem or a counting of discrete peaks over a threshold problem (e.g. Markov chain model), and often are based on the assumption of narrow banded spectra (*Longuet-Higgins*, 1957; *Ewing*, 1973).

Themelis and Spyrou (2007) considered the probability of encountering a wave group defined by a strict threshold-crossing, given wave data of a forecasted ship route, by assuming narrow banded spectra and uncorrelated successive wave up-crossings over the threshold. The authors also make use of a model based on Markov chain assumptions for wave-to-wave dependence by *Kimura* (1980). However, such a formulation requires joint *pdf*'s of significant wave height and wave period in a region of interest, which are generally difficult to attain.

Many authors who consider wave groups by the threshold-crossing criterion do so by employing potentially limiting assumptions. The assumptions may simplify the

calculations but limit the applicability of results to a physical ocean environment. A major challenge, then, is how to carefully define what constitutes a wave group. *Bassler et al.* (2010) discussed the possibility that a threshold-crossing criterion may be too strict for the identification of wave groups. Wave groups restricted to a successive threshold-crossing requirement will not include the more probable wave group sequence in which one or two minor down-crossings, below the required threshold, can occur.

For example, in Figure 1.1, there are two groupings of waves separated in time by Δt, called the 1^{st} and the 2^{nd} group, and some threshold a. The 1^{st} group has three waves which exceed the threshold a, and therefore would be defined as a wave group, given the threshold criteria. The 2^{nd} group does not meet this criterion, as the waves II and V do not exceed a. However, this grouping of six waves may set off interesting dynamic responses, based on the near-constant period between the waves, and the relatively large mean amplitude of the six waves.

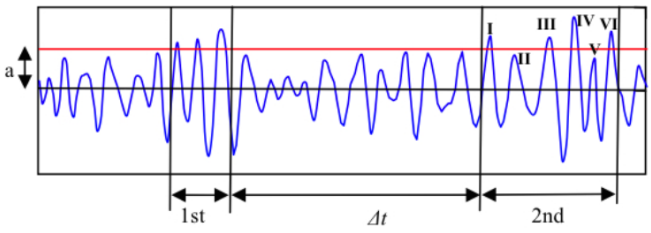

Figure 1.1: Possible wave group (*Bassler et al.*, 2010).

The threshold-crossing definition of wave groups is also challenging for the identification of long group runs from field data, due to either the rarity of long runs exceeding a prescribed high level, or the lack of sufficient data sets containing large wave groups. In addition, when looking at ship dynamical events such as parametric roll, this traditional definition does not account for the large role that the forcing period has on the event. And equally problematic, an ensemble of wave groups restricted to successive threshold-crossings will not include the more probable wave group sequence, targeted for a critical threshold, that still permits the inclusion of minor down-crossings within the grouping. This wave group is, through resonant excitation, also capable of generating extreme responses.

1.2.3 Wave Groups Defined by a Gaussian Derived Process

Kim and Troesch (2013) took advantage of this realization: that wave groups

may be identified by a large mean group amplitude, rather than an individual peak threshold-crossing, with the development of a derived Gaussian process. The authors showed that group-like behavior of a C11 container hull's time-varying metacentric height, $GM(t)$, can lead to parametric roll responses. They found that groups of this metacentric height like the 2^{nd} group in Figure 1.1, which may satisfy the threshold requirement in a mean sense but not in total, can cause significant roll response through resonant, parametric excitation. The derived process, similar in appearance to a moving average, is a sum of k processes (or the same process), each progressively shifted in time by $(p-1)\tau$ seconds for $p = 1, \cdots, k$:

$$z_k(t) = \sum_{p=1}^{k} \eta(t + (p-1)\tau) \tag{1.2}$$

The underlying theory is based on the assumption that the water surface elevation, and by extension the derived process, follows a Gaussian distribution.

1.3 Literature Review: Extreme System Responses due to Combined Excitation

The most severe loading conditions or motions a vessel experiences over its lifetime may not be due to the most obvious definition of an extreme wave, or wave profile. For some vessel responses, it may be clear which wave profiles will lead to extreme responses, e.g. large sagging bending moments may be expected when there is a large wave trough at midships and the wavelength is of order of the ship's length. But for non-linear responses or for vessels with complicated geometry, the connection between wave profile and extreme response may not be so clear. Additionally, for systems whose severe responses are due to various combinations of stochastic loading, the most extreme wave will not, in general, lead to simultaneous extreme load combinations. These sorts of problems require analysis methods that are not limited to obvious cause-and-effect observations.

The interaction of a non-linear threshold with combined, potentially correlated, non-Gaussian, stochastic loading may describe a range of extreme responses for a marine system. Considering the probability of lifetime threshold exceedances, and the wave inputs which lead to such responses, requires the examination of the threshold-crossing problem. This section reviews multiple methods to examine the interactions of combined loading and threshold surfaces, and determine the probability of

threshold-crossings by a vector of random processes.

1.3.1 Threshold-Crossings of Stochastic Load Combinations

The threshold-crossing of a surface by a vector of stochastic inputs has been considered by multiple authors. Following the notation of *Madsen et al.* (2006), given some exposure, T, failure is defined as the first up-crossing of $\xi(t)$ by the process $b(\boldsymbol{Q}(t))$. Here, $\xi(t)$ is a "strength threshold," $\boldsymbol{Q}(t)$ is a vector of stochastic loads, and the function, b, relates the loads to the system response based on the strength threshold. Then, the probability of failure, $p(\mathbb{F})$, or probability of threshold exceedance within the exposure $[0, T]$, based on the number of up-crossings of $\xi(t)$ by $b(\boldsymbol{Q}(t))$, $N_\xi(T)$, is given by Eq.(1.3):

$$p(\mathbb{F}) = p(\mathbb{F} \text{ at t=0}) + p(N_\xi(T) \geq 1) - p(\mathbb{F} \text{ at t=0} \cap N_\xi(T) \geq 1) \tag{1.3}$$

The probability of failure is bounded as:

$$\begin{aligned} p(\mathbb{F}) &\leq p(\mathbb{F} \text{ at t=0}) + p(N_\xi(T) \geq 1) \\ &\leq p(\mathbb{F} \text{ at t=0}) + \sum_{n=1}^{\infty} p(N_\xi(T) = n) \\ &\leq p(\mathbb{F} \text{ at t=0}) + \sum_{n=1}^{\infty} np(N_\xi(T) = n) = p(\mathbb{F} \text{ at t=0}) + E[N_\xi(T)] \end{aligned} \tag{1.4}$$

Madsen et al. note that Eq.(1.4) is a good approximation for "practical situations with high-reliability structures when clustering of crossings can be neglected," and if Eq.(1.5) is satisfied, i.e. if:

$$p(N_\xi(T) = 1) \gg \sum_{n=2}^{\infty} np(N_\xi(T) = n) \tag{1.5}$$

The expected number of up-crossings of $\xi(t)$ by $b(\boldsymbol{Q}(t))$, $E[N_\xi(T)]$, is given by Eq.(1.6), where $\nu(\xi, t)$ is the mean up-crossing rate of $\xi(t)$:

$$E[N_\xi(T)] = \int_{t=0}^{T} \nu(\xi, t) dt \tag{1.6}$$

This mean up-crossing rate $\nu(\xi, t)$ can be solved by Rice's formula (*Rice*, 1944), where $S(t) = b(\boldsymbol{Q}(t))$:

$$\nu(\xi, t) = \int_{\dot{s}=\dot{\xi}}^{\infty} (\dot{s} - \dot{\xi}) f_{S\dot{S}}(\xi, \dot{s}, t) d\dot{s} \tag{1.7}$$

However, very few closed-form solutions for the up-crossing rate of different processes are known, and the joint distribution of a time-varying load vector may be difficult to attain. *Naess and Moan* (2014) follow a similar method to determine the probability of a threshold exceedance by a load vector, but by solving the null problem. The authors also note that the structure of the load vector can be very complicated, which coupled with a high-dimension threshold definition, "makes a direct analytical approach virtually impossible." They suggest pursuing MCS-based approaches to circumvent these analytical challenges.

1.3.2 First & Second Order Reliability Methods

The First and Second Order Reliability Methods (FORM and SORM) are widely-vetted methods from structural reliability theory to consider the interaction of a multivariate random process with a failure surface or threshold definition. These methods calculate the reliability of a system, considered for a specific response output, via *safe* and *unsafe* regions defined by a failure surface. An excitation profile, here for the example of a stochastic wave profile, may be constructed as:

$$\zeta(x,t) = \sum_{j=1}^{N} a_j \sigma_j cos(\omega_j t - k_j x) + b_j \sigma_j sin(\omega_j t - k_j x) \tag{1.8}$$

where

$$\begin{aligned}
\zeta(x,t) &\equiv \text{random time-varying process of the sea surface (assumed Gaussian)} \\
a_j \ \& \ b_j &= \text{uncorrelated standard normal random variables} \\
\omega_j &= \text{discretized wave frequency} \\
k_j &= \text{discretized wave number} \\
\sigma_j^2 &= S(\omega_j)\Delta\omega_j \\
S(\omega) &= \text{input wave spectrum}
\end{aligned}$$

The number of components, N, must be large else the representation will suffer repeatability and resolution issues. The response of the system, which may be non-linear, due to the given wave input, $\zeta(x,t)$, is given as $\phi(t|a_1, b_1, a_2, b_2, ..., a_N, b_N)$. Then, a pre-determined response of interest is given as ϕ_0. The most probable wave sequence which leads to this pre-determined extreme response, ϕ_0, is solved for iteratively. A limit state surface G may be defined which represents an infinite number of potential wave inputs (or combinations of amplitudes and phases) that lead to this

pre-determined response:

$$G = \phi(t|a_1, b_1, a_2, b_2, \cdots, a_N, b_N)|_{t=t_0} - \phi_0 = 0 \tag{1.9}$$

The point on this surface closest to the origin defines the most probable wave profile which leads to the pre-determined response, ϕ_0. *Jensen* (2007) employed the FORM method to generate the most probable wave sequence which leads to a given design event for multiple problems, such as extreme roll of a containership. FORM/ SORM are complicated, though, because they require a joint *pdf* of the random variables which make up the extreme response of the vessel.

The joint *pdf* of the random variables may have a complex definition and is simplified for the iterative solution of the most-probable wave sequence that lead to ϕ_0. This simplification comes from transforming the marginal distributions of the random variables into a standard normal space, where the cumulative distribution function (*cdf*) remains unchanged after the transformation. After this transformation, the variable distributions are zero-mean, unit-variance normal, and have a unit correlation matrix, meaning the transformed variables are independent. The choice of transformation depends on the amount of information known about the random variables.

If the joint distribution is known, a Rosenblatt Transformation may be used to transform the random variables into independent, unit-variance, zero-mean normal random variables (*Rosenblatt*, 1952). In the case where the joint distribution of the incoming random variables is unknown, but their marginal densities and correlations are known, the Nataf Transformation may be applied (*Hurtado*, 2004), similar to the copula method discussed in Section 1.3.5. Regardless of the transformation used, the transformed joint density function is easily integrated as the transformed random variables are independent standard normals, making the contours of the joint distribution concentric circles.

FORM/ SORM also simplifies the evaluation by using a first/ second order Taylor Series Expansion to approximate the limit surface G at the most probable point, or the point of G closest to the origin. Finding this point requires iteration, and the accuracy is best when the surface is linearized around the point which has the highest contribution to the probability integral, i.e. the most probable point. However, it is unclear how useful a most probable wave input which leads to an extreme response is for the consideration of non-linear systems. Without ensembles of statistically

equivalent inputs which lead to design responses, the statistics of a non-linear response cannot be directly determined, but only inferred.

Beyond these challenges, it may be desirable to find the overall reliability of a system, not conditioned on a specific pre-determined output. Specifically, if a system has a multi-dimension allowable threshold, indicating that varying combinations of multiple loads lead to an extreme response, it may be required to link together many FORM/ SORM analyses, potentially diminishing the computational advantages of these methods.

1.3.3 Inverse FORM

Winterstein et al. (1993) introduced inverse FORM to calculate a failure surface that is a function of multiple environmental variables and that has a given deterministic response return period. The authors give the specific example of inverse FORM applied to find contours of significant wave height and peak wave period which lead to a 100-year deterministic response. Inverse FORM was developed to give designers environmental input data that leads to pre-determined return-period responses, which can be translated to a design with a required probability of non-exceedance for failure or load responses. This may be a preferable result than that from FORM or SORM, because inverse FORM allows designers to find a "known response capacity," or response value, given a reliability index that must be satisfied.

One potential limitation of the applicability of inverse FORM, though, is that some input variable which dominates the others in uncertainty must be chosen. Then, the conditional distributions of the other inputs, given the dominating random input, are found. The system response is then approximated by its median value, given the environmental input, plus some random error term to account for assuming a deterministic response. This FORM omission sensitivity factor is most accurate for "linear/Gaussian safety margins," which may limit the application for non-linear systems. All the other input variables are modeled as conditioned on the dominating random variable, but these conditional distributions may not be known for some non-linear loads. This conditional modeling may not be valid for load extremes and may not be feasible to obtain for multiple inputs.

It also may not be true that an extreme response is the result of a single extreme input, as inverse FORM assumes. For stochastic responses, even the "inflated" environment contours provided by inverse FORM, which are the result of a deterministic

response and a random error term, may not give an accurate estimate of a complex system's extreme responses due to non-linear loading. Many methods, including MCS, assume a deterministic response based on the system model and stochastic input. However, inverse FORM deals with this by assuming the response takes its median value plus some error term based on the random input, whereas simulations recover a distribution of responses based on stochastic excitation.

1.3.4 Max-Stability of Asymptotic Distributions & the Conditional Extreme Model

To overcome some of the limitations of inverse FORM, but with a similar idea of finding contours of joint environmental inputs that have a specified response return period, *Ewans and Jonathan* (2014) employ the concept of max-stability of asymptotic distributions. The use of max-stable distributions means that the distributions of the loads do not need to be known at the analysis onset. Scaled and shifted maxima from this class of distributions can be modeled by a generalized extreme value distribution because they share a similar distribution and statistical characteristics. *Ewans and Jonathan* improve the max-stable concept for multi-dimension problems by incorporating the conditional extreme model from *Heffernan and Tawn* (2004).

The conditional extreme model is based on an assumption about the asymptotic forms of conditional distributions for an extreme response. The distributions of environmental loads are given conditioned on a single input being an extreme. Multi-dimensional problems are considered, where the variables may be asymptotically dependent or independent, and semi-parametric models are used to estimate the joint conditional distribution of the variables.

Ewans and Jonathan applied this model to the joint estimation of significant wave height and peak period for extreme storm conditions in the North Sea. This method gave a distribution of these two variables but may not be applicable for problems in which interesting responses come from other load combinations, rather than extremes of individual variables. As well, the tail behavior of the multivariate distribution must be given an assumed form, which may introduce error into the probability estimation for rare responses. Despite advancing extreme response determination, it is unclear how the conditional extreme model, coupled with max-stable asymptotic distributions, could tackle problems in which simultaneous moderate values of different loads interact toward failure.

1.3.5 Copulas

Copulas are utilized in many fields to consider joint distributions of multiple random processes (e.g. *de Waal and van Gelder* (2005); *Bastian et al.* (2009); *Bartoli et al.* (2011); *Knight et al.* (2017)). *Gong et al.* (2014) employed copulas to consider multivariate extremes of dependent loads. A copula assembles a multivariate *pdf* in which each marginal distribution is continuous and uniformly distributed. This property can be automatically satisfied by using as marginals the *cdf* of any random variable, which is by definition uniformly distributed between [0,1]. Therefore, copulas can establish a joint distribution of multiple variables, based on their marginal distributions and some assumed correlation structure. This formulation allows the generation of samples from a multivariate joint *pdf*.

The dimension of the copula complicates the problem, though, with a potential solution being to assume the copula belongs to a parametric family. The use of copulas presents complex challenges, however, specifically because the copula's asymptotic properties strongly affect the evaluation of small probabilities. Results from a copula analysis are dependent on the choice of the random process correlation structure (*Renard and Lang*, 2007), which may be problematic if the choice of the copula structure is not well-founded.

1.3.6 The Design Loads Generator

The Design Loads Generator (DLG) was developed by *Alford* (2008) and *Kim* (2012) to direct simulations for extreme responses, while retaining the excitation profiles that lead to these responses. The DLG method, explained in-depth in Chapter 2.3, constructs ensembles of short input profiles which are representative of a specified operational profile and exposure period, that lead to extreme responses of an associated linear response. The quick construction of short inputs which lead to extreme values means that no brute-force simulations are required to analyze lifetime responses. This capability allows designers to examine specific marine system lifetime responses, because the wave profiles constructed by the DLG can generate pressure and other load distributions on the system. However, the DLG capability is limited to considering a single system response, and system responses are conditioned on the specific excitation input. For systems whose extreme responses may be due to varying levels of combined loading, a single DLG analysis cannot give a general probability of exceeding a defined threshold.

1.4 Overview of Thesis

The above methods each focus on a specific challenge associated with analyzing the extreme responses of a complex marine system. However, these methods, in general, cannot estimate a threshold exceedance probability due to the interaction of combined, non-Gaussian loading with a complex threshold over a long exposure. And, apart from the DLG, the methods do not generate or retain an ensemble of stochastic inputs which lead to lifetime extreme responses. However, the DLG is yet unsuited to consider the interaction of a combined loading vector with a complex threshold surface. This thesis addresses that gap through the development of the *non-linear Design Loads Generator (NL-DLG) process*, which combines extreme value theory, non-linear load combination cases, surrogate processes, and directed simulations from the DLG. The NL-DLG process grew naturally from the work of *Alford* (2008) and *Kim* (2012), and specifically from interesting results associated with the analysis of extreme system inputs and responses. Therefore, the dissertation, as presented here in the following chapters, is truly the chronological progression toward the development of the NL-DLG process.

Chapter I gives an overview of research concerning extreme wave profiles, and the analysis of system responses, or the threshold-crossing of a surface by a vector of combined loads. Chapter II develops the background used in this dissertation, namely: Gaussian random processes, extreme value theory, and the Design Loads Generator (DLG). This chapter also gives an overview of the development of the expected shape of a rare wave group, defined as the maximum of a derived Gaussian process, as first published by *Seyffert et al.* (2016), with the major theoretical derivation by *Troesch*.

Chapter III uses the derived Gaussian process to mine through vast amounts of physical oceanographic data from the Pt. Reyes Buoy to determine if group-like structures exist in an irregular wave environment. Wave groups in an ensemble sense, and individual time records containing these wave groups, are compared with the theoretical wave group formulation, showing strong agreement. This indicates that excitation inputs constructed by the DLG to lead to extreme values of linear surrogate processes do exist in a physical oceanographic environment. This is an important validation of the DLG and gives confidence in using the DLG to construct physically realizable wave profiles that lead to extreme system responses.

Individual time series from the Pt. Reyes Buoy are then used as excitation in a spar platform model in Chapter IV. Spar platforms may experience extreme pitch

responses due to parametric excitation, which in idealized testing cases is usually represented by a regular wave train tuned to the platform heave natural period. Wave groups in individual physical wave records, which were shown to exhibit this group-like behavior in Chapter III, provide the excitation for the spar model. The connection between wave group occurrence in the excitation and a resulting large pitch response some pre-determined period later is examined. The probability of experiencing an extreme pitch response conditioned on the occurrence of a large wave group is given. Specifically, it is found that wave groups of 7, 8, or 9 waves are most likely to set off large pitch responses of the spar.

However, wave groups of similar group index (i.e. wave groups of 7, 8, or 9 waves) may not be mutually exclusive, and performance metrics conditioned on such excitation inputs may not be useful for designers. Therefore, Chapter V develops the NL-DLG process to address these concerns. Namely, the NL-DLG process estimates the probability that a complex threshold, representing a complex system response, is exceeded by combined, potentially correlated, non-Gaussian loading over a long exposure, potentially thousands of hours long. The threshold surface may be exceeded due to varying combinations of the non-linear loads. The NL-DLG process assembles an ensemble of excitation inputs which lead to the threshold exceedances the system is most likely to experience over its exposure period. A hypothetical example is given in Chapter VI to show the utility of the NL-DLG process in a more general sense, and to highlight specific features about system design brought up during an NL-DLG process analysis.

Chapter VII uses the NL-DLG process to determine the probability of stiffened ship panel collapse over a 1000-hour exposure to Hurricane Camille-like conditions. Stiffened panel failure is due to combined lateral and in-plane loading, which are non-linear functions of the wave excitation. The NL-DLG process estimates the failure probabilities and distributions of most-likely failures for 6 panel designs, and both results are verified by full MCS. Due to the far-reduced computational effort of the NL-DLG process, it is then possible to quickly change design features and re-evaluate the panel performance, to determine the panels' sensitivity to failure, based on a small design change. The NL-DLG process illustrates why some panels are more susceptible to failure than others based on panel properties.

Chapter VIII uses the NL-DLG process to examine lifetime combined loading on a trimaran. The DLG assembles distributions of seven global loads, based on a

specific operational profile and sea state. These distributions of combined loading experienced by a single trimaran are compared to combined loading cases based on Lloyd's Register rule load and alternative load approaches, which are offered to evaluate trimaran structural adequacy. The NL-DLG process examines the applicability, conservatism, and exhaustiveness of the rule load and alternative load approaches applied to a specific trimaran hull. It is ultimately found neither the rule load, nor the alternative load method recommended by Lloyd's Register for trimaran structure testing realistically describe the combined loading experienced by the specific trimaran examined. The NL-DLG process is used to determine the probability of simultaneously exceeding all load combination bounds, and is then used to offer more realistic, conservative, and exhaustive loading combination cases.

Finally, Chapter IX concludes the work, and offers some steps for future work. In summary, the major focus of this thesis is to efficiently solve the threshold-crossing problem for non-Gaussian, potentially correlated loading interacting with a multi-dimension non-linear threshold surface over a long exposure and link these threshold-crossings to wave excitation inputs.

CHAPTER II

Background

2.1 Gaussian Random Processes

A random process $x(t)$ can be represented as a sum of cosine functions:

$$x(t) = \sum_{j=1}^{N} a_j cos(\omega_j t + \epsilon_j) \tag{2.1}$$

where

$$\begin{aligned} a_j &= \sqrt{2S(\omega_j)\Delta\omega_j} \\ \omega_j &= \text{discretized frequency} \\ S(\omega) &= \text{single-sided spectrum of the process} \\ \epsilon_j &= \text{uniformly distributed phase angles from } -\pi \text{ to } \pi \end{aligned}$$

The random variable X, represented by the random process $x(t)$, approaches a Gaussian distribution as the number of cosines, N, goes to infinity, as explained by the central limit theorem. The probability density function (*pdf*) of a zero-mean Gaussian function is:

$$f(x) = \frac{1}{\sigma\sqrt{2\pi}} e^{-x^2/(2\sigma^2)} \tag{2.2}$$

where

$$\begin{aligned} \sigma &= \text{standard deviation of the process} \\ &= \int_0^\infty S(\omega)d\omega \approx \sum_{j=1}^{N} S(\omega_j)\Delta\omega_j = \sum_{j=1}^{N} \frac{1}{2} a_j^2 \end{aligned}$$

The Gaussian cumulative density function (*cdf*) may be expressed as:

$$F_X(x) = \int_{-\infty}^{x} \frac{1}{\sigma\sqrt{2\pi}} e^{-t^2/(2\sigma^2)} dt = \int_{-\infty}^{x/\sigma} \frac{1}{\sqrt{2\pi}} e^{-t^2/2} dt = \Phi(\frac{x}{\sigma}) \tag{2.3}$$

2.2 Extreme Value Theory

The ocean environment may well be described as a Gaussian process, specifically for deep-water waves (see, e.g., *Kinsman* (1965)). Many marine system loads can be represented, or at least approximated, by some linear function. Therefore, these loads may also be described as a Gaussian process. To consider the probability that a load exceeds some allowable threshold over its lifetime, the lifetime responses must be examined. This is equivalent to considering the distribution of extreme events of a Gaussian random variable for a specific exposure period. Here, these extreme events can be found by simulating the random variable for a given time, T, and finding the largest event (i.e. largest excursion of the process). This process is repeated n times. *Ochi* (1990) describes the dimensionless *pdf* of the positive maxima as:

$$f_{\Xi}(\xi) = \frac{2}{1+\sqrt{1-\epsilon^2}}\left[\frac{\epsilon}{\sqrt{2\pi}}e^{-\xi^2/(2\epsilon^2)} + \sqrt{1-\epsilon^2}\xi e^{-\xi^2/2}\Phi\left(\frac{\sqrt{1-\epsilon^2}}{\epsilon}\xi\right)\right] \tag{2.4}$$

where

$$\begin{aligned} \xi &= \text{normalized positive maxima } \tilde{x}/\sigma \\ \tilde{x} &= \text{positive maxima} \\ \epsilon &= \text{bandwidth parameter} = \sqrt{1-\frac{m_2^2}{m_0 m_4}} \\ m_k &= \int_0^\infty \omega^k S(\omega) d\omega \end{aligned} \tag{2.5}$$

The extreme value distribution is the distribution of extreme responses that a system experiences for a given exposure. A set of order statistics from a random sample $(x_1, x_2, \cdots, x_n)$ with size n is defined as $Y_1, Y_2, \cdots, Y_n$. This random sample is drawn from a distribution with the *pdf*, $f_X(x)$. The joint *pdf* of $Y_1, Y_2, \cdots, Y_n$ is called $g(y_1, y_2, \cdots, y_n)$:

$$g(y_1, y_2, \cdots, y_n) = n f(y_1) f(y_2) \cdots f(y_n) \tag{2.6}$$

where

$$-\infty < y_1 < y_2 < \cdots < y_n$$

The *pdf* of the largest value, Y_n, is found by successive integration of Eq.(2.6), and is given by Eq.(2.7) for $-\infty < y_n < \infty$:

$$g(y_n) = n f_Y(y_n)\{F_Y(y_n)\}^{n-1} \tag{2.7}$$

The *cdf* of the largest value, Y_n, is then:

$$G(y_n) = \int_{-\infty}^{y_n} g(y_n)dy_n = \{F_Y(y_n)\}^n \tag{2.8}$$

The most probable extreme value, $\widehat{y}_n$, is defined as the solution to Eq.(2.9). The most probable extreme value, $\widehat{y}_n$, is related to the number of samples, n, in the limit as $n \to \infty$ by Eq.(2.10):

$$\frac{d}{dy_n} g(y_n) = 0 \tag{2.9}$$

$$\frac{1}{n} \approx 1 - F_Y(\widehat{y}_n) \tag{2.10}$$

The most probable extreme value, $\widehat{y}_n$, for a given number of cycles per unit time with $\epsilon < 0.9$ is then given by *Ochi* (1990) as:

$$\widehat{y}_n = \sqrt{m_0} \left[2\ ln\left(\frac{2\sqrt{1-\epsilon^2}}{1+\sqrt{1-\epsilon^2}} n \right) \right]^{\frac{1}{2}} \tag{2.11}$$

where

$$n = \frac{1}{4\pi} \left(\frac{1+\sqrt{1-\epsilon^2}}{\sqrt{1-\epsilon^2}} \right) \sqrt{\frac{m_2}{m_0}}, \text{ per unit time} \tag{2.12}$$

$$\epsilon = \sqrt{1 - \frac{m_2^2}{m_0 m_4}} = \text{ broadness/ bandwidth parameter}$$

$$m_k = \int_0^\infty \omega^k S(\omega) d\omega = \ k^{th} \text{ moment of the process spectrum}$$

Combining Eq.(2.11) and (2.12), the most probable extreme maximum for a given exposure time, T in seconds, is found by Eq.(2.13). Note this equation is the same for both narrow and broad band spectra because the broadness parameter is considered by the number of cycles and the spectral moments.

$$\widehat{y}_n = \sqrt{m_0} \left[2\ ln\left(\frac{T}{2\pi} \sqrt{m_2/m_0} \right) \right]^{\frac{1}{2}} \tag{2.13}$$

An issue with using the most probable extreme value as a design value for engineering purposes is that there is a high probability that an exposure-period-maximum value is greater than the value $\widehat{y}_n$. For large n and $\widehat{y}_n$, *Ochi* estimates that the prob-

ability of exceeding the most probable value over the exposure T is:

$$p(X > \widehat{y}_n) \approx \frac{1}{n} \tag{2.14}$$

The probability that the largest value, Y_n, over the exposure exceeds this most probable maximum is approximately 63.2%:

$$\begin{aligned} \lim_{n\to\infty} p(Y_n > \widehat{y}_n) &= 1 - G(\widehat{y}_n) \\ &= \lim_{n\to\infty} [1 - \{F(\widehat{y}_n)\}^n] \\ &= \lim_{n\to\infty} \left[1 - \left(1 - \frac{1}{n}\right)^n\right] \\ &= 1 - e^{-1} = 0.632 \end{aligned} \tag{2.15}$$

Therefore, a risk parameter α can be defined. Then, there is an extreme value $\tilde{y}_n$ that satisfies Eq.(2.16)-(2.18):

$$\int_0^{\tilde{y}_n} g(y_n) dy_n = \{F(\tilde{y}_n)\}^n = 1 - \alpha \tag{2.16}$$

$$p(X > \tilde{y}_n) = 1 - F_Y(\tilde{y}_n) \approx \frac{\alpha}{n} \tag{2.17}$$

$$p(Y_n > \tilde{y}_n) \approx \alpha \tag{2.18}$$

This formulation allows the definition of an extreme value associated with an exposure (which can be expressed by the number of cycles or samples n) and a risk parameter α (i.e. with a given probability of exceedance). Risk parameters can be used when combining an exposure length in a certain sea state with a design probability of exceedance, which is related to a longer exposure length.

For example, given an extreme value distribution based on a 1000-hour exposure for a process with a mean cycle period of 10 seconds (meaning the number of cycles is $n = 3.6e5$), the probability that the maximum value over an exposure exceeds $\widehat{y}_n$ is approximately 0.632, as by Eq.(2.15). Therefore, a designer could apply a risk parameter $\alpha = 0.1$, leading to a new extreme value $\tilde{y}_n$, as by Eq.(2.16)-(2.18). The probability that the largest response in the 1000-hour exposure exceeds $\tilde{y}_n$ is approximately $p(Y_n > \tilde{y}_n) = \alpha = 0.1$, by Eq.(2.18).

This extreme value, $\tilde{y}_n$, could be used to define a new extreme value distribution, with $\tilde{y}_n$ as the most probable value. Since the extreme value, $\tilde{y}_n$, of this new distribution can be related to an exposure T, by Eq.(2.13), the addition of the risk parameter

α to the original 1000-hour exposure is equivalent to considering the extreme value distribution associated with the longer exposure period $T_\alpha = 10,000$ hours. This new extreme value distribution could be used to design a system so that the probability that the largest response during the 1000-hour exposure exceeds this new most probable maximum, $\tilde{y}_n$, is $0.1 \times 0.632 = 0.0632$. A smaller risk parameter α could further lower this probability for the design of more reliable systems for the given 1000-hour exposure.

Designing for a more reliable system is essentially equivalent to designing for a longer exposure period. To examine the reliability of a system over a longer exposure via simulation leads to a larger computational expense. This presents a similar challenge as the problem of estimating small probabilities, in which the number of samples needed to accurately estimate this small probability, $p(\mathbb{S})$, is proportional to $1/p(\mathbb{S})$. For smaller failure probabilities, i.e. a more reliable system, the exposure length and associated computational expense increases. Different variance-reduction techniques like subset simulation (*Au and Beck*, 2001; *Papaioannou et al.*, 2015) are designed to improve the efficiency of brute-force MCS, specifically for estimating such small probabilities through cascading conditional less-rare events. However, these methods do not keep the inputs leading to extreme responses. As noted in Chapter I, it may be desirable to reserve the inputs which lead to the distribution of extreme responses, indicating the need for simulation. These competing interests: efficiently simulating extreme responses while retaining the inputs which lead to the extreme responses, provided the motivation toward the development of the Design Loads Generator.

2.3 The Design Loads Generator

A possible method to balance such competing concerns: efficiently simulating extreme responses associated with long exposures while preserving the inputs that lead to those responses, is found in the Design Loads Generator (*Alford*, 2008; *Kim*, 2012). The DLG generates ensembles of phases for use in Eq.(2.1), to assemble wave profiles which lead to extreme linear responses at time $t = 0$ that are members of the exposure-period extreme value distribution. Whereas in Eq.(2.1) the phases, ϵ, are uniformly distributed from $-\pi$ to π, the DLG finds the phase distribution that tunes waves to lead to extreme linear system responses. By (arbitrarily) assuming that the

extreme event in question occurs at time $t = 0$, Eq.(2.1) may be simplified to:

$$x(0) = \sum_{j=1}^{N} a_j cos(\epsilon_j) \tag{2.19}$$

If multiple realizations are considered, the distribution of maximum events, Y_n, all centered around $t = 0$, may be approximated by Eq.(2.7). The empirical *pdf* of Y_n approaches the theoretical *pdf* from Eq.(2.7) as N approaches infinity. The work of finding the distribution of phases ϵ_j leading to extreme events began with *Alford* (2008), who theorized that these phases are independent and non-identically distributed (*inid*). *Alford* modeled the distribution of the random variable E_j, from the phases ϵ_j, with a modified Gaussian distribution:

$$f_{E_j}(z) = \frac{1}{\lambda_j\sqrt{2\pi}} e^{-z^2/(2\lambda_j^2)} + \frac{1}{2\pi}\left(1 - \text{erf}\left(\frac{\pi}{\lambda_j\sqrt{2}}\right)\right), \quad -\pi \leq z < \pi \tag{2.20}$$

where

$$\begin{aligned} \text{erf}(x) &= \text{standard error function} \\ &= \frac{2}{\sqrt{\pi}} \int_0^x e^{-t^2} dt \\ \lambda_j &\leq 10 \end{aligned}$$

The characteristic function of the theoretical Gaussian extreme value distribution (Eq.(2.7)) is:

$$E[e^{isY_n}] = \int_{-\infty}^{\infty} \frac{n}{\sigma\sqrt{2\pi}} e^{-y^2/(2\sigma^2)} \left(\Phi\left(\frac{x}{\sigma}\right)\right)^{n-1} e^{isy} dy \tag{2.21}$$

This characteristic function should be equivalent to the characteristic function of the values of Eq.(2.19) associated with E_j. Therefore, *Alford* iteratively solved for the desired phases ϵ_j by setting equal the characteristic function of the modified Gaussian distribution (from Eq.(2.20)) with the characteristic function of the distribution of maximum events Y_n from Eq.(2.7):

$$\begin{aligned} \prod_{j=1}^{N} \int_{-1}^{1} \frac{e^{ia_j sx}}{\pi\lambda_j\sqrt{1-x^2}} \left[\sqrt{2\pi} e^{-(cos^{-1}x)^2/(2\lambda_j^2)} - \lambda_j \text{erf}\left(\pi/(\lambda_j\sqrt{2})\right) + \lambda_j\right] dx = \\ = \int_{-\infty}^{\infty} \frac{n}{\sigma\sqrt{2\pi}} e^{-y^2/(2\sigma^2)} \left(\Phi\left(\frac{y}{\sigma}\right)\right)^{n-1} e^{isy} dy \end{aligned} \tag{2.22}$$

Although *Alford*'s solution phases did not perfectly follow the theoretical extreme value distribution, *Kim* (2012) later simplified the expression using a change of variable and Bessel functions. To fix the issue of the discrepancy between the resulting phases and extreme value theory, *Kim* employed the Acceptance-Rejection Algorithm. The Acceptance-Rejection Algorithm is utilized within the DLG framework by the following steps:

1. Generate a random sample, y, from the random variable, Y, generator by producing a set of phase angles, ϵ_j, that follow the modified Gaussian distribution (Eq.(2.20)) based on λ that approximately satisfies Eq.(2.22), and a uniform random number, u, from the uniform distribution between 0 and 1, $U[0,1]$.

2. If $u \leq f_X(y)/cg_Y(y)$, accept y as a sample x from the random variable X and store the associated set of phase angles ϵ_j. If not, repeat the first step. Here, $g_Y(y)$ is the distribution of phases predicted from the modified Gaussian distribution (Eq.(2.20)), c is a constant, and $f_X(x)$ is the desired Gaussian extreme value distribution for the phases (Eq.(2.7)).

3. Repeat the above two steps until n_r sets of N phase angles are collected. Here, n_r is the required number of realizations.

Readers should refer to *Kim* (2012) to a full explanation of the DLG method.

2.4 Expected Shape of a Rare Wave Group

Due to their significant, possibly critical, effect on the performance of marine systems, wave groups have long been a popular topic in oceanographic and ocean engineering research. Anecdotal observations, such as referring to successive large wave peaks as 'the three sisters,' describe wave groups or runs of large waves that were claimed to cause damage, sometimes severe, to ships or marine platforms[1]. Wave groups can be identified by the Gaussian derived process, which was shown by *Kim and Troesch* (2013) to provide parametric excitation which can lead to extreme roll. This expected shape of the Gaussian derived process was first presented by *Seyffert et al.* (2016) (with the derivation of the theoretical wave group by *Troesch*). An overview of that derivation is given here.

[1] *'But do not despise the lore that has come down from distant years; for oft it may chance that old wives keep in memory word of things that once were needful for the wise to know.'*- J. R. R. Tolkien. *The Fellowship of the Ring: Being the First Part of The Lord of the Rings.* Allen & Unwin, 1954.

2.4.1 Fourier Transforms & Expected Values

Below is the standard definition used in this thesis of the Fourier Transform pair of a function $x(t)$, where $\mathscr{F}\{\bullet\}$ denotes the Fourier Transform of "$\bullet$":

$$\begin{aligned} X(\omega) &= \frac{1}{2\pi}\int_{-\infty}^{\infty} dt\ x(t)e^{-i\omega t} \\ x(t) &= \int_{-\infty}^{\infty} d\omega\ X(\omega)e^{i\omega t} \end{aligned} \tag{2.23}$$

Given a continuous, stationary, and ergodic random process $x(t)$, the expected value in terms of the time-dependent function, referenced to a particular time t_o, and mean in terms of ensemble averages of realizations of the time-dependent function, again referenced to t_o, are related by:

$$E[x(t)] = \int_{-\infty}^{\infty} dz\ z\ f_{x(t)}(z) = \lim_{N\to\infty}\frac{1}{N}\sum_{j=1}^{N} x_j(t) \tag{2.24}$$

Note that time in the *pdf*, defined as $f_{x(t)}(z)$, must be related to time in the ensemble averages for Eq.(2.24) to be consistent. This will become apparent when the conditional expected value of the time series, $x(t)$, is compared to ensemble averages of the realizations of the same function. For relevant discussions on conditional expected values, refer to *Boccotti* (2015); *Lindgren* (1970, 1972a,b); *Tromans et al.* (1991); *Jensen* (1996, 2005). Taking the Fourier Transform, $\mathscr{F}\{\bullet\}$ Eq.(2.23), of the expected value and ensemble average, Eq.(2.24), yields:

$$\begin{aligned} \frac{1}{2\pi}\int_{-\infty}^{\infty} dt\ e^{-i\omega t}E[x(t)] &= \frac{1}{2\pi}\int_{-\infty}^{\infty} dt\ e^{-i\omega t}\frac{1}{N}\sum_{j=1}^{N} x_j(t) \\ &= \frac{1}{N}\sum_{j=1}^{N}\frac{1}{2\pi}\int_{-\infty}^{\infty} dt\ e^{-i\omega t}x_j(t) \\ &= \frac{1}{N}\sum_{j=1}^{N} X_j(\omega) \\ &= \frac{1}{N}\sum_{j=1}^{N}\mathscr{F}\{x_j(t)\} \end{aligned} \tag{2.25}$$

2.4.2 Linear Systems & Conditional Expected Values

If $x(t)$ and $y(t)$ are the input and output, with Fourier Transforms $X(\omega)$ and $Y(\omega)$ respectively, of a linear system with frequency transfer function of $H(\omega)$, it can be shown (e.g. *Wirsching et al.* (2006)) that:

$$Y(\omega) = H(\omega)\ X(\omega) \tag{2.26}$$

Substituting Eq.(2.26) into Eq.(2.25), it follows that the Fourier Transform of the expected value of the output is equal to the system transfer function times the Fourier Transform of the expected value of the input:

$$\begin{aligned} \mathscr{F}\{E[y(t)]\} &= \frac{1}{N}\sum_{j=1}^{N} H(\omega)\ X_j(\omega) \\ &= H(\omega)\ \frac{1}{N}\sum_{j=1}^{N} X_j(\omega) \\ &= H(\omega)\ \mathscr{F}\{E[x(t)]\} \end{aligned} \tag{2.27}$$

Now consider conditional expected values. In particular, consider the conditional expected value of the function, $y(t)$, expressed as $E[y(t)\,|\,y(t_o)=\widehat{y}, \dot{y}(t_o)=0]$ where, for a stationary process, t_o is arbitrary and can take any value without loss of generality. If $y(t)$ is Gaussian with zero mean and covariance $r(\tau)$, several authors (e.g. *Boccotti* (2015); *Lindgren* (1970, 1972a,b); *Tromans et al.* (1991); *Jensen* (1996, 2005)) have shown that as $\widehat{y} \to \infty$:

$$E[y(t)\,|\,y(t_o) = \widehat{y}, \dot{y}(t_o) = 0] \to \widehat{y}\frac{r(t-t_o)}{r(0)} \tag{2.28}$$

This expression has been shown to model large waves in the real ocean to a remarkable degree, e.g. *Phillips et al.* (1993); *Jonathan and Taylor* (1995). *Boccotti* (2015) (Sect. 8.1) demonstrates that the condition on the function derivative, $\dot{y}(t_o) = 0$ can be relaxed as $\widehat{y} \to \infty$ to give:

$$E[y(t)\,|\,y(t_o) = \widehat{y}] \to \widehat{y}\frac{r(t-t_o)}{r(0)} \tag{2.29}$$

This is not unexpected since the extreme value *pdf*'s for Normal and Rayleigh processes, with the same most probable extreme value, $\widehat{y}$, are asymptotically equivalent in the limit of infinite $\widehat{y}$. It is now possible to introduce the spectral density functions of the expected values of $x(t)$ and $y(t)$ for large $\widehat{y}$ by considering the Wiener-Khinchine relations. In the derivation of the Wiener-Khinchine relations, the spectral density

function $S_{xx}(\omega)$ is defined in terms of the Fourier Transform of the stochastic process $x(t)$ as in Eq.(2.30), where $X(\omega) = \mathscr{F}\{x(t)\}$ and the over-bar denotes the complex conjugate:

$$S_{xx}(\omega) = \lim_{T\to\infty} \frac{2\pi}{T} X(\omega)\overline{X(\omega)} \tag{2.30}$$

2.4.3 Relationship Between the Derived Process, Group Behavior, and the Shifted Autocorrelation

A derived Gaussian process $z_k(t)$, defined as scaled, shifted sum of a stochastic input $\eta(t)$, was first defined by *Kim and Troesch* (2013). Here, τ is a pre-defined period of interest and k is the group index (i.e. number of times $\eta(t)$ is summed). This is the derived Gaussian process, as first defined by Eq.(1.2) in Chapter 1.2.3:

$$z_k(t) = \sum_{p=1}^{k} \eta(t + (p-1)\tau) \tag{2.31}$$

Using linear systems theory, conditional expected values, and the Wiener-Khinchine relations, the expected shape of a rare wave group is:

$$E[\eta(t)\,|\,z_k(0) = \widehat{z}_k, \dot{z}_k(0) = 0] = \frac{\widehat{z}_k}{{\sigma^2}_{z_k}} \sum_{p=1}^{k} r_{\eta\eta}(t_p) \tag{2.32}$$

The expected form of the derived process, conditioned on the k^{th} derived process being a maximum at t_o, where t_o can arbitrarily be set equal to zero, is proportional to the sum of k autocorrelation functions of $\eta(t)$, $r_{\eta\eta}$, separated in time by $(p-1)\tau$, $p = 1, \ldots, k$ seconds. The constant of proportionality is the value of the maximum of the derived process, with group index k, divided by its variance, ${\sigma^2}_{z_k}$. Similarly, for comparison with ensemble time series conditioned on $z_k(t_o) = \widehat{z}_k$ and $\dot{z}_k(t_o) = 0$, a similar application of Eq.(2.28) yields:

$$\lim_{N\to\infty} \frac{1}{N} \sum_{j=1}^{N} [\eta_j(t) \;|\, z_k(t_o) = \widehat{z}_{k_j}, \dot{z}_{k_j}(t_o) = 0] \;=\; \frac{\widehat{z}_k}{{\sigma^2}_{z_k}} \sum_{p=1}^{k} r_{\eta\eta}(t_p) \tag{2.33}$$

Again, *Boccotti* (2015) removes the condition on the derivative (i.e. $\dot{z}_k(t_o) = 0$) in the limit of infinite $\widehat{z}_k$. Considering the stochastic input $\eta(t)$ as a wave elevation, the Gaussian derived process $z_k(t)$ is related to a wave group of k peaks, with each peak separated in time by τ seconds.

2.4.4 Estimation of the Derived Process Maximum, $\widehat{z}_k$

Eq.(2.32)-(2.33) show that the temporal dependence of the expected wave group is determined by the shifted sum of the autocorrelation function of the wave elevation, $\eta(t)$, while the mean amplitude of the wave group is related to the variance and maximum of the derived process, $z_k(t)$. An important objective is how to estimate the maximum, $\widehat{z}_k$, from the spectral moments of the derived process and the exposure.

A useful way to estimate extreme values of a random process is to assume a counting process whose arrivals above a certain threshold are Poisson distributed (e.g. *Wirsching et al.* (2006), *Ochi* (1990)). That is, assume the samples are collected from independent and identically distributed (*iid*) processes whose arrival times follow a Poisson distribution. However, successive local maxima in $z_k(t)$, and consequently their arrival rates, are clearly not independent and the dependence increases with increasing wave group index k. This results in a clumping or clustering of the peaks which can impact the threshold crossing rate, e.g. *Wirsching et al.* (2006). Declustering the data can be accomplished by constructing block maxima, but this will significantly increase the complexity of the analysis (*Coles*, 2001). The approach used in this dissertation is to assume that the dependence of successive $z_k(t)$ maxima has a limited effect on extreme value predictions and follow the traditional method for estimating probable extreme maxima, as shown in Chapter 2.2 (*Ochi*, 1990).

Given a method for estimating the derived process maxima, the expected shape of a wave group of k waves separated in time by τ seconds is fully defined for a given exposure and operating profile. This theoretical ensemble wave group may represent physical ensembles of group-like behavior. But for use in non-linear systems, the expected input does not yield the expected output. An ensemble of inputs is required to determine a distribution of responses. The question then is: is this theoretical wave group shape representative of a physical ocean environment, and individual wave records? Can these individual time records be used as the ensemble of inputs to lead to a distribution of extreme responses? That is next considered.

CHAPTER III

Identification of Wave Groups in Physical Oceanographic Data

The Gaussian derived process defined in Chapter 2.4.3 can be used to identify rare wave groups in physical oceanographic data. The derived process acts as a filter, similar to a moving average, to quickly sort through wave elevation time series to find time segments which contain rare wave groups. Wave groups of a pre-described k wave peaks separated in time by τ seconds are identified by extreme values of the derived process. These individual time records can be ensemble averaged to compare to the expected wave group definition developed in Chapter 2.4.3. Individual time series which contain these derived process maxima contain clear wave group structure, though 'hidden' within the irregular time series. These oceanographic time series provide a physical basis for constructing ensembles of statistically equivalent time series by the DLG.[1]

3.1 Data Collection

The physical oceanographic data used for the wave group identification is collected by the Pt. Reyes Buoy, which is operated by the Coastal Data Information Program through the University of California, San Diego (*CDIP*, 2018). The Pt. Reyes Buoy operates off the coast of San Francisco, California in approximately 550 m water depth. It is equipped with a GPS tracker to record its moored location and is designed to ride the waves so that the buoy motion tracks the wave height. Specifically, the buoy's accelerometer captures the accelerations of the body. The data is then filtered

[1]Portions of the work presented in this chapter were previously published in *Seyffert and Troesch* (2016a) and *Seyffert and Troesch* (2016c).

Parameter	Value
Heave Range	-20 − 20 m
Heave Resolution	1 cm
Period Range	1.6 − 30 sec
Sampling Frequency	1.28 Hz
Digital Filtering Type	Phase Linear, combined band-pass double-integrating FIR filter

Table 3.1: Buoy specifications.

and two integrations yield the buoy displacement (surface elevation). Shown in Figure 3.1 is a schematic of the buoy along with its reference axes. The buoy specifications are given in Table 3.1. The buoy's ability to capture high wave frequencies is limited by its diameter. Conversely, its ability to measure low frequencies is limited by its mooring. For these limiting cases, the energy is spread over multiple frequencies. Tracking the pitch and roll indicates wave direction. The mooring for the buoy is a combination of an anchor weight at the seabed, then polypropylene rope, and then a stabilizing chain which attaches to the buoy.

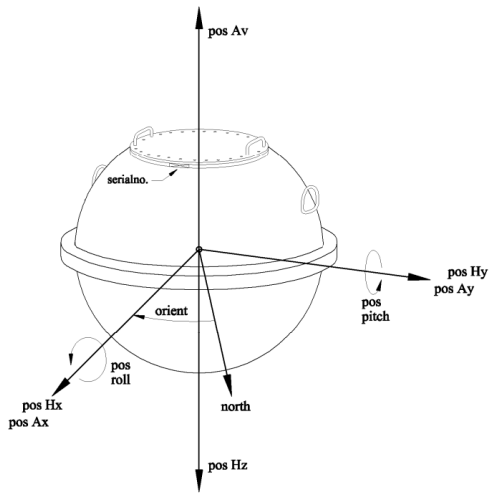

Figure 3.1: Orientation of reference axes for Datawell Directional Buoy (*CDIP*, 2018).

The time series from the buoy are sorted into 30-minute segments (the majority of the data was reported in 30-minute increments) and then linked with additional buoy data to attribute a significant wave height H_s and peak modal period T_p to the temporal elevation data. This allows a filtering of the data to examine rare wave groups within certain ranges, or 'bins,' of H_s and T_p values, for the consideration of stationary statistics.

3.2 General Environmental Conditions

Given the time series data from the Pt. Reyes Buoy, it is possible to find the rarest wave groups for groups of 1 through 15 waves. An initial challenge is the categorization of the different ranges of H_s and T_p values that make up the domain of the 17-year buoy service. In Figure 3.2, the distribution of all recorded time series, given a particular H_s and T_p, are shown, with the color bar representing the number of 30-minute time segments that fit in the individual bins. Based on the CDIP buoy specification sheets, the buoys are only able to resolve certain frequencies, and therefore can only attribute a discrete number of peak modal period values to the time series. Some T_p ranges have no time series due to resolution coarseness in the data process.

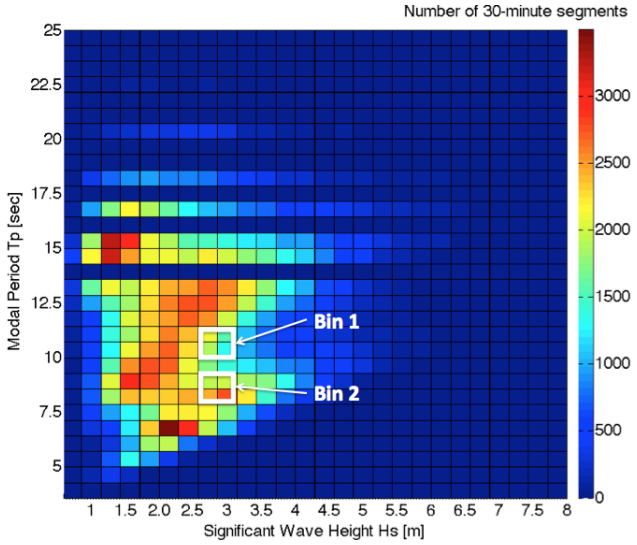

Figure 3.2: Distribution of available time series for H_s and T_p ranges for January 1997-December 2013, along with two bins chosen to classify time series with a given range of H_s and T_p values.

Two bin categories, which contain enough time series for converged statistics, are selected to identify rare wave groups within the available Pt. Reyes Buoy data. These bins have the same H_s range, but different T_p ranges. Comparison of time series from the two bins allows for an initial evaluation of the effects of wave steepness and number of wave cycles in a 30-minute time series on rare wave groups. Figure 3.3 shows a representative spectrum corresponding to an individual time series and the ensemble spectrum for each bin. The parameter ranges of the two bins are given in Table 3.2.

For the two selected bins, the range of significant wave heights remains constant, but the time series have a range of longer (10.0 to 11.5 sec) and shorter (7.9 to

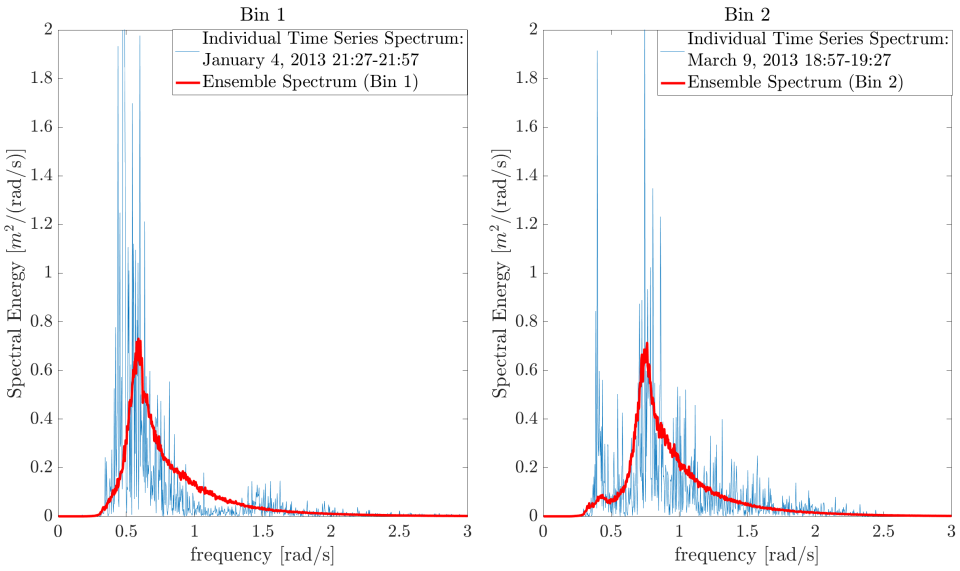

Figure 3.3: Single-sided spectrum for bins 1 & 2.

8.6 sec) peak modal periods. This range of periods yields a measurable difference in the number of oscillations in the two sets of time series as a whole. The time separation between the points in the derived process, τ, can be changed to match a particular dynamic problem. Here, τ is chosen as the peak modal period of the ensemble spectrum for each bin. With the two selected bins, the time series are sorted, and the derived process identifies wave groups for groups of $1 - 15$ waves.

	Parameter	Value
bin 1	H_s Range	2.6 − 3.0 m
	T_p Range	10.0 − 11.5 sec
	Number of 30-minute time series	3350
	Total Time	1675 hours
	4σ (Ensemble Average)	2.75 m
	Ensemble Peak Period	10.65 sec
bin 2	H_s Range	2.6 − 3.0 m
	T_p Range	7.9 − 8.6 sec
	Number of 30-minute time series	2430
	Total Time	1215 hours
	4σ (Ensemble Average)	2.81 m
	Ensemble Peak Period	8.22 sec

Table 3.2: Bin parameter ranges.

3.3 Derived Process Maxima & Wave Group Statistics

The derived process for index k of 1 through 15, corresponding to wave groups of 1 through 15 waves, Eq.(2.31), is calculated for each 30-minute time series that fits into either bin, using $\tau = T_p$ for the specific bin. From these 30-minute derived process time series, the maximum z_k value for a given wave group index k is determined.

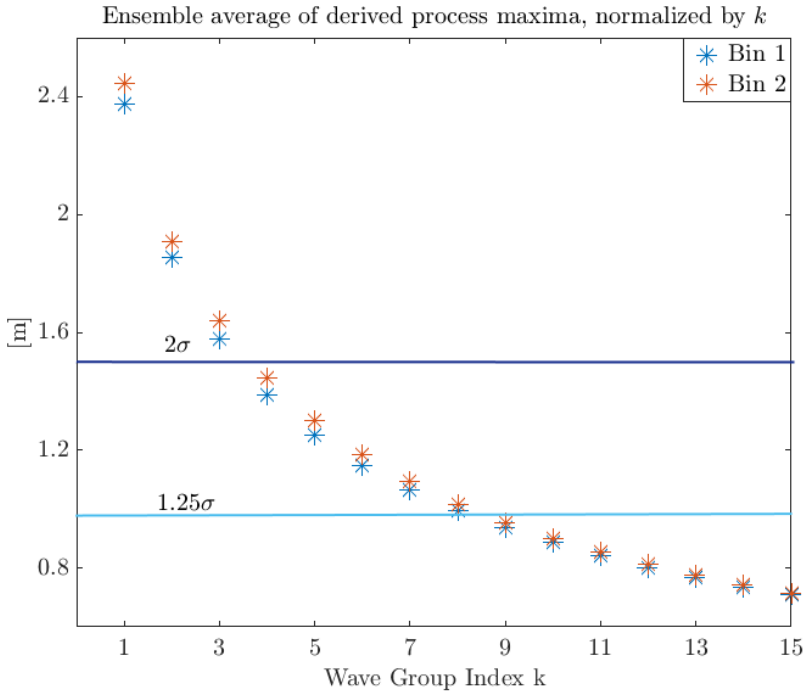

Figure 3.4: Average of derived process maxima for 30-minute time series in bins 1 & 2, normalized by k, along with lines representing 2σ (significant wave amplitude) and 1.25σ (mean wave amplitude), with σ as the average of $\sigma_{\text{bin 1}}$ and $\sigma_{\text{bin 2}}$.

Figure 3.4 shows the maxima of the derived process for all time series in bins 1 and 2, averaged by the wave group index k. This is a valuable measure of the wave groups since it quantifies the inverse relationship between average group amplitude and length of group run. Indeed, the largest normalized value for the derived process occurs for a single wave and decreases as the wave index increases. This indicates that wave groups with many wave peaks should not be expected to have large mean wave group heights. These values are plotted along with lines representing 2σ (significant wave amplitude) and 1.25σ (mean wave amplitude). Here, σ is the average of the σ values for bins 1 and 2.

It is remarkable that for runs even as long as $k = 8$ waves, the average group amplitude exceeds the mean wave amplitude value. Note that the average normalized group amplitudes for bin 2 are slightly larger than for bin 1. This is because the time series in bin 2 have a range of T_p values which is shorter than in bin 1. A shorter cycle period means there are more cycles in the 30-minute exposure. The most probable maximum is proportional to the number of cycles in an exposure, as shown in Chapter 2.2, so it makes sense that the maxima for bin 2 are slightly larger than for bin 1.

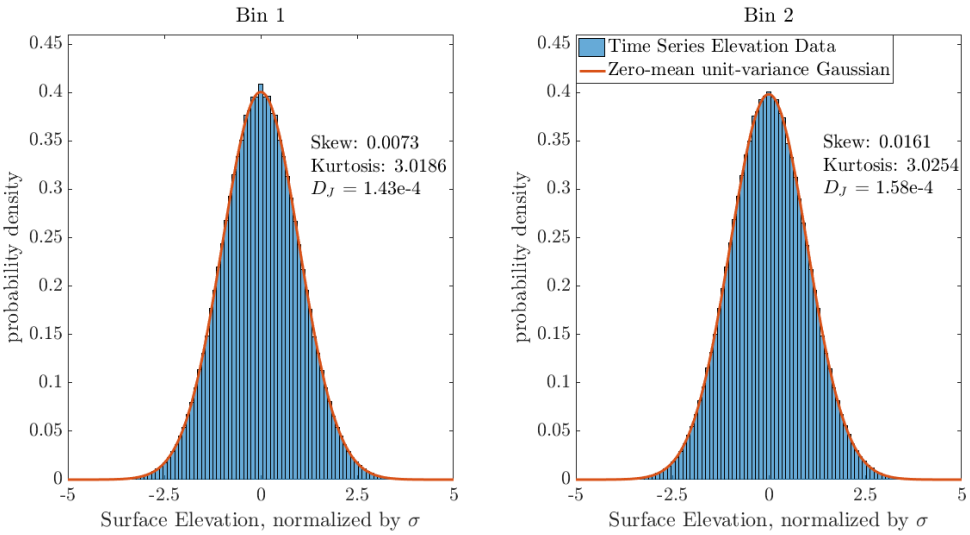

Figure 3.5: Empirical histogram (given as a *pdf*) of wave elevation time series data for all time series in bins 1 and 2, normalized by the respective σ, and overlaid with a zero-mean, unit-variance Gaussian distribution. The number of cycles in bins 1 and 2 are $n = 5.66e^5$ and $n = 5.33e^5$, respectively.

The empirical histogram, given as a *pdf*, of all the wave time series for each bin is given in Figure 3.5, with the time series all normalized by their respective standard deviation, σ. A zero-mean Gaussian *pdf* with $\sigma = 1$ is overlaid and the skewness and

kurtosis for the respective histograms are given. To compare the empirical histograms of the time series data with the Gaussian distribution, the Jeffreys divergence, or the symmetric Kullback-Leibler Divergence, D_J, as given in Eq.(3.1) is calculated for each bin (*Kullback and Leibler*, 1951).

$$D_J(p||q) = \int_x (p(x) - q(x))(ln(p(x)) - ln(q(x)))dx = \sum_i (p(i) - q(i))ln\frac{p(i)}{q(i)} \tag{3.1}$$

where

$D_J(p||q)$ = Jeffreys divergence, or symmetric Kullback-Leibler divergence

$p(x)$ = a distribution over x

$q(x)$ = a different distribution over x

This divergence measures how much information is lost if one distribution approximates another distribution. It follows that D_J can give a good measure to determine if one *pdf* (e.g. a *pdf* based on bin 1) is more Gaussian than another (e.g. a *pdf* based on bin 2). In Figure 3.5, the two D_J values for bins 1 and 2, (i.e. $D_J = O(10^{-4})$) suggest that the empirical wave elevation samples follow a Normal process, as is expected for wave elevation data measured in 550 m water depth.

For wave group indices of $k = 1$, 3, 6 and 9, the time series are lined up such that the maximum of the derived process for each time series occurs at the same time, $t = t_0$, and the ensemble average is calculated. Specifically, the ensemble average of the time series is based on the maximum of $z_k(t_0)$, defined as $\widehat{z_k}$, with the results shown in the left column of Figure 3.6. Two hundred seconds of the wave elevations are shown; the time of the $\widehat{z_k}$ maxima, t_0, has been arbitrarily set equal to 100 sec. The average is an approximation to $E[\eta(t)|z_k(t_0) = \widehat{z_k}]$, Eq.(2.32). The top 50 values of the derived process for each bin are also identified, and those wave groups along with the ensemble average of those top 50 realizations are shown in the right column of Figure 3.6.

The maxima of the derived process clearly identify wave groups. The ensemble averages show little correlation between different wave elevation time series except in the time period immediately following t_0, i.e. $t_0 < t < (k-1)\tau$. In addition, the mean group amplitude matches the trends shown in Figure 3.4, in which wave groups of longer runs have progressively smaller mean amplitudes. The mean wave group amplitudes for the time series with the top 50 derived process values for both bins, shown in the right column of Figure 3.6, are noticeably larger compared to the mean group amplitude for all the time series for both bins, shown in the left column

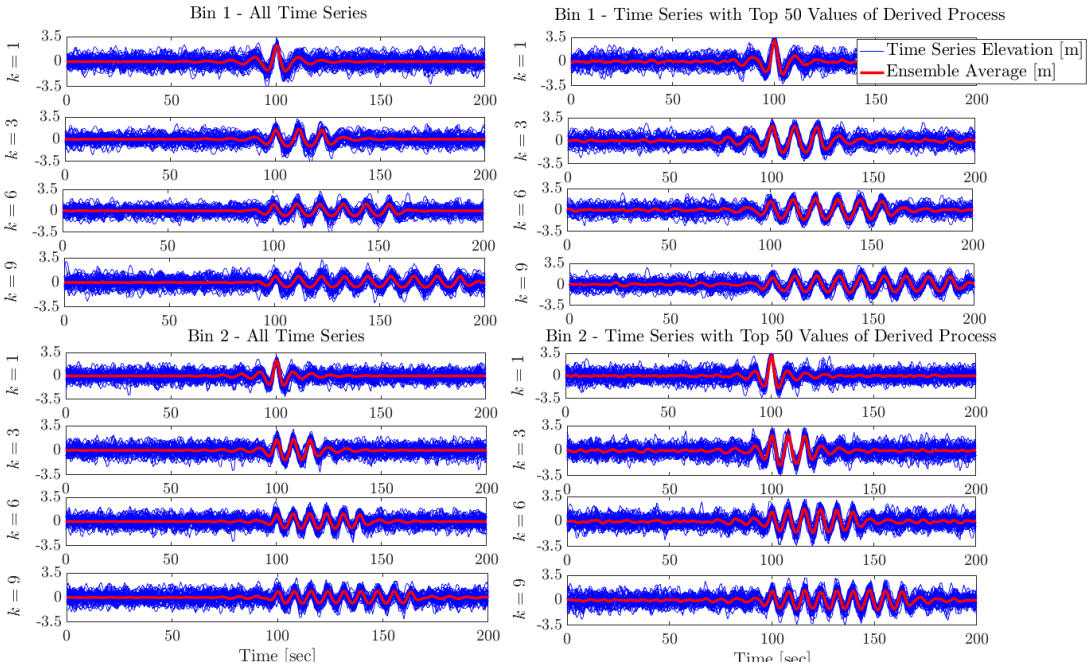

Figure 3.6: In the left column: wave groups and ensemble average for all time series with arbitrary 50 time series plotted for $k = 1$, 3, 6, & 9 with $\tau = T_p$ for bins 1 & 2. In the right column: time series containing top 50 maxima of derived process for $k = 1$, 3, 6, & 9 with $\tau = T_p$ and ensemble average for bins 1 & 2. The time of maximum $z_k(t)$, t_o, is shifted to 100 sec without loss of generality.

of Figure 3.6. This makes sense, as the time series with the top 50 derived process values for either bin represent the set of wave groups with approximate probability of exceedance of $50/3350 = 1.49\%$ and $50/2430 = 2.06\%$, for bins 1 and 2, respectively.

Time series with the maximum value of the derived process for each bin are shown in Figure 3.7. Wave groups for index $k = 1$, 3, 6, and 9 are shown along with the ensemble average of time series containing the top 50 values of the derived process for that index k. Without the superposition of the ensemble average, it would be difficult to identify the individual wave groups in a single realization. In addition, the $k = 6$ wave group for bin 2 might fail to meet the threshold criteria of the traditional wave group definition, since the fifth wave peak amplitude is less than the mean group amplitude.

Figures 3.6-3.7 represent an important validation of the DLG method, because they show that physical waves which lead to extreme values of linear surrogate processes do exist, both in an ensemble and in an individual sense. Therefore, it can be confidently assumed that the waves constructed by the DLG to lead to extreme linear responses are realistic wave profiles.

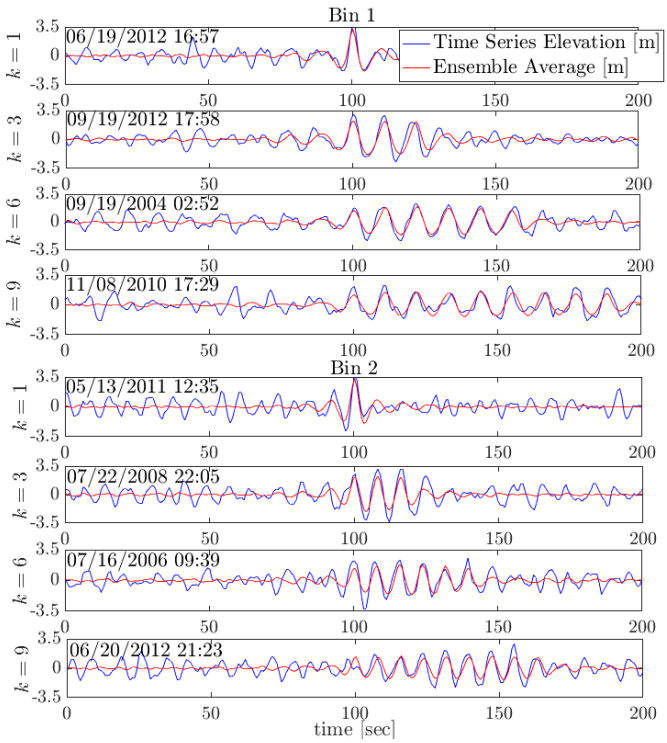

Figure 3.7: Representative time series containing the maximum of the derived process, for $k = 1, 3, 6,$ and 9 with $\tau = T_p$ and (top 50) ensemble average wave groups of $k = 1, 3, 6,$ and 9 waves with $\tau = T_p$ for bins 1 and 2. The time of maximum $z_k(t)$, t_o, is shifted to 100 sec without loss of generality.

3.4 Order Statistics

Continuing in this section, order statistics for the two bins are examined. The overall objective is to determine which statistical models reasonably approximate the various distributions associated with rare wave groups. Figure 3.5, with the low D_J values, suggests that it is reasonable to assume a Normal process for the initial wave elevation. However, this modeling assumption may not necessarily be valid for the tails of the original process histogram. The Gaussian derived process assumes that the seaway can be approximated as a zero-mean Gaussian process. It follows that the derived process, Eq.(2.31), is the sum of normal processes and thus a normal process itself. Given the variance of $z_k(t)$, then, it should be possible to estimate various extreme value statistics and distributions.

Note that Eq.(2.13), which relates the number of cycles, n, over an exposure to the most probable maximum value, is valid only in an asymptotic sense and may be a poor approximation for the maxima associated with the relatively short 30-minute time histories examined here. Therefore, to find the value of n that best describes a Normal extreme value distribution for the 30-minute maxima, the following strategy

is employed. The Gaussian extreme value *pdf*, Eq.(2.7), is evaluated for a range of n values, $g(y_{n_k})$, using the derived process ensemble variance for group index k. Then $g(y_{n_k})$ is compared with the ensemble extreme value histogram using the Jeffreys Divergence (i.e. Eq.(3.1)). The best fit is deemed to be the value of n which results in a minimum value of D_J. This analysis was completed for z_k, $k = 1, \cdots, 15$, using $\tau = T_p$ for bins 1 and 2, with the results shown in Table 3.3.

	k	σ_{z_k}/k	$\overline{\widehat{z}_k}/\sigma_k$	n_k	D_{J_k}	$\overline{\widehat{z}_k}/(\sigma_{z_k} \times E[y_{n_k}])$
	1	0.693	3.424	1548	0.048	1.018
	2	0.553	3.354	1164	0.064	1.021
	3	0.478	3.297	902	0.076	1.027
	4	0.428	3.241	715	0.090	1.031
	5	0.392	3.198	617	0.092	1.032
	6	0.363	3.162	534	0.103	1.034
	7	0.340	3.132	473	0.115	1.037
bin 1	8	0.321	3.102	428	0.113	1.038
	9	0.305	3.072	384	0.116	1.039
	10	0.291	3.047	354	0.112	1.040
	11	0.279	3.021	325	0.113	1.041
	12	0.267	2.994	298	0.117	1.041
	13	0.258	2.974	277	0.118	1.043
	14	0.249	2.955	263	0.113	1.042
	15	0.241	2.935	247	0.110	1.043
	1	0.703	3.478	1855	0.062	1.019
	2	0.567	3.360	1251	0.044	1.017
	3	0.496	3.302	999	0.050	1.019
	4	0.443	3.260	840	0.056	1.022
	5	0.403	3.230	755	0.061	1.022
	6	0.371	3.198	668	0.065	1.024
	7	0.345	3.171	602	0.072	1.025
bin 2	8	0.324	3.144	538	0.074	1.028
	9	0.305	3.117	491	0.074	1.028
	10	0.290	3.100	464	0.074	1.029
	11	0.277	3.082	437	0.075	1.029
	12	0.265	3.060	406	0.075	1.029
	13	0.255	3.043	382	0.075	1.030
	14	0.246	3.026	359	0.076	1.031
	15	0.238	3.012	343	0.078	1.031

Table 3.3: Order statistics for bins 1 & 2.

The derived process maxima, $\widehat{z}_k$, which are based on the physical data samples, correspond to the Normal random variable $y_{n_k}\sigma_{z_k}$. In this sense, then, the mean of the empirical histogram, $\overline{\widehat{z}_k}$, can be compared to the expected value $E[y_{n_k}]$. Table 3.3 contains the following statistical information for each wave group index k in bins 1 and 2: the normalized ensemble σ for $z_k(t)$, σ_{z_k}/k, the histogram mean $\overline{\widehat{z}_k}$

normalized by the ensemble σ, the value of n corresponding to the minimum D_J value, the minimum D_J value, and the histogram mean normalized by the corresponding Gaussian expected extreme value. From Table 3.3, it is observed that:

1. Column 2, σ_{z_k}/k, follows a similar trend as seen in Figure 3.4. The σ of the derived processes, normalized by the wave group index, k, decreases with increasing group index, k.

2. Column 3, $\overline{\widehat{z_k}}/\sigma_{z_k}$, shows the effective rarity of the k^{th} wave group in 30 minutes. The reduction in $\overline{\widehat{z_k}}/\sigma_{z_k}$ as k increases is explained, in part by a finite record (30-minutes) and the nature of the derived process (z_k), including, but not limited to, its tendency to shorten the record as k increases.

3. Column 4, n_k, shows that the number of cycles that best fits the specific group index k diminishes for increasing k. This indicates that the most probable maximum associated with groups of more waves is smaller than the most probable maximum associated with groups of less waves. This is a similar trend to that of $\overline{\widehat{z_k}}/\sigma_{z_k}$, in that the rare wave groups of longer runs seem to be disproportionally smaller than wave groups of shorter runs.

4. Column 5, D_{J_k}. The results for both bins 1 and 2 show that D_{J_k} increases with increasing wave run index, k, although the relative increase is significantly less pronounced for bin 2 than for bin 1. This may be due to the quality of the data in the respective bins or may be due to trends related to wave steepness.

5. Column 6, $\overline{\widehat{z_k}}/(\sigma_{z_k} \times \overline{y_{n_k}})$, shows that while the D_{J_k} comparison suggests a small, but consistent, deviation from a Normal extreme value *pdf*, the mean of the empirical histogram is approximated by the expected value of an equivalent Normal process to within 2%-4%.

3.5 Rare Wave Groups

In this section, a subset of the Pt. Reyes Buoy time series with large wave heights ($H_s > 6$ m) are examined. The subset of significant wave heights and peak modal periods used here are shown below in Table 3.4 and indicated on the histogram in Figure 3.8. There is a significant spread in the ranges of peak modal periods, as can also be seen in the ensemble spectrum of this group of time series in Figure 3.9.

Parameter	Value
H_s Range	6.36 – 8.28 m
T_p Range	10.22 – 19.36 sec
Number of 30-minute time series	70
Total Time	35 hours
4σ (Ensemble Average)	7.09 m
Ensemble Peak Period (T_p)	14.88 sec
Ensemble Zero Crossing Period (T_o)	9.94 sec

Table 3.4: Ranges of significant wave height and peak modal period for examined time series.

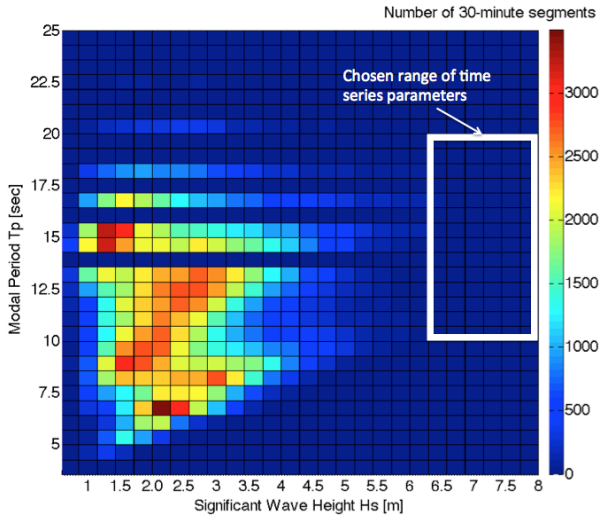

Figure 3.8: Available time series for Pt. Reyes Buoy *CDIP* (2018), and chosen range of time series parameters.

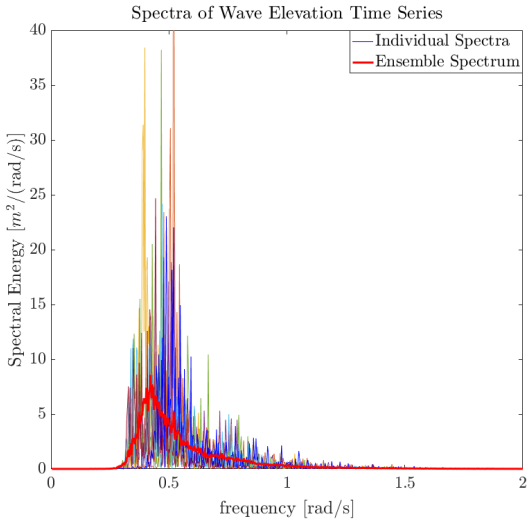

Figure 3.9: Seventy selected wave spectra from the Pt. Reyes Buoy with ensemble average spectrum. The ensemble average is based on seventy 30-minute records with mean $H_s = 7.09$ m and mean $T_p = 14.88$ sec.

3.5.1 Comparison with Ensemble Average

In Figure 3.10 the temporal ensemble average wave group for $k = 5$, $\tau = T_p = 14.88$ sec, is compared with the theoretical result, Eq.(2.32). In the top inset of Figure 3.10, the blue curves are the seventy time series in the bin range from Table 3.4, with a maximum in the derived process shifted, without loss of generality, to 200 sec. The red curve is the ensemble average of these time series. The middle inset is the temporal ensemble average overlaid with the theoretical wave group formulation from Eq.(2.32) for $k = 5$, $\tau = 14.88$ sec. This theoretical curve was calculated as the ensemble average of the summed autocorrelation functions of each of the 70 individual time series, Eq.(2.32), using scaling factors $\sigma^2_{z_k}$ and $\widehat{z}_k$ as defined by Eq.(2.5) and (2.13). The bottom inset shows the theoretical wave group formulation for $k = 5$,

$\tau = 14.88$ sec, along with the time series from 01/20/2010 02:39:00. This time series was chosen as a best representative of the ensemble curves since its value of $\widehat{z}_5$ is close to the mean derived process value of all 70 available time series for $k = 5$ wave groups.

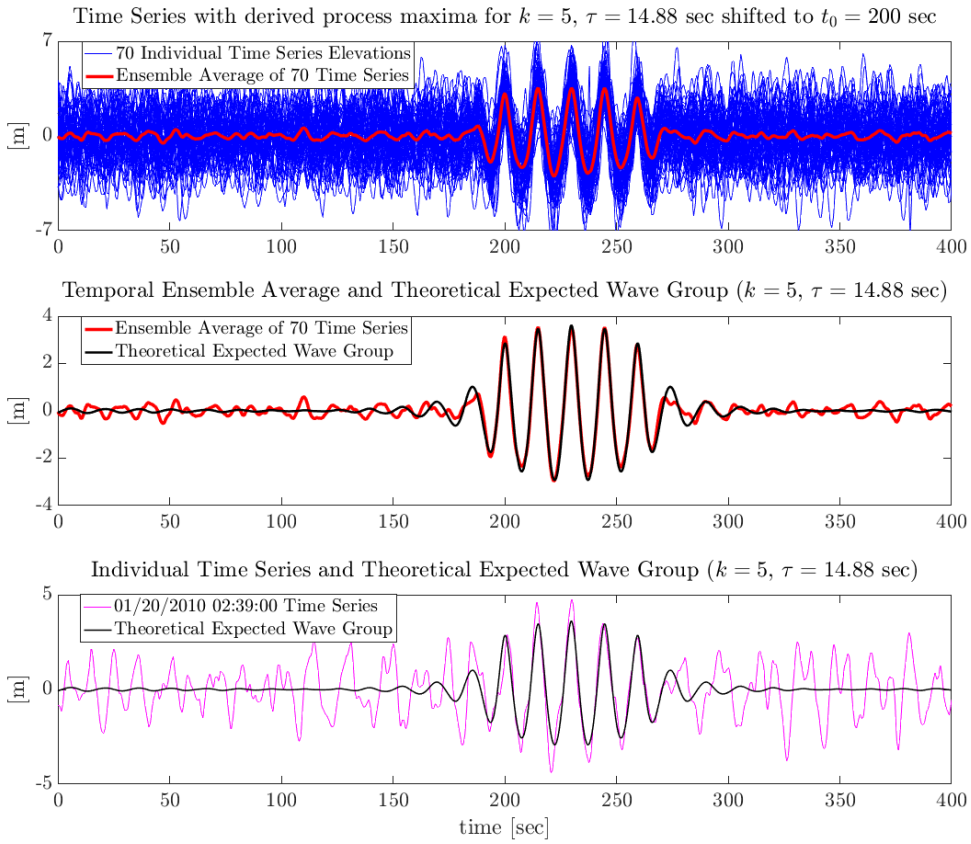

Figure 3.10: Comparison of Pt. Reyes Buoy wave records and ensemble temporal average with theoretical wave group formulation ($k = 5$, $\tau = 14.88$ sec) from Eq.(2.32) using scale factors from Eq.(2.5) and (2.13). This ensemble record is also compared with the wave elevation time series from 01/20/2010 02:39:00.

Clearly this individual record exhibits strong group-like behavior during the time of wave group occurrence. Apart from some small variations, this portion of the wave elevation record exhibits the near-constant 14.88 sec period between wave peaks, and these peaks are additionally quite large. However, without the ensemble group structure, it would be difficult to pick out this time series as one which exhibits strong group-like behavior.

3.5.2 Comparison with Various Order Statistics

A relevant calculation is to determine the difference in scaling ratios between theoretical and empirical values, shown in Table 3.5. The empirical values are based on data from the Pt. Reyes time series. Here, $\widehat{z}_k$ is calculated as the mean of the maximum in the derived process of the 70 time series for k waves and $\sigma^2_{z_k}$ is the mean of the variance of the derived process of the 70 time series. The first column is the wave index k. The second column is the standard deviation of the k^{th} wave group, normalized by k. The third and fourth columns are the average non-dimensional value of the maximum of the derived process, based on Eq.(2.13) for the theoretical calculation (TH) and empirical data or time series (TS) tabulation, respectively. The fifth column is the ratio of the third and fourth columns.

k	$(\sqrt{m_{z_{k_o}}}/k)_{TS}$	$(\widehat{z}_k/\sqrt{m_{z_{k_o}}})_{TH}$	$(\widehat{z}_k/\sqrt{m_{z_{k_o}}})_{TS}$	$\frac{(\widehat{z}_k/\sqrt{m_{z_{k_o}}})_{TH}}{(\widehat{z}_k/\sqrt{m_{z_{k_o}}})_{TS}}$
1	1.773	3.222	3.401	0.947
2	1.456	3.171	3.355	0.945
3	1.270	3.160	3.256	0.971
4	1.139	3.157	3.204	0.986
5	1.040	3.157	3.190	0.990
6	0.963	3.156	3.120	1.012
7	0.900	3.157	3.071	1.028
8	0.847	3.156	3.060	1.032
9	0.802	3.155	3.025	1.043
10	0.764	3.152	2.997	1.052
11	0.731	3.149	2.966	1.062
12	0.701	3.146	2.948	1.067
13	0.675	3.144	2.904	1.083
14	0.652	3.141	2.870	1.095
15	0.631	3.138	2.846	1.103

Table 3.5: Non-dimensional scale factors based on theory (TH) (i.e. Eq.(2.5) and (2.13)) and empirical time series (TS). Separation period $\tau = T_p = 14.88$ sec.

The increase of $(\widehat{z}_k)_{TH}$ relative to $(\widehat{z}_k)_{TS}$ for increasing k is due to the increasing dependence between successive $z_k(t)$ crests. For a fixed duration or exposure period, dependence between successive maxima will act to lower extreme value estimates relative to extreme value estimates for independent maxima.

3.6 Peak to Trough Variations of Wave Groups

In all considered cases in which well-defined wave groups are identified, there is a variation in the peak and trough amplitudes, as noted from theory and empirical time series. Traditionally, this bias towards higher crests and shallower troughs is classified as a second-order effect. However, considering the autocorrelation function, it is clear that the mean shift can also be explained as due to the shape of extreme values of the derived Gaussian process. Based on Eq.(2.32), the structure of the autocorrelation function is the driving factor in the wave group structure.

Wave groups with wave index $k = 8$ and $\tau = T_p = 14.88$ sec, as defined in Table 3.4, are identified in the 70 time series considered in this section. Figure 3.11 examines wave groups of 8 waves separated by $\tau = T_p = 14.88$ sec. The top inset shows the 70 time series (blue lines), where the maximum of z_k, for $k = 8$ and $\tau = 14.88$ sec, for each time series is shifted to $t_o = 200$ sec. The red curve is the ensemble average of these 70 time series. The middle inset shows this temporal ensemble average with the expected wave group formulation from Eq.(2.32) with scale factors from Eq.(2.5) and (2.13). The bottom inset shows a segment from a single time series from January 20, 2010 15:09:00. This record has the largest value of z_k for $k = 8$ and $\tau = 14.88$ sec out of the 70 times series. This record is representative of a rare wave group with probability of non-exceedance $PNE = 0.986$ ($\approx 1 - 1/70$) when selected from a sample set of like wave groups taken from 30-minute records. The time series segment from January 20, 2010 15:09:00 is overlaid with the individual scaled, shifted autocorrelation function of that singular time series.

With this specific record, one can examine the temporal average wave group crest maximum (crest height), the average wave group minimum (trough), the ratio of peak to trough height, and the mean offset for $200 \leq t \leq 309.8$ sec. These values are compared with the average offset as predicted by a second order Stokes wave, defined in Eq.(3.2). The results are shown in Table 3.6.

$$\text{Stokes crest/trough } \approx \pm\frac{H}{2} + \frac{kH^2}{8} = \pm\frac{H}{2} + \frac{H^2\pi^2}{2gT^2} \tag{3.2}$$

Deep water approximations are assumed for simplification, which may be appropriate for data measured in 550 m water depth. For the Stokes offset, the mean wave amplitude, $H/2$, from the physical wave record and the peak modal period (T_p) are used to define the wave number κ for the linear deep water dispersion relation, $\kappa = 4\pi^2/(gT^2)$. For a mean wave amplitude of $H/2 = (4.714 + 3.758)/2 = 4.23$ m,

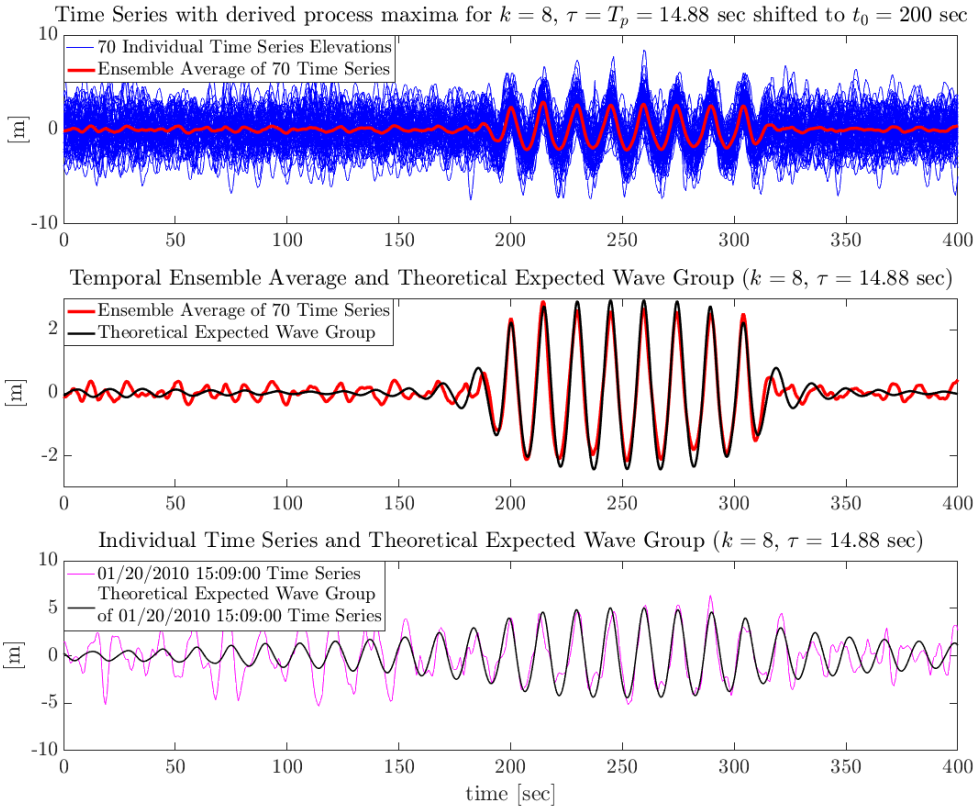

Figure 3.11: Comparison of temporal average and theoretical wave group formulation from Eq.(2.32) with scale factors from Eq.(2.5) and (2.13) for $k = 8$. The ensemble average is based on 70, 30-minute wave records, with mean $H_s = 7.09$ m, $T_p = 14.88$ sec. The theoretical wave group formulation is based on the single 01/20/2010 15:09:00 time series.

the Stokes offset is approximately 0.164 m. This is approximately 1/3 of the offset measured in the time series or 1/3 of the offset predicted by the theory (Eq.(2.32), (2.5), and (2.13)) for a similar mean wave height.

It is interesting that the mathematical wave group formulation captures the mean offset measured in physical wave groups much more closely than a Stokes second order wave, at least for this time series and wave group index. Also of significance is that the mathematical wave group formulation is based on linear operator theory but still manages to capture the mean offset, which is often thought to be a second order effect. Note that the mean amplitude and offset, based on Eq. (2.5), (2.13), and (2.32), and ensemble average of the seventy records are scaled up to match the mean amplitude of the January 20, 2010 15:09:00 record.

	Mean Peak Value [m]	Mean Trough Value [m]	Peak-Trough Ratio	Mean Amplitude [m]	Mean Offset [m]
01/20/2010 15:09:00	4.714	3.758	1.254	4.23	0.478
Eq.(2.32), (2.5), and (2.13)	2.708	2.171	1.248	4.23*	0.466*
Stokes Wave	-	-	-	4.23	0.164

Table 3.6: Comparison of (absolute value) mean peak and trough values for 01/20/2010 15:09:00 time series, theoretical wave group formulation ($k = 8$, $\tau = 14.88$ sec) from 01/20/2010 15:09:00, and ensemble average of 70 samples (Figure 3.11, 200 sec $\leq t \leq$ 309.8 sec).

3.7 Mutual Exclusivity of Rare Wave Groups with Different Group Indices, k

An important consideration in using rare wave groups identified by the derived process filter as excitation in dynamic systems is that the derived process does not choose unique time segments for different wave group indices k. Based on the formulation of the derived process, it is possible that the largest wave group of k waves with some given τ in a time record also contains the largest wave group of $k \pm 1, k \pm 2, \cdots$ waves. This means that the derived process may be maximized for different wave group indices k within the same time interval. An example of this is shown in Figure 3.12.

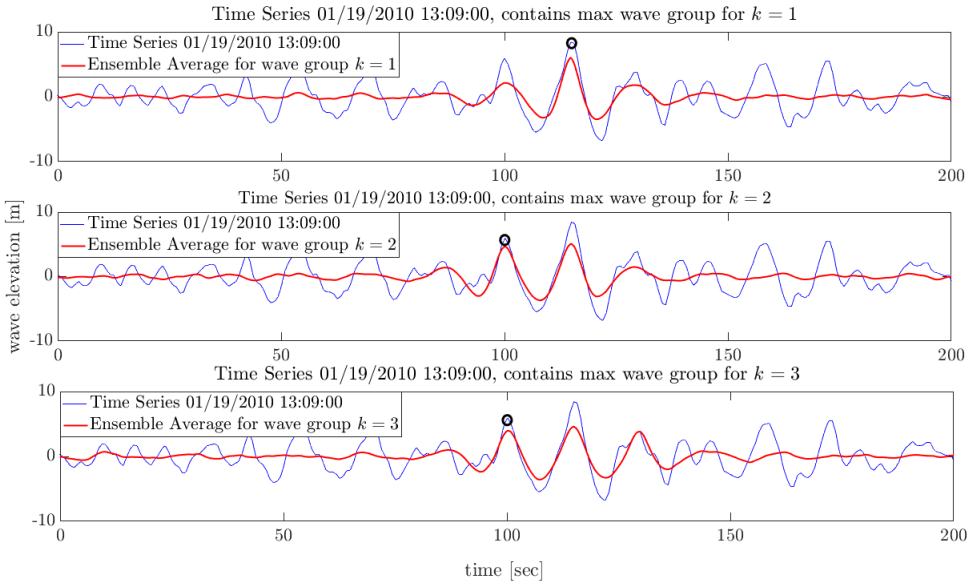

Figure 3.12: A segment from the Pt. Reyes Buoy 01/19/2010 13:09:00 wave record, which contains the maximum z_k value for $k = 1, 2, 3$ waves, $\tau = T_p = 14.88$ sec within the same time segment. The temporal ensemble average wave group for $k = 1, 2, 3$ is overlaid on each inset to highlight the group structure. The black circles indicate the onset of the wave groups.

The derived process maximum in the 01/19/2010 13:09:00 time series occurs at approximately the same time for wave group index $k = 1$, 2, and 3, $\tau = T_p = 14.88$ sec. Looking at the wave elevation record, it is clear that the group of one large wave also looks like a wave group of 2 or even 3 waves. This strongly suggests that wave groups of similar wave indices k may not be mutually exclusive. *Kim and Troesch* (2013) noticed the same challenge, specifically that it may be difficult to separate any statistics on dynamics collected due to the occurrence of k or $k \pm 1$ waves in the excitation, as these wave groups may have a joint occurrence.

Clearly, the mutual exclusivity of wave groups affects the consideration of dynamic events *due* to these wave groups. As well, to use maxima of the derived process as excitation to estimate the probability of extreme responses requires that these derived processes be exhaustive. It would be unwise to estimate an overall probability of extreme responses based on a finite number of excitation inputs, especially if other types of input may also lead to extreme outputs. But clearly this is a competing concern: estimating probabilities through responses to exhaustive inputs, but inputs which are mutually exclusive. Parametric pitch response of a spar platform due to the occurrence of rare wave groups is next considered, which illustrates the challenge of these competing concerns.

CHAPTER IV

Spar Platform Pitch Response due to Rare Wave Groups

Chapter III used the definition of the Gaussian derived process to identify rare wave groups in physical oceanographic data and noted the potential for these wave groups to set off interesting dynamic responses in marine systems. A temporal ensemble average of these wave groups, identified by a maximum in the derived process, was shown to match well with the theoretical expected wave group shape. Additionally, individual time series containing these wave groups also exhibit strong group-like behavior, although without the aid of the derived process it would be difficult to notice the wave sequences with regular characteristics embedded in the irregular time records.

These individual wave group time series may be interesting inputs to study extreme dynamic responses of marine systems, particularly for marine systems susceptible to parametric excitation. Such system responses are often tested using regular waves as the excitation to set off extreme responses, but perfectly sinusoidal wave trains are not representative of an irregular ocean environment. It was shown that wave groups, which exhibit this regular behavior, can be identified in irregular wave elevation time series by the derived process, Eq.(2.31). This chapter investigates whether rare wave groups, as found in individual physical oceanographic time series, may lead to extreme dynamic responses, specifically extreme pitch responses of a spar platform.[1]

[1]The work presented in this Chapter has been previously published in *Seyffert and Troesch* (2016b).

4.1 Parametric Excitation of Spar Platforms

Spar platforms are an attractive option for deep-sea operations due to their minimal motions in ocean waves. Typically, the natural periods for heave and pitch of spar platforms in the Gulf of Mexico are approximately 28 and 60 sec, respectively (*Rho and Choi*, 2005). These long resonant periods protect the spar platform from extreme motion by normal wave excitation, but risk excitation from longer period swells. The addition of mooring lines and tensioners can further lower the heave natural period, closer to what may be experienced in a typical ocean environment. *Perryman et al.* (2009) studied the Holstein spar platform, which operates in the Gulf of Mexico, and found that its mechanical tensioners lower the heave natural period to 18.2-20 sec, matching periods seen in extreme seas in the region.

Extreme responses due to parametric excitation are fundamentally different than those due to a single, episodic (e.g. rogue) wave, as noted in Chapter 1.1. In *Taylor et al.* (1997) a Jack-up platform is subjected to a large wave embedded in an otherwise unremarkable random wave time series. The large wave acts as an impulsive load on a dynamic system. In contrast, an extreme response in parametrically excited systems is generally due to a sequence of successive waves with sufficient amplitude and period. *Rho and Choi* (2002) and *Haslum and Faltinsen* (1999) investigate parametric resonance, or Mathieu instability, and show that it does occur experimentally for spar platforms. They also note that extreme heave-pitch coupling, again described as a Mathieu instability, can occur when the spar platform is excited by regular waves with a constant wave period. Such a wave train may be well represented as a wave group.

Rare wave groups may provide the forcing required to set off parametric resonance in spar platforms. For model tests on spar platforms in irregular waves, even for long-time simulations, it cannot be known a priori if a simulation period includes wave trains expected to cause a rare event. Usually, a sufficiently long run-time is required, and thus assumed to include in the generated seaway wave trains that test the survivability of the platform. If a designer has detailed physical oceanographic data for a potential spar location and is conducting model tests, there is no obvious way to determine which subset of that site-specific data should be used as model test conditions. It generally is not possible to run exhaustive model tests for, say, 100 hours, and a decision must be made about which time series will sufficiently challenge a model's survivability and produce lifetime dynamic responses. A method which can

link large system responses to some characteristic of the wave excitation would give valuable direction about which time series to test. The correlation between naturally occurring wave groups and large pitch responses of a spar platform is examined, the objective being to provide that predictive measure.

4.1.1 Wave Group Excitation

Physical ocean data from the Pt. Reyes Buoy is used as the excitation for the spar model. The parameter range is the same as in Table 3.4 (H_s : $6.36 - 8.28$ m, T_p : $10.22 - 19.36$ sec), which yields 70, 30-minute time records. These records are searched for rare wave groups, which are used as the wave input to drive the resulting heave and pitch responses.

4.2 Parametric Excitation & Mathieu Instability

The Mathieu equation is a second-order differential equation with a time-varying stiffness term. Such a term offers interesting applications for marine dynamics, as restorative forces may be time-varying based on the body's orientation with reference to the wave surface. In this chapter, the Mathieu equation is used to excite one-way heave-pitch coupling to investigate whether large parametrically-induced responses can be observed in spar platforms due to wave groups as excitation. First, the transfer function of a simple spar platform calculates the heave response of the spar due to irregular wave input from the Pt. Reyes Buoy. The non-dimensional heave transfer function is given below:

$$H(\omega) = \frac{1/K_3}{1 - \frac{\omega^2}{\omega_{n3}^2} + 2i\zeta_3\frac{\omega}{\omega_{n3}}} \tag{4.1}$$

where

$K_3 = \rho g \pi R^2 =$ heave stiffness coefficient — $R =$ platform radius

$\rho =$ water density — $\zeta_3 =$ heave damping coefficient

$g =$ gravitational constant — $\omega_{n3} =$ heave natural frequency

The heave response is calculated from an incoming wave elevation by Eq.(4.2):

$$\eta_3(t) = \mathscr{F}^{-1}\{H(\omega)\mathscr{F}\{\eta_0(t)\}\} \tag{4.2}$$

Here, $\eta_3(t)$ is the heave response, $\mathscr{F}^{-1}\{\bullet\}$ indicates the inverse Fourier Transform, as in Eq.(2.23), $H(\omega)$ is the heave transfer function from Eq.(4.2), and $\mathscr{F}\{\eta_0(t)\}$ is the

Fourier Transform of the incoming wave elevation $\eta_0(t)$. Then, the pitch response is found by using MATLAB's ode45 solver (MATLAB Release 2015b, The MathWorks, Inc., Natick, MA.) to integrate Eq.(4.3) below:

$$\ddot{\eta}_5(t) + 2\zeta_5\omega_{n5}\dot{\eta}_5(t) + \omega_{n5}^2\left(1 - \frac{\eta_3(t)}{2GM_0}\right)\eta_5(t) = M_5(t) \tag{4.3}$$

In this equation, $\eta_5(t)$ is the pitch response, ζ_5 is the pitch damping coefficient, ω_{n5} is the pitch natural frequency, GM_0 is the resting metacentric height of the spar platform, and $M_5(t)$ is an external pitch exciting moment due to incident waves (i.e. a Froude-Krylov effect). This exciting pitch moment is included so that the solutions are not initial-condition dependent, as small perturbations are continuously introduced into the system. Representing external noise, $M_5(t)$ is physics-based and is a combination of the incoming wave slope and squared wave horizontal velocity (for a Morison-type effect). This moment is scaled such that when the parametric forcing part of the equation is 'turned off' (i.e. the only forcing comes from this noise term) the pitch response has $\sigma \leq 1^\circ$.

4.3 Spar Platform Specifications

The spar platform specifications are the same as those used by *Rho and Choi* (2005), shown in Table 4.1. The heave and pitch damping coefficients are the average of those for bare hulls and hulls with appendages (damping plate and strakes). The parameters are scaled such that the heave natural period is 14.88 seconds (to match physical wave buoy data T_p). Subsequently, the pitch natural period is set to double the heave period, to test for Mathieu instability in pitch.

Parameter	Value
Radius	5.21 m
Draft	49.98 m
Heave Natural Period	14.88 sec
Pitch Natural Period	29.75 sec
Heave Damping Coefficient ζ_3	0.03
Pitch Damping Coefficient ζ_5	0.03
GM_0	1.9 m

Table 4.1: Spar platform specifications.

4.4 Time between Maximum Pitch Response & Wave Group Onset

To determine the degree of correlation between a maximum pitch response and the occurrence of a wave group in the excitation, 70×15 tests are carried out. First, ensemble wave groups of 1 to 15 waves, with 14.88 sec as the time between peaks, are found from the 70 Pt. Reyes time series. These ensemble wave group of k waves are identified by locating the maximum of $z_k(t)$ with $\tau = 14.88$ sec for each of the 70 Pt. Reyes time series, shifting those maxima to the same arbitrary time t_0 for all time series, then taking an ensemble average.

4.4.1 Pitch Response due to Ensemble Wave Groups

The ensemble wave group time series for $k = 1$ to 15 provide the input to the linear oscillator model of spar heave, Eq.(4.1), providing a heave response time series, Eq.(4.2), which parametrically excites pitch, Eq.(4.3). The ensemble wave group of k waves excites the system along with a $M_5(t)$ external perturbation from one of the 70 wave time series. This pitch forcing, which is the non-homogenous part of the pitch equation, acts as a small noise term, is unique for each time series, and ensures the pitch response is initial-condition independent.

This is repeated for all 70 time series, for each of the 15 ensemble wave groups. Each pitch time series is then examined for the maximum pitch response and where this response occurs in relation to the start of the ensemble wave group. Considering a forced, damped linear oscillator, one would expect a resonant response to initially grow as long as forcing is present, then to decay when the forcing ends. In this way, the maximum pitch response is expected to occur roughly when the ensemble wave group ends (the heave response will be a smoothed version of the wave elevation, with a slight shift, since the heave transfer function is essentially a band-pass filter). The system damping will cause some lag between the forcing and response.

It is important to note that this initial analysis identifies qualitative trends, but not quantitative answers. As the pitch equation is a non-linear equation, the ensemble input does not lead to the ensemble output (as is the case for linear systems). However, this first step gives a direction on where to look for wave groups based on locations of maximum pitch responses, in an attempt to determine some correlation between wave group occurrences and large resulting pitch responses.

The maximum pitch response and the time between the start of the ensemble wave group and pitch maximum, $\tau_{\widehat{z_k}}$, is recorded for each test. $\tau_{\widehat{z_k}}$ is normalized by the wave group period, $T_p = 14.88$ sec. Table 4.2 records the ensemble statistics. Column 2 gives the expected number of wave periods between the start of the ensemble wave group of k waves and a resulting pitch maximum. Column 3 gives the standard deviation of this time period, $\sigma(\tau_{\widehat{z_k}}/T_p)$. Column 4 is the average maximum pitch response of all 70 tests, $\mathrm{E}[\widehat{\eta}_5]$, for each ensemble wave group index k. Figure 4.1 is an example of a single test for the ensemble wave group of 15 waves, with $M_5(t)$ provided by one of the 70 Pt. Reyes Buoy time series.

k	$E\left[\frac{\tau_{\widehat{z_k}}}{T_p}\right]$	$\sigma\left(\frac{\tau_{\widehat{z_k}}}{T_p}\right)$	$\mathrm{E}[\widehat{\eta}_5]$
1	7.37	3.92	4.47^o
2	7.03	2.67	5.13^o
3	7.14	2.35	5.97^o
4	7.15	2.46	6.92^o
5	8.45	2.61	7.37^o
6	9.29	3.35	7.17^o
7	9.26	2.73	7.39^o
8	10.30	2.61	7.66^o
9	10.87	3.51	8.10^o
10	11.75	2.85	7.77^o
11	11.80	2.63	8.22^o
12	13.23	2.41	8.27^o
13	13.80	2.85	8.24^o
14	14.53	2.74	8.52^o
15	15.58	3.11	8.60^o

Table 4.2: Average time between start of ensemble wave group and maximum pitch response.

4.4.2 Expected Causation Period

By examining the time between the maximum pitch response and the start of an ensemble wave group of 1 to 15 waves, information is gained on where wave groups may emerge in time series, relative to large pitch responses in the resulting pitch time series. A 'causation period' is estimated by this process, which looks back in time from a large pitch response to examine any interesting structures, specifically wave groups of k waves separated by the heave natural period $T_p = 14.88$ sec, in the wave elevation record. This causation period is found for each ensemble wave group of k waves, meaning that if a large wave group of k waves occurs, one might expect a correspondingly large pitch response some determined causation period later.

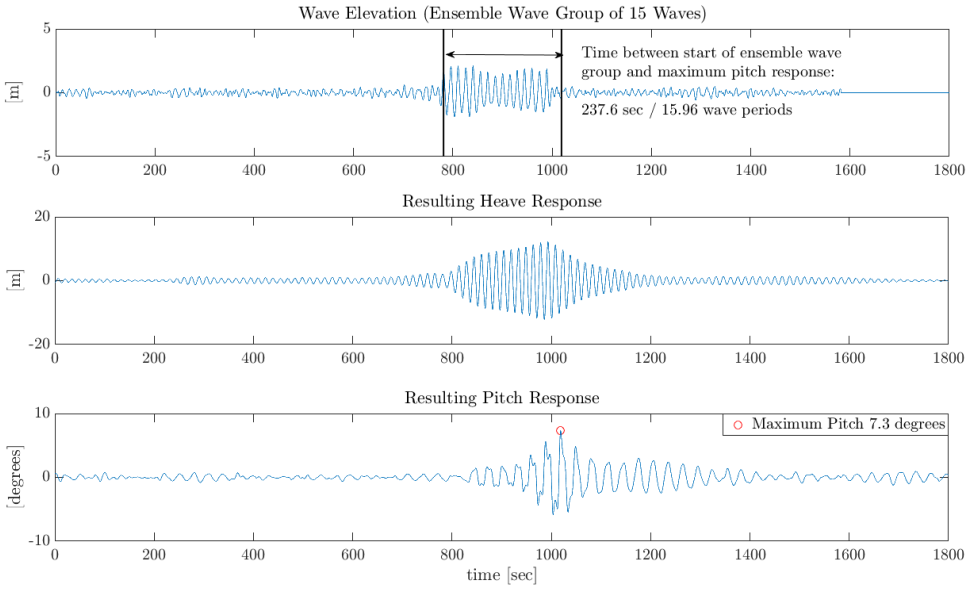

Figure 4.1: Resulting pitch and heave time series resulting from the ensemble wave group of 15 waves.

Table 4.2 shows that the expected time between the start of the wave group and the maximum pitch response, $E\left[\tau_{\widehat{z_k}}\right]$ (normalized by T_p in column 2), increases with wave group index k. Clearly a wave group of 15 waves lasts significantly longer than a wave group of, say, 4 waves, and thus the pitch response will undergo a longer build-up to its maximum response. For wave groups of 9-15 waves, the expected value of the time between wave group start and maximum pitch response begins to converge to the length of the wave group itself.

Considering the nature of the parametric excitation of the model, the pitch response will grow as long as it has large forcing. Once this forcing stops, that is, the wave group ends or the heave motion returns to a low level, the pitch response will decay accordingly. Note that the maximum pitch response generally occurs after the wave group ends. This lag between maximum pitch and wave group termination is a result of continued, albeit decaying, heave motion. Consistent with a damped Mathieu model, parametric heave forcing above a given threshold will generate an increasingly larger pitch response. A time range can be estimated from the statistics of Table 4.2, to consider what, if any, wave groups may be associated with large pitch responses resulting from the 70, 30-minute Pt. Reyes wave time series.

4.5 Pitch Excited by Pt. Reyes Buoy Time Series

With some statistics on a causation range based on Table 4.2 to direct where wave-group-induced pitch responses may occur, a level of correlation can be estimated between the two events. That is, for a given wave group index, $k = 1 - 15$, the sub-period, τ_{search_k}, where the local maximum $\widehat{Z_k}$ is identified (the maximum of $z_k(t)$ within the time range restricted to τ_{search_k}), is defined by Eq.(4.4). The time of the maximum pitch response in a time series is denoted as $\widehat{\tau_{\eta_5}}$.

$$\tau_{search_k} = \widehat{\tau_{\eta_5}} - \left(E\left[\frac{\tau_{\widehat{z_k}}}{T_p}\right] \pm \sigma\left(\frac{\tau_{\widehat{z_k}}}{T_p}\right)\right) \times T_p \tag{4.4}$$

Pitch responses are simulated from Eq.(4.1)-(4.3) due to the 70, 30-minute wave time series from the Pt. Reyes Buoy. These contain physical wave groups whose average structure is captured by the empirically-based ensemble wave groups, as shown in Chapter III. However, these wave groups are 'hidden' among the irregular structure of the time series, and not easily detectable without the derived process method. The maximum pitch response is located within each resulting record, which defines a causation range, τ_{search_k}, for $k = 1 - 15$, as dictated by Table 4.2 and Eq.(4.4). This τ_{search_k} indicates where a wave group of k waves must occur in a wave elevation record, relative to the maximum resulting pitch response, for there to be any expected correlation between the occurrence of the two events.

For a given wave group index k, a ratio can be made of the maximum value of the derived process during the specified range, $\widehat{Z_k}$, and the maximum of the derived process within the entire 30-minute record itself, $\widehat{z_k}$. This $\widehat{Z_k}/\widehat{z_k}$ ratio indicates whether a large value of the derived process (a wave group) may have an effect on the resulting pitch motion. If there is a high correlation between a large value of the derived process (a large wave group) occurring and a large resulting pitch response, one might expect this ratio to converge to 1, meaning the largest wave group in the wave elevation time series is within the predicted range of time preceding the largest pitch response, indicating some potential causation. Conversely, if there is no correlation between pitch response and a wave group occurrence, one might expect this probability to be around 0.38. This 'uncorrelated ratio' comes from the ratio of the expected value of the wave elevation crest for a 30-minute time series, 1.25σ (assuming a Rayleigh distribution), and the average maximum wave crest in 30 minutes, 3.26σ (from the Pt. Reyes buoy data). This ratio comes to $1.25\sigma/3.26\sigma = 0.38$.

For each of the 70 time series, the local derived process maximum, $\widehat{Z_k}$, in the

search period, τ_{search_k} from Eq.(4.4), is compared to the absolute derived process maximum for that time series, $\widehat{z_k}$. Since each time series is considered independent, the probability the ratio $\widehat{Z_k}/\widehat{z_k}$ exceeds some threshold is approximated by the number of individual time series whose ratio exceeds that threshold, normalized by the total number of time series examined. Only time series in which the spar does not capsize (pitch less than 90^o) are considered. Additionally, time series with the maximum pitch occurting so early in the 30-minute time series that the causation period precedes the start of the record are not considered. In total, 60 out of a possible 70 time series are examined.

Shown in Figure 4.2 is an example of an incoming wave elevation (specifically from 01/19/2010 12:39:00) which excites a heave and pitch response of the spar platform. The largest wave group of k waves within each τ_{search_k} is identified, and compared with the largest wave group of k waves within the entire 30-minute record. For the example in Figure 4.2, $\widehat{Z_7}/\widehat{z_7} = 1$, meaning the largest wave group of 7 waves in the 30-minute record also occurs in the expected time before the largest pitch response, τ_{search_7} which indicates the potential for causation. The ensemble wave group of 7 waves is overlaid on the time series at the wave group onset to highlight the structure. Without the derived process, it would be difficult, if not impossible, to pick out a wave group of 7 waves in this time series. The time series clearly exhibits large waves slightly before the time of the largest pitch response, but less clear is the near-constant period between the waves. The period of the wave group, τ, drives the parametric excitation (i.e. heave), in turn causing a large pitch.

4.5.1 Relationship between Wave Group of k Waves & Extreme Pitch Responses

In Figure 4.3, the empirical histograms of the ratio $\widehat{Z_k}/\widehat{z_k}$, normalized as a *pdf*, are depicted for wave groups of $k = 1, 7$, and 15 waves. These three distributions are representative of the 3 shapes of distributions found for $k = 1 - 15$. For $k = 1 - 5$, the distributions are approximately uniform between 0.5 to 1. For $k = 6 - 9$, the distributions all increase sharply near the ratio value of 1. For $k = 10 - 15$, the distributions flatten out attaining a shape somewhere between that of the low-number wave groups and the mid-number wave groups.

These three general distribution shapes reveal how the occurrence of wave groups of different group indices are related to large pitch responses. For wave groups of

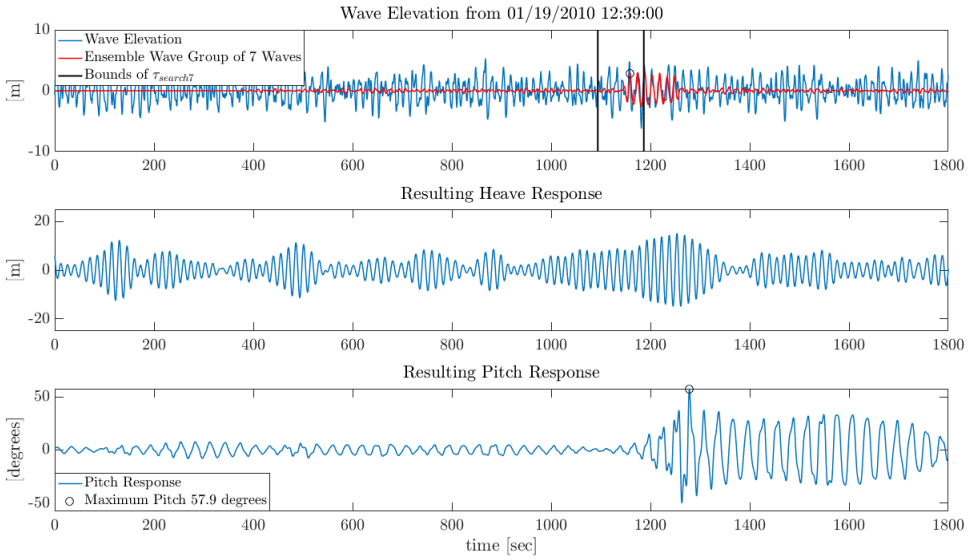

Figure 4.2: Resulting pitch and heave time series from incoming wave elevation 01/19/2010 12:39:00.

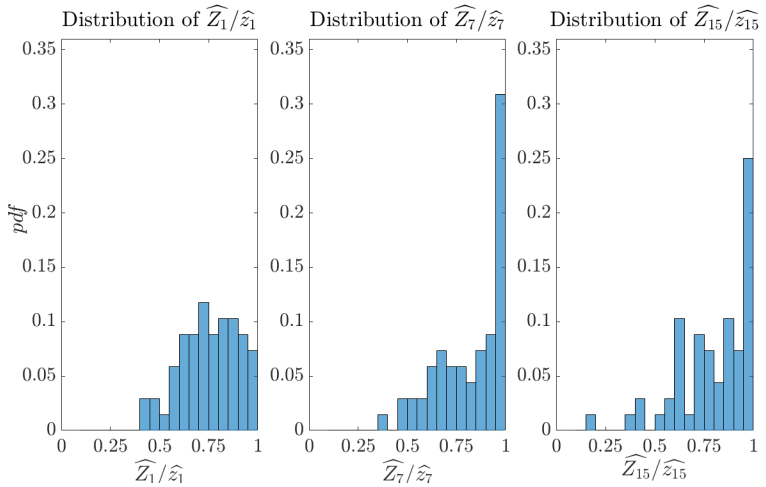

Figure 4.3: Empirical histograms of $\widehat{Z_k}/\widehat{z_k}$ for $k = 1, 7, 15$, normalized as a *pdf* (60 samples for each histogram).

fewer waves ($k = 1 - 5$) there appears not to be a strong correlation between a large wave group of k waves exciting the system and a maximum pitch response occurring. For this subset of wave groups, the maximum pitch response is as likely caused by a smaller-amplitude wave group as a larger-amplitude wave group (i.e. a low ratio of $\widehat{Z_k}/\widehat{z_k}$ vs. $\widehat{Z_k}/\widehat{z_k} = 1$), indicating that the occurrence of wave groups with index $k = 1 - 5$ does not have much effect on pitch response. For wave groups of $k = 6 - 9$ waves, there is a much higher correlation between a large wave group occurring in τ_{search_k}, and a maximum pitch response following. For wave groups of more waves ($k =$

$10 - 15$) the correlation again decreases. Chapter 3.3 showed that mean wave group amplitude drops off rapidly as the wave group index k increases, so this physically makes sense. The wave groups with long runs exhibit more cycles of near-harmonic forcing but have lower mean wave amplitudes. Similar to the behavior of damped Mathieu systems, these groups may not exhibit sufficient forcing to overcome the system damping.

Table 4.3 gives the probabilities that the ratio $\widehat{Z_k}/\widehat{z_k}$ exceeds different threshold values β. There is a higher probability that the largest wave group in the predicted time period (τ_{search_k}) precedes the largest pitch response, particularly for wave groups of 7-9 waves, than would be expected if wave groups as excitation and resulting pitch maxima were uncorrelated. This suggests the conclusion that large pitch responses due to parametric excitation are not independent of large wave groups occurring in the excitation. When considering the most likely wave group to be associated with extreme pitch, wave groups of 7 waves have $\mathrm{p}(\widehat{Z_k}/\widehat{z_k} > 0.999) = 0.3$. This means there is a 30% chance that a wave group of 7 waves found in τ_{search_7} has a mean amplitude at least 99.9% of the mean amplitude of the largest wave group of 7 waves in the entire 30-minute record. Equivalently, this means there is a 30% chance that the largest wave group of 7 waves in a time record will lead the maximum pitch response by a pre-determined period which implies a level of causation. As the ratio threshold β is lowered, this probability continues to increase.

It is also instructive to examine the subset of time series in which the largest wave group of k waves occurs in the expected range before a large pitch response, τ_{search_k}. Figure 4.4 compares the probability that the largest wave group of k waves in the 30-minute record occurs in τ_{search_k} across different k values. Analogous to the first column in Table 4.3, for a wave group of 7 or 8 waves, there is a 30% chance that the largest wave group occurs in τ_{search_7} or τ_{search_8}, respectively, versus only a 6.7% chance the largest wave group of 1 wave occurs in τ_{search_1}. This trend corresponds well to the distributions of $k = 1, 7, 15$ in Figure 4.3. In both cases, for wave groups of around 7 waves, the largest wave groups tend to be in the expected time before the occurrence of a pitch maximum.

Also included in Figure 4.4 is the distribution of the largest pitch responses caused by those wave groups with ratio $\widehat{Z_k}/\widehat{z_k} = 1$. For wave groups of 1 wave with $\widehat{Z_1}/\widehat{z_1} = 1$, the resulting maximum pitch responses are approximately uniformly distributed between the ranges of $2^o - 10^o$, $10^o - 15^o$, $40^o - 50^o$, and $50^o - 60^o$. For wave groups

	$\mathrm{p}(\widehat{Z_k}/\widehat{z_k} > \beta)$			
k	$\beta = 0.999$	$\beta = 0.9$	$\beta = 0.8$	$\beta = 0.5$
1	0.067	0.18	0.42	0.93
2	0.083	0.23	0.42	0.92
3	0.15	0.33	0.53	0.97
4	0.22	0.38	0.53	0.97
5	0.22	0.38	0.55	0.97
6	0.25	0.35	0.55	0.98
7	0.30	0.45	0.58	0.93
8	0.30	0.40	0.60	0.93
9	0.27	0.45	0.62	0.90
10	0.25	0.42	0.57	0.90
11	0.25	0.33	0.50	0.90
12	0.22	0.30	0.48	0.83
13	0.22	0.33	0.48	0.83
14	0.18	0.38	0.52	0.83
15	0.10	0.36	0.53	0.90

Table 4.3: Probability of wave group occurring in period before maximum pitch response (range specified from Table 4.2 and Eq.(4.4)).

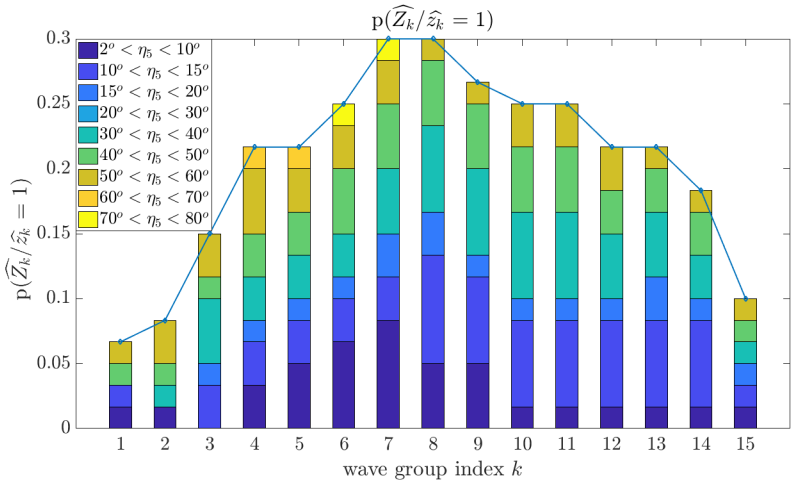

Figure 4.4: Probability that the largest wave group of k waves in a time record precedes the largest resulting pitch response, in the appropriate τ_{search_k} time range. The resulting pitch maxima are broken up by the magnitude of the response.

of 7 with $\widehat{Z_7}/\widehat{z_7} = 1$, approximately 60% of maximum pitch responses are above 20^o. Wave groups of 7 or 8 waves are more likely to cause a large pitch response than a wave group of 1 wave.

These results can be compared with the empirical histogram of the maximum pitch response $\widehat{\eta_5}$ from all 60 time series, normalized as a *pdf*, shown in Figure 4.5. Most of the maximum pitch responses are grouped in the $10^o - 15^o$ range. Conversely,

by considering time series in which the maximum wave group occurs in the expected causation period, there is a greater chance of experiencing larger pitch responses. When considering all time series, the chance of experiencing a pitch maximum larger than 30^o is 33%. But just considering the time series without any connection to structures in the excitation (i.e. wave groups), it may be difficult to determine *why* the large pitch responses occur.

However, considering more specifically time series which contain large wave groups of 7 waves can give more predictive information. For the wave records examined in this chapter, 30% of the largest wave groups of 7 waves in each record indicates the onset of the 30-minute pitch maximum, implying some causation. As well, 50% of those resulting pitch maxima are larger than 30^o. This indicates that wave records which contain large wave groups of 7 waves tuned to the spar heave natural period are good candidates to test the survivability of the platform.

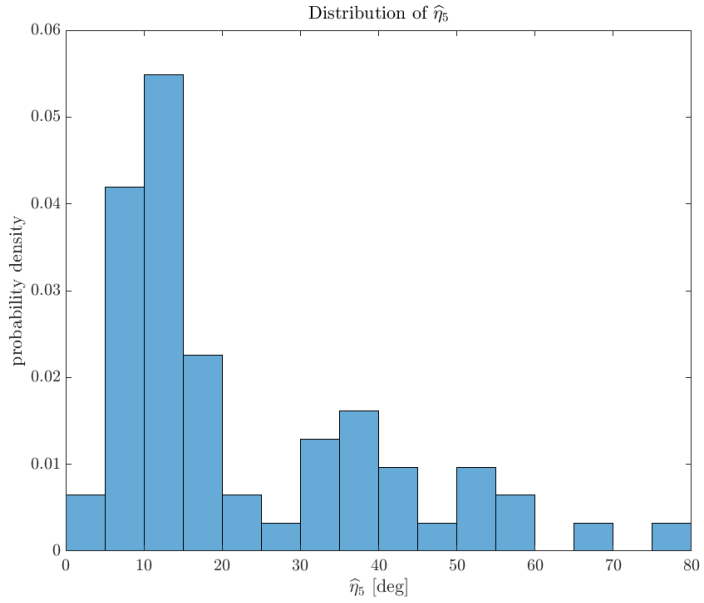

Figure 4.5: Distribution of maximum $\widehat{\eta}_5$ for 60 time series.

4.6 Implications of Results

This analysis answered some interesting questions but brought up many more. The physical oceanographic data from the Pt. Reyes Buoy was examined for rare wave groups, which provided the excitation for spar parametric pitch responses. Chapter III showed that a maximum of the derived process identifies rare wave groups within a

wave elevation record, and that individual time records match well with a theoretical ensemble structure. This indicates that group-like structure exists in physical wave elevation records, though that regular behavior is difficult to notice in an irregular wave train. However, the derived process identifies these wave groups easily.

Such wave groups provided forcing to a spar model, to determine if there is any correlation between the occurrence of a rare wave group in the excitation and a large resulting pitch response. There is a balance between the number of wave peaks in a wave group, and the mean amplitude of those peaks. A single wave will have the largest group amplitude but may not be able to set off parametric resonance, as shown. However, wave groups of longer runs exhibit successively lower mean group amplitudes and may not be able to overcome system damping to provide sufficient excitation.

Wave groups of $k = 7 - 9$ waves were shown to balance these two competing concerns: group length vs. mean group amplitude. It was shown that for wave groups of 7 and 8 waves, there is a 30% chance that the maximum pitch response occurs a pre-determined time after the group onset, indicating some potential causation. Additionally, for those wave groups of 7 waves, 50% of the resulting pitch maxima were larger than 30^o. This has clear implications for model testing, because specific wave records which contain large wave groups of 7 waves can be run to test the performance of a structure, rather than testing for a long exposure with irregular waves, in hopes of recording extreme responses. The Pt. Reyes Buoy time series used here, along with the guided search for rare wave groups using the derived process, can provide directed excitation records which reflect physical operating conditions.

However, not all marine systems operate in regions where there is 17 years worth of historical physical data to mine. To evaluate the performance of such systems requires some notion of the operating profile. To *efficiently* evaluate system performance further requires directed simulations of that operation profile. This spar example showed that extreme responses may be due to excitation which contains extreme values of the derived Gaussian process. This is a form of looking for extreme values via reduced-order modeling. For the spar, it would be difficult, if not impossible, to simulate the system for a long exposure to record severe responses and try to infer causation of extreme pitch responses due to interesting wave structures in the excitation record. Conversely, methods which could analytically solve for a wave form that sets off a large pitch response, like FORM or SORM, may give wave profiles

which are not physically realizable. Instead, the physics of parametric resonance was considered through reduced-order modeling, i.e. searching for group-like behavior in the excitation. This reduced-order modeling method utilized the fact that regular waves can set off parametric resonance. This focused the search to wave groups, which exhibit similar characteristics, but were shown to physically exist in an irregular ocean environment.

Additionally, this spar example showed that extreme responses may be experienced, given a specific input excitation (i.e. given an input which includes a rare wave group of 7, 8, or 9 waves separated by the heave natural period). However, for overall performance analysis, what is of interest is the probability of exceeding some allowable threshold in general, not conditioned on a specific input. Additionally, it was noted in Chapter 3.7 that wave groups of close group numbers may not be mutually exclusive. For the example in Figure 3.12, which is a Pt. Reyes Buoy time series from 01/19/2010 13:09:00, the largest wave group of 1, 2, and 3 waves in the entire time series occurs within the same time range. It is expected that wave groups of a higher group index k will exhibit this overlapping behavior, as Figure 3.4 shows that the difference between mean group amplitudes for sequential k values diminishes for higher k values. Therefore, some specific challenges associated with analyzing extreme responses of complex marine systems remain, namely:

- How can numerical simulations be directed toward interesting responses for systems operating in areas which do not have extensive time history data?
- How can overall system performance be evaluated, and not just conditioned on the occurrence of specific derived process maxima within the excitation?
- How may different derived processes be related (i.e. non-mutually-exclusive), and how does this affect the consideration of lifetime responses?
- Can derived processes be used to define excitation inputs which exhaustively test the possible allowable threshold exceedances for a complex system?

These challenges are addressed in the following chapter through the development of the non-linear Design Loads Generator (NL-DLG) process.

CHAPTER V

The Non-Linear Design Loads Generator Process

Earlier chapters examined the theoretical expected shape of a rare wave group, with a wave group identified by a maximum in the derived Gaussian process (Chapter 2.4), and the existence of physical wave records that exhibit group-like behavior in an ensemble sense and individually (Chapter III). Chapter IV examined the pitch response of a spar platform due to excitation containing wave groups, which provide parametric excitation, and showed that these wave groups can lead to extreme responses of a dynamic system.

However, Chapter IV also brought up a few issues associated with efficiently testing marine systems for extreme responses. First, not all systems operate in areas with extensive excitation data to mine through. Simulation may be required, but these simulations should be directed toward extreme responses to minimize the computational effort. As in that example, the spar platform was not tested with the 17 years' worth of physical oceanographic data, but specific time segments expected to cause interesting responses. Additionally, for the spar platform, all statistics on extreme pitch responses were conditioned on the occurrence of a rare wave group of specific group index k in the excitation. Chapter 3.7, however, indicated that wave groups of wave index k, $k \pm 1$, $k \pm 2$, etc. may not be mutually exclusive.

For design purposes, evaluations of system performance should be based on overall performance, not conditioned on specific events, and certainly not conditioned on inputs which may not be mutually exclusive. Also, using surrogate processes for a reduced-order modeling approach, like in Chapter IV should be exhaustive when considering what sort of inputs may lead to extreme responses. These issues are addressed here through the development of the non-linear Design Loads Generator

(NL-DLG) process, which expands the original Design Loads Generator method.[1]

5.1 NL-DLG Process Motivation

The Design Loads Generator was developed by *Alford* (2008) and *Kim* (2012) to construct ensembles of short excitation time series which lead to extreme linear responses of a specific output. These inputs from the DLG will also lead to a lower bound on non-linear extreme responses. This capability allows designers to test a marine system with an ensemble of statistically equivalent short wave time series to generate a distribution of extreme linear responses for a given output. These short wave records from the DLG can considerably improve the efficiency of high-fidelity analyses, like Computational Fluid Dynamics or Finite Element Analysis time-domain simulations because the DLG can direct inputs for these methods, limiting the simulation of times when no interesting responses occur. However, for the evaluation of a system in terms of lifetime performance, there are a few additional concerns, similar to the questions posed at the end of Chapter IV:

- How can the capability of the DLG be used for systems in which extreme responses are due to varying combinations of a vector of loads?
- What if these combined loads are strongly correlated and/ or non-Gaussian?
- How can system performance be evaluated in general and exhaustively, and not conditioned on specific excitation inputs?

These concerns became evident in the spar example from Chapter IV. Extreme spar pitch responses were found to be related to the presence of wave groups in the excitation, identified by maxima of the derived process. These wave groups were identified in physical oceanographic data, and the example showed that individual time series containing group-like behavior in an irregular ocean environment can set off parametric resonance in a spar platform. Not every system operating location, though, has extensive physical oceanographic data to use in a testing program. The DLG could be used to generate these time series for testing the spar response. Specifically, for the spar example, wave environments which lead to a maximum of the derived process could be constructed by the DLG, and those wave time series would

[1]Portions of this work were previously published in *Seyffert and Troesch* (2018).

contain rare wave groups. Chapter III showed that physical oceanographic time series can exhibit this group-like behavior, identified by a maximum in the derived process.

Then, as in Chapter IV, the probability of an extreme pitch response being set off by a wave group of k waves could be determined. The spar was shown to exhibit large pitch responses due to the occurrence of wave groups of 7, 8, or 9 waves tuned to the spar heave natural period. But, it would be much more useful to know the probability that the spar experiences large pitch responses in general over its lifetime, and not conditioned on the occurrence of a wave group of 7, 8, or 9 waves in the excitation. These concerns: extreme pitch responses due to rare wave groups exciting the system, and the potential non-mutual-exclusivity of rare wave groups of similar group index k, are generalized in this chapter to consider the broader implications associated with performance analysis of complex systems.

5.2 NL-DLG Process Overview

The NL-DLG process is developed to estimate the probability that a non-linear, multi-dimension threshold surface, which relates to the 'strength' of a complex non-linear system, like in Chapter 1.3.1, is exceeded by a vector of potentially correlated, stationary, non-Gaussian loading over a long exposure. An $m-$dimension threshold, here in this chapter referred to generally as a failure surface, similar to the notation of *Madsen et al.* (2006) and *Naess and Moan* (2014), describes how different combinations of m non-linear loads relate to system performance. This surface may be a non-linear function of the m loads acting on the system, and therefore failure, or a threshold exceedance, may be the result of individual load extremes, or simultaneous moderate loading values, depending on the failure surface shape. The general steps of the NL-DLG process to estimate the probability of failure for such a system are as follows:

1. n non-linear load combination cases are defined to focus on specific regions of the surface.

2. n surrogate processes are described to be indicators of extreme behavior for the associated non-linear load combination cases, similar to reduced-order modeling.

3. The DLG is used to construct ensembles of short excitation inputs which lead to exposure-period-maxima of the surrogate processes. These inputs are candidate

environments that may lead to exposure-period-maxima of the associated non-linear load combination cases. It it assumed that these inputs also lead to these exposure-period-maxima.

4. These excitation inputs constructed by the DLG excite the fully non-linear system, and the resulting load vector is mapped onto the failure surface to determine if failure occurs.

5. Conditional probabilities of failure, given the system is excited by an input record which contains the occurrence of a specific surrogate process maxima, are estimated from the DLG simulations.

6. The relation between the surrogate processes is estimated from the DLG simulations (no dependence structure is assumed) to develop maxima configurations, which describe the different ways n surrogate process maxima may be clustered over an exposure.

7. The probability of experiencing each maxima configuration is estimated from the DLG simulations to link together the conditional failure probabilities for a full exposure described by each maxima configuration type.

8. The resulting estimate of the distribution of most-likely failure occurrences can provide feedback to update the overall estimate. This iterative approach aims to cover the failure surface definition in an exhaustive sense. The excitation profiles which lead to these most-likely failures are also retained.

Using the DLG in this expanded context allows the consideration of systems which are subject to long exposures (potentially thousands of hours) to a stationary and stochastic excitation of combined non-Gaussian loading. These combined loads may be non-Gaussian, and their interaction with a complex failure surface determines failure occurrences. The resulting probabilistic framework, called the NL-DLG process, estimates system failure probability. The NL-DLG process also preserves the ensemble of excitation inputs which are representative of the operational condition and that lead to the distribution of most-likely failure occurrences.

5.3 General Problem Formulation

Consider a complex system in which some global, Gaussian input drives multiple processes that excite the system. These processes, or loads, may be non-linear functions of linear transformations of that excitation. The input here is called a 'global, Gaussian input' to emphasize that it is the stochastic input to all of the linear and non-linear loads which excite the system. The system has a failure surface that describes all possible combinations of the non-linear loads which result in failure. Note that the definition of failure might mean that the loads exceed some allowable threshold, or that a physical failure like collapse occurs. Both problems can be considered by the NL-DLG process. The notation is outlined below to describe the different system parameters:

$$
\begin{aligned}
\eta(t) &= \text{time series of the global, Gaussian input} \\
S^{+}(\omega) &= \text{single-sided mean-squared spectrum of } \eta(t) \\
\mathscr{L}_i(\omega) &= i^{th} \text{ linear transfer function} \\
\mathtt{L}_i(t) &= i^{th} \text{ time series with single-sided mean-squared spectral definition } S^{+}(\omega)|\mathscr{L}_i(\omega)|^2 \\
\mathscr{NL}_j(t) &= j^{th} \text{ load time series resulting from a non-linear transformation of } \eta(t), \\
&\qquad \text{which excites the system} \\
G(\mathscr{NL}_1(t), \cdots, \mathscr{NL}_m(t)) = 0 &\equiv \begin{array}{l}\text{failure surface, which may be a non-linear function of} \\ \text{the } m \text{ non-linear loads } \mathscr{NL}_j(t)\end{array}
\end{aligned}
$$

An input/output (I/O) process is outlined in Figure 5.1. Here, the global, Gaussian input $\eta(t)$ drives the complex non-linear system for a specified exposure time, which may be long. There is a failure surface G, which may be a non-linear function of the m non-linear loads, $\mathscr{NL}_i(t)$ $i = 1, \cdots, m$, that excite the system. Assume that G is time-invariant, meaning the failure surface remains constant over the exposure period (i.e. $\frac{d}{dt}G(t) = 0$). The interaction of the load vector $(\mathcal{NL}_1(t), \cdots, \mathcal{NL}_m(t))$ with the surface, G, determines whether system failure occurs. This chapter examines such a system and its probability of failure employing specific system simplifications, using the NL-DLG process.

5.3.1 Complex System Simplifications

For the motivation behind these system simplifications, consider Figures 5.2 and 5.3. Here, a hypothetical system illustrates how failure is determined by the interaction of a failure surface, G, with two non-linear loads, i.e. $m = 2$. The loads are driven

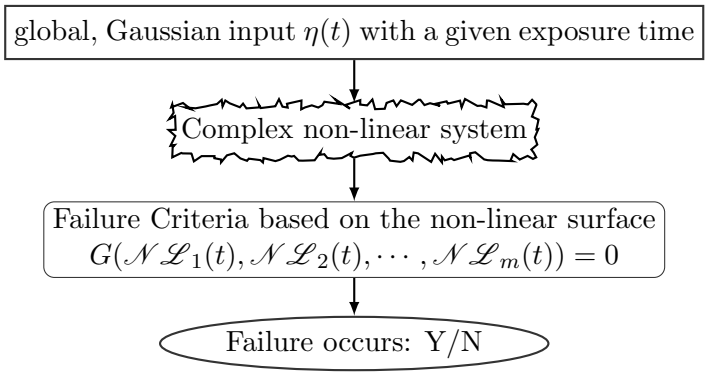

Figure 5.1: Schematic of I/O process for failure assessment.

indirectly by a global, Gaussian input $\eta(t)$ with spectral definition $S^+(\omega)$ for a 10-hour exposure. The time when each load experiences its maximum value over the exposure is marked with a red circle. These loads are non-linear functions of linear transformations of that global, Gaussian input: $\mathscr{NL}_1(\mathtt{L}_1(t))$ and $\mathscr{NL}_2(\mathtt{L}_2(t))$. Figure 5.3 shows the failure surface G for this system, which is a bi-linear function of $\mathscr{NL}_1(\mathtt{L}_1(t))$ and $\mathscr{NL}_2(\mathtt{L}_2(t))$. Failure occurs when the load vector, ($\mathscr{NL}_2(\mathtt{L}_2(t))$,$\mathscr{NL}_1(\mathtt{L}_1(t))$), crosses the failure surface G. The time of failure occurrence is marked with a red star on the load vector in Figure 5.3, and on the excitation input in Figure 5.2. The question then is: what is the probability of failure of this system for the 10-hour exposure period?

The failure surface, G, in Figure 5.3 defines every combination of ($\mathcal{NL}_2(\mathtt{L}_2(t))$, $\mathcal{NL}_1(\mathtt{L}_1(t))$) which leads to failure. A generally non-conservative simplified definition of this failure surface is to define failure as when a single value of $\mathscr{NL}_1(\mathtt{L}_1(t))$ or $\mathscr{NL}_2(\mathtt{L}_2(t))$ reaches an extreme, corresponding to where G meets the two axes, respectively. Indeed, the first (and only) failure occurrence during this 10-hour simulation is when $\mathscr{NL}_1(\mathtt{L}_1(t))$ experiences its maximum value over the 10 hours. The value of $\mathscr{NL}_1(\mathtt{L}_1(t))$ at the time of failure is greater than the value of the failure surface at the y-axis, meaning that this would still be a failure even if there was no acting component of $\mathscr{NL}_2(\mathtt{L}_2(t))$.

Recognizing such behavior suggests an approximate approach. The failure surface G may be simplified so that the infinite number of load combinations ($\mathcal{NL}_2(\mathtt{L}_2(t))$, $\mathcal{NL}_1(\mathtt{L}_1(t))$) which lead to failure are condensed to just a few points on G that approximate the failure surface. These points define specific non-linear load combination cases on G. For example, in Figure 5.3, the failure surface can be reduced to the two

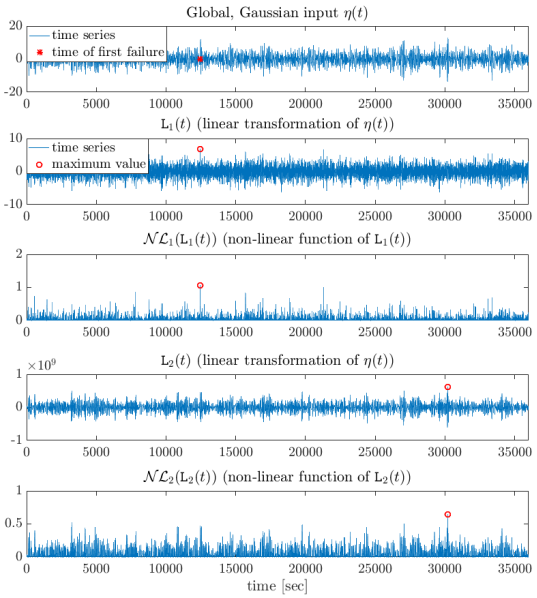

Figure 5.2: Global, Gaussian input $\eta(t)$, resulting linear transformations of that input $\mathtt{L}_1(t)$ and $\mathtt{L}_2(t)$, and non-linear loads $\mathcal{NL}_1(\mathtt{L}_1(t))$ and $\mathcal{NL}_2(\mathtt{L}_2(t))$ over a 10-hour exposure. The time when failure first occurs is shown as a red star on the global, Gaussian input. The 10-hour-maxima of $\mathtt{L}_1(t)$, $\mathtt{L}_2(t)$, $\mathcal{NL}_1(\mathtt{L}_1(t))$, and $\mathcal{NL}_2(\mathtt{L}_2(t))$ are highlighted as a red circle.

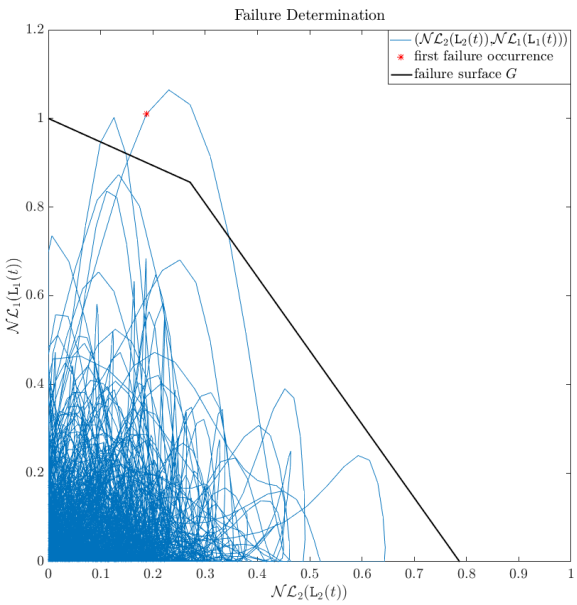

Figure 5.3: Failure surface G, with the 10-hour load vector, $(\mathcal{NL}_2(\mathtt{L}_2(t)), \mathcal{NL}_1(\mathtt{L}_1(t)))$. The point when failure first occurs is noted as the red star. This is not precisely on the failure surface, G, due to discretization of the time series.

non-linear load combinations represented by the points $G(0,1)$ and $G(0.79,0)$, where G meets the two axes. Simplifying the failure surface G to say that failure only occurs when either of the two load combination cases are exceeded would clearly under-predict the probability of failure because it ignores the possibility that failures may occur at other locations along G.

To improve this simplification of G, a third point on G can be selected as another load combination case, say $G(0.5,0.5)$. Then an additional criterion for failure would be those times when $\mathcal{NL}_1(\mathtt{L}_1(t)) \geq 0.5$ *and* $\mathcal{NL}_2(\mathtt{L}_2(t)) \geq 0.5$. This third combination case can be represented by the sum of the components: $\frac{1}{2}\mathcal{NL}_1(\mathtt{L}_1(t)) + \frac{1}{2}\mathcal{NL}_2(\mathtt{L}_2(t))$. While these three non-linear load combination cases do not provide a complete representation of all instances leading to failure, they produce a lower bound that becomes increasingly more accurate as more load combination cases are considered.

The simplification utilized by the NL-LDG process, then, is to consider only segments of the lifetime exposure excitation that leads to extreme values of the non-linear load combination cases $\mathcal{NL}_1(\mathtt{L}_1(t))$, $\mathcal{NL}_2(\mathtt{L}_2(t))$, or $\frac{1}{2}\mathcal{NL}_1(\mathtt{L}_1(t))+\frac{1}{2}\mathcal{NL}_2(\mathtt{L}_2(t))$. The $\eta(t)$ inputs leading to these maxima excite short segments of the load vector,

$(\mathcal{NL}_2(\mathtt{L}_2(t)), \mathcal{NL}_1(\mathtt{L}_1(t)))$, which are then mapped onto G, allowing an estimation of the failure probability. The means to generate short, statistically equivalent input time histories which lead to these load combination maxima may be accomplished through the use of the Design Loads Generator (DLG) methodology, as described in Chapter 2.3, with modifications.

Based on one's understanding of the behavior of the complex system, it is possible to approximate the inputs which lead to extreme responses of the non-linear load combination cases using a linear transfer function as a surrogate process. This approximation exploits the capability of the DLG. A surrogate process may be defined as a weighted sum of normalized linear functions which approximate an associated non-linear load combination case. Or a surrogate process may be defined by reduced-order modeling, like the approach to use wave groups as the excitation to set off parametric pitch in Chapter IV. The Gaussian input time series constructed by the DLG to lead to extreme responses of the surrogate processes may be linked to the Gaussian inputs that lead to extreme responses of the associated non-linear load combination cases.

5.3.2 Impact of System Simplifications

The probability of failure for the system is approximated by assuming that the Gaussian inputs which lead to the exposure-period-maxima of the surrogate processes also lead to the exposure-period-maxima of the corresponding non-linear load combination cases. Instead of running many full-length MCS to estimate the system failure probability, only the system response to the directed ensemble of excitation times series which presumably lead to the exposure-period-maxima of the non-linear load combination cases is examined. The main assumptions used by the NL-DLG process are:

- A finite number (n) of non-linear load combination cases are defined to focus on specific regions of the failure surface, G. The system probability of failure is approximated by the system response to excitation time series which lead to the maximum value of the non-linear load combination cases experienced during the exposure period.

- Surrogate processes are defined as linear approximations to the non-linear load combination cases. The DLG constructs ensembles of the global, Gaussian input which lead to exposure-period-maxima of the surrogate processes. It is

assumed that these Gaussian inputs also lead to the exposure-period-maxima of the associated non-linear load combination cases.

- The system response to these directed simulations is an indicator for the entire exposure. If the system does not fail due to time series which contain the non-linear load combination exposure-period-maximum (based on the associated surrogate process maximum realization), the system is assumed to not fail due to that particular load combination case at all over the exposure.

5.4 Use of Surrogate Processes

For the NL-DLG process, Gaussian surrogate processes are used for extreme value estimation, via the DLG methodology. It is assumed that specific segments of Gaussian input time histories which produce extreme Gaussian responses in linear systems are also capable of producing large non-Gaussian responses in related non-linear systems. The objective is to identify input sequences that excite a non-linear system such that the non-linear responses include extreme values which are samples of an extreme value distribution, with the specified exposure period. The methodology of surrogate processes has similarities with reduced order modeling in which only essential physics are retained, thus producing a system that exhibits relevant behavior.

The surrogate process may be either a linearization of a non-linear system or a characteristic process not directly related to the I/O system, but somehow an indicator of extreme behavior. As an example of the first: a surrogate based on the linearization of a non-linear process is given by *Kim et al.* (2011) in which linear predictions of extreme ship vertical bending are used as a surrogate for non-linear design midship vertical bending and impact-induced bending. Some examples of the second: extreme responses of surrogates that, while not directly related to the output of the complex system, are indicators of non-linear extreme response are given by *Kim and Troesch* (2013); *Seyffert and Troesch* (2016c); *Seyffert et al.* (2016); *Seyffert and Troesch* (2016b). Those works define surrogates whose extreme values are associated with incidences of extreme group-like behavior of the input. Chapter IV utilized this approach, using rare wave groups as a form of parametric excitation for non-linear systems exhibiting parametric resonance.

5.4.1 Non-Linear Load Combination Cases

In this chapter, surrogate processes associated with system failure are constructed from linear approximations to n non-linear load combination cases. Different regions of the failure surface, G, can be emphasized through the definition of n non-linear load combination cases, $\zeta_i(t)$. The m non-linear loads, $\mathcal{NL}_i(t)$, are each normalized by their respective σ so that the weighting factors $\alpha, \beta, \cdots, \gamma$ capture relative magnitudes. The general non-linear load combination case $\zeta_i(t)$ is given by Eq.(5.1):

$$\zeta_i(t) = \alpha \frac{\mathcal{NL}_1(t)}{\sigma_{\mathcal{NL}_1}} + \beta \frac{\mathcal{NL}_2(t)}{\sigma_{\mathcal{NL}_2}} + \cdots + \gamma \frac{\mathcal{NL}_m(t)}{\sigma_{\mathcal{NL}_m}} \tag{5.1}$$

where

$\zeta_i(t)$ = time series of a given non-linear load combination case $i = 1, \cdots, n$

$\mathcal{NL}_i(t)$ = time series of non-linear load $i = 1, \cdots, m$

$\sigma_{\mathcal{NL}_i}$ = standard deviation of the non-linear load $\mathcal{NL}_i(t)$

$\alpha, \beta, \cdots, \gamma = m$ weighting factors

Then, n surrogate processes are defined to approximate the n non-linear load combination cases. These surrogates may be weighted sums of normalized, related linear functions, shown in Eq.(5.2):

$$z(t) = \alpha \frac{\mathtt{L}_1(t)}{\sigma_{\mathtt{L}_1}} + \beta \frac{\mathtt{L}_2(t)}{\sigma_{\mathtt{L}_2}} + \cdots + \gamma \frac{\mathtt{L}_m(t)}{\sigma_{\mathtt{L}_m}} \tag{5.2}$$

where

$z(t)$ = surrogate process that approximates the related non-linear load combination case, $\zeta_i(t)$

$\mathtt{L}_i(t)$ = linear function that best captures the effects of the non-linear load $\mathcal{NL}_i(t)$, the i^{th} contributing load associated with failure

$\sigma_{\mathtt{L}_i}$ = standard deviation of the linear function $\mathtt{L}_i(t)$

$\alpha, \beta, \cdots, \gamma = m$ weighting factors

By varying the weighting factors $\alpha, \beta, \cdots, \gamma$ using n different combinations, it is possible to emphasize some of the linear functions while de-emphasizing others, to approximate the n non-linear load combination cases. The flexibility afforded by Eq.(5.1) and (5.2) recognizes that failure may occur when a singular non-linear load attains an extreme value, or when multiple non-linear loads simultaneously experience a specific weighting of large, but not extreme, values.

The surrogate processes, combined with the DLG methodology, yield ensembles of short excitation time series which lead to realizations of surrogate process maxima.

Note that the global, Gaussian inputs constructed by the DLG to produce exposure-period-maxima of $z_i(t)$ also are inputs to the other surrogate processes $z_j(t)$. When determining the total failure probability, it is possible that extremes of $z_j(t)$ also occur from this input, and the potential overlap between the i^{th} and the j^{th} surrogate process maxima must be accounted for. To formally derive the extreme value probabilities of the various surrogate processes, notation is defined:

$g(z_{i,T})$ = extreme value distribution of the surrogate process $z_i(t)$, based on the exposure period, T

$\eta_i(t)$ = ensemble sample of DLG global, Gaussian input with spectral definition, $S^+(\omega)$, constructed to lead to an exposure-period-maximum of the i^{th} surrogate process, $z_i(t)$

$z_{ii}(t)$ = ensemble sample time series of the i^{th} surrogate process, $z_i(t)$, driven by $\eta_i(t)$

$\widehat{z_{ii}}$ = maximum of $z_{ii}(t)$, which is a member of the exposure period extreme value distribution of $z_i(t)$, $g(z_{i,T})$; i.e. $\widehat{z_{ii}} \in g(z_{i,T})$

$z_{ij}(t)$ = ensemble sample time series of the j^{th} surrogate process, $z_j(t)$, driven by $\eta_i(t)$

$\widehat{z_{ij}}$ = ensemble sample maximum of $z_{ij}(t)$

Figure 5.4 is a schematic illustrating the way the NL-DLG process approximates the system probability of failure. This figure is similar to Figure 5.1, in which a global, Gaussian input, $\eta(t)$, drives the non-linear loads, $\mathcal{NL}_i(t)$ $i = 1, \cdots, m$, which are mapped onto the failure surface, G, to determine if failure occurs. The difference is that instead of an exposure-length $\eta(t)$ input, as in Figure 5.1, in Figure 5.4, ensembles of short $\eta_i(t)$ $i = 1, \cdots, n$ time series from the DLG excite the system. These unique, but statistically equivalent short time series are constructed by the DLG to produce exposure-period-maxima of $z_i(t)$ $i = 1, \cdots, n$.

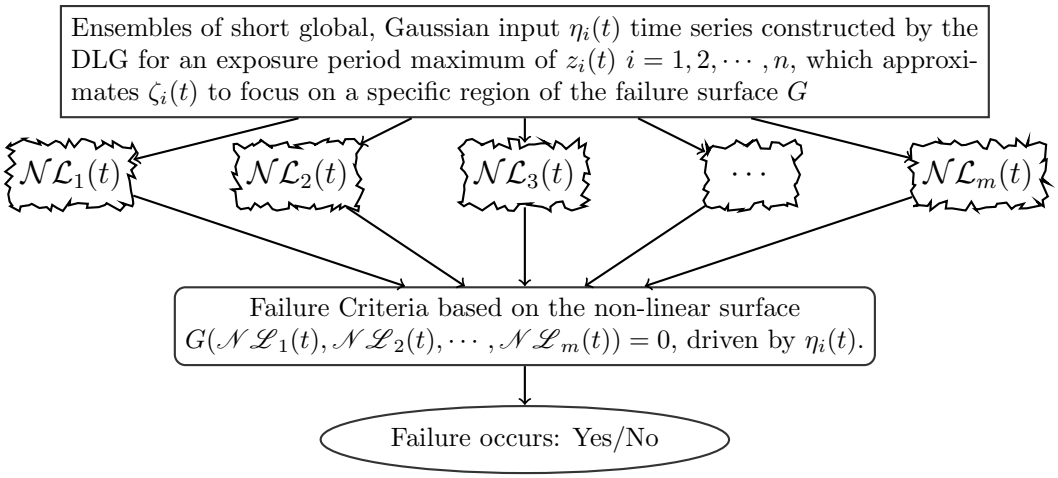

Figure 5.4: Approximation of system's failure probability from the NL-DLG process using ensembles of DLG-generated time series.

5.5 Approximations of the NL-DLG Process

To summarize: the estimate of system failure probability is determined through the consideration of the non-linear system response due to excitation time series that lead to exposure-period-maxima of the surrogate processes $z_i(t)$, $i = 1, \cdots, n$. These $z_i(t)$ approximate the non-linear load combination cases, $\zeta_i(t)$, which focus on specific areas on the failure surface, G. The DLG constructs an ensemble of $\eta_i(t)$ for $i = 1, \cdots, n$ that lead to a maximum value of the surrogate process: $\widehat{z_{ii}} \in g(z_{i,T})$. These short global, Gaussian input time series drive the non-linear loads $\mathcal{NL}_i(t)$ $i = 1, \cdots, m$, which are mapped onto the failure surface, G, presumably in the area directed by $\zeta_i(t)$, to determine if failure occurs. The system's probability of failure is approximated based on the system's response to the short $(\mathscr{NL}_1(t), \cdots, \mathscr{NL}_m(t))$ time series driven by $\eta_i(t)$. Relevant details on the approximation provided by the DLG and on the resulting time series are:

- The surrogate process maxima constructed by the DLG are a lower bound on the true exposure-period-maxima for $z_i(t)$ and give a lower bound for the extremes of the corresponding non-linear load combination case. Therefore, the probability of failure given by the short DLG time series conditioned for a specific exposure-period-maximum is a lower bound on the probability of failure from full MCS. This is because only certain parts of the exposure are simulated, with the assumption that these times are when failure exclusively occurs, whereas full MCS allow for failure to occur any time during the exposure.

- The global, Gaussian inputs constructed by the DLG are statistically valid time series which could be experienced during the exposure, implying that the response time series are also physically realizable. Therefore, the constructed $(\mathscr{NL}_1(t), \mathscr{NL}_2(t), \cdots, \mathscr{NL}_m(t))$ time series are statistically possible responses within the exposure. The approximation is in the assumption that these time series contain the maximum value that $\zeta_i(t)$ experiences over the full exposure.

- The global, Gaussian inputs $\eta_i(t)$ which lead to extreme load responses are approximated, not the non-linear loads. The non-linear loads driven by these inputs are constructed and compared to the failure surface, G, to determine if a failure has occurred, as would be the case for full MCS. The only difference between this method and full MCS is that the surrogate processes are used to estimate which global, Gaussian inputs are most likely to lead to extremes of the non-linear load combination cases.

- The global, Gaussian time series $\eta_i(t)$ constructed by the DLG are short, and the length is user defined, but the length of the time series should be no longer than a relevant autocorrelation period. Here, the length of $\eta_i(t)$ is limited to the autocorrelation period of $\eta(t)$ itself, which comes from its spectral definition $S^+(\omega)$. Since $\eta_i(t)$ is assembled to produce a maximum $\widehat{z_{ii}}$, it would not be constructive to examine the statistics of $z_{ii}(t)$ far from the $\widehat{z_{ii}}$ event itself.

5.6 Linking Surrogate Process Maxima to System Failure Probability, Assuming Un-Clustered Maxima

Surrogate processes are defined as linear approximations, or linear reduced-order models, to non-linear load combination cases and the DLG generates ensembles of the global, Gaussian input which lead to exposure-period-maxima of these surrogate processes. To use the DLG process for the notional system in Figures 5.2-5.3, surrogate processes like in Eq.(5.2) would first be defined. Based on the failure surface G shown in Figure 5.3, one might assume failures are linked to independent extremes of the non-linear loads - regions represented by extremes of $\mathcal{NL}_1(\mathtt{L}_1(t))$ and by extremes of $\mathcal{NL}_2(\mathtt{L}_2(t))$. G can be approximated by these two non-linear load combination cases. Two surrogate processes are defined using the notation of Eq.(5.2) as

$z_1(t) = \mathtt{L}_1(t)/\sigma_{\mathtt{L}_1}$ and $z_2(t) = \mathtt{L}_2(t)/\sigma_{\mathtt{L}_2}$ to approximate the two non-linear load combination cases $\zeta_1(t) = \mathcal{NL}_1(\mathtt{L}_1(t))/\sigma_{\mathcal{NL}_1}$ and $\zeta_2(t) = \mathcal{NL}_2(\mathtt{L}_2(t))/\sigma_{\mathcal{NL}_2}$, respectively.

Employing the DLG process, two ensembles of many short time series of $\eta_1(t)$ and $\eta_2(t)$ that lead to exposure-period-maxima of $z_1(t)$ and $z_2(t)$, respectively, would be constructed. It is assumed that $\eta_1(t)$ constructed to lead to exposure-period-maxima of $z_1(t)$ also lead to exposure-period-maxima of $\zeta_1(t)$, and that $\eta_2(t)$ constructed to lead to exposure-period-maxima of $z_2(t)$ also lead to exposure-period-maxima of $\zeta_2(t)$. Indeed, from the single MCS shown in Figure 5.2 with the plotted linear and non-linear loads (not normalized by the respective σ), it can be seen that this is true, indicating the appropriate choice of surrogate processes for these two non-linear load combination cases.

More load combination cases could be defined to capture more regions of the failure surface, but here only two are used for simplicity. Ensembles of the non-linear system response time series $(\mathcal{NL}_2(\mathtt{L}_2(t)), \mathcal{NL}_1(\mathtt{L}_1(t)))$, are next generated from each ensemble of inputs, $\eta_i(t)$, and mapped onto G. Then, the probability of failure *given* the system experiences an exposure-period-maximum of the surrogate process, $z_i(t)$, is found. The search for failure is restricted to the time segment containing one system autocorrelation period of $\eta(t)$, centered around the instant of extreme surrogate response. The challenge is now to determine how to patch together these failure probabilities from different DLG surrogate processes to a full description of the system failure probability.

In a full-length MCS, all surrogate processes will experience an exposure-period-maximum. For unrelated surrogate processes, the probability that multiple surrogate processes experience their exposure-period-maximum at the same time (or within a short time window) goes to zero as the exposure length increases. Sufficiently unrelated surrogate processes will experience their respective exposure-period-maxima at different times over the exposure.

Possible outcomes in the time segments around each surrogate exposure-period-maximum include one failure, multiple failures, or no failures. This is similar to the classic probability problem described in Chapter 1.3.1 in which failure is due to the first excursion above a certain level, and is additionally complicated by combined, non-linear, and non-Gaussian loading. Rather than determine the order and probability of multiple failures, which would be problematic if not impossible, it is better to consider the null problem. That is: what is the probability that the system does *not*

fail during its exposure period?

For unrelated surrogate processes whose exposure-period-maxima occur at different times over the exposure, the system must not fail due to the realization of each surrogate process maximum. The non-failure problem does not include any notion of time (i.e. which maximum occurs first) and only requires that the $(\mathcal{NL}_1(t), \cdots, \mathcal{NL}_m(t))$ time series driven by the excitation $\eta_i(t)$ for all $i = 1, \cdots, n$ which leads to a $z_i(t)$ maximum does not lead to failure. Therefore, for unrelated surrogate processes, the non-failure events due to the realization of unrelated surrogate process maxima are independent. The system responses due to excitation time series containing these un-clustered surrogate process maxima can be viewed as independent trials of an experiment. The experiment here is: does this time series lead to failure or not? This is similar to estimating the statistics of a system by running many MCS, in which each individual trial is independent. For unrelated surrogate processes whose maxima are not clustered together over an exposure, the system response to excitation which leads to a single exposure-period-maximum is independent of its response to a different time which contains a different exposure-period-maximum. With this simplification, the system's probability of failure, based on the conditional probability of failure from n individual surrogate process exposure-period-maxima as estimated by the DLG, is defined in Eq.(5.3):

$$\begin{aligned} p(\mathbb{F}) &= p(\cup_{i=1}^{n} \widehat{z_{ii}}^{F}) \\ p(\mathbb{F}) &= 1 - p(\mathbb{F}^c) \\ p(\mathbb{F}) &= 1 - p((\cup_{i=1}^{n} \widehat{z_{ii}}^{F})^c) \\ p(\mathbb{F}) &= 1 - p(\cap_{i=1}^{n} \widehat{z_{ii}}^{F^c}) \\ p(\mathbb{F}) &= 1 - p(\widehat{z_{11}}^{F^c}) p(\widehat{z_{22}}^{F^c}) \cdots p(\widehat{z_{nn}}^{F^c}) \end{aligned} \tag{5.3}$$

where

$\mathbb{F} \equiv$ event that system failure occurs within the exposure period

$\mathbb{F}^c \equiv$ event that system failure does not occur within the exposure period

$\widehat{z_{ii}} \equiv$ maximum of $z_{ii}(t)$, which is a member of $g(z_{i,T})$

$\widehat{z_{ii}}^{F} \equiv$ event that the time series of $(\mathcal{NL}_1(t), \cdots, \mathcal{NL}_m(t))$, driven by $\eta_i(t)$ which leads to $\widehat{z_{ii}}$, mapped onto G leads to failure

$\widehat{z_{ii}}^{F^c} \equiv$ event that the time series of $(\mathcal{NL}_1(t), \cdots, \mathcal{NL}_m(t))$, driven by $\eta_i(t)$ which leads to $\widehat{z_{ii}}$, mapped onto G does not lead to failure

A beneficial consequence of this formulation is that if a non-linear load combination case, or associated surrogate process, is chosen which is completely unrelated to

system failure, including it in Eq.(5.3) does not skew the final result. A surrogate process maximum associated with excitation with a 0% chance of causing failure has a 100% probability of non-failure, which multiplies the final expression in Eq.(5.3) by 1. In this way, the estimate of the system's failure probability is unaffected by the addition of an unrelated load combination case.

This preliminary expression, Eq.(5.3), links the failure (or non-failure) probabilities from the individual DLG surrogate process time series, $\eta_i(t)$, to an estimate of overall probability of failure for the system's full exposure period. The independence of the non-failure events due to excitation records containing un-clustered surrogate process maxima allows the simplification of the intersection of the non-failure events into the individual maxima events. Should the surrogate processes be sufficiently unrelated, and their maxima occur at separate times over the exposure, meaning that the exposure-period-maxima of $z_i(t)$ $i = 1, 2, \cdots, n$ are not clustered, it is straightforward to estimate the total probability of system failure using Eq.(5.3). In general, however, multiple surrogate processes may not produce un-clustered maxima (i.e. as discussed in Chapter 3.7 and shown in Figure 3.12). Therefore, the next step is to determine how the different surrogate processes and their maxima may be related.

5.7 Relation of Surrogate Processes via the Exposure-Period-Maxima

Eq.(5.3) assumes that all the surrogate process maxima are un-clustered over an exposure and the independence of the non-failure events associated with the realization of these maxima allows for the simple formulation. However, it is possible that the realization times of the surrogate process maxima are not unrelated. The relation between surrogate-process-maxima can be estimated by examining the Gaussian inputs which lead to the surrogate process extrema. The DLG constructs ensembles of $\eta_i(t)$ which drive time series for all surrogate processes - $z_{ii}(t), z_{ij}(t), \cdots, z_{in}(t)$. By construction, $\widehat{z_{ii}} \in g(z_{i,T})$. All of the other time series, $z_{ij}(t), \cdots, z_{in}(t)$, also contain a maximum: $\widehat{z_{ij}}, \cdots, \widehat{z_{in}}$. If two surrogate processes are related, there may be some values of $\widehat{z_{ip}}$, $p = j, \cdots, n$ with $\widehat{z_{ip}} \in g(z_{p,T})$. In this case, it may not be correct to say that the maxima of the surrogate processes $z_i(t)$ and $z_p(t)$ occur un-clustered during the exposure period.

5.7.1 Clustering of Surrogate Process Maxima

To account for the event that different surrogate processes experience exposure-period-maxima due to the same global, Gaussian input, or within the same autocorrelation period window, more notation is defined. For a total of n different surrogate processes that approximate n non-linear load combination cases:

$\widehat{Z_i}$ = this event occurs from $\eta_i(t)$, with $\widehat{z_{ii}} \in g(z_{i,T})$, and all $\widehat{z_{ij}} \notin g(z_{j,T})$
where $j = 1, \cdots, n$ and $j \neq i$

$\widehat{Z_i Z_j}$ = this event occurs in 2 occasions from $\eta_i(t)$ or $\eta_j(t)$:
1) from $\eta_i(t)$: $\widehat{z_{ii}} \in g(z_{i,T})$, $\widehat{z_{ij}} \in g(z_{j,T})$, and all $\widehat{z_{ik}} \notin g(z_{k,T})$ where $k = 1, \cdots, n$ and $k \neq i, j$
2) from $\eta_j(t)$: $\widehat{z_{jj}} \in g(z_{j,T})$, $\widehat{z_{ji}} \in g(z_{i,T})$, and all $\widehat{z_{jk}} \notin g(z_{k,T})$ where $k = 1, \cdots, n$ and $k \neq i, j$

$\widehat{Z_i Z_j Z_k}$ = this event occurs in 3 occasions from $\eta_i(t)$, $\eta_j(t)$, or $\eta_k(t)$:
1) from $\eta_i(t)$: $\widehat{z_{ii}} \in g(z_{i,T})$, $\widehat{z_{ij}} \in g(z_{j,T})$, $\widehat{z_{ik}} \in g(z_{k,T})$, and all $\widehat{z_{ip}} \notin g(z_{p,T})$
where $p = 1, \cdots, n$ and $p \neq i, j, k$
2) from $\eta_j(t)$: $\widehat{z_{jj}} \in g(z_{j,T})$, $\widehat{z_{ji}} \in g(z_{i,T})$, $\widehat{z_{jk}} \in g(z_{k,T})$, and all $\widehat{z_{jp}} \notin g(z_{p,T})$
where $p = 1, \cdots, n$ and $p \neq i, j, k$
3) from $\eta_k(t)$: $\widehat{z_{kk}} \in g(z_{k,T})$, $\widehat{z_{ki}} \in g(z_{i,T})$, $\widehat{z_{kj}} \in g(z_{j,T})$, and all $\widehat{z_{kp}} \notin g(z_{p,T})$
where $p = 1, \cdots, n$ and $p \neq i, j, k$

and

$\widehat{Z_i}^F, \widehat{Z_i Z_j}^F, \widehat{Z_i Z_j Z_k}^F \equiv$ event that failure occurs due to $(\mathcal{NL}_1(t), \cdots, \mathcal{NL}_m(t))$ driven by the time series $\eta_i(t)$, $\eta_j(t)$, or $\eta_k(t)$ which leads to $\widehat{Z_i}$, $\widehat{Z_i Z_j}$, or $\widehat{Z_i Z_j Z_k}$, respectively

$\widehat{Z_i}^{F^c}, \widehat{Z_i Z_j}^{F^c}, \widehat{Z_i Z_j Z_k}^{F^c} \equiv$ event that failure does not occur due to $(\mathcal{NL}_1(t), \cdots, \mathcal{NL}_m(t))$ driven by the time series $\eta_i(t)$, $\eta_j(t)$, or $\eta_k(t)$ which leads to $\widehat{Z_i}$, $\widehat{Z_i Z_j}$, or $\widehat{Z_i Z_j Z_k}$, respectively

This same notation expands for any and every combination of n surrogate processes. Note that all of the above events are mutually exclusive, by definition. Now the probability of non-failure due to the experience of $(\mathcal{NL}_1(t), \cdots, \mathcal{NL}_m(t))$, driven by the time series $\eta_i(t)$, $\eta_j(t)$, or $\eta_k(t)$ which leads to $\widehat{Z_i}$, $\widehat{Z_i Z_j}$, or $\widehat{Z_i Z_j Z_k}$ is determined by examining the short time series $\eta_i(t)$ from the DLG. The conditional probability

of non-failure given the system experiences certain types of maxima is found by:

$$
\begin{aligned}
p(\widehat{Z_i}^{F^c}) &= \frac{\text{number of } \widehat{Z_i}^{F^c} \text{ events}}{\text{number } \widehat{Z_i} \text{ events}} \\
p(\widehat{Z_i Z_j}^{F^c}) &= \frac{\text{number of } \widehat{Z_i Z_j}^{F^c} \text{ events}}{\text{number of } \widehat{Z_i Z_j} \text{ events}} \\
p(\widehat{Z_i Z_j Z_k}^{F^c}) &= \frac{\text{number of } \widehat{Z_i Z_j Z_k}^{F^c} \text{ events}}{\text{number of } \widehat{Z_i Z_j Z_k} \text{ events}}
\end{aligned}
\tag{5.4}
$$

5.8 Surrogate Process Maxima Configurations

As shown above, it is possible that a system experiences the exposure-period-maximum of two or more different surrogate processes clustered at the same time, or within the same autocorrelation period. This is a separate type of event, and Section 5.7 derived the probability of non-failure due to $(\mathcal{NL}_1(t), \cdots, \mathcal{NL}_m(t))$ driven by the time series $\eta_i(t), \cdots, \eta_n(t)$ associated with these mutually exclusive events. However, these separate events must be linked back to the fact that over the full exposure period, the system experiences the exposure-period-maximum of each defined surrogate process. Some of these exposure-period-maxima may occur within the same autocorrelation period and are considered a single joint event rather than separate events that test the system.

As an example, consider a system characterized by three non-linear load combination cases $\zeta_i(t)$ $i = 1, 2, 3$, represented by three surrogate processes $z_i(t)$ $i = 1, 2, 3$. Each surrogate process experiences its maximum over the exposure, but those maxima may be grouped or clustered, depending on the relationship between the surrogate processes. For the three surrogate processes $z_1(t)$, $z_2(t)$, and $z_3(t)$, there are five ways for these maxima to be grouped. All three maxima may occur separately: defined by the overall event $\{\widehat{Z_1}, \widehat{Z_2}, \widehat{Z_3}\}$. Two surrogate process maxima may cluster together with the third separate: defined by $\{\widehat{Z_1 Z_2}, \widehat{Z_3}\}$, $\{\widehat{Z_1 Z_3}, \widehat{Z_2}\}$, or $\{\widehat{Z_2 Z_3}, \widehat{Z_1}\}$. Or, all three maxima may cluster together: defined by $\{\widehat{Z_1 Z_2 Z_3}\}$.

These five possible groupings of the three surrogate process maxima are called maxima configurations, and are noted *ci* with $i = 1, 2, \cdots, 5$. For $n = 3$, these configurations are defined *c1* : $\{\widehat{Z_1 Z_2}, \widehat{Z_3}\}$, *c2* : $\{\widehat{Z_1 Z_3}, \widehat{Z_2}\}$, *c3* : $\{\widehat{Z_2 Z_3}, \widehat{Z_1}\}$, *c4* : $\{\widehat{Z_1 Z_2 Z_3}\}$, and *c5* : $\{\widehat{Z_1}, \widehat{Z_2}, \widehat{Z_3}\}$. These maxima events are defined so that the mutually exclusive sub-groups within a maxima configuration (i.e. $\widehat{Z_1 Z_2}$ and $\widehat{Z_3}$ are sub-groups within *c1*) are, by definition, un-clustered. Therefore, the probabilities of non-failure

due to the realization of the sub-groups within a specific maxima configuration are independent. Then Eq.(5.3) can be expanded for the potential of related surrogate processes through these maxima configurations.

5.8.1 Possible Maxima Configurations

The next step is to determine the probability of experiencing the possible maxima configurations. All exposure-period-maxima are experienced over a full exposure, but they may be clustered. This indicates that for n surrogate processes, the different maxima configurations, ci, which describe all possible groupings of the surrogate process maxima are exhaustive. Every exposure fits the criteria of one single maxima configuration type. It is clear that:

$$p(\mathrm{c}\mathit{1}) + p(\mathrm{c}\mathit{2}) + \cdots + p(\mathrm{c}B_n) = 1 \tag{5.5}$$

where

$c\mathit{1}$,$c\mathit{2}, \cdots, cB_n \equiv$ maxima configuration 1, 2, $\cdots$, B_n

$p(ci) =$ probability of experiencing the maxima configuration ci with $i = \mathit{1}, \mathit{2}, \cdots, B_n$

$B_n =$ total number of possible configurations to group n surrogate process maxima, given by the Bell number, B_n

$$= \sum_{k=0}^{n} \left\{ {n \atop k} \right\} = \sum_{k=0}^{n} \frac{1}{k!} \sum_{j=0}^{k} (-1)^{(k-j)} \binom{k}{j} j^n$$

The Bell number, B_n, gives the number of possible maxima configurations for n surrogate processes (*Bell*, 1938). The configurations are all possible groupings of n surrogate process maxima, in which the maxima may all be un-clustered, may all cluster together, or may be clustered with any non-zero number of other maxima. For a system represented by three surrogate processes, there are five possible maxima configurations, i.e. $B_3 = 5$.

The partitioning of these configurations is a possible limitation of the analysis; the number of configurations increases rapidly with n, as shown in Table 5.1. Clearly n should be limited to maintain computational advantages over brute-force MCS, though a high B_n represents a more organizational, rather than computational, challenge. For example, it would not be a beneficial simplification to reduce the infinite number of points on a failure surface, G, to 10 representative load combination cases (making $n = 10$ surrogate processes), since this would result in an unreasonable number of maxima configurations to analyze ($B_{10} = 115,975$). The partitioning of

maxima configurations is not a formidable task for a few surrogate processes, as B_n is not proportional to the number of DLG simulations which must be run, which is the only notable computational cost of the NL-DLG process. However, a high B_n means many maxima configurations to analyze.

Number of Surrogate Processes n	Number of maxima configurations (Bell number B_n)
1	1
2	2
3	5
4	15
5	52
6	203
7	877
8	4,140

Table 5.1: Number of maxima configurations possible for n surrogate process exposure-period-maxima (Bell number B_n).

With these maxima configurations, the last step in the NL-DLG process is to determine the probability of experiencing each maxima configuration. Although not computationally expensive, this requires a strict definition of the problem's probability space. Section A.1 in the Appendix contains an in-depth discussion of the probability space, and the experiment to determine the probability of experiencing specific maxima configurations. The final result for the probabilities of experiencing the maxima configurations possible for three surrogate processes is given by Eq.(A.8)-(A.13).

5.8.2 Probability of Complex System Failure

Expanding Eq.(5.3) to account for the different possible maxima configurations produces Eq.(5.6), which is illustrated in Figure 5.5 for a system with a failure surface G approximated by three non-linear load combination cases. The possibility that the surrogate process exposure-period-maxima may be clustered is considered by defining the new notation to account for these events, i.e. $\{\widehat{Z_i Z_j}\}$. The probabilities of non-failure due to these un-clustered maxima configuration sub-groups are independent. Eq.(5.6) can be expanded to any number of surrogate processes by taking into account the number of all possible maxima configurations, B_n. The conditioning for each configuration is implied in the definition for the different exposure-period-maxima events.

The probability of non-failure given the exposure is represented by the maxima configuration $c1 - c5$ is the product of the probabilities of non-failure due to the individual sub-groups (i.e. Eq.(5.4)). For example, the probability of non-failure due to configuration $c1$ is $p(\widehat{Z_1 Z_2}^{F^c})p(\widehat{Z_3}^{F^c})$. To find the overall system failure probability, $p(\mathbb{F})$, the probabilities of non-failures given a specific maxima configuration are considered in light of experiencing that maxima configuration (i.e. $p(c1)$).

$$
\begin{aligned}
p(\mathbb{F}) &= 1 - p(\mathbb{F}^c) \\
p(\mathbb{F}^c) &= p(\widehat{Z_1 Z_2}^{F^c} \cap \widehat{Z_3}^{F^c} | c1)p(c1) + p(\widehat{Z_1 Z_3}^{F^c} \cap \widehat{Z_2}^{F^c} | c2)p(c2) + p(\widehat{Z_2 Z_3}^{F^c} \cap \widehat{Z_1}^{F^c} | c3)p(c3) + \cdots \\
&\quad p(\widehat{Z_1 Z_2 Z_3}^{F^c} | c4)p(c4) + p(\widehat{Z_1}^{F^c} \cap \widehat{Z_2}^{F^c} \cap \widehat{Z_3}^{F^c} | c5)p(c5) \\
&\quad = p(\widehat{Z_1 Z_2}^{F^c})p(\widehat{Z_3}^{F^c})p(c1) + p(\widehat{Z_1 Z_3}^{F^c})p(\widehat{Z_2}^{F^c})p(c2) + p(\widehat{Z_2 Z_3}^{F^c})p(\widehat{Z_1}^{F^c})p(c3) + \cdots \\
&\quad p(\widehat{Z_1 Z_2 Z_3}^{F^c})p(c4) + p(\widehat{Z_1}^{F^c})p(\widehat{Z_2}^{F^c})p(\widehat{Z_3}^{F^c})p(c5)
\end{aligned}
\tag{5.6}
$$

where

$$
\begin{aligned}
\mathbb{F} &\equiv \text{event that system failure occurs within the exposure} \\
\mathbb{F}^c &\equiv \text{event that system failure does not occur within the exposure} \\
p(\widehat{Z_i}^{F^c}), p(\widehat{Z_i Z_j}^{F^c}), p(\widehat{Z_i Z_j Z_k}^{F^c}) &= \text{given by Eq.(5.4)} \\
p(ci), i = 1, 2, 3, 4, 5, &= \text{given by Eq.(A.8)-(A.13)} \\
\sum_{i=1}^{5} p(ci) &= 1
\end{aligned}
$$

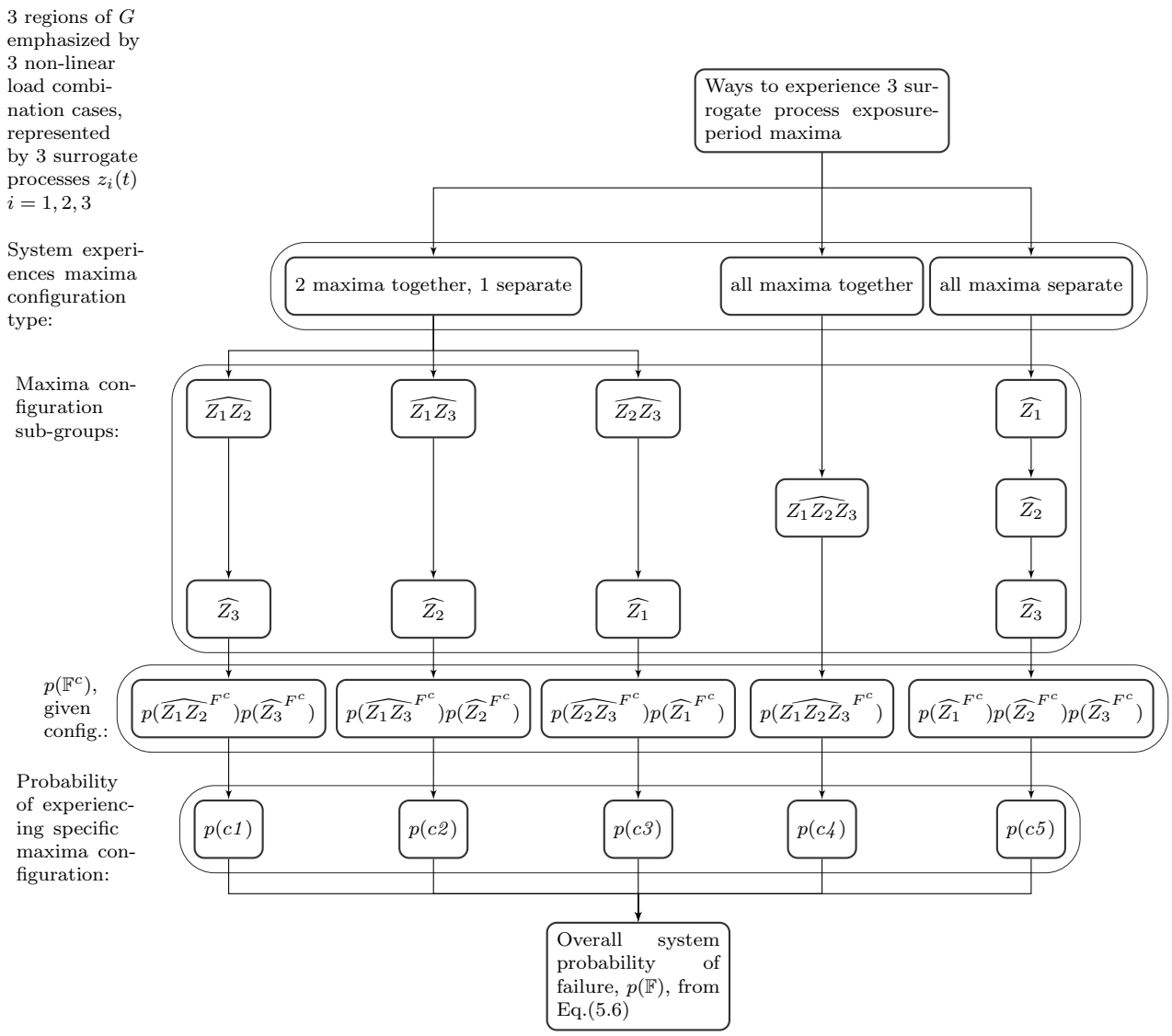

Figure 5.5: Schematic illustrating Eq.(5.6) for a system with a failure surface, G, where three regions are emphasized by three non-linear load combination cases, approximated by three surrogate processes, $z_i(t)$ $i = 1, 2, 3$. Five different maxima configurations are possible, and the probability of non-failure is given for each configuration. For configurations with multiple sub-groups (i.e. ci, $i = 1-3, 5$), the ordering of the sub-group does not matter because of the independence of the non-failure events associated with un-clustered surrogate process maxima events. The final probability of failure, $p(\mathbb{F})$, is determined by combining the conditional probabilities of non-failure of the given maxima configurations with the probability of each maxima configuration occurring.

5.9 Estimated Distribution of Most-Likely Failures

In addition to estimating a system's probability of failure, it is also helpful to know the types of failure the system experiences when subjected to combined loading. Given such a distribution of failure occurrences, a designer can improve the system design

to protect against certain weaknesses. The distribution of failure modes is implicitly the distribution of first failure occurrences, because once a system first experiences failure, it can no longer experience other failures. This is similar to finding the first out-crossing of the failure surface, G, by the loading vector. Although the NL-DLG process is formulated so that failures can occur due to excitation containing any of the surrogate process exposure-period-maxima, an important aspect is to determine what type of failures are most likely to occur first, which are the most-likely failures.

This distribution is estimated by combining the failures due to the specific maxima configurations with the probability of experiencing a specific maxima configuration, $p(ci)$, $i = 1, 2, \cdots, B_n$. To estimate a distribution of the failures a system is most likely to experience over its full exposure, pick a large number of exposure realizations g (similar to conducting g full-length MCS for converged statistics). Then, the probability of experiencing each maxima configuration $p(ci)$, $i = 1, 2, \cdots, B_n$ dictates the percentage of those g realizations which fall into each of the maxima configurations ci (i.e. $g \times p(ci)$, $i = 1, 2, \cdots, B_n$) to be considered for the distribution estimate.

The question then is, for maxima configurations ci, $i = 1, 2, \cdots, B_n$ which have multiple separate maxima sub-groups, which sub-group occurs first? For example, in Figure 5.5, $c1$ is the event $\{\widehat{Z_1 Z_2}, \widehat{Z_3}\}$, meaning that the three surrogate process maxima are grouped into two maxima sub-groups: $\{\widehat{Z_1 Z_2}\}$ and $\{\widehat{Z_3}\}$. Which one of these sub-groups occurs first during an exposure? Consider that the DLG constructs $\eta_i(t)$ which lead to $\widehat{z_{ii}} \in g(z_{i,T})$. Regardless of how these exposure-period-maxima are later partitioned into different maxima groups (i.e. $\widehat{Z_i}$, $\widehat{Z_i Z_j}$, or $\widehat{Z_i Z_j Z_k}$) all of these maxima have the same return period. This implies that each maxima sub-group has the same probability of occurring first. The probability of experiencing a specific maxima sub-group is then defined.

Figure 5.6 gives the probability of experiencing a specific maxima sub-group in a given maxima configuration first. These probabilities are combined with the number of exposure realizations, g, the distribution is estimating to give the number of DLG time series from each maxima sub-group (i.e. $\widehat{Z_i}$, $\widehat{Z_i Z_j}$, or $\widehat{Z_i Z_j Z_k}$) that should be considered for this distribution. Empirical histograms can be constructed of the DLG time series which fall into each sub-group $\{\widehat{Z_1}\}$, $\{\widehat{Z_2}\}$, $\{\widehat{Z_3}\}$, $\{\widehat{Z_1 Z_2}\}$, $\{\widehat{Z_1 Z_3}\}$, $\{\widehat{Z_2 Z_3}\}$, and $\{\widehat{Z_1 Z_2 Z_3}\}$. Note that the $\widehat{Z_i}$ distributions are univariate histograms, whereas the $\widehat{Z_i Z_j}$ and $\widehat{Z_i Z_j Z_k}$ distributions are bivariate and trivariate histograms, respectively. The time series in each sub-group to be considered are selected based

on the associated histogram distribution. If the chosen time series contain a failure, that failure is plotted on the distribution of most-likely failures.

Considering the maxima configuration *c1*, the number of time series to be considered from all DLG time series which satisfy the $\{\widehat{Z_1 Z_2}\}$ criterion is $g \times p(c1) \times 1/2$. The empirical histogram of all $\{\widehat{Z_1 Z_2}\}$ values dictates how these $g \times p(c1) \times 1/2$ time series are selected. Any failures which result from those time series are plotted on the failure distribution estimate. In the same way, $g \times p(c1) \times 1/2$ times series which satisfy the $\{\widehat{Z_3}\}$ criterion are selected, based on the empirical histogram distribution of those $\{\widehat{Z_3}\}$ values. Any failures which result are plotted on the distribution estimate. All maxima configurations ci, $i = 1, 2, \cdots, B_n$, and the maxima sub-groups within those maxima configurations, are considered in the same way to estimate the distribution of failures the system is most likely to experience over its exposure.

This process gives an overall ensemble of short excitation time series which lead to the most-likely failure occurrences. These excitation time series could be used as the input to more high-fidelity models, like Computational Fluid Dynamics, Finite Element Analysis, or even physical model tests, to determine system performance. These inputs can be seen as a selected group of excitation records which presumably lead to the same converged statistics of failure occurrences as would be recorded from brute-force MCS.

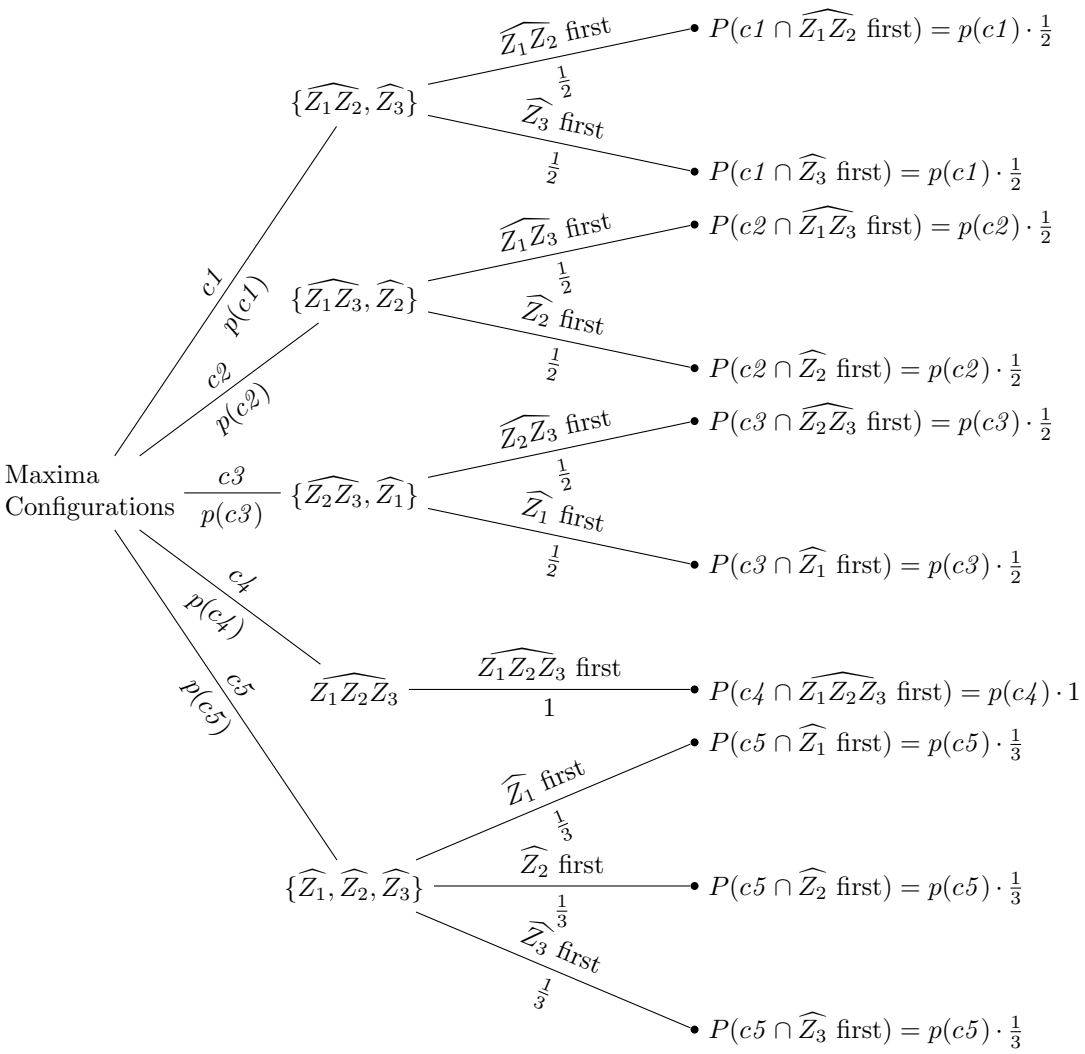

Figure 5.6: Probability tree outlining the probability of experiencing a specific maxima sub-group first.

5.10 Implications of the NL-DLG Process

This chapter developed the NL-DLG process to estimate the probability of complex system failure governed by multiple, potentially correlated, non-linear, and non-Gaussian loading over a long, stationary exposure period without resorting to brute-force MCS. A finite number of non-linear load combination cases focus on different regions of the failure surface, G, which relates non-linear loading to the system response.

Then, excitation inputs which lead to the exposure-period-maxima of these load combination cases are approximated by the DLG using associated linear surrogate processes. These surrogate processes may be defined by linearization or reduced-order

modeling and are meant to be an indicator for extreme responses of the non-linear load combination cases. Subsequently, the DLG constructs short global, Gaussian time series that lead to exposure-period-maxima of the surrogate processes, and presumably the associated non-linear load combination cases. The vector of the non-linear loads $(\mathcal{NL}_1(t), \cdots, \mathcal{NL}_m(t))$ due to these inputs is constructed and plotted on the failure surface, G, to determine whether or not failure occurs. The probability of system failure is estimated by the system response due to these short-time non-linear load vectors. Mutual exclusivity of the surrogate process maxima is not assumed and any potential overlap between surrogate processes is considered in the analysis. The assumptions used to develop the NL-DLG process are:

- The global environment that drives the non-linear loads is Gaussian with a given spectral definition.
- The failure surface G is time-invariant.
- Different regions of G are emphasized by a finite number, n, of non-linear load combination cases.
- The Gaussian inputs which lead to exposure-period-maxima of the surrogate processes also lead to exposure-period-maxima of the associated non-linear load combination cases.
- Failure occurs exclusively during times in the excitation when the surrogate processes experience their exposure-period-maxima.
- Over a full exposure, the exposure-period-maximum of each surrogate processes is experienced, but these maxima may be clustered. When the maxima occur within a relevant autocorrelation period of each other, they are assumed to occur together, meaning that their joint occurrence is the only time during the full exposure either exposure-period-maximum is experienced.

Using the above assumptions, the NL-DLG process was developed to use surrogate processes to efficiently estimate a complex system's probability of failure and estimate the distribution of failures that a system is most likely to experience over the exposure. The NL-DLG process allows consideration of a system's performance earlier in a design spiral because of reduced computation and allows failure analysis to become a part of the design process. An illustrative, multi-dimension example is now presented, utilizing the NL-DLG process to illustrate its capability.

CHAPTER VI

An Illustrative, Multi-Dimension Example using the NL-DLG Process

To illustrate the capability of the NL-DLG process, a simple hypothetical example is presented. This example includes a 3−dimension failure surface and a system subject to three combined, potentially correlated, non-Gaussian loads over a 1000-hour exposure. Two iterations of the NL-DLG process are performed to show how the failure estimate can be improved by considering feedback. Some general notes on the NL-DLG process are highlighted to indicate strengths of the process and additional challenges to be considered.[1]

6.1 Complex System Definition

For this example, a single-sided mean-squared spectrum $S^+(\omega)$ describes the global, Gaussian input, $\eta(t)$, which provides the input to the stochastic loading on the system. This spectrum is given in Figure 6.1. The characteristic period of the input is 12 seconds suggesting 3×10^5 cycles per exposure period.

Non-dimensional magnitude and phase information for three linear transfer functions $\mathcal{L}_1(\omega)$, $\mathcal{L}_2(\omega)$, and $\mathcal{L}_3(\omega)$, are shown in Figure 6.2 and defined by Eq.(8.2). The three linear transfer functions are different dynamic oscillators, all of which are excited by the same global, Gaussian input $\eta(t)$. $\mathcal{L}_1(\omega)$ is a static response, $\mathcal{L}_2(\omega)$ has a resonant frequency near the peak excitation frequency, and $\mathcal{L}_3(\omega)$ has a resonant frequency that leads to a bimodal response for excitation with spectral density of $S^+(\omega)$. The single-sided mean-squared response spectra are also shown in Figure 6.2.

[1]Portions of this work were previously published in *Seyffert and Troesch* (2018).

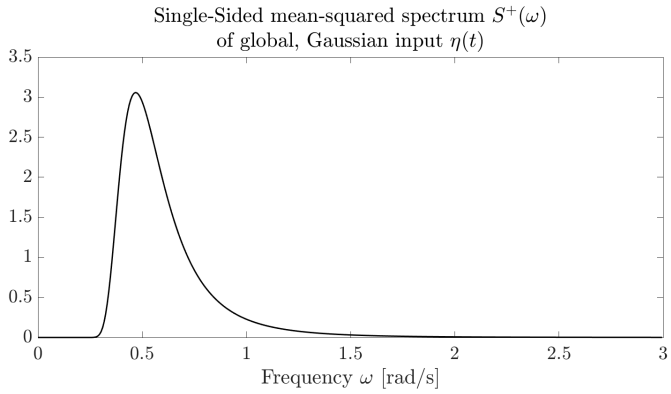

Figure 6.1: Single-sided mean-squared spectrum, $S^+(\omega)$, of the global, Gaussian input $\eta(t)$.

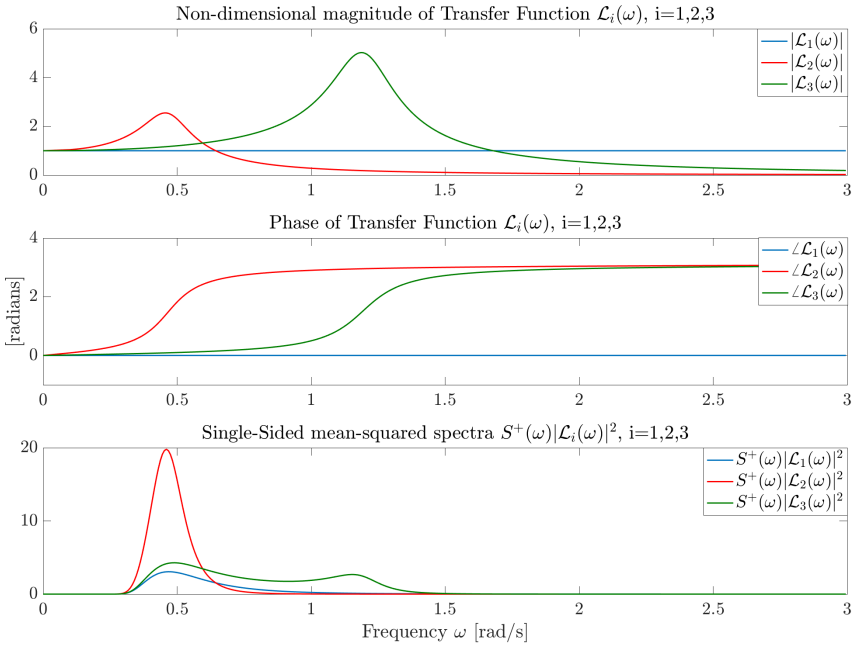

Figure 6.2: Non-dimensional magnitude and phase information for linear transfer functions $\mathcal{L}_1(\omega)$, $\mathcal{L}_2(\omega)$, and $\mathcal{L}_3(\omega)$, along with single-sided mean-squared spectra $S^+(\omega)|\mathcal{L}_1(\omega)|^2$, $S^+(\omega)|\mathcal{L}_2(\omega)|^2$, and $S^+(\omega)|\mathcal{L}_3(\omega)|^2$.

$$
\begin{aligned}
\mathcal{L}_1(\omega) &= 1 \\
\mathcal{L}_2(\omega) &= \left| \frac{1}{\sqrt{\left(1 - \left(\frac{\omega}{0.475}\right)^2\right)^2 + \left(2\zeta_2 \frac{\omega}{0.475}\right)^2}} \right| \text{ with } \zeta_2 = 0.2 \\
\mathcal{L}_3(\omega) &= \left| \frac{1}{\sqrt{\left(1 - \left(\frac{\omega}{1.2}\right)^2\right)^2 + \left(2\zeta_3 \frac{\omega}{1.2}\right)^2}} \right| \text{ with } \zeta_3 = 0.1
\end{aligned}
\tag{6.1}
$$

6.1.1 Non-Linear Loading on System & Failure Surface

For this system, there are three non-linear loads, defined in Eq.(6.2), whose interaction with a failure surface determines system failure. The failure surface, G, for the system is shown in Figure 6.3 and defined by the bounding planes given in Eq.(6.3).

$$\begin{aligned} \mathcal{NL}_1(t) &= \mathtt{L}_1(t)^3 + \mathtt{L}_1(t)^2 + \mathtt{L}_1(t) \\ \mathcal{NL}_2(t) &= \mathtt{L}_2(t)^3 + \mathtt{L}_2(t)^2 + \mathtt{L}_2(t) \\ \mathcal{NL}_3(t) &= \mathtt{L}_3(t)^3 + \mathtt{L}_3(t)^2 + \mathtt{L}_3(t) \end{aligned} \tag{6.2}$$

where

$\mathcal{NL}_i(t)$ = time series of non-linear load which potentially contributes to failure

$\mathtt{L}_i(t)$ = time series with spectral definition $S^+(\omega)|\mathcal{L}_i(\omega)|^2$ as shown in Figure 6.2

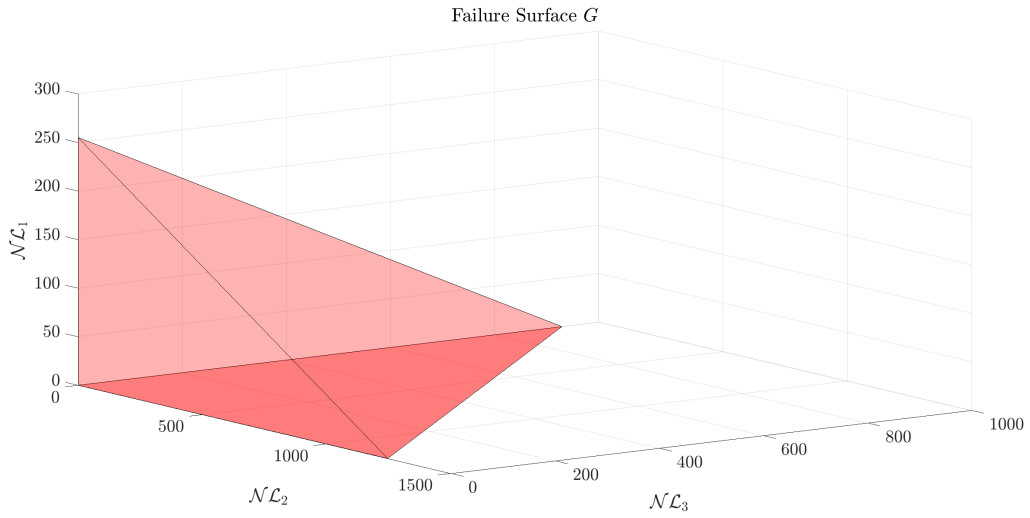

Figure 6.3: Failure surface, G, for illustrative example.

$$\begin{aligned} \mathcal{NL}_1 &= 0 \\ \mathcal{NL}_2 &= 0 \\ \mathcal{NL}_3 &= 0 \\ \mathcal{NL}_1 &= 255.2 - 0.2\mathcal{NL}_2 - 0.3\mathcal{NL}_3 \end{aligned} \tag{6.3}$$

6.1.2 Probabilistic System Design

There are three stochastic non-linear loads acting on this system, $\mathcal{NL}_i(t)$, $i = 1, 2, 3$. In many problems, it is difficult to define how non-linear loads interact with

each other and with the system failure surface. This is due to the stochastic nature of the loading, and the non-linear relationship between the overall environment and the system's response to those loads (i.e. the failure surface shape).

The system strength in this example is designed for each load independently in a 'divide and conquer' approach by constraining each individual load with a high probability of non-exceedance (PNE). This is similar to testing systems with a conditional maximum approach by bounding individual loads with a high PNE. The intercept values of G at each axis are designed to correspond to the $\mathcal{NL}_i$ value resulting from the input of the 1000-hour maximum of $\mathtt{L}_i$ associated with $PNE = 0.990$. These intercepts are defined by Eq.(6.4):

$$\mathcal{NL}_{i-intercept} = \mathcal{NL}_i(PNE_{0.990}\mathtt{L}_i) \tag{6.4}$$

where

$$\begin{aligned} \mathcal{NL}_{i-intercept} &= \text{axis intercept of } \mathcal{NL}_i,\ i = 1,2,3 \\ \mathcal{NL}_i(t) &= \text{non-linear function described by Eq.(6.2)} \\ PNE_{0.99}\mathtt{L}_i &= \text{1000-hour maximum of } \mathtt{L}_i,\ i = 1,2,3 \text{ which has } PNE = 0.990 \end{aligned}$$

This is not an unusual design decision, especially for a system where a long exposure precludes brute-force MCS and the level of dependence between the non-linear loads is unknown. This illustrative example examines whether or not a failure surface defined by constraining individual non-linear load maxima, coupled with a high PNE bound, actually leads to a system with a low failure probability. Of equal interest is whether the PNE bound affects each load equally, and leads to a balanced design, where failures are equally distributed across the failure surface.

6.2 Selection of Non-Linear Load Combination Cases & Surrogate Processes

Having defined the complex system, exposure period, failure surface, and the combined loading, the probability of system failure over the 1000-hour exposure is evaluated by the NL-DLG process. Non-linear load combination cases are chosen to focus on specific regions of G. These non-linear load combination cases are weighted sums of the three non-linear loads acting on the system, as shown by the general load

combination case in Eq.(6.5):

$$\zeta_i(t) = \alpha\frac{\mathcal{NL}_1(t)}{\sigma_{\mathcal{NL}_1}} + \beta\frac{\mathcal{NL}_2(t)}{\sigma_{\mathcal{NL}_2}} + \gamma\frac{\mathcal{NL}_3(t)}{\sigma_{\mathcal{NL}_3}} \tag{6.5}$$

Three non-linear load combination cases are chosen to approximate the failure surface, G. The cases are defined as the individual extremes of the three non-linear loads which contribute to failure, given by Eq.(6.6):

$$\begin{aligned}\zeta_1(t) &= \frac{\mathcal{NL}_1(t)}{\sigma_{\mathcal{NL}_1}}\\ \zeta_2(t) &= \frac{\mathcal{NL}_2(t)}{\sigma_{\mathcal{NL}_2}}\\ \zeta_3(t) &= \frac{\mathcal{NL}_3(t)}{\sigma_{\mathcal{NL}_3}}\end{aligned} \tag{6.6}$$

Linear functions associated with the Gaussian input leading to the extreme behavior of the non-linear load combinations are chosen and constructed as surrogate processes. The natural choice is weighted sums of the three linear functions of the global, Gaussian input - $\mathtt{L}_1(t)$, $\mathtt{L}_2(t)$, and $\mathtt{L}_3(t)$. Eq.(6.7) defines the general surrogate process, and weighting factors are chosen to approximate the different non-linear load combination cases given by Eq.(6.6):

$$z(t) = \alpha\frac{\mathtt{L}_1(t)}{\sigma_{\mathtt{L}_1}} + \beta\frac{\mathtt{L}_2(t)}{\sigma_{\mathtt{L}_2}} + \gamma\frac{\mathtt{L}_3(t)}{\sigma_{\mathtt{L}_3}} \tag{6.7}$$

The load cases $\zeta_i(t)$ $i = 1, 2, 3$ are approximated by the surrogate processes $z_1(t)$, $z_2(t)$, and $z_3(t)$ in Eq.(6.8):

$$\begin{aligned}z_1(t) &= \frac{\mathtt{L}_1(t)}{\sigma_{\mathtt{L}_1}} \text{ (which approximates } \zeta_1(t))\\ z_2(t) &= \frac{\mathtt{L}_2(t)}{\sigma_{\mathtt{L}_2}} \text{ (which approximates } \zeta_2(t))\\ z_3(t) &= \frac{\mathtt{L}_3(t)}{\sigma_{\mathtt{L}_3}} \text{ (which approximates } \zeta_3(t))\end{aligned} \tag{6.8}$$

6.3 Estimation of Target Extreme Value (TEV)

With the defined surrogate processes, three ensembles of short DLG time series, $\eta_i(t)$, are generated which lead to 1000-hour-maxima of $z_i(t)$ for $i = 1, 2, 3$. The DLG requires information about the surrogate process to link an exposure period to the magnitude of the exposure-period-maxima. The number of cycles a process experiences in a given exposure period is linked to the most probable extreme maximum for

the given exposure, as explained in Chapter 2.2. The target extreme value, or TEV, expresses the most probable maximum given in terms of the standard deviation of the process, as shown by *Ochi* (1990). Chapter 2.2 gives the most probable maximum in terms of the spectral moments, Eq.(2.13), but this value can also be expressed simply by the number of cycles in the exposure, as in Eq.(6.9):

$$TEV = \frac{\overline{z}}{\sigma_z} = \sqrt{2ln\,(N)} = \sqrt{2ln\left(\frac{T}{T_c}\right)} \tag{6.9}$$

where

TEV = target extreme value

$\overline{z}$ = most probable maximum of $z(t)$ over the exposure, T

σ_z = standard deviation of the process $z(t)$

N = number of cycles that $z(t)$ experiences over the exposure, T

T = exposure, T, in seconds

T_c = calibration period of the process $z(t)$, in seconds

The estimation of the number of cycles experienced over the exposure, N, is critical in determining the appropriate TEV. If the TEV used for input in the DLG simulations is significantly different from what is seen from full MCS, then the surrogate process maxima given by those DLG simulations may not accurately represent the true exposure-period-maxima.

All the linear transfer functions $\mathcal{L}_i(\omega)$ pass some level of high-frequency content. Using spectral moments to estimate N for use in Eq.(2.13) may not be the most accurate, since the higher spectral moments are influenced by frequency truncation. This leads to the use of Eq.(6.9), and instead of calculating a TEV based on N from spectral moments, the calibration period T_c which most accurately represents the process is estimated from short MCS, based on the empirical exposure-period-maxima. This calibration period can be used, as in Eq.(6.9), to give a TEV estimate for a 1000-hour exposure.

To do this, 1000, $T-$length MCS of $\eta(t)$ are run, where T is of sufficient record duration for converged averages. For each $\eta(t)$ simulation, the time series $z_1(t)$, $z_2(t)$, and $z_3(t)$ are constructed and the $T-$length-maxima for each $z_i(t)$ are collected. Then, a histogram of the 1000, $T-$length-maxima for each surrogate process is assembled, which is the extreme value distribution for exposure length T. The most probable maximum of these histograms is estimated, and the calibration period, T_c, which leads to this maximum for the T exposure is calculated using Eq.(6.9). Then, T_c can

be used in Eq.(6.9) to solve for the TEV associated with a 1000-hour exposure.

The most probable maximum, or TEV, is estimated by assembling closed-form Gaussian extreme value distributions for a range of TEV values, and finding the distribution which has the minimum Jeffreys/ symmetric Kullback-Leibler divergence with the empirical histogram, as described in Chapter 3.3 (*Kullback and Leibler*, 1951). This divergence allows the comparison between many closed-form extreme value distributions for distinct TEV values and the empirical histogram in question, and is calculated by Eq.(3.1). A minimum divergence value indicates the best fit. Note the closed-form distribution used for comparison with the empirical histograms is the extreme value distribution for a Gaussian process (see, e.g., *Ochi* (1990)), which is an appropriate comparison as all $z_i(t)$ processes are Gaussian.

Using Eq.(3.1), the TEV associated with the best-fit extreme value distribution for each $z_i(t)$, $i = 1, 2, 3$, $T-$length empirical histograms is approximated. This TEV indicates the calibration period, T_c, that best describes the $z_i(t)$ process. This experiment was carried out for exposure periods of 1, 2, 4, 8, 16, and 32 hours, and the results, along with the computation time[2] are tabulated in Table 6.1. Notice that the calibration period calculated from Eq.(6.9) converges as the length of the simulation increases. The 1000-hr TEV's from the 32-hour MCS are used in the DLG simulations for the NL-DLG process estimations.

		$z_1(t)$		$z_2(t)$		$z_3(t)$	
T (exposure)	Computation time [sec]	T_c [sec]	1000-hr TEV	T_c [sec]	1000-hr TEV	T_c [sec]	1000-hr TEV
1 hr	23.1	10.73	5.04	14.83	4.98	8.26	5.10
2 hr	30.3	11.09	5.04	15.83	4.97	8.80	5.08
4 hr	47.9	12.13	5.02	16.34	4.96	9.23	5.07
8 hr	88.3	11.93	5.02	16.06	4.96	9.55	5.07
16 hr	171.2	12.52	5.01	16.79	4.96	10.09	5.06
32 hr	348.3	12.37	5.02	17.66	4.94	9.89	5.06

Table 6.1: Calibration period, T_c, from 1, 2, 4, 8, 16, and 32-hour MCS, resulting 1000-hour TEV for surrogate processes $z_i(t)$, $i = 1, 2, 3$ using Eq.(6.9), and computation time. The 1000-hr TEV values estimated from the T_c from the 32-hr MCS are used in the DLG simulations.

[2]These computation times reflect running on a MacBook Pro personal laptop, 2.5 GHz Intel Core i7.

6.4 First Iteration of the NL-DLG process

With these 1000-hour TEV values for $z_1(t)$, $z_2(t)$, and $z_3(t)$, the DLG was used to construct 2000 short $\eta_i(t)$ time series which lead to 1000-hour maxima of the surrogate processes. Then, the NL-DLG process approximated the overall probability of failure of the system as described by Chapter V. Using the surrogate processes $z_i(t)$, $i = 1, 2, 3$, the estimate of system's probability of failure over a 1000-hour exposure is $p(\mathbb{F}) = 0.839$. Figure 6.4 gives the estimate of the most-likely failure distribution for this system over the 1000-hour exposure.

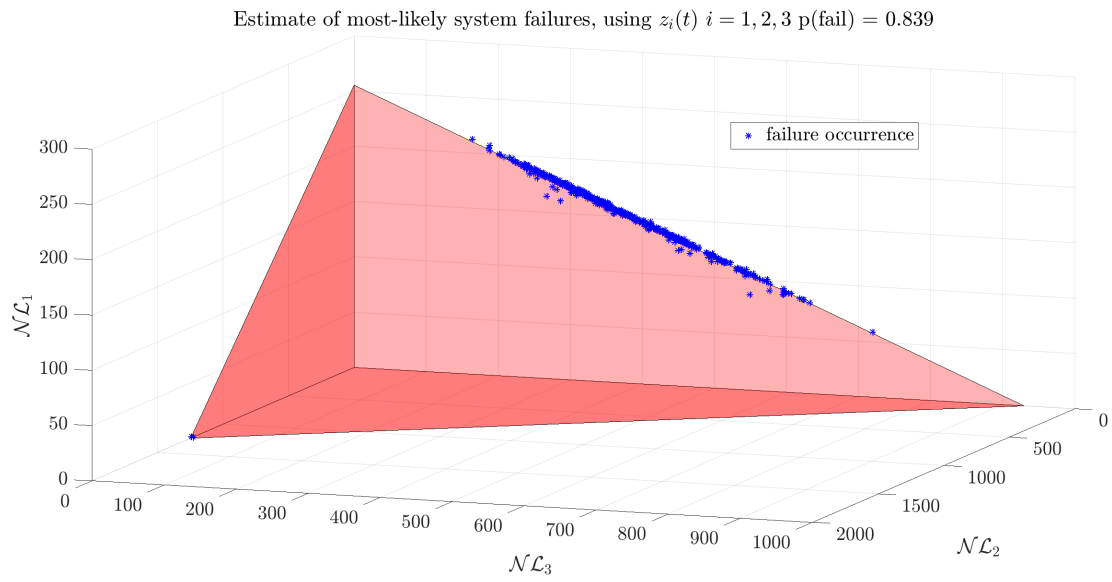

Figure 6.4: Estimate of the distribution of most-likely failures from the NL-DLG process using surrogate processes $z_i(t)$, $i = 1, 2, 3$ from Eq.(6.8).

An initial impression of this result is that the probability of failure is significantly higher than anticipated given the system constraints (failure surface at $PNE = 0.990$ intercepts). In addition, even though the non-linear load combination cases focused on failures due to individual extremes of $\mathcal{NL}_1(t)$, $\mathcal{NL}_2(t)$, and $\mathcal{NL}_3(t)$, most of the failure occurrences lie on the $\mathcal{NL}_1 - \mathcal{NL}_3$ plane. This unexpected result can be used to improve the estimate of the system's probability of failure.

6.5 Second Iteration of the NL-DLG process

The failure probability estimate from the first iteration of the NL-DLG process can be used to improve the estimate. Figure 6.4 revealed that many failure occurrences

lie on the $\mathcal{NL}_1 - \mathcal{NL}_3$ plane. This information can be used as feedback to update the estimate by adding another non-linear load combination case. Since many failures occurred purely on the $\mathcal{NL}_1 - \mathcal{NL}_3$ plane, adding another non-linear load combination case that focuses on this region should improve the failure probability estimate. The four non-linear load combination cases used by the second iteration of the NL-DLG process are given by Eq.(6.10):

$$\begin{aligned}
\zeta_1(t) &= \frac{\mathcal{NL}_1(t)}{\sigma_{\mathcal{NL}_1}} \\
\zeta_2(t) &= \frac{\mathcal{NL}_2(t)}{\sigma_{\mathcal{NL}_2}} \\
\zeta_3(t) &= \frac{\mathcal{NL}_3(t)}{\sigma_{\mathcal{NL}_3}} \\
\zeta_4(t) &= \frac{\mathcal{NL}_1(t)}{2\sigma_{\mathcal{NL}_1}} + \frac{\mathcal{NL}_3(t)}{2\sigma_{\mathcal{NL}_3}}
\end{aligned} \tag{6.10}$$

The surrogate process $z_4(t)$ approximates this additional non-linear load combination case, $\zeta_4(t)$, giving the four surrogate processes in Eq.(6.11):

$$\begin{aligned}
z_1(t) &= \frac{\mathtt{L}_1(t)}{\sigma_{\mathtt{L}_1}} \text{ (which approximates } \zeta_1(t)) \\
z_2(t) &= \frac{\mathtt{L}_2(t)}{\sigma_{\mathtt{L}_2}} \text{ (which approximates } \zeta_2(t)) \\
z_3(t) &= \frac{\mathtt{L}_3(t)}{\sigma_{\mathtt{L}_3}} \text{ (which approximates } \zeta_3(t)) \\
z_4(t) &= \frac{\mathtt{L}_1(t)}{2\sigma_{\mathtt{L}_1}} + \frac{\mathtt{L}_3(t)}{2\sigma_{\mathtt{L}_3}} \text{ (which approximates } \zeta_4(t))
\end{aligned} \tag{6.11}$$

The new surrogate process $z_4(t)$ focuses on failures due to a moderate simultaneous combination of $\mathcal{NL}_1(t)$ and $\mathcal{NL}_3(t)$, since that is where the first analysis revealed many unexpected failures. A similar test as with Table 6.1 was run to estimate a 1000-hour TEV for $z_4(t)$, and the estimate from the 32-hour MCS is used for the 1000-hour TEV for $z_4(t)$ ($TEV = 5.014$). The NL-DLG process again estimated the system probability of failure, this time using the four non-linear load combination cases from Eq.(6.10). The new estimate of the system's failure probability is $p(\mathbb{F}) = 0.929$. Figure 6.5 gives the estimate of the distribution of most-likely failure occurrences.

Again, most of the first failure occurrences are clustered on the $\mathcal{NL}_1 - \mathcal{NL}_3$ plane. A higher probability of failure is estimated by adding the non-linear load combination case $\zeta_4(t)$, with the associated surrogate process $z_4(t)$, to focus on this region. The iterative nature of the NL-DLG process illustrates the natural advantage of using

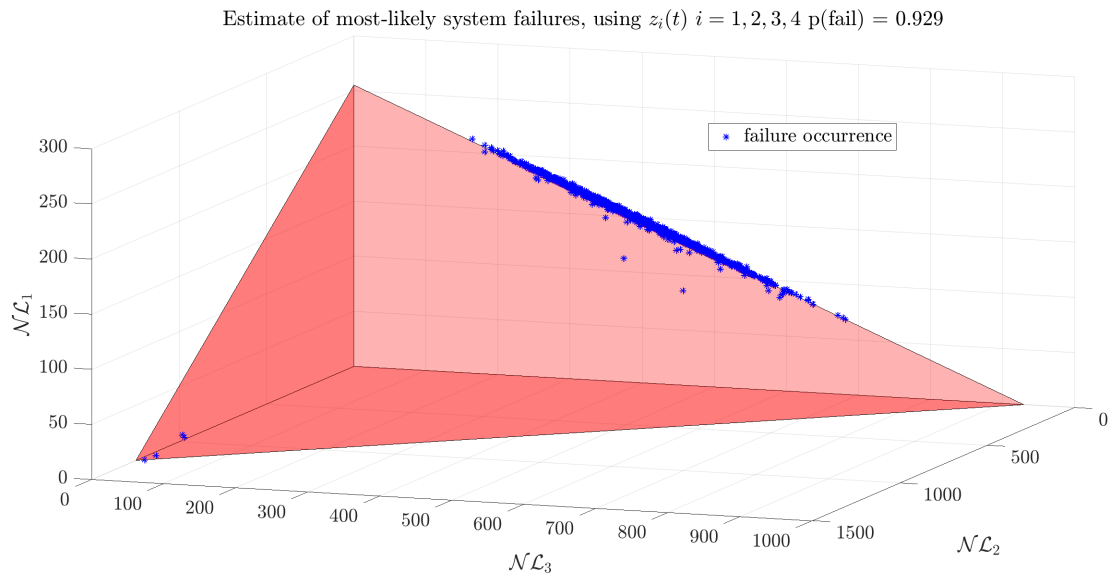

Figure 6.5: Estimate of the distribution of most-likely failures from the NL-DLG process using surrogate processes $z_i(t)$, $i = 1, 2, 3, 4$ from Eq.(6.11).

surrogate processes, coupled with the ability of the NL-DLG process to determine the relation between them. Mutually exclusive surrogates do not need to be defined, so surrogates can be added in specific regions of interest.

6.6 Monte Carlo Simulation Validation

For comparison with full MCS, 10,000 1000-hour simulations were conducted.[3] The distribution of failure occurrences is assembled in Figure 6.6. Using a full MCS analysis, the system's probability of failure is $p(\mathbb{F}) = 0.908$. The final estimate of the system's failure probability using four surrogate processes is close to what is seen from full MCS ($p(\mathbb{F}_{NL-DLG}) = 0.929$ vs. $p(\mathbb{F}_{MCS}) = 0.908$).

The MCS analysis also shows that the majority of the first failure occurrences are clustered on the $\mathcal{NL}_1 - \mathcal{NL}_3$ plane, just as seen from the NL-DLG process. The results from the two iterations of the NL-DLG process and the full MCS analysis, along with computation times, are given below in Table 6.2.

Both the estimate of the system probability of failure and the distribution of most-likely failure occurrences from the final iteration of the NL-DLG process closely approximate what is given from a full MCS analysis. Of equal significance, Table 6.2

[3]The MCS were run on an Ubuntu desktop with 12x Intel(R) Xeon(R) CPU E5-2609 v3 @ 1.90GHz.

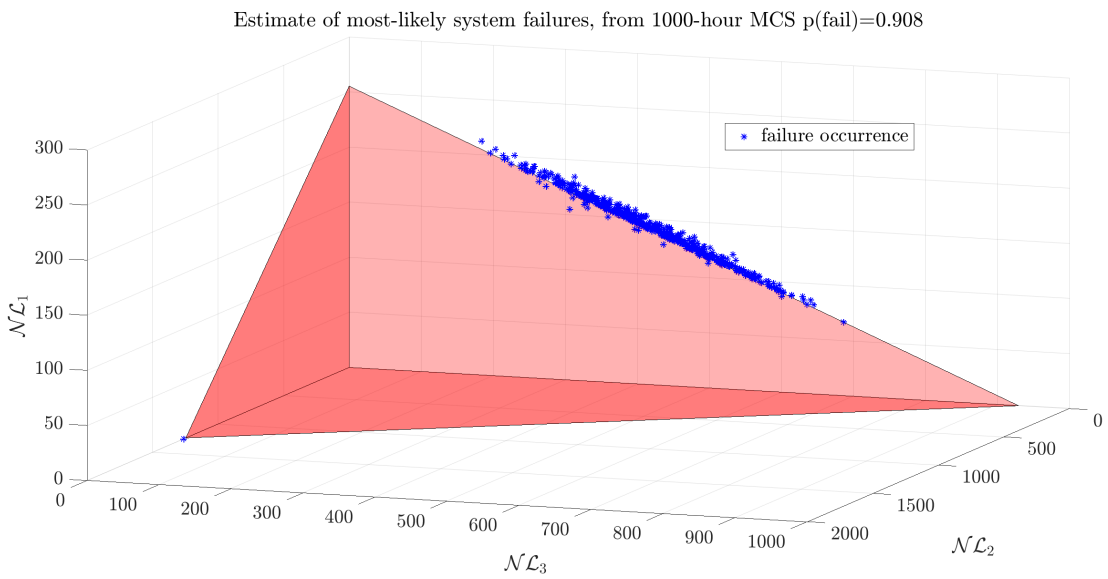

Figure 6.6: Estimate of the distribution of most-likely failures from 10,000 1000-hour MCS.

	NL-DLG process		10,000 MCS
	$z_i(t)$, $i = 1, 2, 3$	$z_i(t)$, $i = 1, 2, 3, 4$	
$p(\mathbb{F})$ = p(fail)	0.839	0.929	0.908
computation time	8.07 min	10.86 min	46.14 hours

Table 6.2: System failure probability over 1000-hour exposure from the NL-DLG process using $z_i(t)$ $i = 1, 2, 3$, $z_i(t)$ $i = 1, 2, 3, 4$, and 10,000 MCS, along with computation time.

shows a major savings in computation time for the NL-DLG process vs. MCS. As an auxiliary benefit, using the NL-DLG process allows users to update the estimate using feedback from earlier iterations, giving a quick method to check how design changes affect the system's performance. For example, a user could easily change the failure surface, which would reflect a change in design for continued analysis. This would require no new DLG simulations, only a mapping of the same simulations onto a new failure surface, meaning the added computation is negligible.

6.7 Remarks on System Design Aspects

From this illustrative example, it is clear that the NL-DLG process closely recovers a system's probability of failure over a long exposure. This method also gives a reasonable estimate of the distribution of most-likely failures with a significantly smaller computational expense than a traditional MCS analysis. The DLG simulations associated with assembling this distribution form an ensemble of wave profiles

which could be used in a more high-fidelity analysis and are representative of the operating profile and exposure. Beyond these capabilities, there are multiple interesting aspects of complex system failure analysis that the NL-DLG process reveals, some of which are discussed in the following sections.

6.7.1 Individual Load *PNE* Bounds

Recall that the failure surface, G, was sized so that the failure surface value at each individual load axis is the $\mathcal{NL}_i(t)$ value, using as input the 1000-hour maximum $\mathtt{L}_i(t)$ value associated with a $PNE = 0.990$. However, even with this seemingly stringent design criteria, many failures were recorded. The question is, do any of the loads exceed the design criteria? Figure 6.5 shows an estimate of the distribution of most-likely failure occurrences for a 1000-hour exposure using the surrogate processes in Eq.(6.11). The vast majority of these failures occur nowhere near the extremes of a single non-linear load (i.e. the intersection of G at the three axes). The only failure occurrences that can be classified as due to an extreme of a single load occur near the $\mathcal{NL}_2(t)$ axis.

Figures 6.7 and 6.8 are projections of Figure 6.5 on the $\mathcal{NL}_1 - \mathcal{NL}_2$ plane and $\mathcal{NL}_3 - \mathcal{NL}_2$ plane, respectively. Note that the failures near the extremes of the $\mathcal{NL}_2(t)$ axis do not occur with a contribution due to only $\mathcal{NL}_2(t)$. They all have some component, regardless how small, of $\mathcal{NL}_1(t)$ and $\mathcal{NL}_3(t)$. This shows that none of the failure occurrences exceed any $\mathcal{NL}_i(t)$ $i = 1, 2, 3$ $PNE = 0.990$ value, which was the original design criteria. Despite the fact that no non-linear load exceeded the 1000-hour $PNE = 0.990$ criteria, this high PNE bound did not translate to a safe design, as was expected.

6.7.2 (In)dependence of Loads

The system failure surface was designed by assuming that all three loads act independently and that failure occurs only if any individual load exceeds its $PNE = 0.990$ value in a 1000-hour exposure. A valid independence assumption, along with assuming that the non-linear loads have a negligible impact when a different non-linear load is maximized, would suggest the system should have a probability of failure of about 0.03 ($p(\mathbb{F}) = 1 - p(\mathbb{F}^c) = 1 - 0.99 \times 0.99 \times 0.99 = 0.0297$). The NL-DLG process estimated that the system's failure probability for the exposure is over 90%, and the full MCS analysis confirmed the high system failure probability. How did the

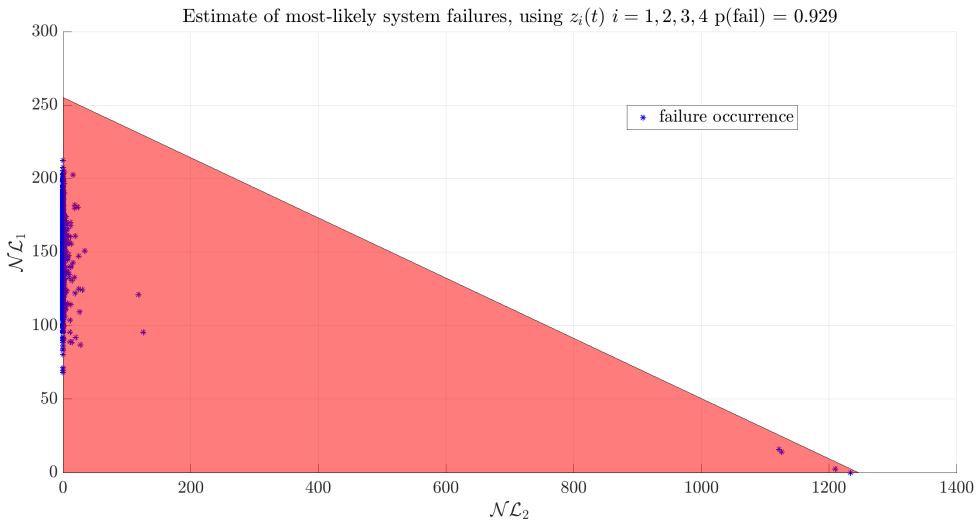

Figure 6.7: Estimate of the distribution of most-likely failures from the NL-DLG process using 4 surrogate processes $z_i(t)$ $i = 1, 2, 3, 4$. This is a projection of Figure 6.5 on the $\mathcal{NL}_1 - \mathcal{NL}_2$ plane.

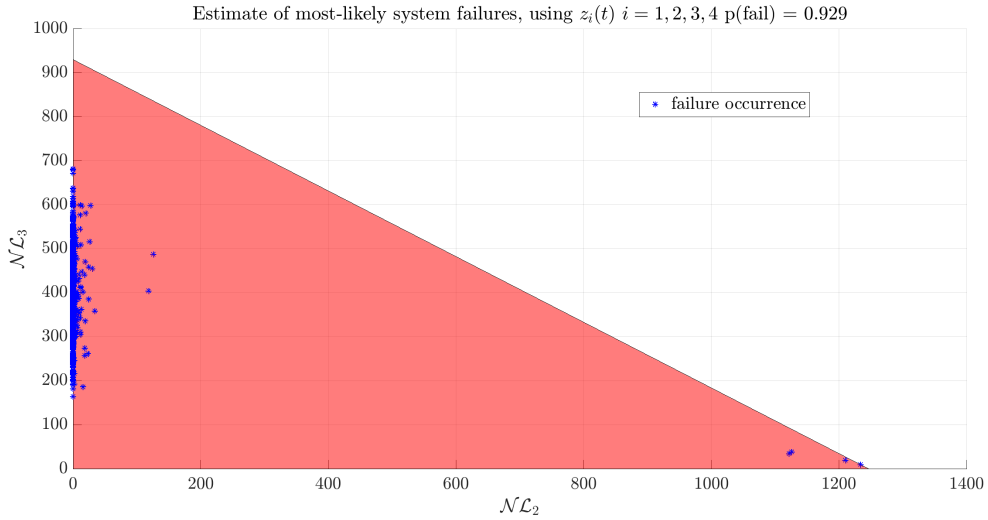

Figure 6.8: Estimate of the distribution of most-likely failures from the NL-DLG process using 4 surrogate processes $z_i(t)$ $i = 1, 2, 3, 4$. This is a projection of Figure 6.5 on the $\mathcal{NL}_3 - \mathcal{NL}_2$ plane.

$PNE = 0.990$ criteria lead to such a high failure probability?

The system design in this example satisfied the criterion that no non-linear load which contributes to failure exceeds its axis value. Despite satisfying this criterion, the system still has a probability of failure higher than 90%. Every failure on the estimate of the most-likely failure distribution has a component of $\mathcal{NL}_1(t)$, $\mathcal{NL}_2(t)$, and $\mathcal{NL}_3(t)$. This is especially apparent for the failures clustered on the $\mathcal{NL}_1 - \mathcal{NL}_3$ plane. The failure surface, G, was designed without considering how the non-linear loads may interact, specifically the values of the non-linear loads when a different

load is maximized, and how simultaneous moderate load combinations may lead to extreme system responses. The resulting system was significantly prone to failures due to such moderate simultaneous loading, resulting in an unacceptably high probability of failure.

Many of the system failures are on the $\mathcal{NL}_1 - \mathcal{NL}_3$ plane, and have an equally weighted sum of $\mathcal{NL}_1(t)$ and $\mathcal{NL}_3(t)$. Also, many of these failures have a small $\mathcal{NL}_2(t)$ component. If this $\mathcal{NL}_2(t)$ contribution were absent, many of these failures would not be failures at all. However, it would be difficult to quantify the dependence of these non-linear loads using other methods which rely on extrapolation, or even conditional maxima.

Since the surrogate processes are sums of linear functions of a Gaussian input, every surrogate process is also Gaussian. The DLG constructs excitation inputs leading to their extreme responses, and the NL-DLG process estimates the relation between the surrogate processes, regardless of the level of relation. Clearly, the interaction of the non-linear loads has a major impact on the ability of a design to withstand failure. This example is a cautionary note illustrating the danger of assuming independence among loads for system design, and how that assumption can lead to a dramatically non-conservative estimate of a system's probability of failure.

6.7.3 Unbalanced Design

With the same $PNE = 0.990$ criteria for all non-linear loads driving the failure surface, it would seem a balanced design should result, where any failures are equally spread across the failure surface. Clearly this was not the case. In the estimated distributions of most-likely failure occurrences assembled from both the NL-DLG process and the full MCS validation, the majority of failures are clustered on the $\mathcal{NL}_1 - \mathcal{NL}_3$ plane. This at first seems unexpected, until the linear transfer functions which are inputs to the non-linear loads are considered.

The linear input to $\mathcal{NL}_1(t)$ is the result of a unit gain filter, the input to $\mathcal{NL}_2(t)$ is filtered to emphasize the peak frequency of the original Gaussian process, and the input to $\mathcal{NL}_3(t)$ is filtered to yield a bimodal response spectrum. The majority of the failures have a large component of $\mathcal{NL}_1(t)$ and $\mathcal{NL}_3(t)$, and a small component of $\mathcal{NL}_2(t)$ present. The failure surface along the $\mathcal{NL}_2$ axis is designed to withstand large values of the resonant response. On the other hand, the $\mathcal{NL}_1$ axis is sized against the static response, and the $\mathcal{NL}_3$ axis is sized against a bimodal response of

the excitation. All of these axes, corresponding to the three non-linear loads, had the same applied $PNE = 0.990$ bound, but clearly this did not affect all three loads equally. This illuminates the difficulty of joint environmental inputs: they may have different probabilities of occurrence. Constraining multiple loads with the same high PNE bound does not affect each load equally and does not translate to a low overall system failure probability.

The iterative nature of this analysis allows a quick design reformulation. To evaluate a new design, a new failure surface can be created, and evaluated with the same method as explained above. The same DLG simulations can be used because they are based on the operating profile and not the system design, which allows the quick testing of new designs, or families of designs. As well, it may be desirable to design the way a system fails. Failure in some modes may not be as catastrophic as failure in others, and this can be accommodated by varying the failure surface. When all competing designs can be quickly compared, it is possible to determine the trade-offs between designs.

6.7.4 Bounds of the NL-DLG Process Estimation

It is important to determine what bounds, if any, exist for the probability of failure estimated by the NL-DLG process. For this illustrative example, the probability of failure from the NL-DLG process using the three surrogate processes in Eq.(6.8) is less than the probability of failure from the MCS validation. However, the probability of failure from the NL-DLG process using the four surrogate process in Eq.(6.11) is greater than the MCS validation. One potential reason that these probabilities are not on the same bound of the MCS failure probability is based on the estimate of the TEV for use in the DLG simulations as compared to full MCS.

Figure 6.9 shows the 1000-hour distributions of the maxima for the four surrogate processes from Eq.(6.11), from the DLG simulations and MCS. For each surrogate process, the TEV used in the NL-DLG process, as well as the TEV estimated from 1000-hour MCS, is given. For all surrogate processes, the TEV used in the DLG simulations, which was estimated by a representative period, T_c, from 32-hour MCS, is slightly higher than the 1000-hour TEV found from full 1000-hour MCS. This inflated TEV is equivalent to a slightly longer exposure, as discussed in Chapter 2.2, and means that the loads on the system analyzed by the NL-DLG process are more intense than those from the MCS analysis. This can explain why the probability

of failure estimated from the NL-DLG process using the four surrogate processes in Eq.(6.11) is higher than the estimate from the MCS analysis.

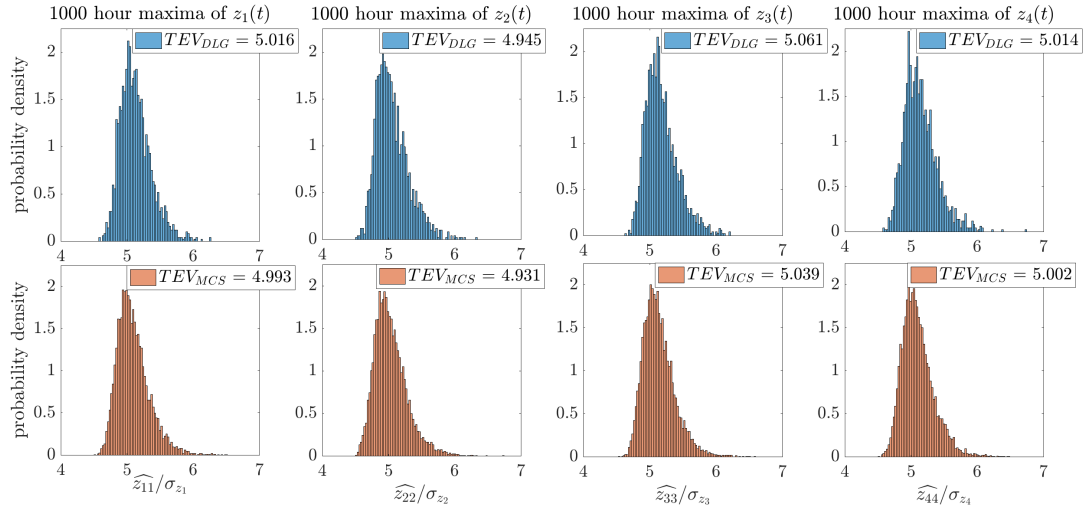

Figure 6.9: Comparison of the empirical histograms of the 1000-hour maxima of surrogate processes $z_i(t)$ $i = 1, 2, 3, 4$, normalized as a *pdf*, from DLG simulations (2000 samples) and MCS (10,000 samples), along with the 1000-hour TEV.

An interesting test is to compare the probability of failure from the NL-DLG process to that from the MCS validation if the TEV values used in the DLG simulations are the same as those seen in full 1000-hour simulations. The TEV values for the surrogate processes from Eq.(6.11), as found from the MCS (shown in Figure 6.9) are used to drive new DLG simulations. This ensures that the distributions of assembled surrogate process maxima constructed by the DLG are statistically equivalent to extrema from full MCS. The 'original TEV' values that were estimated from 32-hour MCS, which gave the results found in Figures 6.4, 6.5, 6.7, and 6.8, along with the 'new TEV' values found from 1000-hour MCS, are given in Table 6.3. With the updated 'new TEV' values, the new probability of system failure can be calculated. The results are shown in Table 6.4.

surrogate process	original TEV values from 32-hour MCS	new TEV values from 1000-hour MCS
$z_1(t)$	5.016	4.993
$z_2(t)$	4.945	4.931
$z_3(t)$	5.061	5.039
$z_4(t)$	5.014	5.002

Table 6.3: The original TEV values for surrogate processes $z_i(t)$ $i = 1, 2, 3, 4$ from Eq.(6.11) which are estimated from 32-hour MCS, along with the new TEV values estimated from 1000-hour MCS.

	NL-DLG process				10,000 MCS
	$z_i(t)\ i = 1,2,3$		$z_i(t)\ i = 1,2,3,4$		
	original TEV	new TEV	original TEV	new TEV	
$p(\mathbb{F})$ = p(fail)	0.839	0.797	0.929	0.905	0.908

Table 6.4: System failure probability over 1000-hour exposure from the NL-DLG process using three surrogate processes $z_i(t)\ i = 1,2,3$, four surrogate processes $z_i(t)\ i = 1,2,3,4$, both the original TEV and new TEV values from Table 6.3, along with the result from 10,000 1000-hour MCS.

Using the new TEV values estimated from 1000-hour MCS to drive the new DLG simulations, the probability of system failure for both the three and four surrogate processes case (Eq.(6.8) vs. Eq.(6.11)) is less than the original failure probabilities which use the TEV values estimated from 32-hour MCS. This is an expected result, as a lower TEV results in a distribution of surrogate process maxima whose most probable value is of smaller magnitude, meaning the system experiences less intense loading. With these updated TEV values, the probability of system failure for both NL-DLG process iterations is a lower bound on the probability of failure seen from the full MCS analysis for this example. This indicates that a NL-DLG process result based on accurate TEV values gives a lower probability bound on the result from full MCS.

Another potential area that affects the bound of the NL-DLG process estimate are the estimates of the probabilities of experiencing different maxima configurations, from Eq.(A.8)-(A.13). The NL-DLG process assumes that the sum of these probability estimates is unity, i.e. that these are the only notable surrogate processes which describe the system. However, if a major system non-linear load combination case/ surrogate process is neglected, these maxima configuration probabilities may be inflated. Adding another surrogate process necessarily increases the number of possible maxima configurations (i.e. Table 5.1). If this surrogate process is sufficiently unrelated to the other surrogates, meaning there are an appreciable number of times when this surrogate process exposure-period-maxima occur un-clustered with other surrogate process exposure-period-maxima, the probability of experiencing the maxima configurations will change to accommodate the addition of the new surrogate. The addition of the new surrogate, though, does not guarantee that the failure probability estimate will increase. How the addition, or neglect, of surrogate processes leads to the NL-DLG process estimate being an upper or lower bound on a MCS result is an area of active research.

It is noted, though, that even with the marginally inaccurate estimate of the

TEV values shown in Table 6.3, and with the assumption that four non-linear load combination cases/ surrogate processes sufficiently describe the system, the NL-DLG process still estimated a failure probability that is within 2% of the MCS value.

6.8 A Cautionary Note on the NL-DLG Process

The NL-DLG process, like any analysis method, gives results that are implicitly conditioned on the system, method assumptions, and user-input. While the iterative nature of the NL-DLG process allows updated estimates of system failure probability based on feedback from earlier results, it is possible that only considering early iterations of the NL-DLG process will give misleading information. The ability to use feedback to improve the failure probability estimate highlights a potential danger of not using the NL-DLG process thoughtfully. Essentially, any result from the NL-DLG process is conditioned on the choice of non-linear load combination cases and associated surrogate processes. While a low estimated failure probability may well indicate a robust system, this estimate could also be due to a poor choice of non-linear load combination cases.

This is a somewhat obvious conclusion. For example, in the presented example, the non-linear loads which interact toward failure are functions of dynamic oscillators. A designer *could* choose non-linear load cases which focus on the humidity and temperature describing the system environment over its exposure. However, it is rather unlikely that extremes of humidity and temperature would lead to failures on the surface G. In this case, a low estimate of failure probability would be due to an errant choice of non-linear load combination cases. In reality, this system has a high probability of failure, and such a low estimate of that probability would be due to a focus on the wrong non-linear load combination cases.

In the same way, a designer might choose non-linear load combination cases which, though more applicable than humidity and temperature, do not truly test the system. Or, the cases may not include all of the possible failure modes. Again, for the example, a designer may only be concerned about the resonant response of the system, and therefore focus solely on $\mathcal{NL}_2(t)$. As seen in Figures 6.4-6.6, very few failures occur due to extremes of the resonant response. Only considering $\mathcal{NL}_2(t)$ as a load case would give a falsely conservative view of the system's failure probability.

These challenges highlight the danger of considering the NL-DLG process as a black-box-method, as is the case for most analysis methods. For systems with a

defined failure surface, it is possible for a designer to consider many different non-linear load combination cases to cover the whole failure surface. In this example, that is how many failures were discovered on the $\mathcal{NL}_1 - \mathcal{NL}_3$ plane, which directed another iteration of the NL-DLG process to utilize this unexpected result. For a system with a more ambiguous or expansive failure definition, it may be difficult to choose non-linear load combination cases which are exhaustive. However, the quick computation of the NL-DLG process allows a designer to trawl the design space in search of important non-linear load combination cases. This may be a necessary first step to gain confidence in the choice of load cases used for the NL-DLG process estimation.

The capability of the NL-DLG process is further highlighted in two examples in the next two chapters. Chapter VII examines stiffened ship panel collapse for six different panel designs. The failure surface is two-dimensional, so the choice of non-linear load combination cases is straightforward. The NL-DLG process evaluates the design performances, and some design changes are made to evaluate the sensitivity of the panels to failure. This iteration allows failure analysis to help drive design decisions. Chapter VIII considers combined loading on a trimaran hull and evaluates load cases suggested by the Lloyd's Register rule load and alternative load procedures for the structural design of trimarans. Here, there is no obvious failure surface definition, and threshold surfaces defining allowable load exceedances are at least three-dimensions, requiring some investigative work to examine the load cases. The iterative nature of the NL-DLG allows a probabilistic assessment of these load cases to evaluate whether the cases are sufficiently conservative, exhaustive, and realistically applicable for the trimaran hull in question.

CHAPTER VII

Combined Stochastic Lateral & In-Plane Loading on a Stiffened Panel Leading to Collapse

Stiffened panel collapse is governed by the interaction of combined lateral and in-plane loading effects. In this chapter, the performances of six different panel designs, related to the probabilities of collapse over a set exposure and operational profile, are compared using the NL-DLG process. The information gained from the NL-DLG process allows a designer to evaluate the panel design options, based on the performance characteristics of the designs.[1]

7.1 Stiffened Panel Collapse

Stiffened panel failure can occur due to effects from combined lateral and in-plane loading (*Hughes*, 1988). Figure 7.1 shows an example of a failure surface for a stiffened ship panel, with the y-axis as lateral loading, and the x-axis as in-plane loading. There are multiple modes of failure, corresponding to different combinations of simultaneous lateral and in-plane loading effects which can lead to collapse. Given specific loading combinations, the panel will collapse in different ways. Tensile yield of the stiffener flange occurs due to large lateral loading effects, while compression failure of the plating is caused by large in-plane loading effects. The panel can also fail due to compression yield of the stiffener flange. All of these failure modes are possible over a lifetime for a stiffened panel, though some stiffened panel designs may be more vulnerable to certain modes of failure than others. The NL-DLG process developed in Chapter V is used here to estimate the probability of failure for different panel designs, given a specific operational profile and exposure period.

[1]Portions of this work are in preparation to be published in *Seyffert et al.* (2018a).

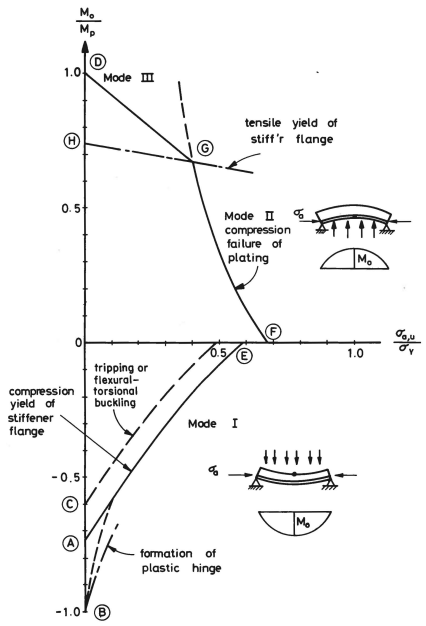

Figure 7.1: Collapse mechanism of a stiffened panel due to lateral and in-plane loading effects (*Hughes*, 1988).

7.2 Stiffened Panel Design Options

In the design process, different design options must be evaluated and compared to choose the optimal design. However, not all designs perform equally well. As an example, consider a stiffened panel on the external shell strake at the inner bottom of the David Taylor Model Basin vessel 5415 (DTMB 5415), which is representative of a modern destroyer-like hull. The proceedings of the 17^{th} *International Ship and Offshore Structures Congress* (committee V.5 Naval Ship Design) compared strength calculations from existing naval rules of different classification societies for this panel on the DTMB 5415 (*Ashe et al.*, 2009). Six different classification societies designed ship scantlings resulting from their respective structural rules. These different scantling designs allow an interesting design comparison, namely in that all designs have been vetted by some classification society but may perform differently. The panel specifications are given below in Table 7.1.

A designer choosing a panel structure for this vessel might assume that all of these designs perform equally well. This chapter examines the validity of that assumption using the NL-DLG process to evaluate and compare the performance of each panel design when subject to a specific sea state, operating profile, and exposure. An assumed operating profile for the DTMB 5415 is defined in Table 7.2, and the details

Panel from Class Society	1	2	3	4	5	6
Design Pressure [kPa]	$p_{\text{stiffener}} = 60.6$ $p_{\text{web}} = 33.6$	103.6	$p_{\text{stiffener}} = 59.75$ $p_{\text{web}} = 33.89$	86.6	127.45	174.55
Plate Thickness [mm]	9	11	8.1	7	8	10
H_{web} x T_{web} [mm]	160 x 6.2	150 x 9	154.4 x 6	113.64 x 6.35	246.9 x 5.8	220 x 6
H_{flange} x T_{flange} [mm]	120 x 9.8	90 x 14	101.8 x 8.9	63 x 13.36	101.6 x 6.9	200 x 6
Stiffener Spacing [mm]	672	700	500	364	600	400
Plate determining factor	buckling	stiffener compression	buckling	buckling	yield	buckling
Stiffener determining factor	minimum required	stiffener compression	min. required web thickness	local pressure	yield	buckling

Table 7.1: Panel and stiffener design from 6 classification societies (class societies are anonymous in ISSC report) (*Ashe et al.*, 2009).

of the full-scale DTMB 5415 geometry are in Table 7.3:

Parameter	Value
Lifetime	20 years
Exposure in specific condition	1000 hours
Spectrum Type	ITTC 2-parameter (H_s & T_p)
Significant Wave Height H_s	12.2 m
Peak Modal Period T_p	13.4 sec
Ship Speed	5 kts
Heading	head seas

Table 7.2: Operating profile for the DTMB 5415.

Principal Characteristics	Value
Length between perpendiculars (Lpp)	142 m
Length on water line (Lwl)	142.18 m
Beam on water line (Bwl)	19.06 m
Draft (T)	6.15 m
Displacement (∇)	8424.4 m^3
Block Coefficient (CB)	0.507
Longitudinal Center of Buoyancy (LCB) (% Lpp fwd+)	-0.683
Panel Location (fwd of midships +)	13.96 m
Midship section modulus (s)	3.34 m^3
Web frame spacing	1905 mm
Stiffener Yield Stress σ_{Y_s}	320 MPa
Plate Yield Stress σ_{Y_p}	320 MPa

Table 7.3: Specifications of the DTMB 5415 (*Ashe et al.*, 2009).

7.3 Construction of the Failure Surface

For the stiffened panel, only failure caused by in-plane loading effects from compressive global bending moments and lateral loading effects which put the flange into

tension are considered (i.e. failure modes 2 and 3 in Figure 7.1). Mode 2 (compression failure of the plating) and mode 3 (tensile yield of the stiffener flange) collapse lines are calculated based on the panel properties and a given value of initial loading on the panel. This process is iterated until the collapse lines intersect. This intersection point is the value of the moment due to lateral pressure and stress due to in-plane bending which simultaneously cause both mode 2 and mode 3 failure. A full description of this process is given by *Hughes* (1988).

7.4 Origin of Loading Effects on the Panel

With the failure surface defined, the next step is the determination of the loading effects acting on the panels. Lateral loading effects are assumed to be caused by impact pressure from slam events at the stiffened panel location, and in-plane loading effects are assumed due to global bending of the main hull girder. These load effects are calculated based on the vessel geometry and panel properties. The vessel's velocity relative to the water surface excites the lateral loading due to impact pressure and the global bending moment drives the in-plane loading. Linear transfer functions of the relative velocity and bending moment at the given ship panel location (13.96 m forward of midships) are determined using SHIPMO.BM, a linear, slender-body motions program (*Beck and Troesch*, 1990).

These transfer functions transform the stochastic wave excitation into time series of relative velocity and bending moment at the panel location. The time series are constrained to only consider relative velocity when the panel is entering the water (i.e. relative velocity is negative and relative motion is positive) and when the panel is under compressive bending load (i.e. hogging condition, corresponding to a negative bending moment). Any point in the relative velocity and bending moment time series that does not satisfy those sign conditions is not considered as a potential time for failure to occur. This corresponds to considering only failure modes 2 and 3.

7.4.1 Lateral Load Effect Determination

The relative velocity of the stiffened ship panel determines the lateral load effect due to potential slam events, specifically an applied lateral bending moment normalized by the plastic hinge moment. The relative velocity is converted to strain following the model from *Faltinsen* (2005). *Faltinsen* conducted experiments by dropping

a one-third scale elastic hull with wedge-shaped cross sections into an initially calm water surface. These experiments indicate when fluid-structure interaction has an appreciable effect based on the wedge deadrise angle and impact velocity. These results produced a functional relationship between impact velocity (i.e. relative velocity between hull and water surface) and the resulting maximum strain. This velocity/ strain relationship is given by Eq.(7.1), with the corresponding stress found by Eq.(7.2). The lateral load effect is a lateral moment due to a lateral stress, normalized by the plastic hinge moment, as shown in Eq.(7.3).

$$\epsilon(t) = \frac{\epsilon_{ND}(t) Y_c RV(t)^2 \rho a^2}{EI_3 tan(\beta)} \tag{7.1}$$

where

$\epsilon_{ND}(t)$ = 'non-dimensional' strain value, from *Faltinsen* (2005) Figure 8.20

Y_c = location of neutral axis from plate

$RV(t)$ = time series of relative velocity at panel location

ρ = water density

β = panel deadrise angle = 5°

a = panel length between transverse frames (web frame spacing)

E = Young's modulus = 190 GPa

I_3 = panel moment of inertia about neutral axis, normalized by breadth of stiffener flange, b_f

$$\sigma_{lateral}(t) = \epsilon(t) E \tag{7.2}$$

where

$\epsilon(t)$ = strain time series, from Eq.(7.1)

E = Young's modulus = 190 GPa

The time series of the applied moment due to the lateral load effect, normalized by the plastic hinge moment, $\frac{M_0}{M_P}(t)$, is found from Eq.(7.3):

$$\frac{M_0}{M_P}(t) = \frac{\sigma_{lateral}(t) I_{tr}}{Y_f M_P} \tag{7.3}$$

where

$\sigma_{lateral}(t)$ = lateral stress time series, from Eq.(7.2)

I_{tr} = transformed moment of inertia about neutral axis, from Eq.(7.5)

Y_f = distance to the neutral axis as measured from the flange

M_P = plastic hinge moment, from Eq.(7.4)

The plastic hinge moment M_P is given by Eq.(7.4):

$$M_P = \overline{\sigma_Y} ZP \tag{7.4}$$

where

$$ZP = Z_f + Z_w + Z_p \qquad H_\bullet = \text{height of } \bullet$$
$$Z_f = A_f(H_w + g + 0.5T_f) \qquad A_p = \text{plate area} = H_pT_p$$
$$Z_w = A_w(0.5H_w + g) \qquad A_w = \text{web area} = H_wT_w$$
$$Z_p = A_pT_pC2 \qquad A_f = \text{flange area} = H_fT_f$$
$$C1 = \frac{A_p + A_w + A_f}{2A_p} \qquad A_T = \text{total effective area} = A_w + A_f + A_p$$
$$C2 = C1^2 + C1 + 0.5 \qquad \overline{\sigma_Y} = \frac{\sigma_{Y_s}(A_f + A_w) + \sigma_{Y_p}A_p}{A_T}$$
$$g = C1T_p \qquad \sigma_{Y_s} = \text{yield stress of stiffener}$$
$$T_\bullet = \text{thickness of } \bullet \qquad \sigma_{Y_p} = \text{yield stress of plate}$$

The transformed moment of inertia about the neutral axis, used in Eq.(7.3), is calculated the same way as the normal moment of inertia about the neutral axis, except that it uses a transformed flange height, $H_{f_{tr}}$, and transformed total effective area, $A_{T_{tr}}$, as given below in Eq.(7.5):

$$\begin{aligned} H_{f_{tr}} &= H_fT \\ A_{T_{tr}} &= A_TT \end{aligned} \tag{7.5}$$

where

$$T = \text{secant modulus} = \frac{1}{4}\left(2 + \zeta - \sqrt{\zeta^2 - \frac{10.4}{\gamma^2}}\right) \qquad \zeta = 1 + \frac{2.75}{\gamma^2}$$
$$\gamma = \text{slenderness parameter} = \frac{b_f}{T_p}\sqrt{\frac{\overline{\sigma_Y}}{E}} \qquad A_T = \text{total effective area} = A_w + A_f + A_p$$
$$b_f = \text{breadth of stiffener flange}$$

7.4.2 In-Plane Load Effect Determination

The global midship bending moment excites the in-plane loading effect, $\frac{\sigma_{a,u}}{\overline{\sigma_Y}}(t)$, by converting the vertical main-hull girder bending moment at the longitudinal coordinate of the panel to an applied stress, as shown below in Eq.(7.6):

$$\frac{\sigma_{a,u}}{\overline{\sigma_Y}}(t) = \frac{\sigma_F(t)}{\overline{\sigma_Y}} \tag{7.6}$$

where

$$\sigma_F(t) = \sigma_A(t)\left(1 + \frac{A_T \frac{a}{750} y\phi}{I}\right)$$

$$\sigma_A(t) = \frac{BM(t)}{s}$$

$BM(t)$ = time series of global midship bending moment at stiffened panel

s = midship section modulus of the vessel

$\frac{a}{750}$ = estimate of original plate deflection from *Hughes* (1988)

y = neutral axis, as measured from the plate

$$\phi = \frac{1}{1 - \frac{\sigma_A(t)}{\sigma_E}}$$

$$\sigma_E = \text{Euler column buckling stress} = \frac{\pi^2 EI}{A_T a^2}$$

A_T = total effective area = $A_w + A_f + A_p$

a = panel length between transverse frames (web frame spacing)

The panel specifications affect both the shape of the failure surface, including the intersection of the two failure modes and their slopes, and how the relative velocity and bending moment time series are non-linearly transformed to the lateral and in-plane loading effects, as shown above in Eq.(7.1)-Eq.(7.6).

7.5 Non-Linear Load Combination Cases & Surrogate Processes

Given a vessel, operating profile and conditions, sea spectrum, and exposure period, stochastic time series of relative velocity and global bending moment at the panel location are defined. Then, the different stiffened panel designs from Table 7.1 define failure surfaces and transformations of the relative velocity and bending moment time series to the lateral and in-plane loading effects, respectively. The NL-DLG process determines the probability of failure for each panel design and estimates a distribution of most-likely failure occurrences grouped into the possible failure modes.

Different regions of the failure surface, G, for each panel are emphasized by n non-linear load combination cases which are weighted sums of the two non-linear load effects, $\frac{\sigma_{a,u}}{\overline{\sigma_Y}}(t)$ and $\frac{M_0}{M_P}(t)$ as in Eq.(7.7):

$$\zeta_i(t) = \alpha \frac{M_0}{M_P}(t) + \beta \frac{\sigma_{a,u}}{\overline{\sigma_Y}}(t) \tag{7.7}$$

where

$\zeta_i(t)$ = time series of a given non-linear load combination case $i = 1, \cdots, n$

$\frac{M_0}{M_P}(t)$ = time series of lateral loading effect from Eq.(7.3)

$\frac{\sigma_{a,u}}{\overline{\sigma_Y}}(t)$ = time series of in-plane loading effect from Eq.(7.6)

α, β = weighting factors

For this example, three non-linear load cases are defined to estimate the total failure probability of each stiffened panel. The choice of three (and not more, or fewer) non-linear load combination cases is somewhat arbitrary but is based on the intuition that three points may be a reasonable approximation to a 2-dimensional bi-linear curve in a single quadrant. These load combination cases are given by Eq.(7.8) and focus on three areas of the failure surface: the failure surface intersect on the y-axis (failures due to pure lateral loading effect), the failure surface intersect on the x-axis (failures due to pure in-plane loading effect), and the 'middle' region of the failure surface (failures due to moderate, equally weighted, simultaneous lateral and in-plane loading effects):

$$\begin{aligned} \zeta_1(t) &= \frac{M_0}{M_P}(t) \\ \zeta_2(t) &= \frac{\sigma_{a,u}}{\overline{\sigma_Y}}(t) \\ \zeta_3(t) &= \frac{1}{2}\frac{M_0}{M_P}(t) + \frac{1}{2}\frac{\sigma_{a,u}}{\overline{\sigma_Y}}(t) \end{aligned} \tag{7.8}$$

Three surrogate processes, meant to capture relevant physics of the associated non-linear load combination cases, are defined. Each surrogate process is defined as a weighted sum of linear functions that best reflects the corresponding weighted sum of non-linear load effects. The three surrogate processes are given as $z_1(t)$, $z_2(t)$, and $z_3(t)$:

$$\begin{aligned} z_1(t) &= \frac{RV(t)}{\sigma_{RV}} \text{ (which approximates } \zeta_1(t)) \\ z_2(t) &= \frac{BM(t)}{\sigma_{BM}} \text{ (which approximates } \zeta_2(t)) \\ z_3(t) &= \frac{1}{2}\frac{RV(t)}{\sigma_{RV}} + \frac{1}{2}\frac{BM(t)}{\sigma_{BM}} \text{ (which approximates } \zeta_3(t)) \end{aligned} \tag{7.9}$$

Note that the relative velocity and bending moment time series are the excitation inputs to the lateral and in-plane loading effects in Eq.(7.1) and (7.6), respectively. This makes $RV(t)$ and $BM(t)$ potential indicators of extreme behavior for the lateral and in-plane load effects. The $RV(t)$ and $BM(t)$ time series are normalized by their respective standard deviation to reflect the relative percentage of each load for the surrogate process. Since the lateral and in-plane load effects are normalized by an ultimate value, this preserves the relative weighting of the weighting factors α and β from Eq.(7.8).

7.6 TEV of Relative Velocity and Bending Moment

To generate the DLG simulations for use in the NL-DLG process, the exposure period must be considered to construct the global, Gaussian inputs $\eta_i(t)$ $i = 1, 2, 3$ that lead to exposure-period-maxima of the associated surrogate processes. This information comes from the target extreme value, TEV, of each surrogate process. As in Chapter 6.3, 32-hour MCS are conducted to estimate a calibration period, T_c, to estimate the number of cycles over the exposure, and to calculate a 1000-hour TEV for each surrogate process, using Eq.(6.9). These values are given in Table 7.4, along with the computation time to run these short MCS[2]:

Surrogate Process	1000-hr TEV
$z_1(t)$	5.2400
$z_2(t)$	5.0519
$z_3(t)$	5.1846

Table 7.4: Estimated calibration period, T_c, from 1000 32-hour MCS (computation time about 5 minutes) and resulting 1000-hour TEV, using Eq.(6.9), for the surrogate processes $z_i(t)$, $i = 1, 2, 3$ from Eq.(7.9).

7.7 Failure Probability from the NL-DLG Process

Given the non-linear load combination cases from Eq.(7.8) that focus on three common regions of each failure surface, 2000 DLG simulations are run for each surrogate process from Eq.(7.9). Note that these wave excitation inputs do not need to be constructed for each panel, since the relative velocity and bending moment time series are based on global vessel properties, not panel properties. Each panel design dictates how those relative velocity and bending moment time series are non-linearly transformed to lateral and in-plane loading effects, respectively.

The constructed $\eta_i(t)$, $i = 1, 2, 3$ time series are then assigned to the possible categories $\{\widehat{Z_1}\}$, $\{\widehat{Z_2}\}$, $\{\widehat{Z_3}\}$, $\{\widehat{Z_1 Z_2}\}$, $\{\widehat{Z_1 Z_3}\}$, $\{\widehat{Z_2 Z_3}\}$, or $\{\widehat{Z_1 Z_2 Z_3}\}$, as defined by Chapter 5.7. The probability of failure given such an event is calculated as in Eq.(5.4). Given the number of surrogate processes, the total number of possible maxima configurations is expressed by the Bell number, Eq.(5.5). The probabilities of experiencing these mutually exclusive and exhaustive configurations are discussed in detail and derived in Appendix A.

[2]These computation times reflect running on a MacBook Pro personal laptop, 2.5 GHz Intel Core i7.

Then, the overall failure probability for each panel due to the three non-linear load combination cases from Eq.(7.8) is found using Eq.(5.6). The failure probabilities for panels 1-6 are tabulated below in Table 7.5. 10,000 1000-hour MCS were conducted to validate these results, which are also tabulated in Table 7.5[3]. Clearly, the NL-DLG process very closely recovers the probability of failure for each panel design with a significant reduction in computation time from full MCS.

	Panel Probability of Failure	
Panel	NL-DLG process	MCS
1	0.8738	0.8883
2	0.5916	0.5955
3	1.0000	1.0000
4	1.0000	1.0000
5	0.1192	0.1166
6	0.0288	0.0273
Computation time	∼13 minutes	∼42 hours

Table 7.5: Probability of failure for stiffened panels 1-6 using the NL-DLG process, compared with 10,000 1000-hour MCS, given the operating and environmental conditions in Table 7.2.

It is also interesting to consider an estimate of the distribution of most-likely failure occurrences for each panel. The histograms of estimated most-likely failures for panels 1-6 from the NL-DLG process, and from full MCS, are given in Figure 7.2. These histograms, normalized as a probability distribution, are given in Figure 7.3. In Figures 7.2-7.3, the number of samples for each distribution is proportional to the probability of failure for each panel and analysis method (i.e. NL-DLG process vs. MCS). The MCS distributions of most-likely failures have significantly more occurrences due to pure lateral loading effect (on the y-axis), and pure in-plane loading effect (on the x-axis) than do the distributions assembled by the NL-DLG process.

7.7.1 Comparisons between the NL-DLG Process & MCS

To understand this difference, a few comparisons between the NL-DLG process and MCS can be made. First, it is helpful to compare the TEV values for the surrogates used in the NL-DLG process to construct the simulations, and those values estimated from 1000-hour MCS. Figure 7.4 shows the empirical histograms of the 1000-hour maxima of the surrogate processes $z_1(t)$, $z_2(t)$, and $z_3(t)$ from 2000 DLG simulations per surrogate, and from 10,000 MCS, both normalized as a *pdf*. The

[3]The MCS were run on an Ubuntu desktop with 12x Intel(R) Xeon(R) CPU E5-2609 v3 @ 1.90GHz. The NL-DLG process computation times are from running on a MacBook Pro personal laptop, 2.5 GHz Intel Core i7.

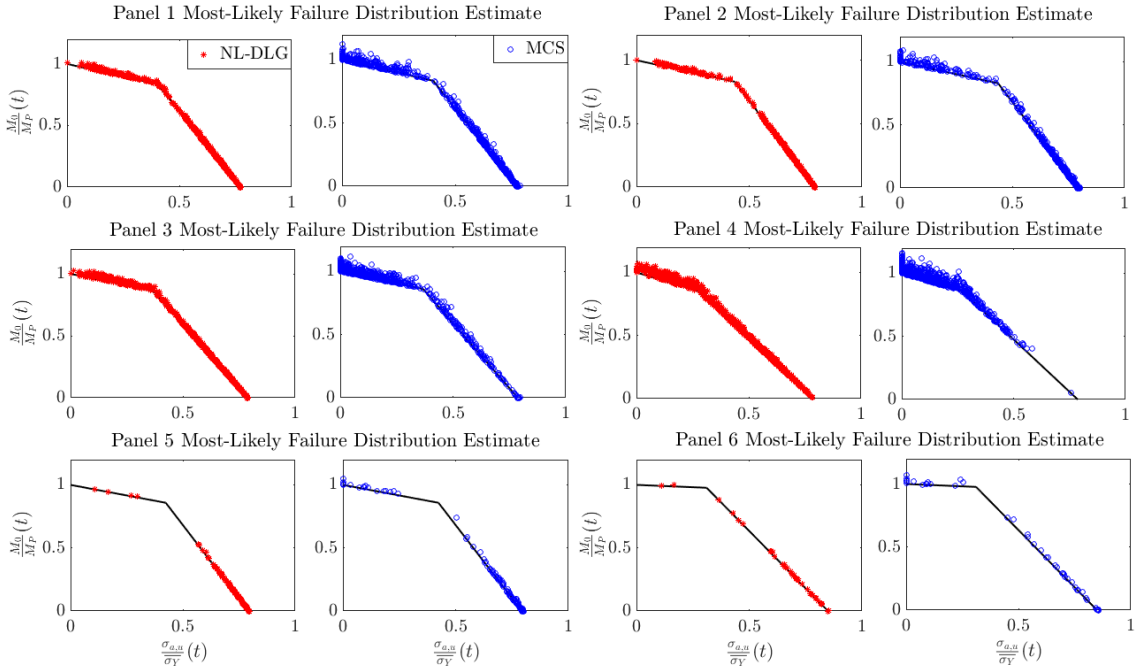

Figure 7.2: Estimate of the most-likely failure occurrences for panels 1-6 from the NL-DLG process and 10,000 MCS, given the operating and environmental conditions in Table 7.2.

TEV of each histogram, as estimated by the closed-form Gaussian extreme value distribution with the minimum Jeffreys divergence, Eq.(3.1), is given for each distribution. The DLG distributions for all surrogate processes have higher TEV values than the MCS distributions. Recall that the TEV values for the DLG simulations were estimated from a calibration period, T_c, from 32-hour MCS, as in Chapter 6.3. As in the example in Chapter 6.3, these TEV estimates are a bit higher than the TEV estimates from full 1000-hour MCS. Despite this, the NL-DLG process estimates of the failure probabilities of panels 1-6 are generally slightly smaller than the MCS estimates. This may be due to the estimation of the probability of experiencing the maxima configurations, and due to only using three non-linear load combination cases/ surrogate processes in the NL-DLG process, as discussed in Chapter 6.7.4. However, this does not explain why the MCS estimate of most-likely failures have significantly more failures due to pure lateral and pure in-plane loading effects than do the NL-DLG process estimates.

As in the DLG simulations used in the NL-DLG process, the most-likely failure is the failure which occurs *first* during an exposure. The NL-DLG process assumes that failure occurrences are exclusively associated with times when one of the surrogate

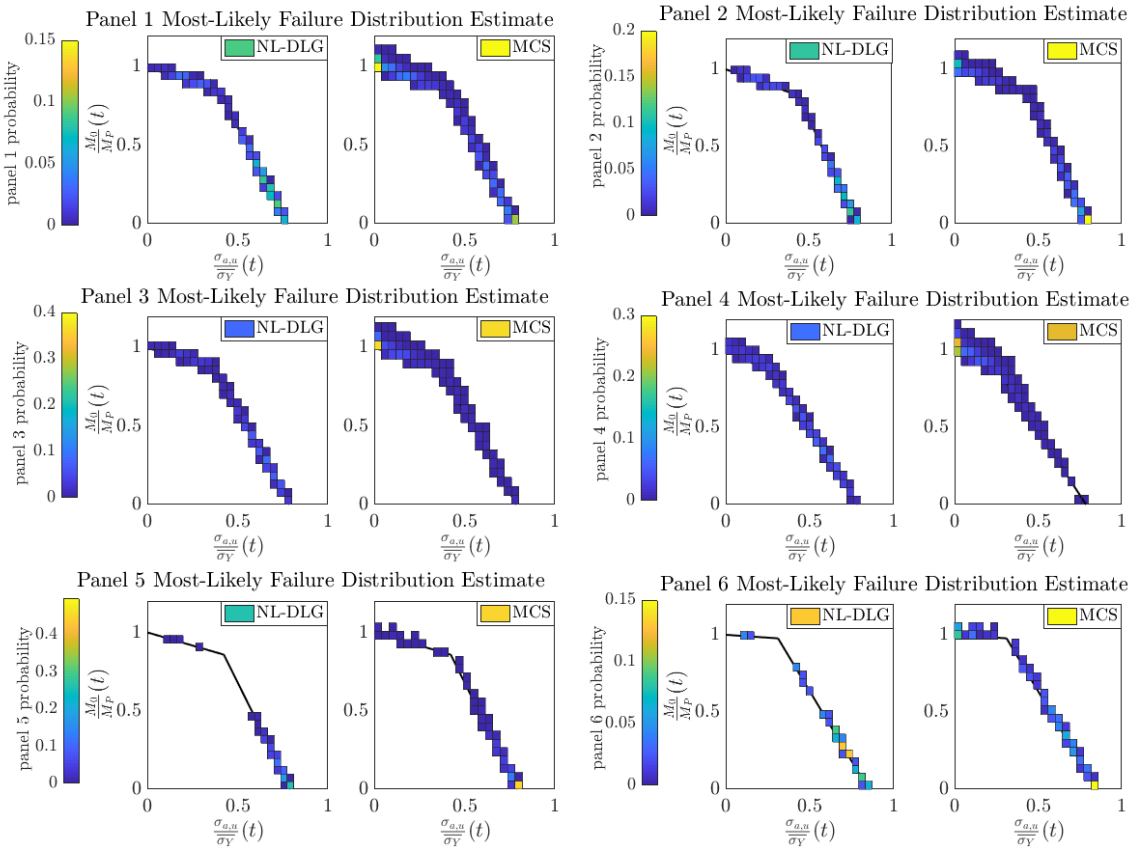

Figure 7.3: Estimate of the probability distribution of most-likely failure occurrences for panels 1-6 from the NL-DLG process and 10,000 MCS, given the operating and environmental conditions in Table 7.2.

processes experiences an extreme value. Out of the 10,000 MCS, 3326 exposures have the 1000-hour maximum of $z_1(t)$ occur first, 3333 simulations have the 1000-hour maximum of $z_2(t)$ occur first, and 3341 simulations have the 1000-hour maximum of $z_3(t)$ occur first. That each surrogate process exposure-period-maximum has nearly the same probability of occurring first makes sense, as each surrogate process maximum has the same 1000-hour return period. This confirms the logic used to construct the estimate of most-likely failures, as described in Chapter 5.9, but does not explain why the MCS exhibit significantly more failures due to pure lateral loading than what the NL-DLG process estimates.

This deviation between the NL-DLG process and the MCS validation is examined further in Section 7.8.1.1. It is an area of active research, and future work, to further understand this difference and improve the accuracy of the estimations from the NL-DLG process.

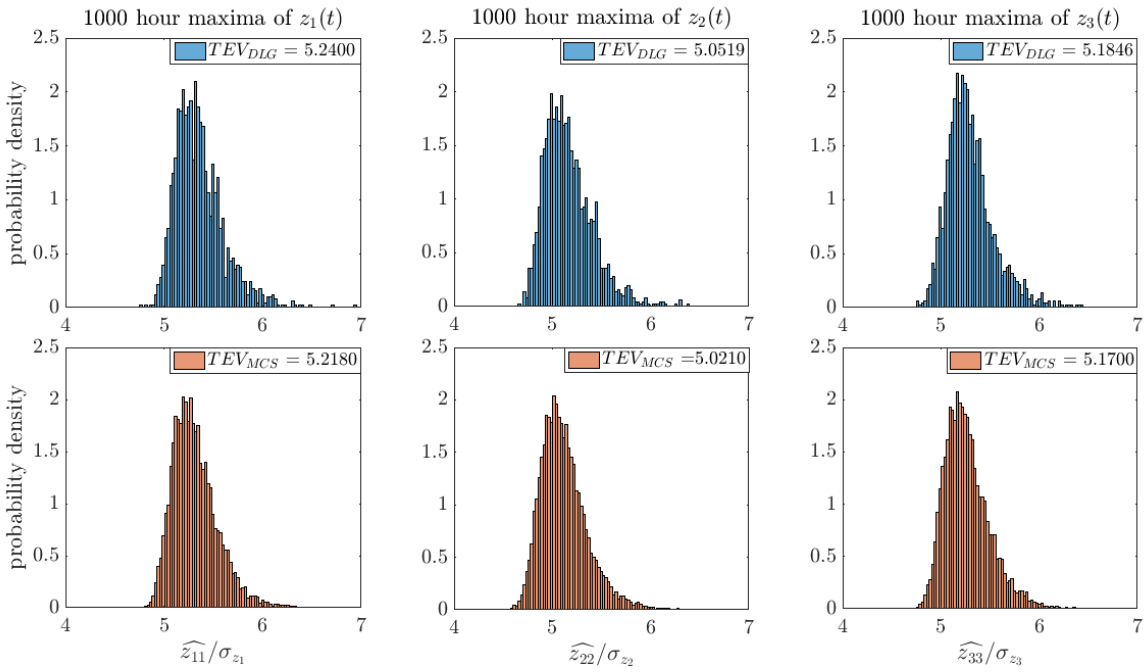

Figure 7.4: 1000-hour maxima of for surrogate processes $z_1(t)$, $z_2(t)$, and $z_3(t)$, from 2000 DLG simulations and 10,000 MCS, given the operating and environmental conditions in Table 7.2.

7.8 Vulnerability of Panel Designs

Clearly the different panel designs from Table 7.1 do not perform equally well for the same operational profile and exposure. A natural question is: are there certain design aspects which makes some of these panels perform better than others? It may be difficult to determine which specific panel properties lead to a better or worse performance, mainly because these properties are inputs to both the lateral and in-plane loading effects, as well as the failure surface definition. Varying these properties may lead to opposing trends in how a wave excitation leads to the lateral and in-plane loading effects, and how a panel bears those loads via the failure surface definition.

It is possible, though, to compare how the different panels handle the lateral and in-plane loading effects, and to compare the failure surfaces for the different panel designs. The lateral and in-plane load effects are non-linear functions of the panel properties and the relative velocity and bending moment at the panel location, which are driven by the stochastic wave excitation. The failure surface definition is also a non-linear function of the panel properties. There are two major factors which relate the panel failure probabilities over the exposure with the panel properties, those being:

1. How the wave excitation is non-linearly transformed to lateral and in-plane loading effects for the different panels, via the panel properties.

2. The level of lateral and in-plane loading effects which is required for each panel to fail (i.e. the failure surface definition).

These two aspects are closely related, and are both based on the panel properties, but it is possible to control one aspect and examine the effect of the other. In this way, different aspects of the panel designs which make the panels more or less susceptible to failure may become apparent.

7.8.1 Ensemble Wave Excitations

The relative velocity and bending moment at the panel location are defined by the vessel properties and the excitation environment. This means that for a given wave excitation, each panel design experiences the same relative velocity and bending moment. Then, based on the panel properties, each panel experiences different lateral and in-plane loading effects due to that relative velocity and bending moment. The way the different panels experience different loading effect magnitudes based on the same wave excitation can be compared by considering ensemble wave records as the excitation input.

Figure 7.5 shows the wave elevations $\eta_1(t)$ constructed by the DLG to maximize $z_1(t)$, with the ensemble average $\overline{\eta_1(t)}$ in red. The time series of $z_1(t)$, $z_2(t)$, and $z_3(t)$ are plotted, along with the ensemble averages of these curves, $\overline{z_1(t)}$, $\overline{z_2(t)}$, and $\overline{z_3(t)}$ in red. Note that $z_3(t)$ is normalized by σ_{z_3} so that all surrogate process values are given in terms of the respective σ.

Even though the $\eta_1(t)$ waves are constructed for maximum $z_1(t)$ response, resulting in the clear ensemble structure of $\overline{z_1(t)}$, $\overline{z_2(t)}$ and $\overline{z_3(t)}$ also have a clear ensemble structure. The same can be said for wave elevations $\eta_2(t)$ constructed to maximize $z_2(t)$ in Figure 7.6 and for $\eta_3(t)$ constructed to maximize $z_3(t)$ in Figure 7.7. All $z_1(t)$ time series have noticeable high-frequency content, because the relative velocity transfer function passes significant high-frequency wave energy. However, the $\overline{z_1(t)}$ time series driven by all the ensemble waves $\overline{\eta_i(t)}$ $i = 1, 2, 3$ exhibit a strong ensemble structure. Likewise, $z_3(t)$, which has a weighted component of the relative velocity leading to noticeable high-frequency content, still has a clear ensemble structure.

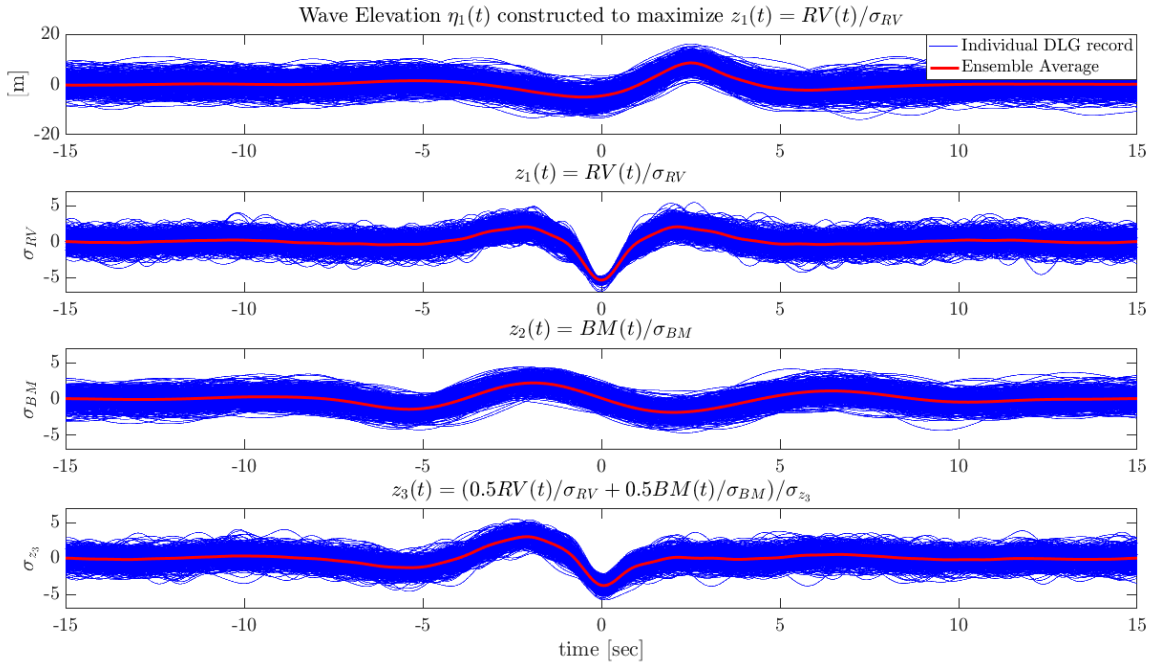

Figure 7.5: Wave elevations from the DLG, $\eta_1(t)$, constructed to maximize $z_1(t) = RV(t)/\sigma_{RV}$, along with resulting time series of $z_1(t)$, $z_2(t)$, and $z_3(t)/\sigma_{z_3}$. The ensemble averages are shown as the red curves.

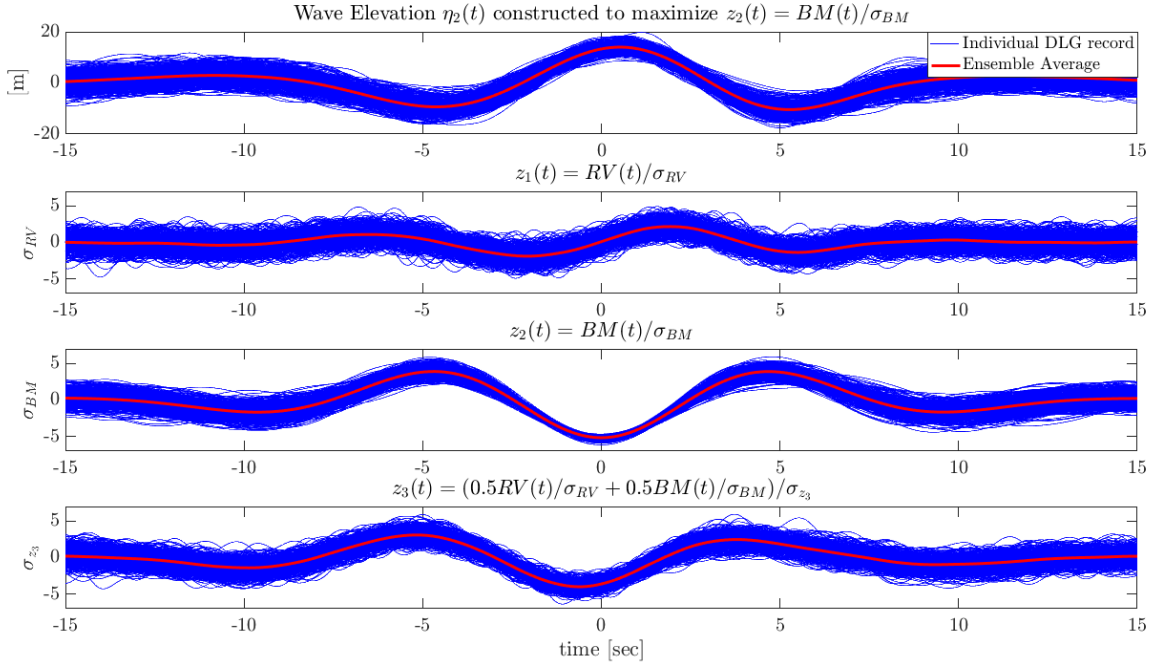

Figure 7.6: Wave elevations from the DLG, $\eta_2(t)$, constructed to maximize $z_2(t) = BM(t)/\sigma_{BM}$, along with resulting time series of $z_1(t)$, $z_2(t)$, and $z_3(t)/\sigma_{z_3}$. The ensemble averages are shown as the red curves.

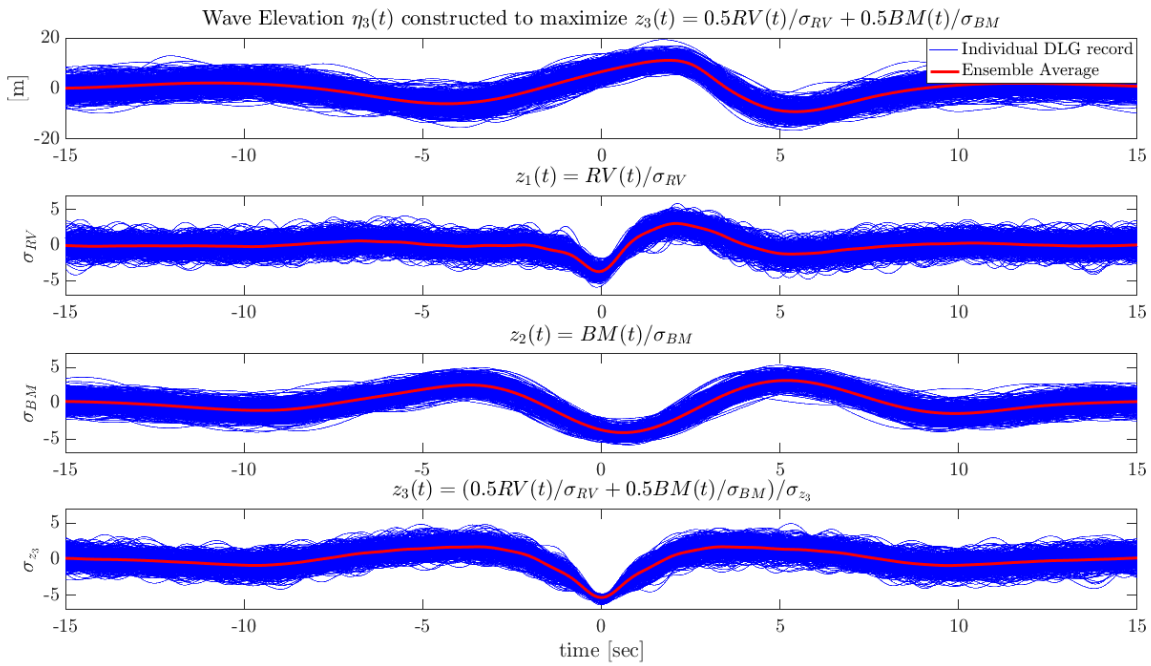

Figure 7.7: Wave elevations from the DLG, $\eta_3(t)$, constructed to maximize $z_3(t) = 0.5RV(t)/\sigma_{RV} + 0.5BM(t)/\sigma_{BM}$, along with resulting time series of $z_1(t)$, $z_2(t)$, and $z_3(t)/\sigma_{z_3}$. The ensemble averages are shown as the red curves.

Regardless of which surrogate process, $z_i(t)$, the waves are constructed to maximize, all surrogate processes exhibit a clear ensemble structure given that wave input, $\overline{\eta_i(t)}$. This indicates that the panels can be compared based on their loading effect responses to the three types of ensemble waves, $\overline{\eta_1(t)}$, $\overline{\eta_2(t)}$, and $\overline{\eta_3(t)}$. Given any wave excitation, each panel experiences the same relative velocity and bending moment. The panel design determines how those relative velocity and bending moment time series lead to the lateral and in-plane loading effects. The ensemble waves, $\overline{\eta_1(t)}$, $\overline{\eta_2(t)}$, and $\overline{\eta_3(t)}$ can be used to compare the different magnitudes of panel loading effects given the same excitation input. Even though the lateral and in-plane load effects are non-linear transformations of the relative velocity and bending moment (which are based on the wave elevation), it can be instructive to consider how the different panels experience loading effects given the same wave excitation input, to determine any potential trends.

7.8.1.1 Failures due to 'Superficial' Pure Lateral and In-Plane Loading Effects

These ensemble wave profiles partially explain the discrepancy in the most-likely failure estimate from the NL-DLG process versus the MCS estimate, in which the MCS result showed significantly more failures due to pure lateral and pure in-plane loading effects for most panel designs. For the probability of stiffened panel failure, only failure modes 2 and 3 are considered, corresponding to compression failure of the plating and tensile yield of the stiffener flange, respectively. The lateral loading effect for mode 3 failure is due to negative relative velocities, representing slam events, while the in-plane loading effect for mode 2 failure is due to negative, hogging global bending moments. Any times when the bending moment or relative velocity time series are positive are mapped to zero, because they cannot provide the excitation required for the loading to cause mode 2 or 3 failure.

However, it is possible that a wave can lead to a hogging (negative) bending moment, and positive relative velocity at the same instant (see Figure 7.6 between times $0 \leq t \leq 2.5$ sec). This time segment would be mapped to some level of in-plane loading effect, with zero lateral loading effect (i.e. on the x-axis). In the same way, a wave can lead to negative relative velocity and positive bending moment at the same time, like during time $-2.5 \leq t \leq 0$ sec in Figure 7.5. This time segment would lead to a positive lateral loading effect, with zero in-plane loading effect, i.e. mapped to the y-axis. Any failures due to such time series would represent failures due to 'superficial' pure lateral or pure in-plane loading effects. If the entire failure surface were considered (i.e. more than modes 2 and 3), these failures would not be in quadrant 1, and would not be due to pure lateral or pure in-plane loading effects.

The wave excitation profiles constructed by the DLG to test the system will exhibit some instances when loads are superficially mapped to the x-axis or y-axis due to the signage from the relative velocity or bending moment time series, respectively. However, these times will always exhibit the ensemble structures shown in Figures 7.5-7.7. In the MCS, any instance when the bending moment or relative velocity do not have the correct sign to lead to modes 2 or 3 failure is similarly mapped to zero. However, a full-length MCS will have many more wave profile shapes than the three ensemble wave profiles from Figures 7.5-7.7. This could potentially lead to many more instances of failures due to superficial pure lateral or pure in-plane loading effects from the MCS, simply due to the mapping of positive relative velocity

and positive bending moment to zero. The NL-DLG process would never simulate these other wave profiles which could lead to superficial pure lateral or pure in-plane loading effects, because the DLG is focused only on the three surrogate processes $z_1(t)$, $z_2(t)$, and $z_3(t)$.

This difference illustrates the potential challenges, described in Chapter 6.8, associated with the NL-DLG process. The estimates from the NL-DLG process of failure probability and most-likely threshold-crossing/ failure occurrence are conditioned on the failure surface definition, and the choice of the non-linear load combination cases and surrogate processes. The computational efficiency of the NL-DLG process comes from only simulating times when extreme responses of the surrogate processes are expected to occur. The NL-DLG process assumes that these are the only times when failure may occur, although that is potentially not the case. This example highlights that challenge, because some unexpected MCS results came from times that the NL-DLG process does not simulate.

As well, this discrepancy between the NL-DLG process and MCS shows how the NL-DLG process is implicitly conditioned on the failure surface definition. Since only modes 2 and 3 failure were considered, all other failure types are mapped to the failure diagram axes. If the NL-DLG process were estimating the probability a stiffened panel experiences mode 1, 2, or 3 failure, meaning the panel can also fail due to compression yield of the stiffener flange (negative lateral loading effect), it is likely that fewer failures due to pure lateral or pure in-plane loading effects would be recorded.

On the other hand, there is a minimal difference between the failure probabilities from the NL-DLG process versus the MCS verification. It is unclear how the NL-DLG process so accurately estimates the failure probabilities found from full MCS, even with the differences between the methods, as noted in this section and in Chapter 6.7.4. This is an area of active research.

7.8.2 Lateral Load Effect Vulnerability due to Ensemble Wave Excitation

Figure 7.8 shows the ensemble wave excitation $\overline{\eta_1(t)}$, the resulting $\overline{z_1(t)}$ and $\overline{z_2(t)}$ time series driven by $\overline{\eta_1(t)}$, and the lateral and in-plane loading effects for each panel design driven by $\overline{\eta_1(t)}$. Given the ensemble excitation $\overline{\eta_1(t)}$, the panels all experience nearly the same in-plane loading effect. However, this wave input leads to significantly different lateral load effects. The lateral loading effect time series for each panel all

follow a similar profile but have different relative magnitudes. Given the same $\overline{\eta_1(t)}$ excitation, the lateral loading effect magnitudes for each panel are ranked from largest to smallest as those experienced by panel: 4, 3, 1, 2, 6, and then 5.

This trend is also clear in Figure 7.9, where the vector of lateral and in-plane loading effects experienced by each panel, which is excited by $\overline{\eta_1(t)}$, is plotted on the left. The right plot of Figure 7.9 shows these same time series normalized by the maximum experienced lateral load effect for each panel. When normalized by the maximum lateral loading effect for each panel, these time series all collapse to an ensemble curve, revealing that the panels all experience about the same in-plane load effect, and are only different due to their respective levels of lateral load effect.

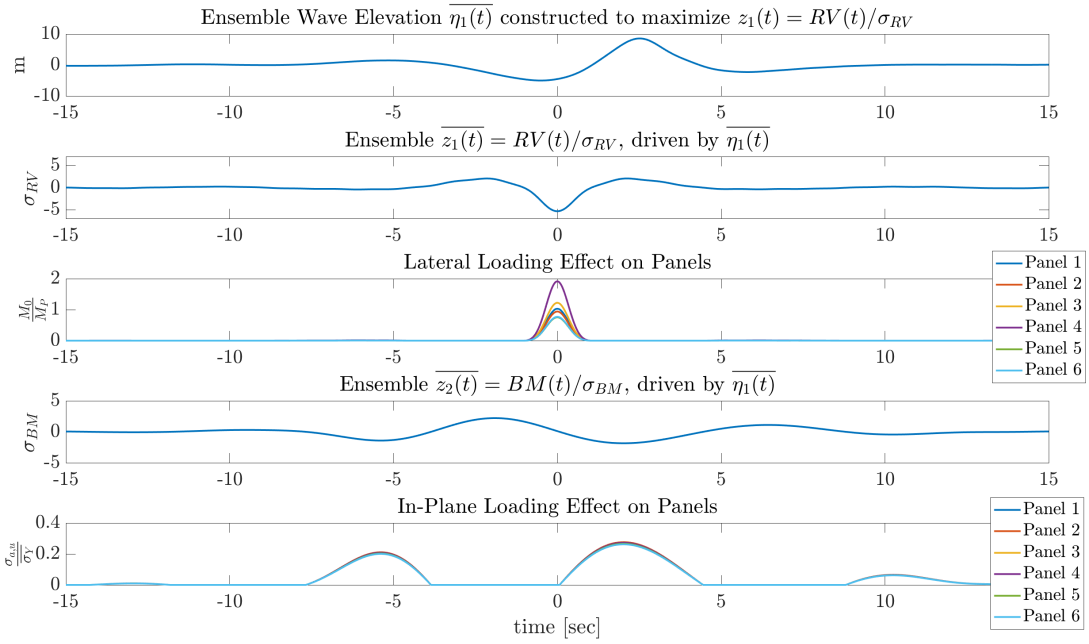

Figure 7.8: Ensemble wave elevation $\overline{\eta_1(t)}$ constructed to maximize $z_1(t)$, along with resulting time series of $\overline{z_1(t)}$ and $\overline{z_2(t)}$ driven by $\overline{\eta_1(t)}$. These time series are constant for all panels given a wave input. The lateral and in-plane loading effects due to the ensemble excitation $\overline{\eta_1(t)}$ are given for each panel.

Figures 7.8-7.9 indicate that panel 4 experiences the largest lateral loading effect of all panels, and that panels 5 and 6 experience the least lateral loading effect of all panels, given the same excitation input. These trends may also partially explain the discrepancy between the most-likely failure distribution estimate from the NL-DLG process versus from MCS. Note that in Figure 7.3, MCS predicted that nearly 30% of failure occurrences are due to pure lateral loading effects for panels 3 and 4. While

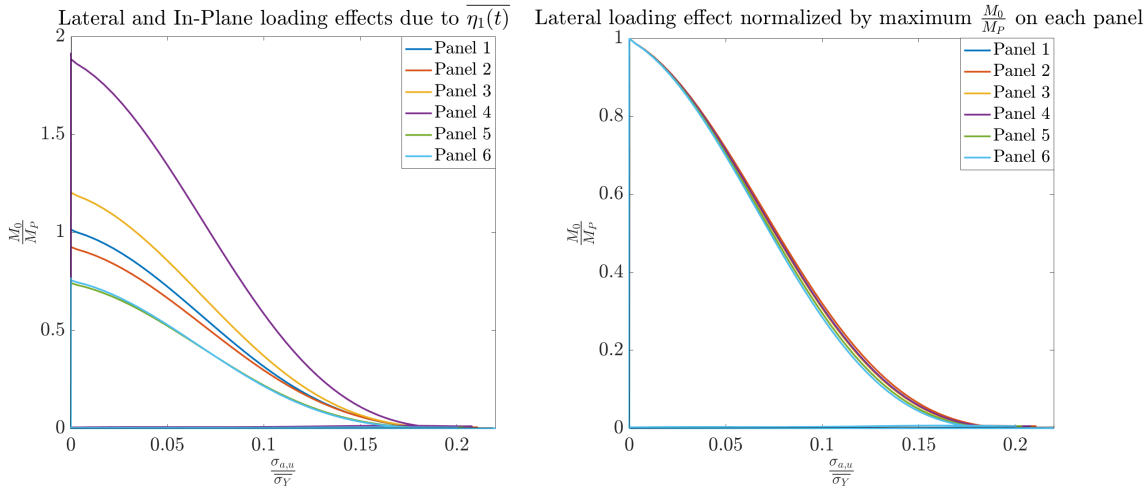

Figure 7.9: Vector of lateral and in-plane loading effects for each panel driven by $\overline{\eta_1(t)}$ (left) and the same loading effect time series normalized by the maximum experienced lateral loading effect for each panel (right).

some other panels exhibit many failure occurrences due to pure lateral load effects from the MCS estimates (i.e. panels 1 and 2), none of the probabilities of experiencing that kind of failure are nearly as high. Since panels 3 and 4 experience the harshest lateral loading effects of all panels given a common wave excitation, as evidenced in Figure 7.9, the findings from Figure 7.3 are unsurprising.

7.8.3 In-Plane Load Effect Vulnerability due to Ensemble Wave Excitation

Figure 7.10 shows the ensemble wave excitation $\overline{\eta_2(t)}$, and the resulting time series of $\overline{z_1(t)}$, $\overline{z_2(t)}$, lateral, and in-plane loading effects. Here, $\overline{\eta_2(t)}$ is constructed by the DLG to maximize $z_2(t)$, which relates to the in-plane loading effect. Note that the same trends from Figures 7.8-7.9 are still apparent, even given a different ensemble wave input. Each panel experiences nearly the same in-plane loading effect due to the $\overline{\eta_2(t)}$ wave excitation, but significantly different lateral loading effects. The relative ordering of the lateral loading effect magnitudes due to $\overline{\eta_2(t)}$ from largest to smallest, as those experienced by panel: 4, 3, 1, 2, 6, and then 5, is the same ranking as from the $\overline{\eta_1(t)}$ input.

Figure 7.11 shows the lateral and in-plane loading effects excited by $\overline{\eta_2(t)}$ for each panel design, and those curves normalized by the maximum lateral load effect experienced by each panel. Here, it is clear that the only noticeable differences between the six load curves is the y-ordinate, or the level of lateral loading effect. All the panels

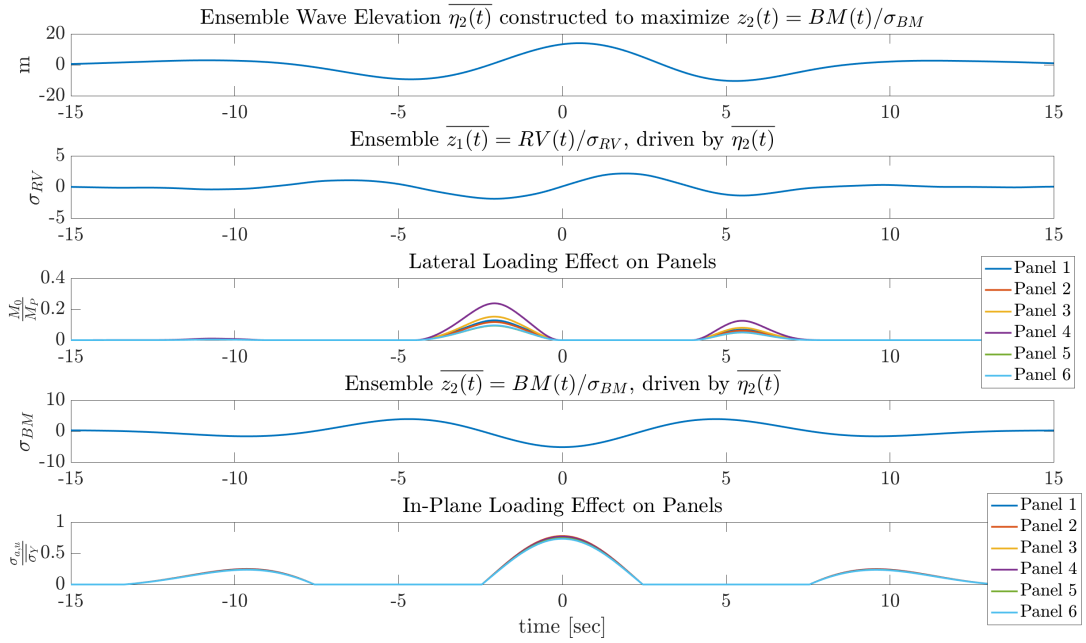

Figure 7.10: Ensemble wave elevation $\overline{\eta_2(t)}$ constructed to maximize $z_2(t)$, along with resulting time series of $\overline{z_1(t)}$ and $\overline{z_2(t)}$ driven by $\overline{\eta_2(t)}$. These time series are constant for all panels given a wave input. The lateral and in-plane loading effects due to the ensemble excitation $\overline{\eta_2(t)}$ are given for each panel.

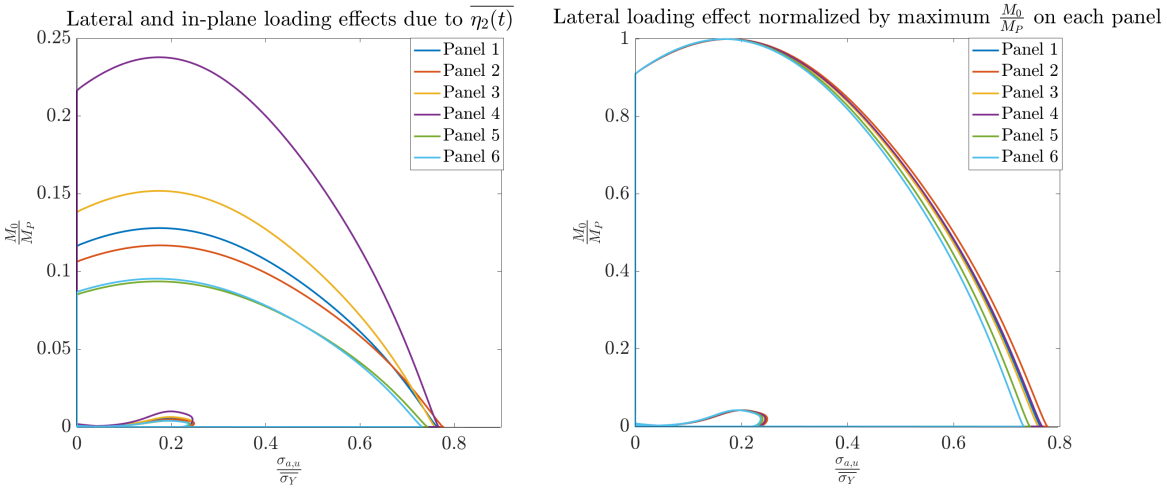

Figure 7.11: Vector of lateral and in-plane loading effects for each panel driven by $\overline{\eta_2(t)}$ (left) and the same loading effect time series normalized by the maximum experienced lateral loading effect for each panel (right).

experience about the same in-plane loading effects given the $\overline{\eta_2(t)}$ excitation input.

7.8.4 Load Effect Vulnerability Trends

Figure 7.12 shows the ensemble wave excitation $\overline{\eta_3(t)}$, and the resulting $\overline{z_1(t)}$, $\overline{z_2(t)}$, lateral, and in-plane loading effects due to this excitation. Although the $\eta_3(t)$ waves are constructed to maximize the equally weighted sum of relative velocity and bending moment, the same trends from Figures 7.8-7.11 are apparent. All panels experience the same level of in-plane loading effect given a common wave excitation, but different levels of lateral loading effect. Panel 4 experiences the harshest lateral loading effect, while panels 5 and 6 experience the least-harsh lateral loading effect given the same excitation.

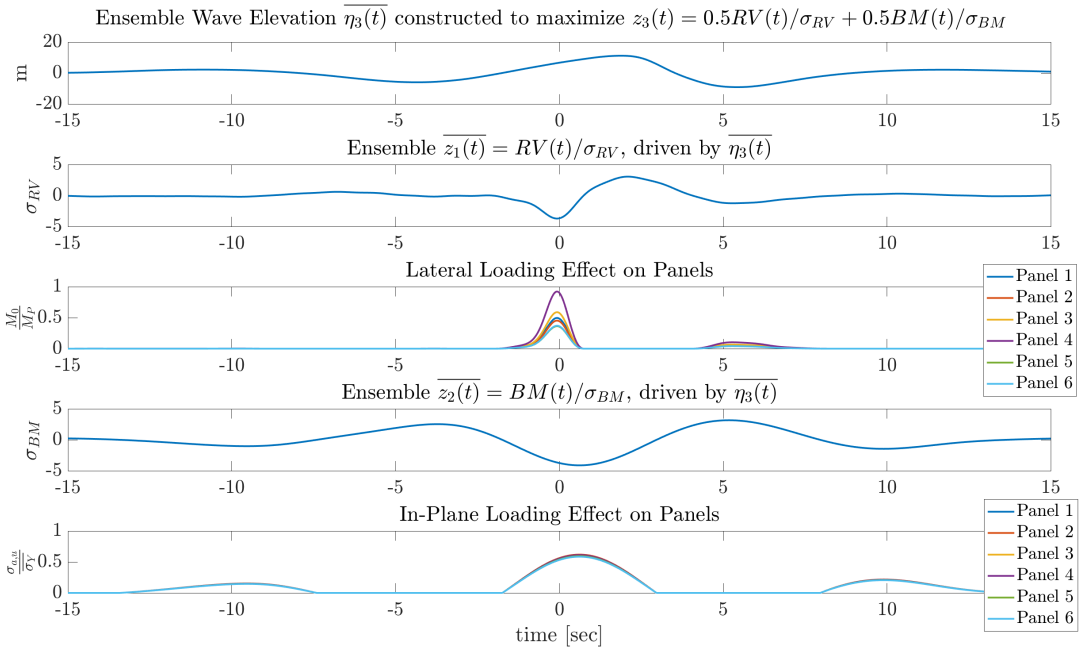

Figure 7.12: Ensemble wave elevation $\overline{\eta_3(t)}$ constructed to maximize $z_3(t)$, along with resulting time series of $\overline{z_1(t)}$ and $\overline{z_2(t)}$ driven by $\overline{\eta_3(t)}$. These time series are constant for all panels given a wave input. The lateral and in-plane loading effects due to the ensemble excitation $\overline{\eta_3(t)}$ are given for each panel.

Visual inspection of all the time series $\eta_i(t)$ $i = 1, 2, 3$ from the DLG confirmed these trends, indicating that the trends due to the ensemble waves $\overline{\eta_i(t)}$ $i = 1, 2, 3$ are representative of the trends due to all the wave records constructed by the DLG to excite the system. These trends may be related to the different performance characteristics of the different panels. The failure probabilities, ranked from highest to lowest, are associated with panels: 4 & 3 (tied), 1, 2, 5, and then 6. Note that the panel ranking by failure probability nearly mirrors the panel ranking by the harshness

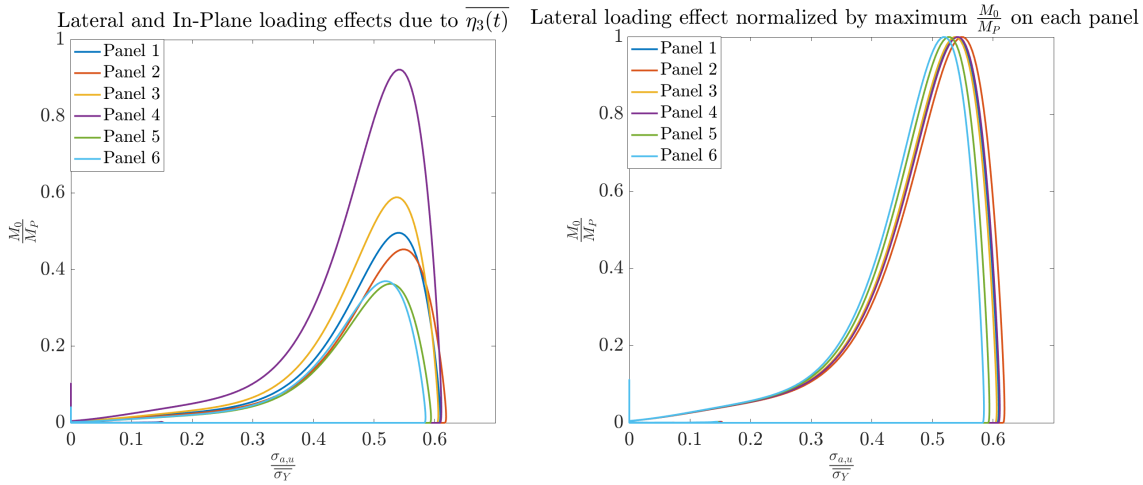

Figure 7.13: Vector of lateral and in-plane loading effects for each panel driven by $\overline{\eta_3(t)}$ (left) and the same loading effect time series normalized by the maximum experienced lateral loading effect for each panel (right).

of the lateral loading effect they experience, given a common wave excitation. Panel 4 experiences the harshest lateral loading effect and has the highest failure probability, while panels 5 and 6 experience the least-harsh lateral loading effect given that same excitation and have the lowest failure probabilities. This relation is interesting, but the loading effects must also be related to the failure surface definition for further understanding of the different panel performances based on the panel designs.

7.8.5 Failure Surface Vulnerability

Two interesting trends were observed for the different panel designs given the same wave excitation input: there is a clear magnitude ordering of how the panels experience lateral loading effect, and all panels experience nearly the same in-plane loading effect. These are interesting trends, especially when considered with the failure surface for each panel. Note that the failure surface separates what may be considered as a 'safe' area from the 'failure' area. The non-dimensional area contained by the failure surface, or the area of the safe region, is tabulated below for the failure surface for each panel design in Table 7.6 along with the failure probabilities for the panels.

Table 7.6 reveals an interesting trend related to the panel performances and the safe region area. The area of the safe region is generally inversely proportional to the failure probability for each panel design. Panels 5 and 6 have the largest safe regions given their failure surface definitions and have the lowest failure probabilities.

Panel	Area of Safe Region [units^2]	Failure Probability
1	0.4642	0.8738
2	0.4944	0.5916
3	0.4766	1.0000
4	0.4346	1.0000
5	0.5031	0.1192
6	0.5501	0.0288

Table 7.6: Area of the safe region and the probability of failure for each panel design.

Panel 4 has the smallest safe region and is tied for the largest failure probability. It is unsurprising that a smaller safe region area is related to a higher failure probability, and vise-versa, as the failure surface defines the level of loading a panel can bear before collapse. But the failure probability is related to the safe region area *and* the shape of the failure surface, which describes how the safe area is distributed across the possible loading combinations a panel may experience. Therefore, the 'safe' area of a failure surface may not be the most important driver for panel performance.

It was observed in Figures 7.8-7.13 that the panels all experience about the same level of in-plane loading effect for any wave excitation. The only major difference in the panel responses is related to the lateral loading effect that each panel experiences. Therefore, it may be interesting to compare the level of lateral loading effect required for a panel to fail, given a specific in-plane loading effect. This is, by definition, the failure surface, which defines the lateral loading effect as a function of the in-plane loading effect a panel can handle before collapse, or vise-versa. All of the failure surfaces for panels 1-6 are plotted in Figure 7.14. The middle inset of Figure 7.14 magnifies the region of the failure surface where $0 \leq \sigma_{a,u}/\overline{\sigma_Y} \leq 0.4$, and the right inset of Figure 7.14 magnifies the region where $0.4 \leq \sigma_{a,u}/\overline{\sigma_Y} \leq 0.85$.

Until the point $\sigma_{a,u}/\overline{\sigma_Y} \approx 0.37$, magnified in the middle inset of Figure 7.14, which is where the failure surface for panel 3 experiences a change in derivative, there is a constant ordering of the failure surfaces based on the lateral loading effect each panel can bear before failure, given an in-plane loading effect. In order from the largest lateral load effect a panel can bear before collapse to the smallest lateral load effect, given an in-plane loading effect up to $\sigma_{a,u}/\overline{\sigma_Y} \approx 0.37$, this is panel: 6, 5, 3, 2, 1, and then 4.

Panels 6 and 5, which can bear the largest lateral loading effect for a given in-plane loading effect before collapse, have the lowest failure probabilities of any panel design. As well, panel 4, which can handle the lowest value of lateral loading effect for a given

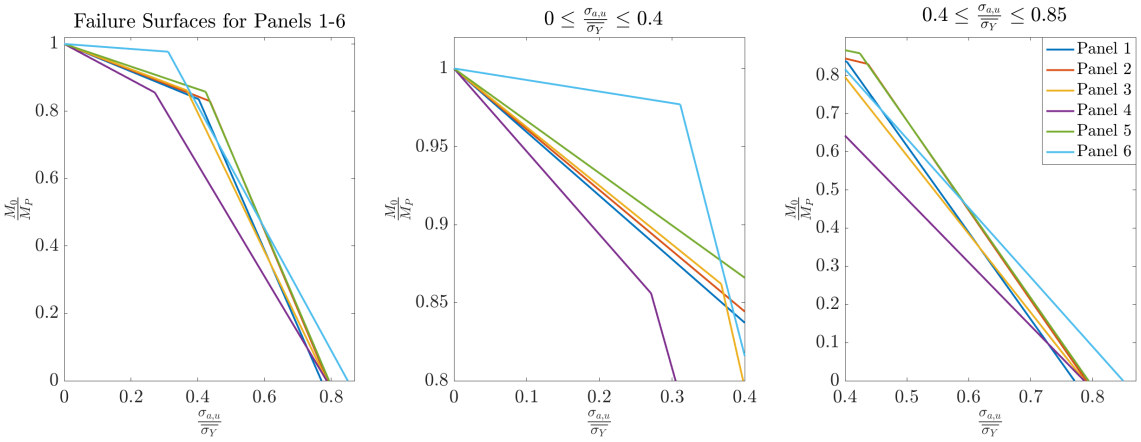

Figure 7.14: Failure Surfaces for panels 1-6 with different ranges of $\sigma_{a,u}/\overline{\sigma_Y}$ to highlight trends.

in-plane loading effect before collapse, has the highest (tied) failure probability. In fact, up to $\sigma_{a,u}/\overline{\sigma_Y} \approx 0.75$, the failure surface for panel 4 has the lowest lateral load effect value required for collapse, given an in-plane loading effect, of any panel design. This means that for any level of in-plane loading effect up to $\sigma_{a,u}/\overline{\sigma_Y} \approx 0.75$, panel 4 requires the lowest magnitude of lateral loading effect of any panel to fail.

As panel 4 experiences the largest lateral loading effect for a given wave excitation and requires the smallest lateral load effect to fail of all the panels given an in-plane loading effect, it is unsurprising that this design has the highest failure probability. It is difficult to elicit any trends related to the failure probability closer to the x-axis, mainly because it was shown that the panels all experience about the same level of in-plane loading effect given a wave excitation. Also, the failure surfaces do not maintain a ranking of the lateral loading effect required for failure given an in-plane loading effect closer to the x-axis, as seen in the right inset of Figure 7.14.

7.8.6 Lateral Loading Effect due to Global Panel Properties

Recall that the lateral loading effect experienced by each panel, given in Eq.(7.3), is proportional to the transformed moment of inertia, I_{tr}, and is inversely proportional to the distance to the neutral axis from the flange, Y_f, and the plastic hinge moment, M_P. These panel properties are given below in Table 7.7, along with the effective panel area, A_T, and probability of failure for each panel.

Considering the transformed moment of inertia, I_{tr}, there is a clear trend associated with the failure probability: a higher I_{tr} indicates a lower failure probability. Eq.(7.3) shows the lateral loading effect on a panel is proportional to I_{tr}, though

Panel	Transformed moment of inertia, I_{tr} [cm^4]	Distance to the Neutral Axis from Flange, Y_f [cm]	Plastic Hinge Moment, M_P [Nm]	Effective Panel Area, A_T [cm^2]	Failure Probability
1	2,543.6	13.50	9.4367e4	82.16	0.8738
2	2,817.1	13.21	1.0629e5	103.1	0.5916
3	1,926.4	12.50	7.3403e4	58.82	1.0000
4	949.99	8.79	4.8168e4	41.11	1.0000
5	4,664.5	20.23	1.1793e5	69.33	0.1192
6	5,385.3	16.28	1.3806e5	65.20	0.0288

Table 7.7: Panel properties relating to the lateral moment, along with the panel failure probabilities.

incorporating Eq.(7.1) indicates that the effect of the moment of inertia may cancel out, as the strain on the panel is inversely proportional to the panel moment of inertia normalized by the stiffener flange breadth. The distance from the neural axis to the flange, Y_f also loosely trends with the failure probability. A larger Y_f relates to panels with lower failure probabilities. As well, panels with lower failure probabilities have higher plastic hinge moments, M_P, which physically makes sense because M_P represents plastic bending, indicating the start of collapse.

It may be difficult though, to extend these trends to individual panel dimensions, as there may be no single panel dimension which is the major driver for panel performance. This is illustrated by comparing the panel effective area A_T with the failure probability. Panels 3 and 4, which have the lowest A_T, have the highest failure probabilities of all panels. However, the effective panel area may not be the sole driving factor for performance, as panels 5 and 6, which have the lowest failure probabilities, do not have the highest A_T values. Structural performance is clearly to the distribution of panel area (i.e. the moment of inertia), and not just the panel area.

This illustrates the challenge of identifying a single property which drives the panel performance. All properties affect both the loading effects a panel experiences given a wave excitation, and how a panel responds to those loading effects before collapse. These properties may be proportional to one loading effect, and inversely proportional to the other loading effect, making it difficult to relate failure probability trends to specific panel properties. One thing that is clear is that the panel responses diverge when considering the experienced lateral loading effect, and trends related to this loading effect became apparent when examining the load effects and failure surfaces separately. Some trends associated with global panel properties, like those in Table 7.7, were shown to have strong relations to the panel performance. This sort of information may be useful for designers to explain why some panels have a higher failure probability than others.

7.9 Panel Performance based on Web Frame Spacing

The NL-DLG process was able to compare the performance of panels 1-6, and these estimates are close to the MCS values. Section 7.8 showed that it may be difficult to pick a single panel property which drives the performance characteristics. However, one design parameter which may be a straight-forward indicator of panel failure probability is the web frame spacing, a. A larger web frame spacing relates to both a larger lateral and in-plane loading effect given a wave excitation (see Eq.(7.3) and (7.6)), implying that the web frame spacing should be proportional to the panel failure probability. Changing this design parameter may also be an easier design adjustment than changing other panel properties, which makes it an interesting factor to consider. It is important to be aware of how the design performance may change with varying web frame spacing, which could be changed by a designer to improve performance but may also be inadvertently altered during production or construction.

The NL-DLG process estimates the failure probability for the panels in Table 7.1 with a varying web frame spacing. The probability of failure estimated by the NL-DLG process for each panel over the 1000-hour exposure, given a specific web frame spacing and the operating profile in Table 7.2, is shown in Figure 7.15. To calculate the probability of failure for each web frame spacing for all of the panels, the computation time is about 3 minutes. No new DLG simulations need to be run, since these time series are generated based on the operating profile and vessel geometry, not the panel design. Only the failure surface definition, and the non-linear transformations of the wave excitation to the lateral and in-plane loading effects changes with an altered design. The same wave excitation inputs constructed by the DLG excite the lateral and in-plane loading effects to determine the updated failure probability.

The non-constant decrement in the web frame spacing is due to seeking different levels of refinement in Figure 7.15 to capture where the failure probability for each panel starts to change given a different a. Figure 7.15 reveals stark changes in the stiffened panel failure probabilities with varying web frame spacing, though not all panels are as sensitive to this design change as others. Panels 5 and 6 have lower failure probabilities overall for the varying web frame spacing, and do not exhibit any sharp changes for the range of a shown. Panel 4 appears insensitive to the reducing web frame spacing until crossing the $a = 1.45$ m threshold, where the failure probability drops sharply. In fact, panels 1-4 all exhibit a sharp drop in failure probability at some web frame spacing threshold. This means that a potentially small design change may

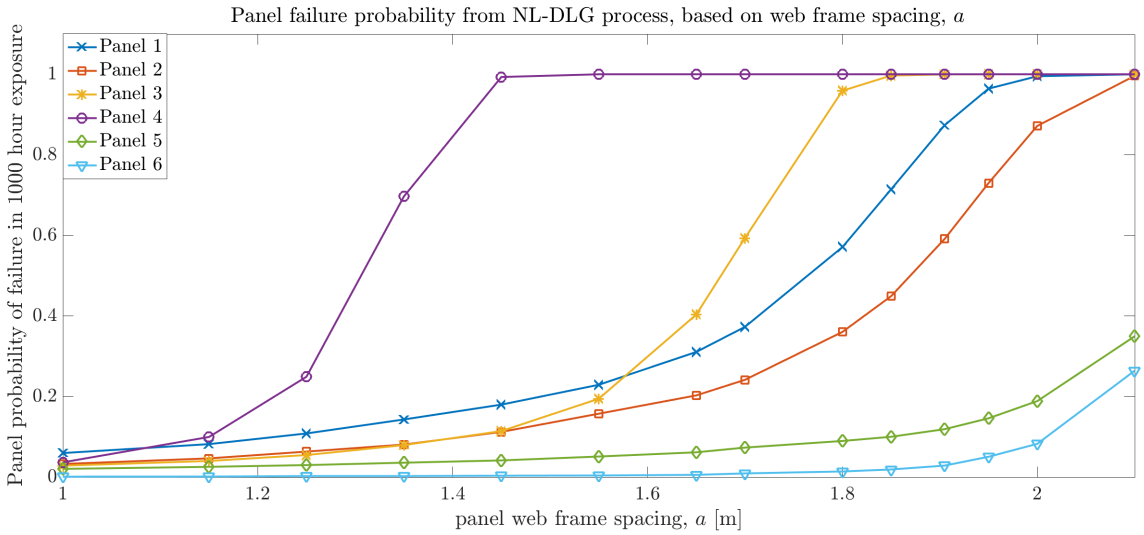

Figure 7.15: Probability of failure for each panel over the 1000-hour exposure, given a specific web frame spacing and the operating and environmental conditions in Table 7.2. Note that the web frame spacing specified by the ISSC report is $a = 1905$ mm, which gives the panel failure probabilities in Table 7.5.

result in a drastically different panel performance. A designer may take advantage of this by realizing that only a small change in web frame spacing is required to decrease the panel failure probability to a more acceptable level. However, the inverse is also true − failure probability can increase drastically by a small increase in the web frame spacing, which a designer may not recognize as an important change.

The estimate of most-likely failure occurrences for each panel, given a web frame spacing, is also quickly assembled by the NL-DLG process. Figure 7.16 gives this estimate for web frame spacing $a = 1.25$ m, and Figure 7.17 gives this estimate for $a = 1$ m. Figure 7.2 gives this estimate for $a = 1.905$ m, which is the original web frame spacing specified by the ISSC report. Note that as the web frame spacing decreases, the failure probability decreases and the failure occurrences move closer to the x-axis. This indicates that decreasing the web frame spacing has a favorable effect on the panel performance, and specifically seems to target failures due to large lateral loading effects. A smaller web frame spacing means fewer failures due to large lateral loading effects.

Again, the overall trend relating the web frame spacing and the panel failure probability can be examined by considering the effect of a on the failure surface definition, and the loading effects separately.

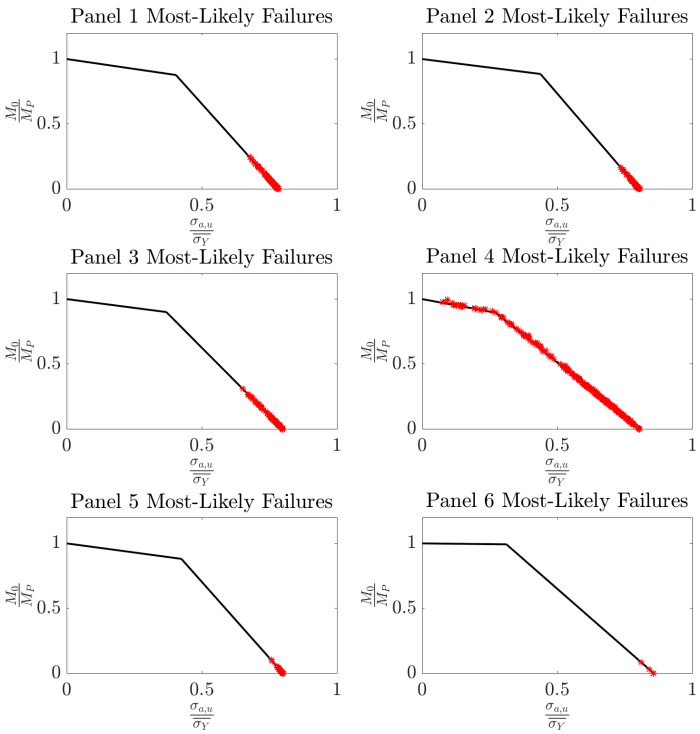

Figure 7.16: Most-likely failure occurrences for panels with web frame spacing $a = 1.25$ m.

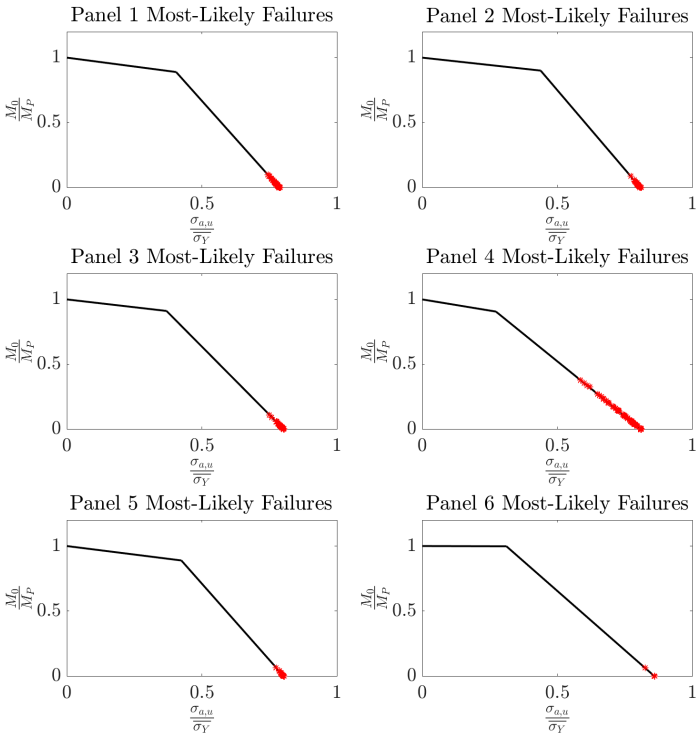

Figure 7.17: Most-likely failure occurrences for panels with web frame spacing $a = 1$ m.

7.9.1 Failure Surface based on Web Frame Spacing

Given a different web frame spacing, a panel will have a different failure surface. As a representative example, Figure 7.18 shows the failure surface for panel 4, for different values of web frame spacing, a, zoomed in to highlight the trends. For this panel, decreasing the web frame spacing, a, marginally changes the failure surface by shifting it farther away from the origin (i.e. increasing the safe area enclosed by the failure surface). This trend is observed for the failures surfaces for all the panel designs and confirms the trend that for a smaller web frame spacing, all panels have a lower failure probability. However, Figure 7.18 shows that the panel failure surfaces do not drastically change given a different web frame spacing, indicating that this factor alone may not account for the strongly diminishing failure probabilities given smaller web frame spacing, seen in Figure 7.15.

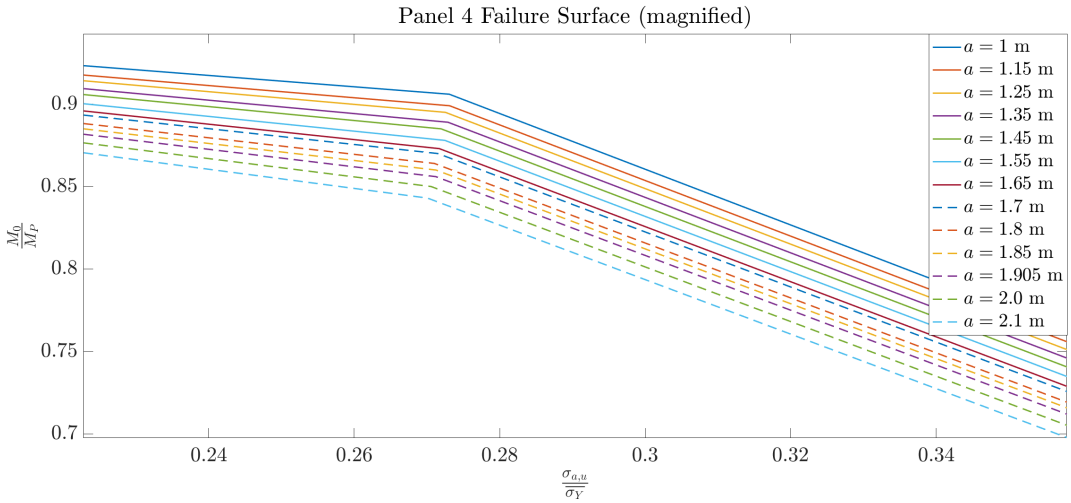

Figure 7.18: Failure surface for panel 4, for different values of web frame spacing, a. The figure is magnified and focused on a specific area to highlight the trend, which is maintained over the entire failure surface. This trend is also seen for the other panel failure surfaces.

7.9.2 Lateral & In-Plane Loading Effects based on Web Frame Spacing

It was observed in Figures 7.8-7.13 that the different panel designs all experience about the same in-plane loading effect given a wave excitation, but very different lateral loading effects. Here, it is examined whether changes in the web frame spacing have a strong effect on the lateral and in-plane loading effects experienced by a panel, given a wave excitation input. As a representative example, consider Figure 7.19. In this figure, panel 4, with varying levels of web frame spacing, is excited by the

ensemble wave $\overline{\eta_1(t)}$. For this panel, given an excitation input, the experienced in-plane loading effect is not noticeably different for the varying web frame spacing, which matches the trends from Figures 7.8-7.13. However, the experienced lateral loading effect given a wave excitation changes significantly for different web frame spacing.

This specific example is shown for two reasons. The intent is to determine any trends between the web frame spacing of a panel design and the experienced lateral loading effect. It has already been observed that panels 1-6 all experience about the same in-plane loading effect given a wave excitation. First, the ensemble wave elevation $\overline{\eta_1(t)}$ is chosen to excite the system because this wave is constructed to maximize the vessel relative velocity, leading to large lateral load effect values. It will be easier to determine any trends given the lateral load effects are large to begin with. Second, panel 4 is examined with varying values of web frame spacing because this panel experiences the largest lateral load effect of all panels given a wave excitation. Again, this will make it easier to notice any trends between the web frame spacing and the experienced lateral load effect. The curve for $a = 1.905$ m is the time series vector of lateral and in-plane loading effects experienced by panel 4, with dimensions in Table 7.1, given the input $\overline{\eta_1(t)}$, as shown in Figure 7.9.

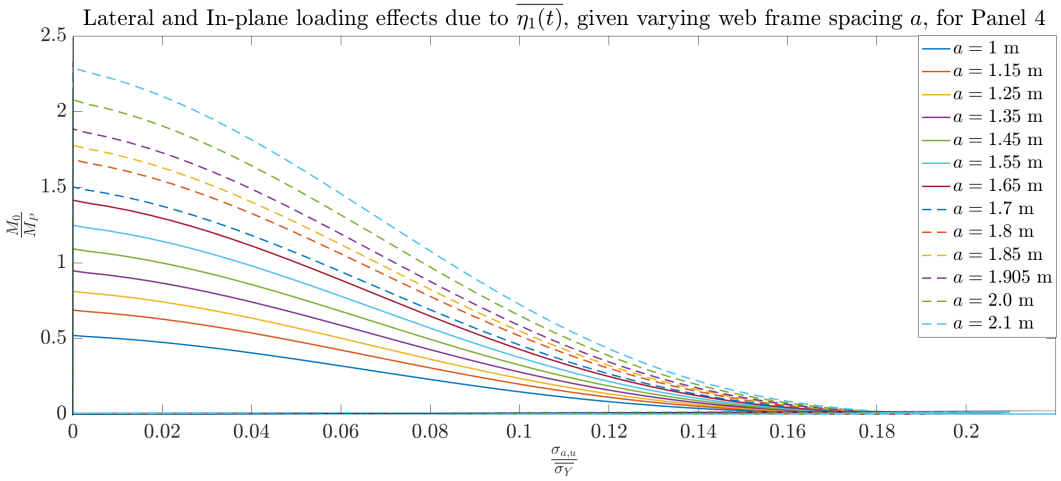

Figure 7.19: Lateral and in-plane loading effects experienced by panel 4 for different values of web frame spacing, a.

Figure 7.19 shows a clear trend between the web frame spacing for a panel design and the experienced lateral loading effect, given a common wave excitation. Panel 4 with the smallest web frame spacing experiences the smallest lateral loading effect,

which increases as a increases. This trend was similarly observed using all other panel designs, and the ensemble waves $\overline{\eta_2(t)}$ and $\overline{\eta_3(t)}$.

7.10 Design Implications

Figures 7.18 and 7.19 imply that a smaller web frame spacing, a, results in both smaller lateral loading effects, and a failure surface with a larger safe region. Together, these trends indicate that a smaller web frame spacing leads to a lower failure probability, which is reinforced by the results in Figure 7.15. Figures 7.18 and 7.19 are able to explain this trend, giving valuable insight about a panel property that strongly affects the panel performance. Using the NL-DLG process to examine these panels explains why certain panel designs are more susceptible to failure.

The ability to generate this sort of information is useful for designers, because different panel design aspects can be examined using wave records which are statistically possible excitations to the system. It would be difficult to determine these trends from brute-force MCS without significant computational expense and effort. Since the NL-DLG process starts with ensemble wave structures which are expected to lead to extreme system responses, there are clear links between wave excitation, experienced loading effects, system response, and overall performance. This allows the control of different aspects, like the failure surface definition and the load effects driven by ensemble wave excitation profiles, to reveal trends relating panel properties and panel performance.

Given that MCS test the system for the full exposure, which is long, the temporal ensemble average of many MCS will likely show no correlation. This would preclude any possibility of examining system trends due to ensemble wave structures which lead to extreme responses. Even if these MCS were examined to focus solely on times when failures occur, it is likely no correlation would be noticed between the excitation inputs. The NL-DLG process showed that there are multiple excitation input forms (i.e. $\overline{\eta_1(t)}$, $\overline{\eta_2(t)}$, and $\overline{\eta_3(t)}$) which can lead to panel failures. But without an explicit definition of the ensemble waves which excite the system, it might not be possible to determine the trends found by the NL-DLG process.

Overall, the capabilities afforded by the NL-DLG process allow designers to better understand stiffened panel collapse, and different aspects of panel designs which make a panel more vulnerable to failure. This can help assess whether designs are sufficiently robust and can lead to better-performing systems.

CHAPTER VIII

Probabilistic Assessment of Combined Loading on Trimarans

Combined loading presents formidable challenges to the design of multihulls. Without the canon of anecdotal knowledge, legacy designs, and test data that benefits monohull design, significant concerns around multihulls remain open-ended questions. In Lloyd's Register's *Rules for the Classification of Trimarans,* two procedures are offered to design load combination cases to ensure that the "hull structure complies ... with the [LR] acceptance criteria" (*Lloyd's Register*, 2017). Seven cases are constructed to examine seven global loads acting on the trimaran hull. Each case is associated with a specific loading combination, conditioned on a single global load being maximized, to be applied to a FEA model to test structural adequacy given LR's acceptance criteria. In the rule load approach, seven standard load cases are given which apply to any trimaran within a specific geometry range. In the alternative load procedure, these seven cases are constructed using a deterministic Equivalent Design Wave (EDW) methodology tailored to the trimaran hull in question.

The load combinations from either the rule load or the alternative load approach, though, do not explicitly include probabilistic aspects apart from the underlying LR Rule assumption (20-year load return period, or probability of exceedance at 10^{-8}). Given that the small number of load combination cases is a "practical attempt to reduce the number of load cases to a reasonable number," it is not clear whether these cases are exhaustive; nor is the degree of conservatism apparent. This chapter conducts a probabilistic assessment of the lifetime combined loading on a trimaran hull and the applicability of the two load procedures using the NL-DLG process.[1]

[1]Portions of this work were previously published in *Seyffert et al.* (2018b). The author gratefully thanks Navatek for supplying the trimaran hull form and parameters, and running Aegir to produce

8.1 Lloyd's Register Combined Loading Rules for Trimarans

Lloyd's Register (2017) specifies that seven load combination cases should be constructed as testing cases to determine whether the "longitudinal, transverse, and shear strength of the hull structure complies with the acceptance criteria." The coordinate system used by LR and the NL-DLG analysis to evaluate combined loading on a trimaran is given in Figure 8.1:

$$
\begin{aligned}
M_{WH}/M_{WS} &= \text{hogging/ sagging vertical wave bending moment} \\
M_{SPH}/M_{SPS} &= \text{hogging/ sagging splitting bending moment} \\
M_{LT} &= \text{longitudinal torsional bending moment} \\
M_{H} &= \text{horizontal bending moment} \\
M_{TT} &= \text{transverse torsional bending moment}
\end{aligned}
$$

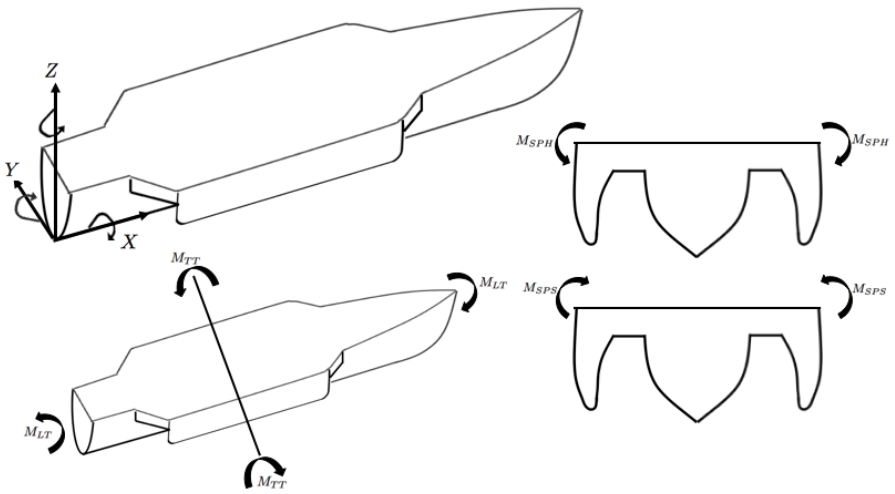

Figure 8.1: Coordinate system of trimaran hull used in this chapter. The arrows indicate positive directions of the specified loads. The vertical wave bending moment, M_{WH}/M_{WS}, is the wave pressure distribution integrated across the depth of the ship and the horizontal bending moment, M_H, is the pressure distribution integrated across the breadth of the vessel.

8.2 Applicability of Load Procedures to a Specific Trimaran

The major question that arises from the definition of the two LR loading procedures is what, if any, probabilistic basis exists to justify the load cases when applying

the transfer functions used in this chapter.

these loads to a specific trimaran hull. Regardless of whether the rule load or alternative load procedure is utilized, seven load combination cases will be defined, with each load described by a single representative value. However, individual values may not accurately describe the distribution of load responses possible due to an irregular wave environment over a long exposure. It is also unclear how conservative or exhaustive the load combination cases are, defined by either the rule load or alternative load procedure. As well, the standard LR load cases may not be fully applicable for all hull forms, and an EDW approach may not completely capture the complex load phasing relationships for a trimaran.

To address the validity of these concerns, the DLG is used to assemble distributions of lifetime loading for a specific trimaran hull form. These DLG distributions, normalized by the load design values, are directly comparable to the load cases described by the LR rule load and alternative load procedure. The DLG assembles wave profiles constructed to lead to an exposure-period-maximum of a specific global load and these wave profiles then can drive the other global loads included in a specific case to assemble load distributions. This allows a direct comparison to the LR rule and alternative load cases, as the simultaneous values of all global loads in a specific case, conditioned on a specific maximized global load, are determined by the DLG.

8.2.1 Trimaran Specifications

The trimaran hull considered in this chapter has the lines plan given by Figure 8.2 and the hull specifications given in Table 8.1. The linear version of the high-order potential flow code, Aegir, is used to generate transfer functions of multiple loads at the planes indicated in Table 8.1, with respect to the coordinate frame in Figure 8.1 (*Kring et al.*, 2004). Aegir generates transfer functions of the global loads from Table 8.3 at the planes indicated in Table 8.1, with the relationship between the loads and load planes given in Table 8.2. The transfer function non-dimensional amplitudes and phases are shown in Figures 8.3-8.5. For the vertical wave and splitting bending moments, only the hogging conditions are plotted. The sagging conditions have the same amplitudes, with phases 180° out of phase with the hogging phases.

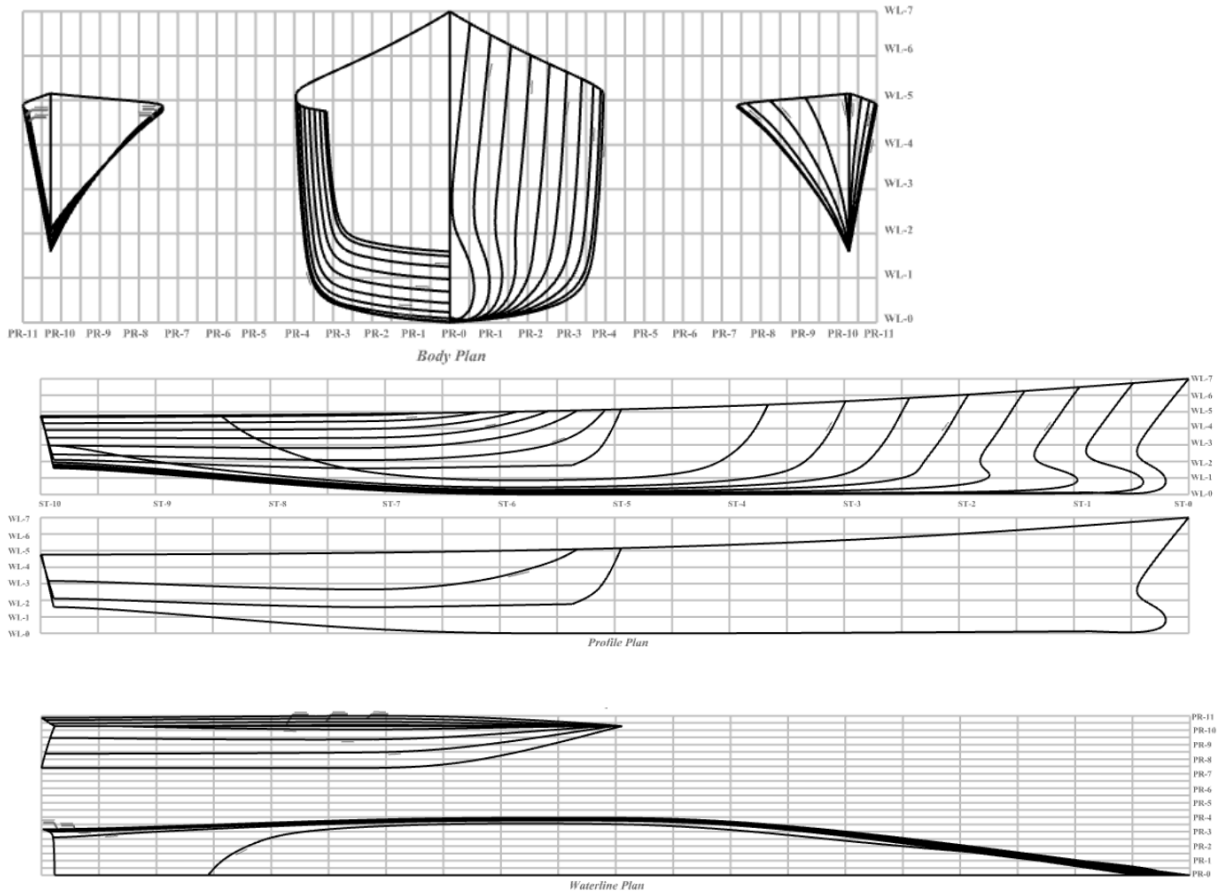

Figure 8.2: Lines of trimaran hull (*Knight et al.*, 2017).

Parameter	Value
Hull overall length (LOA)	110.0 m
Hull waterline length (L)	106.4 m
Total Draft	4.897 m
Beam	30.48 m
Origin of midship load plane [x,y,z]	[45.14, 0, 3.0] m
Origin of center-hull load plane [x,y,z]	[26.75, 5.48, 3.0] m
Water density	1026.06 kg/m^3
Vessel mass	3,301,440 kg
Number of wave frequency components	100
Speed (Froude Number)	12.803 m/s (0.4)

Table 8.1: Vessel & Aegir simulation specifications. Note that the [x,y,z] origins of the midship and center-hull planes are with respect to the coordinate frame given by Figure 8.1.

Load	Transfer Function
M_{WH}/M_{WS}	midship vertical bending
M_{SPH}/M_{SPS}	center-hull vertical bending
M_{LT}	midship torsional bending
M_H	midship horizontal bending
M_{TT}	center-hull torsional bending

Table 8.2: Transfer Functions of Loads from Table 8.3.

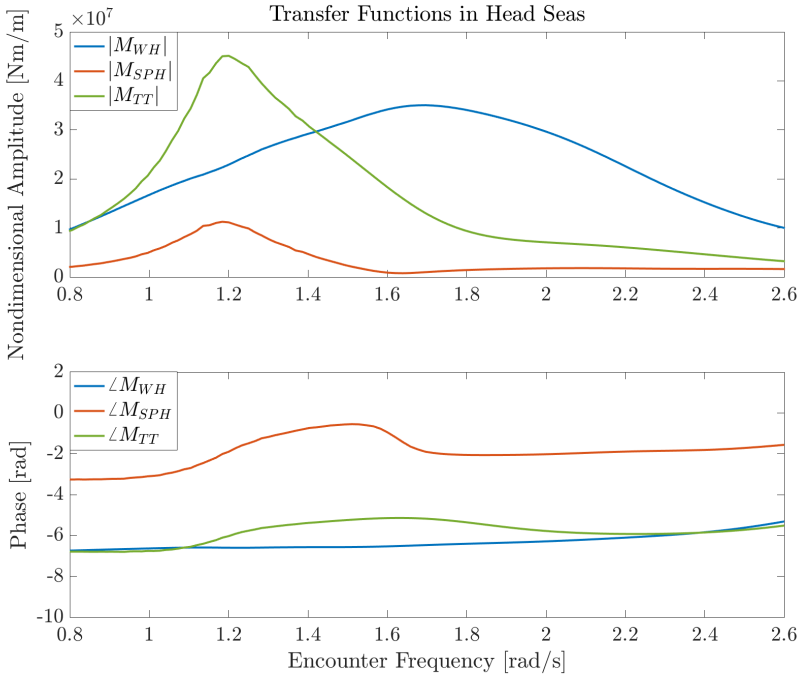

Figure 8.3: Head seas transfer functions.

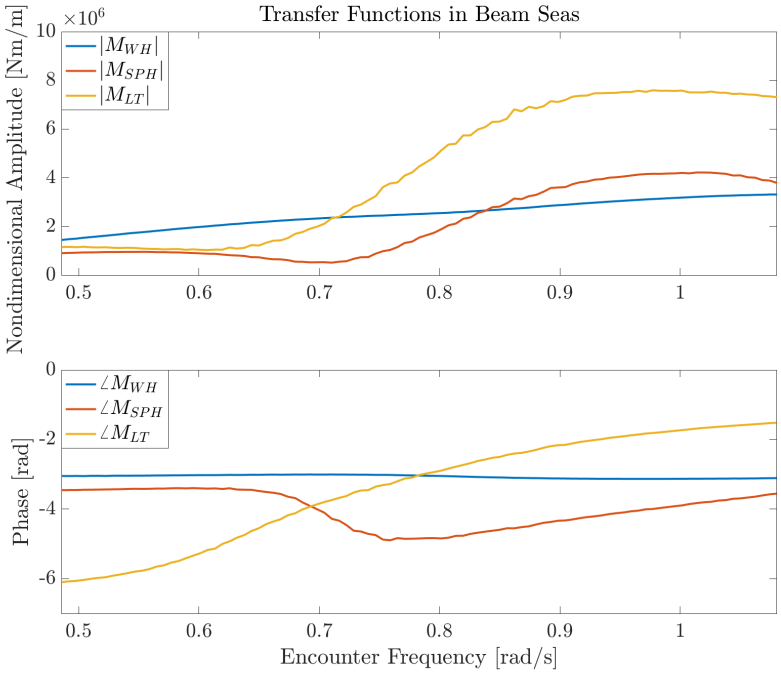

Figure 8.4: Beam seas transfer functions.

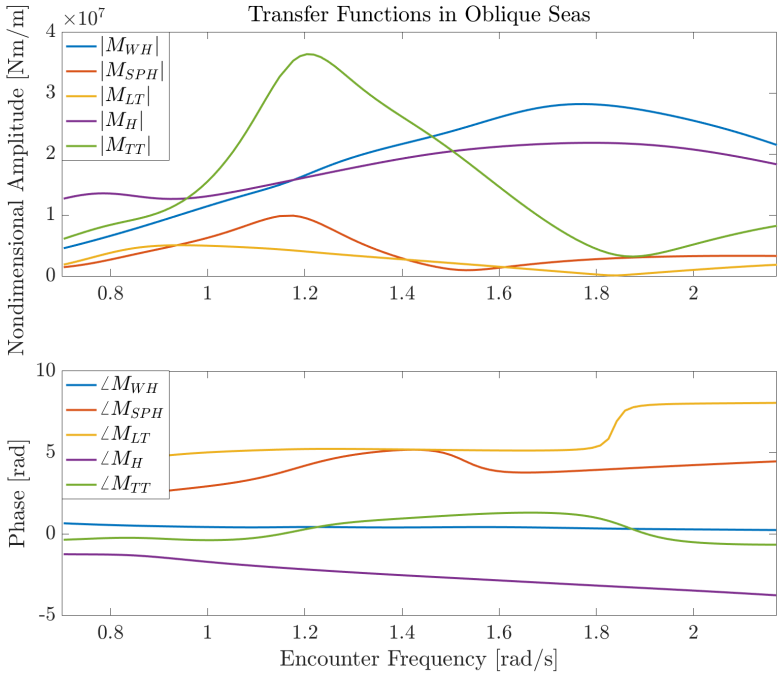

Figure 8.5: Oblique seas transfer functions.

8.3 Development of Rule Load Cases

The rule load combination cases defined by Lloyd's Register are designed so that in each case, a single global load is maximized in the specific heading where the load (presumably) experiences its largest value. Some of the other global loads have an acting component as well, which are also included in the load case. Each standard case is developed using the Equivalent Design Wave approach (*Blanchard and Ge*, 2007). This design wave is a regular wave which leads to a response with a given long-term design value. The design value is defined as the largest value a load experiences over the exposure, associated with the given probability of exceedance, 10^{-8}. The seven cases give specific load combinations to test structural adequacy; in each case a single global load on the trimaran is maximized. These cases include head, beam, and oblique seas headings.

Seven standard load combination cases are defined by LR, shown in Table 8.3. The total loading that the trimaran structure must survive is the sum of the dynamic loads (within the respective planes), as a percentage of the respective design value. A load combination factor, or LCF, indicates the percentage of the design value that a load experiences in a specific case. The loading condition from each case is to be applied to a FEA model to determine whether the structural performance is adequate.

Case & Heading	M_{max}	Dynamic Loads						
		M_{WH}	M_{WS}	M_H	M_{SPH}	M_{SPS}	M_{LT}	M_{TT}
1) Head	M_{WH}	1.0	0	0	0.3	0	0	-0.2
2) Head	M_{WS}	0	1.0	0	0	0.3	0	-0.2
3) Beam	M_{SPH}	0.1	0	0	1.0	0	0.2	0
4) Beam	M_{SPS}	0	0.1	0	0	1.0	0.2	0
5) Oblique	M_{LT}	0	0	-0.3	0.4	0	1.0	0.3
6) Oblique	M_H	0	0	1.0	0.4	0	0	-0.2
7) Oblique	M_{TT}	0	0.2	-0.2	0.6	0	0	1.0

Table 8.3: Rule load cases, along with heading and load combination factors (LCF) defined by *Lloyd's Register* (2017). The maximized load, M_{max}, is also noted for each case.

Note that for load cases in which the LCF is negative (i.e. $LCF_{M_{TT}}$ is negative in Cases 1, 2, and 6, and LCF_{M_H} is negative in Cases 5 and 7), the negative sign indicates the component is "considered reversible." To analyze these rule load combination cases, hogging moments are considered positive and sagging moments are considered negative, as with the LR coordinate system in Figure 8.1. Any LCF value which relates to a sagging moment corresponds to a negative value, whereas the negative

"reversible" LCF values given in Table 8.3 are considered positive in the assessment.

It is important to note that these rule load cases are not meant to be tailored to a specific trimaran hull. LR calls the cases in Table 8.3 "standard load cases," and indicates that the acceptance criteria due to the application of all of these cases is "for all structure." It is implied by *Blanchard and Ge* that these load combination cases are based on the analysis of "21 trimaran variants." The authors do say that the rules are applicable for length ranges between $70-250$ m and for trimarans whose individual side-hull maximum displacement is less than 6% of the total displacement. The LR rules do allow an "alternative procedure for load development" (Vol. 4, Part 1, Ch. 3, Sec. 4.2), in which the EDW method designs load combination cases tailored for a specific trimaran hull. However, the Lloyd's Register rules indicate that the rule loads procedure, which involves the standard load combination cases from Table 8.3, is an acceptable approach (Vol. 4, Part 1, Ch. 2, Sec. 3.2.2).

This brings up an important question, that being: are these standard load combination cases applicable for every trimaran hull form? Or, do these LCF values from LR accurately describe the lifetime combined loading experienced by all trimaran hulls? As these load cases and LCF values are meant to test structural adequacy, they should be both conservative and exhaustive, although it is possible that Lloyd's Register encodes conservatism in the acceptance criteria for the structural adequacy *given* the application of these loading combination cases.

Whether these standard cases prove applicable and realistic can be considered by comparing distributions of the loads on a specific trimaran hull assembled by the DLG with the combined load levels suggested by the LR rule load cases. Then the NL-DLG process can give a probabilistic assessment of these rule load cases applied to that trimaran hull to evaluate the conservatism and exhaustiveness of the load cases. It will be interesting to compare the rule LCF values from LR with distributions constructed by the DLG. The LR rules do note that the vessel response, and corresponding LCF values, may vary for different trimaran hulls, specifically that the fore-aft placement of the side-hulls can have a major impact. This may lead to a significant difference in the observed combined loading on a specific trimaran hull.

8.4 Design Value Specification

The LR rules reference *Standard Wave Data*, *IACS Rec. No. 34* (2001), for the determination of design values. Based on this recommendation, a load design value

is determined by the 20-year return-period load response (corresponding to 10^8 wave encounters) in a North Atlantic environment defined by a Bretschneider spectrum. It is assumed that all wave headings have an equal probability of occurrence. The Lloyd's Register rules stipulate that the evaluation of a long-term load response be based on a design value with an overall 10^{-8} probability of exceedance in any heading.

8.4.1 Operational Profile

An operation profile is assigned to match the LR specifications in Table 8.4. To satisfy the overall required 10^{-8} probability of exceedance criterion for each load specified by Lloyd's Register, the risk parameter α is applied, as demonstrated by Eq.(2.16)-(2.18) in Chapter 2.2. From the spectrum definition and the *Standard Wave Data* specifications, the probability of the sea state occurrence is defined, leading to a 7.71-hour exposure out of the 20-year lifetime. The design value of each load is then the maximum linear load value in any heading in the 7.71-hour exposure in the given sea state, with a probability of non-exceedance $= 1-\alpha = 0.9998$. This criterion leads to the required overall load probability of exceedance 10^{-8}. Each heading is given the full 7.71-hour exposure to lead to a more conservative estimate, as directed by the LR rules.

Parameter	Value
Spectrum type	Bretschneider (H_s & T_z)
Significant Wave Height H_s	12.5 m
Zero-Crossing period T_z	9.5 s
Probability of sea state occurrence (*IACS Rec. No. 34*, 2001)	4.4e-5
Lifetime of vessel	20 years
Total exposure of vessel in given sea state	7.71 hours
Risk parameter α	2.27e-4
Probability of Non-exceedance PNE $= 1-\alpha$	0.9998
Overall load probability of exceedance	10^{-8}

Table 8.4: Operation Profile (North Atlantic).

It is important to note that this overall load probability of exceedance (10^{-8}) defined by LR seems to be based upon "the number of low stress reversals that might occur on a period of 20 years" (*Blanchard and Ge*, 2007), which is a long-term estimate based on all sea states and operational conditions. A design value could be defined as the most-probable maximum in 7.71 hours (out of the 20-year service life), but the maximum load in 7.71 hours has approximately a 63.2% chance of exceeding

this design value (see Chapter 2.2). This makes necessary the addition of the risk parameter, α, to achieve the required 10^{-8} probability of exceedance. However, it is not clear how to relate a short-term analysis, like that performed here, to the long-term analysis parameters defined by LR. Without applying a risk parameter, α, the analysis would be unacceptably non-conservative, while the risk parameter α =2.27e-4 might be extreme.

Ochi (1981) acknowledges the difficulty of choosing an appropriate risk parameter for a short-term analysis to relate to long-term parameters. *Ochi* uses the example of a vessel designed using an extreme design value in a given sea state, associated with $\alpha = 0.01$, and notes that if the vessel is expected to encounter that sea severity 20 times during its lifetime, α must be divided by 20 to maintain the 99% criteria. Considering extreme midship bending moments of the MARINER-type ship (*Russo and Sullivan*, 1953) *Ochi* finds that "design extreme values do not increase substantially with increasing $\alpha-$value," and concludes that a short-term approach can be adequate for the estimation of extreme values as long as the difference in the number of encounters is considered. This in some ways indicates that the choice of α is ambiguous. However, the DLG method and the NL-DLG process are valid for any choice of α, which is likely to be set by classification societies as empirical data is collected. Therefore, the risk parameter α =2.27e-4 will be used, as given in Table 8.4.

8.4.2 Trimaran Load Design Values

The design values R based on the operation profile in Table 8.4, conditioned on heading, and associated with α =2.27e-4 are given in Table 8.5, along with the heading in which the true (i.e. largest) design value occurs. Note that these headings do not necessarily line up with the LR rule load cases given in Table 8.3. For example, M_{SPH}/M_{SPS} is predicted to experience its maximum value in beam seas, by LR Cases 3-4, but the design value for M_{SPH}/M_{SPS} occurs in oblique seas for this hull. This already is an important consideration. Based on the vessel geometry, the load transfer functions will vary, meaning that the rule load cases may assume a particular load is maximized in a certain heading, when in reality, the design value occurs in a different heading. This indicates that the standard rule load combinations suggested by LR may not be 'one size fits all' for evaluating different trimarans.

Load	Head Seas	Beam Seas	Oblique Seas
M_{WH}/M_{WS}	**4.311e8 Nm**	3.993e7 Nm	3.090e8 Nm
M_{SPH}/M_{SPS}	9.054e7 Nm	3.551e7 Nm	**9.159e7 Nm**
M_{LT}	–	**7.264e7 Nm**	5.879e7 Nm
M_H	–	–	**2.829e8 Nm**
M_{TT}	**4.224e8 Nm**	–	3.509e8 Nm

Table 8.5: Design values for loads in all headings associated with a $PNE = 0.9998$. The values in bold-face are the largest design value seen in any heading; these are R. Note that "–" indicates no transfer function was constructed for a load in a particular heading.

8.4.3 TEV of Combined Loads

With the DLG, it is necessary to define the exposure, which dictates the rareness of the distribution of extreme values. This exposure is captured by the target extreme value, or TEV. Using the notation of Eq.(2.7)-(2.18), the TEV for the maximized load, M_{max}, TEV_{max}, is defined in Eq.(8.1), where σ_{max} is the standard deviation of the load, M_{max}. Here, the extreme load value, $\widehat{y}_n$, associated with the risk parameter, α, is used to define TEV_{max}:

$$TEV_{max} = \frac{\widehat{y}_n}{\sigma_{max}} \tag{8.1}$$

$TEV_{max}\sigma_{max}$ is the design value for the maximized load, M_{max}. The DLG constructs an ensemble of short wave time series that lead to a distribution of responses for the maximized load, M_{max}, where the $TEV_{max}\sigma_{max}$ event (e.g. a 5σ event) is the most probable. This distribution follows the Gaussian extreme value distribution as given in Eq.(2.7) which satisfies Eq.(2.16)-(2.18).

8.5 Assessment of Rule Load Case Applicability using the DLG

This section assesses the applicability of the standard rule load combination cases offered by LR in a qualitative sense. Based on the ambiguity of the choice of risk parameter α, it is not constructive to compare dimensional loading values found in this analysis to those that LR would indicate. Therefore, this section compares the relative distributions of loads, not specifically load magnitudes.

For each load case in Table 8.3, the DLG constructs an ensemble of wave inputs that lead to a distribution of responses for the maximized load, M_{max}, about the most probable $TEV_{max}\sigma_{max}$ event. $TEV_{max}\sigma_{max}$ is the design value conditioned on

heading, given in Table 8.5. This design value corresponds to the maximum load value in 7.71 hours, with the specific heading from Table 8.3, in the sea state out of the 20-year exposure, with an overall probability of exceedance of 10^{-8}, calculated by Eq.(2.16)-(2.18) and (8.1). These wave input time series are all representative of the operation profile spectral definition, and time series of all loads due to those wave inputs are constructed. At the time of the maximum value of the maximized load, each load is normalized by its respective design value R (Table 8.5), which gives the load normalized as a LCF.

8.5.1 Head Seas, Cases 1-2

The load histograms, normalized as probability distributions, constructed by the DLG for Case 1 are shown in Figure 8.6. Case 2 DLG distributions look the same, except are reflected across $LCF = 0$, since all the transfer functions are linear. The vertical lines are the rule LCF values indicated by LR for each load. While $LCF_{M_{WH}/M_{WS}}$ follows a typical extreme value *pdf*, the other loads are more normally distributed. The most probable values of the $LCF_{M_{SPH}/M_{SPS}}$ and $LCF_{M_{TT}}$ distributions from the DLG are significantly different than the rule LCF values from LR, both in relative ordering and relative value.

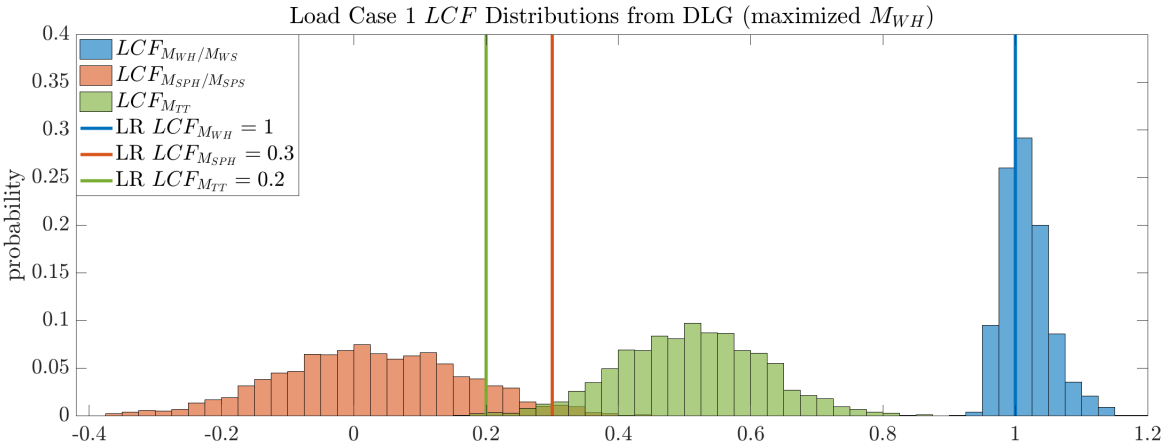

Figure 8.6: Empirical histograms, normalized as probability distributions, of LCF values from the DLG for Case 1, compared with the rule LCF values reported by LR in Table 8.3. For Case 2 (not plotted), all distributions are reflected across $LCF = 0$.

8.5.2 Beam Seas, Cases 3-4

The load histograms, normalized as probability distributions, assembled by the DLG for Case 3 are shown in Figure 8.7. Case 4 distributions are reflected across $LCF = 0$. Again, the vertical lines are the rule LCF values indicated by LR for the appropriate load. Recall that although the maximized load for Case 3 is the hogging splitting moment, M_{SPH}, the design value for M_{SPH} for this trimaran occurs in oblique seas, not in beam seas. That is why the distribution of $LCF_{M_{SPH}}$ is not centered around $LCF = 1$. The splitting moment does not achieve its design value in beam seas. Even though the DLG is constructing wave environments which lead to exposure-period-maxima of M_{SPH}, these maxima are not as large as they would be if the DLG constructed waves in oblique seas meant to maximize M_{SPH}. This trimaran experiences about 40% of the largest possible splitting moment (i.e. design value) in beam seas. Conditioned on maximum splitting moments, the distribution of $LCF_{M_{WH}/M_{WS}}$ from the DLG is significantly lower than predicted by the LR rules. The conditioned distribution of $LCF_{M_{LT}}$ from the DLG is significantly larger than predicted by LR.

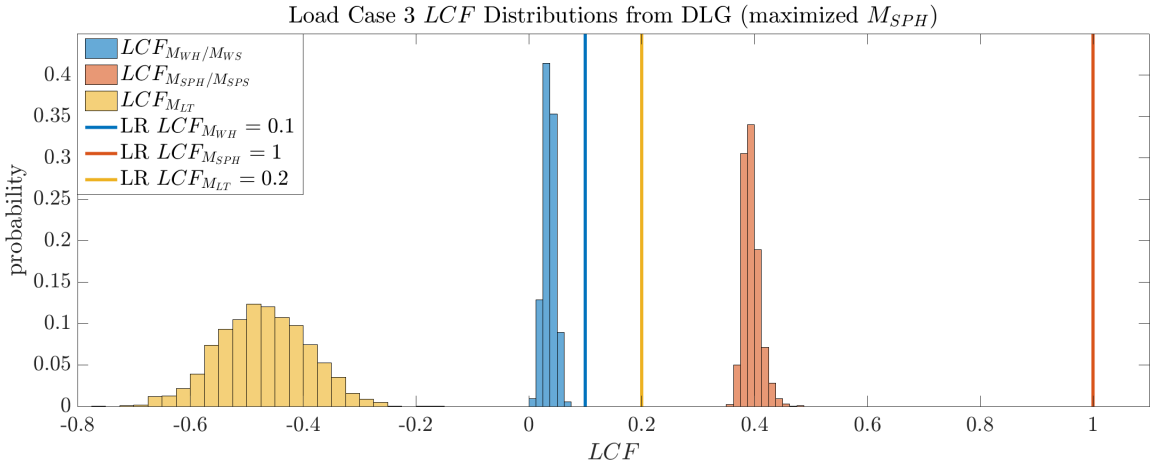

Figure 8.7: Empirical histograms, normalized as probability distributions, of LCF values from the DLG for Case 3, compared with the rule LCF values reported by LR in Table 8.3. For Case 4 (not plotted), all distributions are reflected across $LCF = 0$.

8.5.3 Oblique Seas, Cases 5-7

In Cases 5-7, the maximized loads are the longitudinal torsional, horizontal, and transverse torsional bending moments, respectively, in oblique seas. These distributions are shown in Figure 8.8. Note that only M_H achieves its design value in oblique

seas. That is why the distributions of $LCF_{M_{LT}}$ and $LCF_{M_{TT}}$ are not centered around $LCF = 1$. For Case 5, the distributions of $LCF_{M_{WH}/M_{WS}}$ and $LCF_{M_{SPH}/M_{SPS}}$ are both clustered around $LCF = 0$. For Case 6, the distributions of $LCF_{M_{SPH}/M_{SPS}}$ and $LCF_{M_{LT}}$ both lie around $LCF = 0.3$, though the $LCF_{M_{SPH}/M_{SPS}}$ distribution has a much higher variance. Note that for none of the cases do the LR rule LCF values really capture the distributions of loads assembled by the DLG.

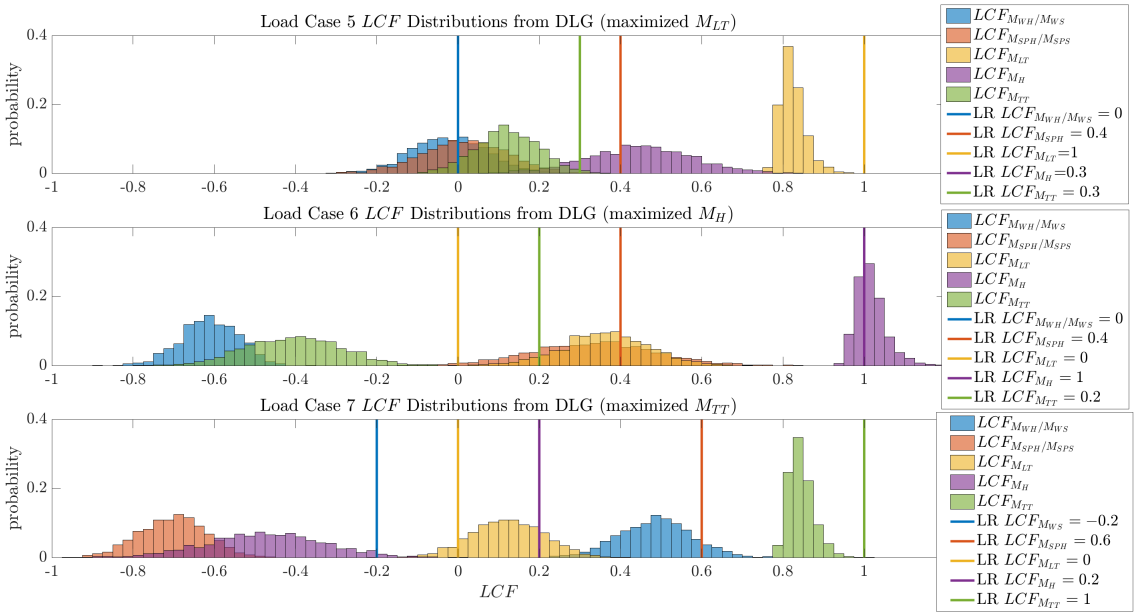

Figure 8.8: Empirical histograms, normalized as probability distributions, of LCF values from the DLG for Cases 5-7, compared with the rule LCF values reported by LR in Table 8.3.

Figures 8.6-8.8 indicate that the rule LCF values suggested by LR in Table 8.3 do not accurately represent the loads experienced by the trimaran from Figure 8.2. These standard LCF value are meant to represent lifetime combined loading, conditioned on a specific maximized global load. The DLG can assemble these distributions, leading to a fair comparison between the distributions and the suggested LCF values which are presumably meant to represent them. However, it is clear that the rule LCF values from LR do not accurately or consistently describe the lifetime combined loading experienced by this trimaran in the specific operational profile. Considering that these rule load cases are meant to be applied to a FEA model to determine structural adequacy, this lack of agreement may be a problem for design purposes.

8.6 Probabilistic Assessment of Rule Load Cases using the NL-DLG Process

Figures 8.6-8.8 compared the LCF distributions from the DLG and the LCF values indicated by the LR rule load combination cases, showing for most of the cases poor agreement. Since these LCF values are meant to be used in a FEA model for structural design purposes, it is important to determine whether the rule load cases are sufficiently conservative and exhaustive for this trimaran hull form.

One way to do this is to examine the probability that the standard LCF values offered by Lloyd's Register are exceeded over the vessel's lifetime, which can give an estimate of how conservative the LR load cases are. This may be a helpful metric to add to these loading combination cases, or to help define different load combination cases that reflect a more acceptable level of risk. The probability of simultaneously exceeding all LCF values in a given case can be estimated by the NL-DLG process. Then, a qualitative assessment of the load distributions from Figures 8.6-8.8 can assess whether the LR load cases are exhaustive in terms of lifetime extremes of the seven global loads.

8.6.1 Definition of Threshold Surface

For each standard case i defined by LR, n non-zero LCF_{M_m} values are assigned to loads M_m, $m = 1, \cdots, n$. Consider an $n-$dimensional Euclidean space with n axes that correspond to the n non-zero LCF_{M_m} values. These axes are called axis_{M_m}, $m = 1, \cdots, n$, to relate back to each load M_m considered in the case i. An un-bounded threshold surface, $G_{LR,\text{ case } i}$, can be defined as the intersection of the regions where $\text{axis}_{M_m} \geq LCF_{M_m}$ for all $m = 1, \cdots, n$:

$$\begin{aligned} G_{LR,\text{ case } i} &= \text{threshold surface defined by the } n \text{ non-zero LR rule } LCF_{M_m} \text{ values for case } i \\ &= \{\text{axis}_{M_1} \geq LCF_{M_1}\} \cap \{\text{axis}_{M_2} \geq LCF_{M_2}\} \cap \cdots \cap \{\text{axis}_{M_n} \geq LCF_{M_n}\} \end{aligned}$$

Similar notation from Chapter 1.3.1 defines the event that all loads, given as a LCF, simultaneously exceed $G_{LR,\text{ case } i}$ for a specific case i:

$$\begin{aligned}
\mathbf{LCF}(t) &= \text{vector of } n \text{ global load time series included in a particular case } i, \\
&\quad \text{each normalized as } LCF_{M_m}(t),\ m = 1, \cdots, n \\
N_{G_{LR,\ \text{case } i}}(T) &= \text{the number of up-crossings of } G_{LR,\ \text{case } i} \text{ by } \mathbf{LCF}(t) \text{ in [0,T]} \\
p(N_{G_{LR,\ \text{case } i}}(T) \geq 1) &= \text{probability that the threshold } G_{LR,\ \text{case } i} \text{ is exceeded by } \mathbf{LCF}(t) \\
&\quad \text{at least once over the exposure } T
\end{aligned}$$

Whereas in Chapter 1.3.1 the probability that a load vector exceeds some threshold surface is conditioned on an exceedance *not* occurring at time $t = 0$, no such condition is required for the NL-DLG process estimation of $p(N_{G_{LR,\ \text{case } i}}(T) \geq 1)$. The NL-DLG process estimates the probability that over the exposure, the vector of global loads considered in a specific case i, $\mathbf{LCF}(t)$, exceeds the threshold surface, $G_{LR,\ \text{case } i}$. Any subscript, $\{\bullet\}$, of $G_{\{\bullet\}}$ indicates which LCF values define the threshold surface, and from which case.

Note that Chapters V-VII developed and applied the NL-DLG process to estimate failure probabilities. In those chapters, a load vector and failure surface were defined, with failure occurring when the vector exceeded the failure surface. In Chapter VII, a physical failure was associated with exceeding specific load combinations. Here, there is no such association. The NL-DLG process estimates the probability that a load vector exceeds a defined threshold surface. The intent in this chapter is to examine the combined loading that this trimaran hull experiences, and not a structural response *to* those load combinations, which would require a FEA model to relate load combinations to physical failure. The NL-DLG process simply offers metrics on the lifetime probability of exceeding specific load combinations.

8.6.2 Conservatism of the Rule Load Cases

For the NL-DLG process, load cases and surrogate processes can be defined, like in Chapter 5.4, to estimate $p(N_{G_{LR,\ \text{case } i}}(T) \geq 1)$ for each case i. It is likely that a wave time series which leads to loads that simultaneously exceed all rule LCF values for a specific case will contain an extreme value of a load which experiences its design value in that heading. Therefore, it is likely that $\mathbf{LCF}(t)$ exceeds $G_{LR,\ \text{case } 1}$ when M_{WH} is maximized in head seas. It is also possible, though, that $\mathbf{LCF}(t)$ exceeds $G_{LR,\ \text{case } 1}$ when one of the secondary loads from Case 1 is maximized (e.g. when M_{SPH} is maximized in head seas). This means that waves which lead to extreme values of each global load considered for a particular case i may lead to an out-crossing of

$G_{LR,\text{ case } i}$ by $\mathbf{LCF}(t)$. All of the loads in each case, then, are considered as separate load combination cases, like used in Eq.(5.1), to estimate $p(N_{G_{LR,\text{ case } i}}(T) \geq 1)$ for each case i by the NL-DLG process.

The load combination cases used by the NL-DLG process are similar to LR's method of considering each global load, maximized within a specific heading. Each case from LR focuses solely on the simultaneous load combinations due to a wave which maximizes a specific global load. The NL-DLG process examines simultaneous load combinations due to waves which lead to extreme values of each individual load in that case. The NL-DLG process says that $\mathbf{LCF}(t)$ may exceed $G_{LR,\text{ case } i}$ for case i due to a wave time series which leads to an extreme value of *any* of the global loads included in case i. Therefore, for each case from Table 8.3, the NL-DLG process uses as load cases each global load included in the LR case. Here, only individual extremes of the global loads are considered for the non-linear load combination cases. That is, no weighted sums of the global loads are defined as load cases within the NL-DLG process. As the loads from Aegir are all linear loads, the load cases *are* the surrogate processes. Then, the NL-DLG process estimates $p(N_{G_{LR,\text{ case } i}}(T) \geq 1)$ given the surrogate processes and threshold surface definition. This is done for all cases $i = 1 - 7$, with the results given in Table 8.6. Below for each case i, axis_{M_m}, $m = 1, \cdots, n$ is defined by each load name (i.e. $\text{axis}_{M_{WH}}$) for clarity.

Table 8.6 indicates that $p(N_{G_{LR,\text{ case } i}}(T) \geq 1)$, or simultaneously exceeding all LR rule LCF values from Table 8.3 for a given case i, is very low, except for case 6. This might indicate to a designer that the LR rule load cases give a conservative estimate of the lifetime combined loading this trimaran experiences over its lifetime. However, these exceedance probabilities must also be considered in light of whether the threshold surfaces defined by the LR rule LCF values for the different cases sufficiently bound the combined loading experienced by this trimaran hull.

As discussed in Chapter 6.8, probability estimates from the NL-DLG process are conditioned on the choice of load cases and surrogate processes, and how well those relate to the threshold definition. Notice that Cases 3, 4, 5, and 7, which have $p(N_{G_{LR,\text{ case } i}}(T) \geq 1) = 0$, each have a threshold surface, $G_{LR,\text{ case } i}$, that bounds a maximized global load with a design value that cannot occur in that particular heading (i.e. reference Table 8.3 vs. 8.5). The DLG distributions of these loads, given in Figures 8.7 and 8.8, already indicate that there is no chance of simultaneously exceeding all LCF values defined by LR. For example, in Case 3 the distribution of

Case & Heading	Load Cases/ Surrogate Processes	$G_{LR,\text{ case } i}$ definition:	$p(N_{G_{LR,\text{ case } i}}(T) \geq 1)$
1) Head	$\zeta_1(t) = z_1(t) = M_{WH}$ $\zeta_2(t) = z_2(t) = M_{SPH}$ $\zeta_3(t) = z_3(t) = M_{TT}$	$\{\text{axis}_{M_{WH}} \geq 1\} \cap$ $\{\text{axis}_{M_{SPH}} \geq 0.3\} \cap$ $\{\text{axis}_{M_{TT}} \geq 0.2\}$	0.0590
2) Head	$\zeta_1(t) = z_1(t) = M_{WS}$ $\zeta_2(t) = z_2(t) = M_{SPS}$ $\zeta_3(t) = z_3(t) = M_{TT}$	$\{\text{axis}_{M_{WS}} \leq -1\} \cap$ $\{\text{axis}_{M_{SPS}} \leq -0.3\} \cap$ $\{\text{axis}_{M_{TT}} \geq 0.2\}$	0.0577
3) Beam	$\zeta_1(t) = z_1(t) = M_{SPH}$ $\zeta_2(t) = z_2(t) = M_{WH}$ $\zeta_3(t) = z_3(t) = M_{LT}$	$\{\text{axis}_{M_{SPH}} \geq 1\} \cap$ $\{\text{axis}_{M_{WH}} \geq 0.1\} \cap$ $\{\text{axis}_{M_{LT}} \geq 0.2\}$	0
4) Beam	$\zeta_1(t) = z_1(t) = M_{SPS}$ $\zeta_2(t) = z_2(t) = M_{WS}$ $\zeta_3(t) = z_3(t) = M_{LT}$	$\{\text{axis}_{M_{SPS}} \leq -1\} \cap$ $\{\text{axis}_{M_{WS}} \leq -0.1\} \cap$ $\{\text{axis}_{M_{LT}} \geq 0.2\}$	0
5) Oblique	$\zeta_1(t) = z_1(t) = M_{LT}$ $\zeta_2(t) = z_2(t) = M_{SPH}$ $\zeta_3(t) = z_3(t) = M_H$ $\zeta_4(t) = z_4(t) = M_{TT}$	$\{\text{axis}_{M_{LT}} \geq 1\} \cap$ $\{\text{axis}_{M_{SPH}} \geq 0.4\} \cap$ $\{\text{axis}_{M_H} \geq 0.3\} \cap$ $\{\text{axis}_{M_{TT}} \geq 0.3\}$	0
6) Oblique	$\zeta_1(t) = z_1(t) = M_H$ $\zeta_2(t) = z_2(t) = M_{SPH}$ $\zeta_3(t) = z_3(t) = M_{LT}$	$\{\text{axis}_{M_H} \geq 1\} \cap$ $\{\text{axis}_{M_{SPH}} \geq 0.4\} \cap$ $\{\text{axis}_{M_{TT}} \geq 0.2\}$	0.2375
7) Oblique	$\zeta_1(t) = z_1(t) = M_{TT}$ $\zeta_2(t) = z_2(t) = M_{WS}$ $\zeta_3(t) = z_3(t) = M_{SPH}$ $\zeta_4(t) = z_4(t) = M_H$	$\{\text{axis}_{M_{TT}} \geq 1\} \cap$ $\{\text{axis}_{M_{WS}} \leq -0.2\} \cap$ $\{\text{axis}_{M_{SPH}} \geq 0.6\} \cap$ $\{\text{axis}_{M_H} \geq 0.2\}$	0

Table 8.6: Case, heading, load cases, surrogate processes, threshold $G_{LR,\text{ case } i}$ definition, and probability of simultaneously exceeding all rule LCF values defined by LR, $p(N_{G_{LR,\text{ case } i}}(T) \geq 1)$, estimated by the NL-DLG process. The load cases/ surrogate processes are defined by the loads included in each case in Table 8.3.

$LCF_{M_{SPH}}$ is centered around 40% of the design value. No M_{SPH} value approaches its design value in beam seas, so there is no chance that $\mathbf{LCF}(t)$ exceeds $G_{LR,\text{ case } 3}$ given this load case in beam seas. Cases 3, 4, 5, and 7 defined by the LR rule load cases have a 0% chance of exceeding $G_{LR,\text{ case } i}$, but that does not mean there is a 0% chance of experiencing large combinations of the loads included in those cases in general. These loads experience larger values in different headings, but no rule load cases are defined to capture these responses.

Many of the cases from Table 8.3 are simply not applicable, because they do not line up each global load in the heading where its design value is experienced. The low exceedance probabilities, therefore, are due to the mis-direction of the cases, rather than a conservative definition of load cases. Some of these cases have no chance of simultaneously exceeding all LCF values, but that doesn't mean the trimaran doesn't experience that sort of loading over its lifetime. It is difficult to label these

rule load combination cases from Table 8.3 as conservative, because they do not bound extreme lifetime load combinations, only those load combinations conditioned on specific headings. Since these headings do not necessarily line up with extreme load values, the testing profile does not examine the largest global load values this trimaran experiences in its lifetime.

It *is* possible that the conservatism of these load cases is included in the acceptance criteria for structural adequacy given the loading applied to a FEA model. However, the Lloyd's Register rules do not indicate whether that is the case. It may be desirable for a designer using these rule load cases to be aware of what conservatism is applied, and where that conservatism is applied (i.e. to the load combination cases, or the structural response to that loading). Since the rule load cases do not realistically describe the load distributions actually experienced by this trimaran, these rule load cases from LR cannot be labeled applicable or conservative in their description of lifetime loading for this trimaran.

8.6.3 Exhaustiveness of the Rule Load Cases

The LR rule load cases additionally do not appear to be exhaustive concerning the global loading on this trimaran. This is mainly due to the fact that the cases do not line up with the headings where each load experiences its design value. Based on this, not all of the global loads experience their design value in the testing profile offered by the rule loads. This may be problematic, as structural vulnerabilities to specific loadings may not be fully examined. With the load cases from Table 8.3, no case has a M_{SPH}/M_{SPS} value larger than about 80% of its design value. If a structure's design is susceptible to the splitting moment, the rule load cases may not truly test that vulnerability.

The analysis of these rule loads cases highlights the potential pitfall of using a standard set of load cases for a variety of trimaran designs. Given a different placement of the side-hulls, the interaction between the global loads acting on the vessel can change drastically. The LR rule loads assume relationships between the global loads. But, since the LR load combination cases are not specifically tailored to this trimaran hull, the predicted simultaneous load LCF values, conditioned on a specific maximized global load, were often inaccurate. The rule load cases do not give an accurate or conservative estimate of the loads experienced by this trimaran hull with the operational profile defined by Table 8.4.

8.7 Development of Alternative Load Cases

The rule load values from Table 8.3 do not realistically describe the combined loading experienced by this specific trimaran hull, which was also examined by load distributions assembled by the DLG for each specific case. This indicates that the trimaran hull in this example has a frequency response which is significantly different than the hull, or range of hulls, used to generate the standard LCF values in Table 8.3. LR also offers an "alternative procedure for load development" to using the rule load cases in Table 8.3 (*Lloyd's Register* (2017), Vol. 4, Part 1, Ch. 3, Sec. 4.2). The alternative procedure is to tailor load combination cases for the specific trimaran in question using the EDW methodology. LR says that this alternative approach "provides more realistic loading scenarios, improving the user's confidence in the loads which are to be applied to the finite element model" (*Lloyd's Register*, 2017).

In the EDW methodology, a regular wave is determined which leads to the design value for a specific global load in the heading where that design value occurs. This wave then drives the other global loads to determine simultaneous values of all global loads in the given heading. The LCF for each load, M_i, in a case is calculated by examining the RAO of the maximized load, M_{max}, within the given heading. The maximum value of that RAO, a_{max}, is determined along with the corresponding phase, ϵ_{max}, and encounter frequency, $\omega_{e,max}$. The time, t_{max}, when M_{max} experiences its maximum value is calculated by Eq.(8.2). The height of the equivalent design wave, h_{max}, is then given by Eq.(8.3):

$$cos(\omega_{e,max} t_{max} + \epsilon_{max}) = \pm 1 \tag{8.2}$$

$$h_{max} = \frac{R}{a_{max}} \tag{8.3}$$

R is the design value for M_{max}. The amplitude, a_i, and phase, ϵ_i, of each secondary load, M_i, at $\omega_{e,max}$ are identified. The LCF for the load M_i is calculated by Eq.(8.4). Note that by construction, the LCF of the maximized load M_{max} is 1, as for M_{max}, $h_{max} a_i / R_i = h_{max} a_{max} / R = 1$, and $cos(\omega_{e,max} t_{max} + \epsilon_{max}) = \pm 1$. R_i is the design value for the given secondary load, M_i. This value reflects the operating profile (speed, heading, exposure), and specifically the heading that leads to the largest response.

$$LCF = \frac{h_{max} a_i cos(\omega_{e,max} t_{max} + \epsilon_i)}{R_i} \tag{8.4}$$

The spirit of the EDW approach and the DLG are the same, as both methods consider a single maximized load and recover simultaneous responses of other loads due to the same wave excitation. The difference, though, is that the DLG constructs ensembles of *irregular* wave inputs that lead to this maximum load response, giving a distribution of responses. The other global loads considered in a specific case are driven by this constructed irregular wave input. The EDW method, on the other hand, constructs a regular wave to return a single representative value of the loads in a case at the given maximized instant. Whether the deterministic EDW approach can accurately capture the simultaneous response of multiple loads, and whether a single value is even representative of a distribution of responses, will be assessed.

Theoretically, this alternative approach should generate more applicable load cases than the rule loads, which assume that the global loads are maximized in certain headings and assume specific levels of load dependence. A natural question is: does the alternative load procedure more realistically describe the combined loading experienced by this trimaran to "improve the user's confidence in the loads which are to be applied to the [FEA] model," as the LR rules suggest? (*Lloyd's Register*, 2017)

These alternative LCF values are calculated using the transfer functions from Figures 8.3-8.5 with Eq.(8.2)-(8.4). In this alternative approach, each global load is maximized in the heading where it experiences its design value, i.e. Table 8.5. This indicates that Cases 3, 4, 5, and 7, are in different headings than in Table 8.3. The alternative load cases, developed using the EDW method, are given in Table 8.7. In Table 8.7, all signs represent the physical signs of the loads, and do not imply any "reversible" effects, as in Table 8.3.

Case & Heading	M_{max}	Dynamic Loads						
		M_{WH}	M_{WS}	M_H	M_{SPH}	M_{SPS}	M_{LT}	M_{TT}
1) Head	M_{WH}	1.0	0	0	0	0.02	0	0.1
2) Head	M_{WS}	0	1.0	0	0.02	0	0	-0.1
3) Oblique	M_{SPH}	0	0.31	0.51	1.0	0	0.18	-0.59
4) Oblique	M_{SPS}	0.31	0	-0.51	0	1.0	-0.18	0.59
5) Beam	M_{LT}	0.02	0	0	0	0.25	1.0	0
6) Oblique	M_H	0	0.8	1.0	0.27	0	-0.03	-0.07
7) Head	M_{TT}	0.42	0	0	0	0.62	0	1.0

Table 8.7: Alternative load cases, along with heading and load combination factors (LCF) defined using the EDW approach. The maximized load, M_{max}, is also noted for each case.

8.8 Assessment of Alternative Load Cases using the DLG

The DLG can assess how accurately the alternative load LCF values represent the loading on the trimaran hull from Figure 8.2. The process is the same as in Section 8.5, where the DLG constructs short wave profiles which maximize a specific global load in each case, M_{max}, with the given heading from Table 8.7. Those waves drive all the loads in the case, and the simultaneous load values, all normalized as a LCF, are plotted to give the load distributions.

8.8.1 Head Seas, Cases 1-2

The alternative load Cases 1-2 are in head seas, as in Table 8.3. The empirical histograms, normalized as probability distributions, for Case 1 are plotted in Figure 8.9. For Case 2, the distributions are reflected across $LCF = 0$. The DLG distributions remain unchanged from Figure 8.6 because this case remains in head seas. The alternative load LCF values, denoted as 'ALT' are plotted as the vertical lines. Although these alternative values capture the relative magnitudes of the $LCF_{M_{SPH/SPS}}$ and $LCF_{M_{TT}}$ distributions better than the rule load values (i.e. Figure 8.6), $LCF_{M_{TT}}$ is far larger than the alternative LCF value predicts.

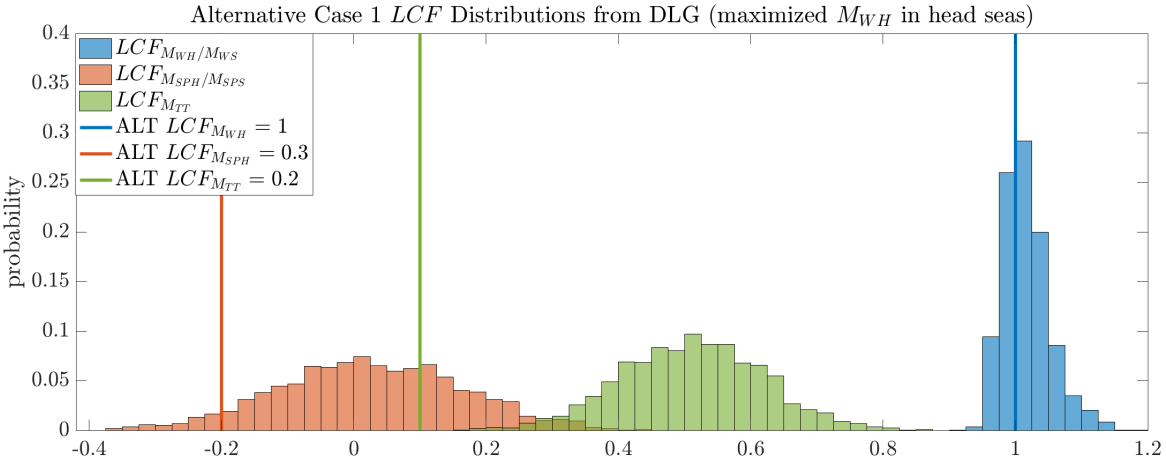

Figure 8.9: Empirical histograms, normalized as probability distributions, of LCF values from the DLG for Case 1 for maximized M_{WH} in head seas. Case 2 distributions (not plotted) are reflected across $LCF = 0$. The alternative LCF values from Table 8.7 are shown as the vertical lines.

8.8.2 Oblique Seas, Cases 3-4

The alternative Cases 3-4 maximize the splitting moment, M_{SPH}/M_{SPS}, in oblique seas, leading to the empirical histograms, normalized as probability distributions, shown in Figure 8.10. For some loads, like M_{TT} and M_{WS}, the alternative LCF values from Table 8.7 accurately describe the sign and relative magnitude of the loading distributions assembled by the DLG. However, both the distribution of M_{LT} and M_H are rather significantly smaller than predicted by the alternative LCF values.

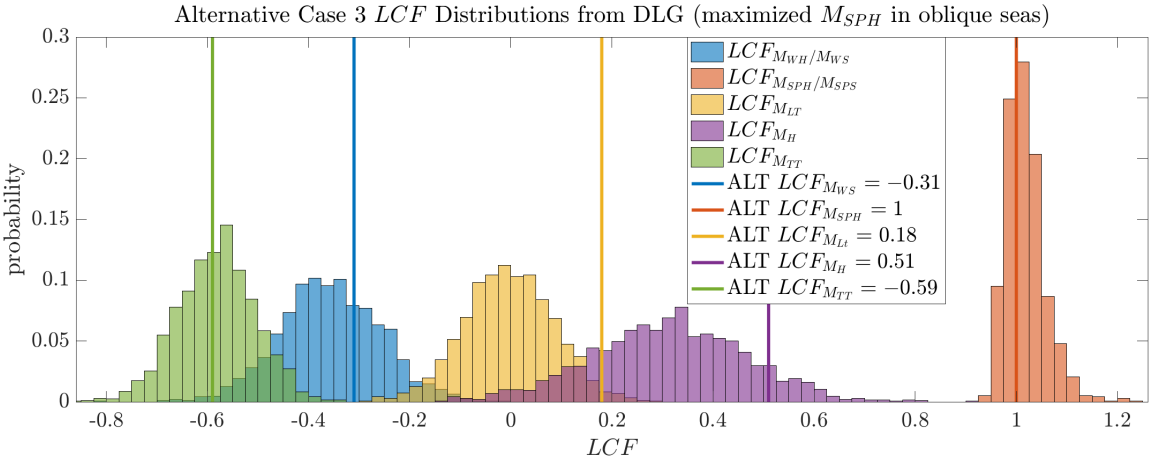

Figure 8.10: Empirical histograms, normalized as probability distributions, of LCF values from the DLG for Case 3 for maximized M_{SPH} in oblique seas. Case 4 distributions (not plotted) are reflected across $LCF = 0$. The alternative LCF values from Table 8.7 are shown as the vertical lines.

8.8.3 Beam Seas, Case 5

For Case 5, the longitudinal torsional load, M_{LT}, is maximized in beam seas, with the empirical histograms, normalized as probability distributions, shown in Figure 8.11. Although the alternative LCF value for M_{SPS} is a bit larger than the DLG distribution, in general, these alternative LCF values accurately describe the combined loading experienced by this trimaran hull for this case.

8.8.4 Oblique Seas, Case 6

Figure 8.12 shows the simultaneous load empirical histograms, normalized as probability distributions, from the DLG when M_H is maximized in oblique seas. Note these are the same distributions from the middle inset Figure 8.8, as the heading for Case 6 remains in oblique seas. The alternative LCF values seem to be generally more

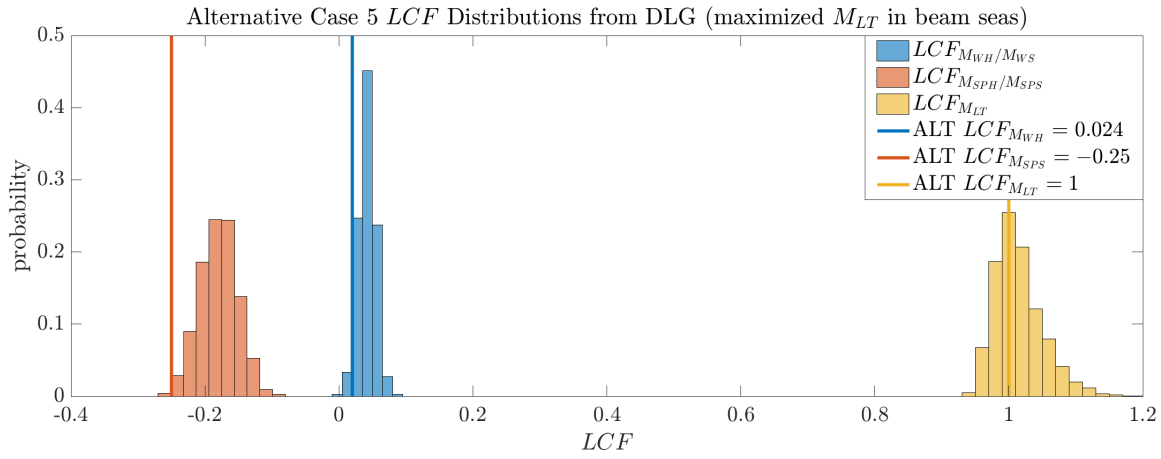

Figure 8.11: Empirical histograms, normalized as probability distributions, of LCF values from the DLG for Case 5 for maximized M_{LT} in beam seas. The alternative LCF values from Table 8.7 are shown as the vertical lines.

accurate than the rule load LCF values, but do not consistently describe these load distributions in oblique seas conditioned on maximum M_H.

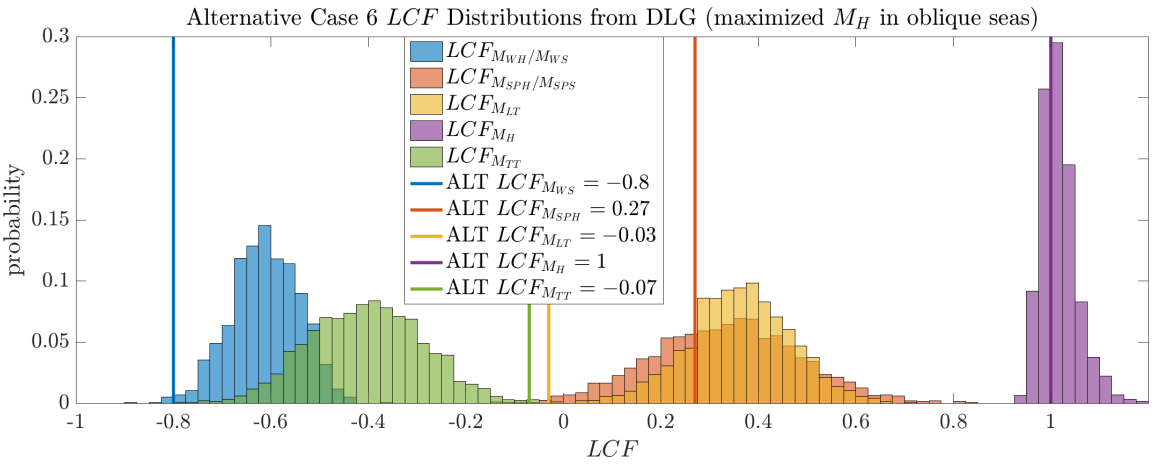

Figure 8.12: Empirical histograms, normalized as probability distributions, of LCF values from the DLG for Case 6 for maximized M_H in oblique seas. The alternative LCF values from Table 8.7 are shown as the vertical lines.

8.8.5 Head Seas, Case 7

Figure 8.13 shows the empirical histograms, normalized as probability distributions, of M_{TT} maximized in head seas, with the simultaneous distributions of M_{WH} and M_{SPS}. The alternative LCF values are generally accurate descriptions of the

DLG load distributions than the rule load values in Figure 8.8. However, the alternative LCF value for M_{SPS} presents a high bound on the most-probable point of the DLG distribution, while the alternative LCF value for M_{WH} presents a low bound on the most probable point of the DLG distribution.

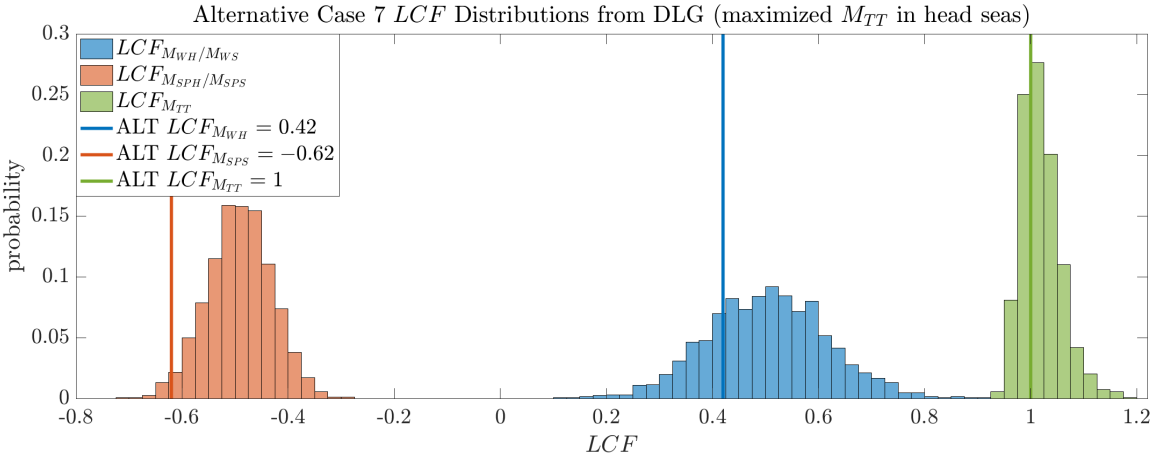

Figure 8.13: Empirical histograms, normalized as probability distributions, of LCF values from the DLG for Case 7 for maximized M_{TT} in head seas. The alternative LCF values from Table 8.7 are shown as the vertical lines.

8.9 Probabilistic Assessment of Alternative Load Cases using the NL-DLG Process

A new threshold surface, $G_{ALT,\text{ case } i}$, is defined by the alternative LCF values for each case i. The same vector of global loads, $\mathbf{LCF}(t)$ is used for each case, but now to test a potentially more appropriate threshold surface, $G_{ALT,\text{ case } i}$. The surface, $G_{ALT,\text{ case } i}$, is defined the same way as in Section 8.6.1, except using the alternative load LCF values instead of the rule load LCF values for each case i.

For Cases 1-7, Table 8.8 gives the alternative LCF values calculated using the EDW method for this trimaran hull, LCF_{ALT}, and the most probable LCF of the assembled DLG distribution, LCF_{DLG}. The NL-DLG process evaluates the probability that the vector of LCF global load time series in a case i exceeds the threshold surface $G_{ALT,\text{ case } i}$, $p(N_{G_{ALT,\text{ case } i}}(T) \geq 1)$. For Cases 1 and 2, and for Cases 3 and 4, this probability is specifically from Case 1 and Case 3, respectively. Since the loads are linear, in the limit of infinite realizations, the exceedance probabilities for Cases 2 and 4 are equal to those of Cases 1 and 3, respectively. This is

observed in Table 8.6 in which $p(N_{G_{LR,\text{ case }1}}(T) \geq 1) \approx p(N_{G_{LR,\text{ case }2}}(T) \geq 1)$ and $p(N_{G_{LR,\text{ case }3}}(T) \geq 1) \approx p(N_{G_{LR,\text{ case }4}}(T) \geq 1)$.

Case & Heading	Load	LCF_{ALT}	LCF_{DLG}	$p(N_{G_{ALT,\text{ case }i}}(T) \geq 1)$
Case 1-2, Head Seas	M_{WH}/M_{WS}	± 1	± 1	0.3595
	M_{SPH}/M_{SPS}	∓ 0.02	0	
	M_{TT}	± 0.10	± 0.51	
Case 3-4, Oblique Seas	M_{WH}/M_{WS}	∓ 0.31	∓ 0.38	0.0904
	M_{SPH}/M_{SPS}	± 1	± 1	
	M_{LT}	± 0.18	∓ 0.01	
	M_H	± 0.51	± 0.34	
	M_{TT}	∓ 0.59	∓ 0.56	
Case 5, Beam Seas	M_{WH}/M_{WS}	0.02	0.04	0.2522
	M_{SPH}/M_{SPS}	-0.25	-0.19	
	M_{LT}	1	1	
Case 6, Oblique Seas	M_{WH}/M_{WS}	-0.8	-0.61	0.001
	M_{SPH}/M_{SPS}	0.27	0.36	
	M_{LT}	-0.03	0.37	
	M_H	1	1	
	M_{TT}	-0.07	-0.37	
Case 7, Head Seas	M_{WH}/M_{WS}	0.42	0.51	0.2638
	M_{SPH}/M_{SPS}	-0.62	-0.51	
	M_{TT}	1	1	

Table 8.8: Cases 1-7 alternative LCF values calculated for the specific trimaran hull, LCF_{ALT}, the most probable LCF of the assembled DLG distributions, LCF_{DLG}, and the probability of simultaneously exceeding all LCF_{ALT} values, $p(N_{G_{ALT,\text{ case }i}}(T) \geq 1)$.

Using the EDW method, the alternative LCF_{ALT} values for this trimaran hull are generally more representative of the combined load distributions assembled by the DLG than the rule load LCF_{LR} values. However, the LCF_{ALT} values are not always accurate, and sometimes predict a different load sign than what the trimaran experiences. Even in cases where the LCF_{ALT} values are generally accurate, like in Case 7, the alternative LCF_{ALT} values do not give a constant bounding on the most-probable point of the DLG distributions. In Case 7, the LCF_{ALT} value for M_{SPS} is a upper bound, but the LCF_{ALT} value for M_{WH} is a lower bound. Additionally, even for cases where the LCF_{ALT} values are reasonable estimates for the DLG load distributions, like in Cases 3, 5, and 7, a single LCF value does not capture the observed variance in those load distributions.

This, along with the high $p(N_{G_{ALT,\text{ case }i}}(T) \geq 1)$ probabilities, makes it difficult to definitively say whether these alternative LCF values are sufficiently conservative. Defining a threshold surface $G_{ALT,\text{ case }i}$ by the LCF_{ALT} values for these cases may not be any more conservative or representative of the lifetime loads than using $G_{LR,\text{ case }i}$ for these cases. This is reinforced by the high probabilities $p(N_{G_{ALT,\text{ case }i}}(T) \geq 1)$

observed for these cases, using the LCF_{ALT} values to define the threshold surface, $G_{ALT,\text{ case } i}$. The EDW method tailored to this trimaran hull does not appear to accurately describe the combined loading experienced for this hull.

8.10 Recommendation on Load Case Definitions

Based on the above sections, it is clear neither the rule load approach (Table 8.3 and 8.6) nor the alternative load approach (Table 8.7 and 8.8) seem to accurately and consistently describe the combined loading experienced by this trimaran hull. However, the spirit of load combination cases is still applicable. It is important to consider the vessel response to the major global loads shown in Figure 8.1. New load combination cases are defined in Table 8.9 to more accurately represent the combined loading that this trimaran hull experiences, based on a global load being maximized in the heading where the design value occurs.

Case & Heading	M_{max}	Dynamic Loads							$p(N_{G_{*,\text{ case } i}}(T) \geq 1)$
		M_{WH}	M_{WS}	M_H	M_{SPH}	M_{SPS}	M_{LT}	M_{TT}	
$1*a$) Head	M_{WH}	1.0	0	0	0.3	0	0	0.6	0.0016
$1*b$) Head	M_{WH}	1.0	0	0	0	0.3	0	0.6	0.0320
$2*a$) Head	M_{WS}	0	1.0	0	0.3	0	0	-0.6	0.0346
$2*b$) Head	M_{WS}	0	1.0	0	0	0.3	0	-0.6	0.0017
$3*$) Oblique	M_{SPH}	0	0.45	0.4	1.0	0	0	-0.6	0.1167
$4*$) Oblique	M_{SPS}	0.45	0	-0.4	0	1.0	0	0.6	0.1277
$5*$) Beam	M_{LT}	0	0	0	0	0.35	1.0	0	0.0199
$6*$) Oblique	M_H	0	0.60	1.0	0.40	0	0.40	-0.40	0.0770
$7*$) Head	M_{TT}	0.6	0	0	0	0.6	0	1.0	0.0902

Table 8.9: LCF_* values for the recommended Cases $1* - 7*$ and probability of simultaneously exceeding those LCF_* values, $p(N_{G_{*,\text{ case } i}}(T) \geq 1)$.

The combined load distributions for these recommended Cases $1* - 7*$ from the DLG are given in Figures 8.9-8.13. Based on these distributions of loads from the DLG, conditioned on the heading where each load achieves its design value, new LCF values, called LCF_* are defined in Table 8.9. These LCF_* values are based on the DLG distributions from Figures 8.9-8.13, coupled with a bounding value. These values are chosen so that there is a low probability of simultaneously exceeding all LCF_* bounds, defining a new threshold surface $G_{*,\text{ case } i}$ for each case i. For Cases $1* - 2*$, two sub-cases are defined to account for the high variance in M_{SPH}/M_{SPS}. It is important to note that there are an infinite number of possible load combinations

for each case i that will lead to a given probability, $p(N_{G_{*,\text{ case }i}}(T) \geq 1)$. Therefore, the LCF_* values chosen for these new load cases are somewhat an arbitrary choice and are simply based on bounding the distributions of loads experienced in the updated cases. Again, as in Table 8.7, negative signs represent actual load signs, and do not imply reversibility as in Table 8.3.

8.10.1 Mutual Exclusivity of Load Cases & Threshold Definitions

The load cases in Table 8.9 are designed to be more conservative and exhaustive than the rule load cases in Table 8.3 and the alternative load cases in Table 8.7. What may be most interesting to a designer is the probability that over an exposure in a given heading, a threshold surface defined by *any* case is exceeded, rather than considering the probabilities, $p(N_{G_{*,\text{ case }i}}(T) \geq 1)$, separately. This would correspond to having an overall allowable risk factor, rather than individual risk factors applied to different cases. However, to determine this overall probability from the NL-DLG process, and to define each case separately, requires that each case be disjoint. This means that during any single wave record constructed by the DLG (during the time $[0, T_{DLG}]$, where T_{DLG} is the length of each DLG simulation), there can only be one type of threshold out-crossing, or an out-crossing of only one $G_{*,\text{ case }i}$ by $\mathbf{LCF}(t)$. Essentially, for the probability of exceeding any threshold surface over the exposure, $p(N_{G_{*,\text{ overall}}}(T) \geq 1)$:

$$p(N_{G_{*,\text{ overall}}}(T) \geq 1) = \sum_{i=1a*}^{7*} p(N_{G_{*,\text{ case}i}}(T) \geq 1) \text{ iff:}$$

during the DLG simulation length $[0, T_{DLG}]$:

$$p(N_{G_{*,\text{ case }i}}(T_{DLG}) \geq 1) \cap p(N_{G_{*,\text{ case }j}}(T_{DLG}) \geq 1) = 0 \text{ for all } i = 1a* - 7* \text{ and } j = 1a* - 7*$$

It may be difficult, though, to define mutually exclusive load combination cases that are exhaustive. As an example, consider Cases $3*$ and $4*$ which define a different type of threshold exceedance. Each of these threshold exceedances are mutually exclusive at a single instant; i.e. at a single instant, it is impossible for a splitting moment to exceed both its hogging *and* sagging design value, since these have opposite signs. However, these threshold definitions do not require that only that one specific type of threshold exceedance occurs due to the same short wave excitation input. It is possible that multiple different thresholds are exceeded within the same short time length $[0, T_{DLG}]$.

In general, a designer may want to know the probability of exceeding a threshold surface defined by *any* case over the exposure. This may not be an easy probability to determine if the wave excitations which lead to these different threshold exceedance events are not mutually exclusive. Specifically, consider the threshold exceedance criteria for Cases 3$*$ and 4$*$. It is possible that a single DLG wave record exceeds both $G_{*,\text{ case 3}}$ and $G_{*,\text{ case 4}}$, as seen below in Figure 8.14.

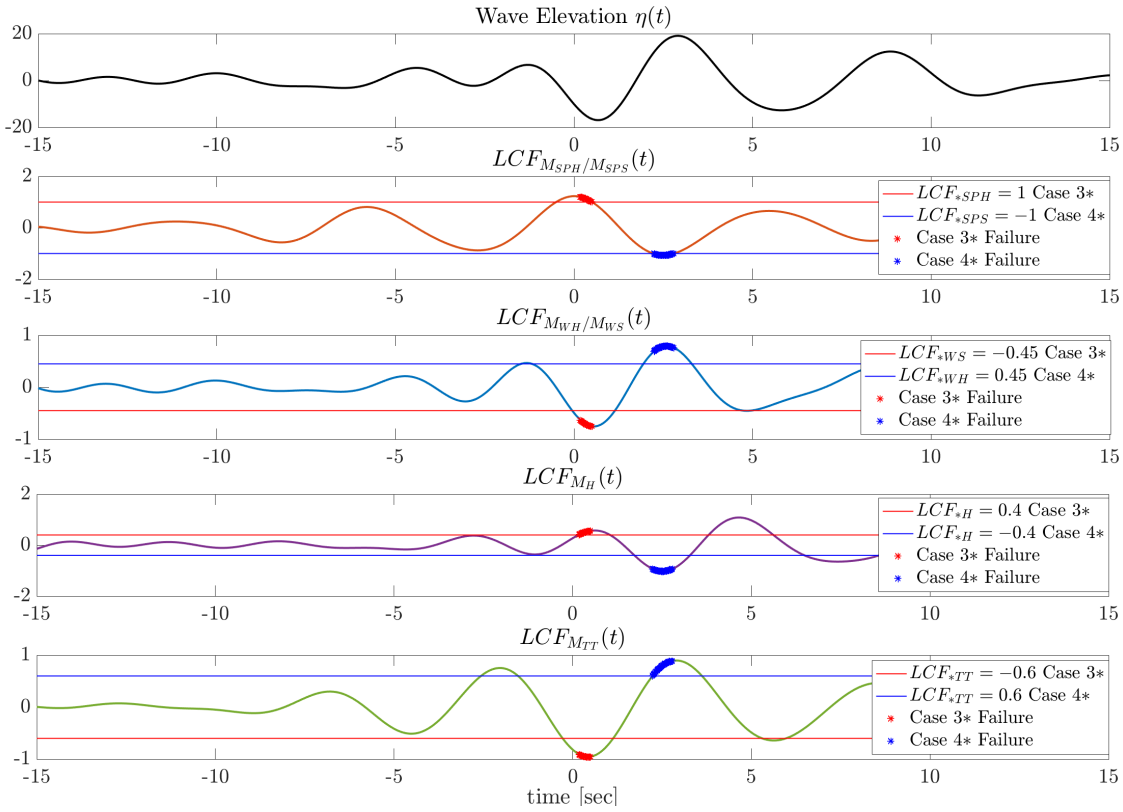

Figure 8.14: Wave elevation $\eta(t)$ in oblique seas constructed by the DLG to produce a maximum M_{SPH} at time $t = 0$, which drives time series of $LCF_{M_{SPH}/M_{SPS}}(t)$, $LCF_{M_{WH}/M_{WS}}(t)$, $LCF_{M_H}(t)$, and $LCF_{M_{TT}}(t)$. Lines which indicate the LCF_* bound for Cases 3$*$ (red line) and 4$*$ (blue line) are plotted. This time series has simultaneous LCF_* exceedances that fit the criteria for both Case 3$*$ (red stars, when $\mathbf{LCF}(t)$ exceeds $G_{*,\text{ case 3}}$ from time $t = 0.18 - 0.5$ sec) and Case 4$*$ (blue stars, when $\mathbf{LCF}(t)$ exceeds $G_{*,\text{ case 4}}$ from time $t = 2.4 - 2.8$ sec).

In Figure 8.14, a wave elevation record $\eta(t)$ in oblique seas is constructed by the DLG to lead to an exposure-period-maximum of M_{SPH} at time $t = 0$. Time series of all loads considered in Cases 3$*$ and 4$*$ are driven by this $\eta(t)$ time series, normalized by the respective design value, and plotted as a LCF. The LCF_* bounds for Case 3$*$ are plotted as red lines. Between times $t = 0.18 - 0.5$ sec, marked with red stars, $\mathbf{LCF}(t)$ exceeds $G_{*,\text{ case 3}}$. The LCF bounds for Case 4$*$ are the blue lines, and between the times $t = 2.4 - 2.8$ sec, marked with blue stars, $\mathbf{LCF}(t)$ exceeds $G_{*,\text{ case 4}}$.

Note that the short periods of these loads are confirmed by the transfer functions in Figure 8.5.

The existence of such a time series, like shown in Figure 8.14, illustrates the difficulty of separately considering seemingly mutually exclusive events. By considering Cases 3∗ and 4∗ separately, both count an exceedance of $G_{*,\text{ case }3}$ or $G_{*,\text{ case }4}$ by $\mathbf{LCF}(t)$ due to the same DLG wave record, meaning that the two cases are not mutually exclusive. In fact, there are 20 wave records from the DLG which lead to a Case 3∗ threshold exceedance *and* 4∗ threshold exceedance. This indicates that Cases 3∗ and 4∗ should not be considered separately, because they do not represent mutually exclusive events.

The NL-DLG process was formulated to consider the probability of a threshold exceedance due to potentially non-mutually-exclusive surrogate processes. However, to separately use the NL-DLG process to estimate the probability of exceeding different case threshold definitions does not consider whether waves which lead to exceedances of the threshold surfaces $G_{*,\text{ case }3}$ or $G_{*,\text{ case }4}$ are, or are not, mutually exclusive. The potential non-mutual-exclusivity of these threshold exceedances can only be considered in the NL-DLG process estimation if the probability of exceeding $G_{*,\text{ case }3}$ or $G_{*,\text{ case }4}$ is considered *within* the same NL-DLG process estimation.

8.11 Load Cases Conditioned on Vessel Heading

The existence of wave records which contain more than one type of threshold exceedance defined by the cases in Table 8.9 suggests the necessity of another update to the recommended load cases. This update is to account for the possibility that $\mathbf{LCF}(t)$ driven by a DLG wave excitation may lead to exceedances of $G_{*,\text{ case }i}$ for multiple different threshold definitions. It may be wise to combine all the cases that share a common heading. In head seas, there are Cases $1*a, 1*b, 2*a, 2*b$, and 7∗. It is possible that multiple DLG wave excitation records lead to more than one type of exceedance event using the LCF_* bounds from these cases. Indeed, there are 11 DLG wave records in head seas in which $G_{*,\text{ case }i}$ is exceeded by $\mathbf{LCF}(t)$ for at least one of case $i = 1*a, 1*b, 2*a, 2*b$, or 7∗. This is not surprising, considering the loads, and the respective load bounds, examined in these cases. For example, an LCF_* bound for Case $1*a$ and $1*b$ is $LCF_{*WH} \geq 1$. Case 7∗ has the bound $LCF_{*WH} \geq 0.6$. In this way, Cases $1*a, 1*b, 2*a, 2*b$, and 7∗ all 'trade-off' upper bounds on the same global loads.

Therefore, an overall head seas load case is defined, with a threshold surface definition, G_{head}, that considers the maximum load value, positive or negative, examined by any of Cases $1*a, 1*b, 2*a, 2*b$, or $7*$ in head seas. The same can be done for oblique seas, by combining Cases $3*, 4*$, and $6*$ for the single threshold surface G_{oblique}. In beam seas, there is only Case $5*$ (only M_{LT} experiences its design value in beam seas), so only the bounds of Case $5*$ are considered for the threshold surface G_{beam}. The new cases defined by heading, along with the LCF values, are given in Table 8.10. The threshold definition $G_{\text{head/beam/oblique}}$ for each heading, and the probability $p(N_{G_{head/beam/oblique}}(T) \geq 1)$, estimated by the NL-DLG process, is given below in Table 8.11. The loading combination cases within each heading, and associated surrogate processes, are also given.

Heading	Dynamic Loads				
	$\lvert M_{WH}/M_{WS}\rvert$	$\lvert M_H\rvert$	$\lvert M_{SPH}/M_{SPS}\rvert$	$\lvert M_{LT}\rvert$	$\lvert M_{TT}\rvert$
Head	1.0	0	0.3	0	1.0
Beam	0	0	0.35	1.0	0
Oblique	0.6	1.0	1.0	0	0.6

Table 8.10: Load cases by heading with load combination factors.

Note that these overall heading cases implicitly consider each maximized global load through the definition of the load cases. In this way, the maximum value of each global load is considered, plus the simultaneous values of the other loads. The new threshold definitions $G_{\text{head/beam/oblique}}$ just ensure that the heading cases are mutually exclusive in terms of allowable load values. Additionally, these three cases based on heading are exhaustive for the seven global loads, because each load is maximized in the heading where its design value occurs, and these headings cover all operating conditions for the trimaran in the given sea state.

Chapter 5.8 noted the difficulty of using the NL-DLG process to estimate an exceedance probability using many surrogate processes, due to the number of surrogate process maxima configurations which must be examined, given by the Bell number. The oblique seas case in Table 8.11 has seven surrogate processes, to account for the seven global loads considered in oblique seas. However, using all seven surrogate processes would require examining 877 maxima configurations. Even the head and beam seas cases, which have five surrogate processes, would result in too many maxima configurations to consider ($B_5 = 52$). The formulation to consider the maxima configurations given more than four surrogate process maxima has not been attempted,

Heading	Load Cases/ Surrogate Processes	$G_{head/beam/oblique}$ definition:	$p(N_{G_{head/beam/oblique}}(T) \geq 1)$
Head Seas	$\zeta_1^*(t) = z_1^*(t) = M_{WH}$ $\zeta_2^*(t) = z_2^*(t) = M_{WS}$ $\zeta_3^*(t) = z_3^*(t) = M_{SPH}$ $\zeta_4(t) = z_4(t) = M_{SPS}$ $\zeta_5^*(t) = z_5^*(t) = M_{TT}$	$\{\lvert\text{axis}_{M_{WH}/M_{WS}}\rvert \geq 1\} \cap$ $\{\lvert\text{axis}_{M_{SPH}/M_{SPS}}\rvert \geq 0.3\} \cap$ $\{\lvert\text{axis}_{M_{TT}}\rvert \geq 1\}$	0.0029
Beam Seas	$\zeta_1^*(t) = z_1^*(t) = M_{LT}$ $\zeta_2^*(t) = z_2^*(t) = M_{SPH}$ $\zeta_3^*(t) = z_3^*(t) = M_{SPS}$ $\zeta_4(t) = z_4(t) = M_{WH}$ $\zeta_5^*(t) = z_5^*(t) = M_{WS}$	$\{\lvert\text{axis}_{M_{LT}}\rvert \geq 1\} \cap$ $\{\lvert\text{axis}_{M_{SPH}/M_{SPS}}\rvert \geq 0.35\}$	0.0312
Oblique Seas	$\zeta_1^*(t) = z_1^*(t) = M_{SPH}$ $\zeta_2^*(t) = z_2^*(t) = M_{SPS}$ $\zeta_3(t) = z_3(t) = M_{WH}$ $\zeta_4(t) = z_4(t) = M_{WS}$ $\zeta_5^*(t) = z_5^*(t) = M_H$ $\zeta_6^*(t) = z_6^*(t) = M_{TT}$ $\zeta_7(t) = z_7(t) = M_{LT}$	$\{\lvert\text{axis}_{M_{SPH}/M_{SPS}}\rvert \geq 1\} \cap$ $\{\lvert\text{axis}_{M_{WH}/M_{WS}}\rvert \geq 0.6\} \cap$ $\{\lvert\text{axis}_{M_H}\rvert \geq 1\} \cap$ $\{\lvert\text{axis}_{M_{TT}}\rvert \geq 0.6\}$	0.0003

Table 8.11: Loading cases defined by heading, including the threshold definition, $G_{\text{head/beam/oblique}}$, and the individual load cases and associated surrogate processes used by the NL-DLG process to estimate $p(N_{G_{head/beam/oblique}}(T) \geq 1)$ for each heading. Only load cases/ surrogate processes marked with a '$*$' are considered in the NL-DLG process estimation.

due to the complexity.

Therefore, these cases are simplified to consider only four surrogate processes. The load cases/ surrogate processes for each heading case which are used in the NL-DLG process estimation are noted as $\zeta_i^*(t) = z_i^*(t)$. The other surrogate processes are not considered in the NL-DLG process estimate of $p(N_{G_{head/beam/oblique}}(T) \geq 1)$ for each case. Neglecting some surrogate processes may be fair, as the surrogate processes which are not examined for each case lead to few, if any, exceedances of $G_{\text{head/beam/oblique}}$ by $\mathbf{LCF}(t)$ within the DLG simulation length T_{DLG}, as shown in Table 8.12. Including these surrogates in the NL-DLG process estimation for each heading would likely increase the exceedance probability (if the surrogate leads to any threshold exceedances), but not significantly.

8.11.1 Conservatism of Load Cases Conditioned on Vessel Heading

Given the three threshold surfaces based on heading, $G_{\text{head/beam/oblique}}$, and the probabilities, $p(N_{G_{head/beam/oblique}}(T) \geq 1)$, from Table 8.11, an overall probability of exceeding any threshold definition over the exposure can be determined. Since the cases are defined by heading, which are mutually exclusive, the probabilities can be

Heading	Neglected Load Cases/ Surrogate Processes	$N_{G_{head/beam/oblique}}(T_{DLG})$ (out of 2000 DLG simulations)
Head Seas	$\zeta_4(t) = z_4(t) = M_{SPS}$	1
Beam Seas	$\zeta_4(t) = z_4(t) = M_{WH}$	1
Oblique Seas	$\zeta_3(t) = z_3(t) = M_{WH}$	0
	$\zeta_4(t) = z_4(t) = M_{WS}$	0
	$\zeta_7(t) = z_7(t) = M_{LT}$	0

Table 8.12: Neglected surrogate processes from the cases in Table 8.11, along with the number of threshold exceedances, $N_{G_{head/beam/oblique}}(T_{DLG})$, due to these neglected surrogate processes, out of 2000 wave excitation records, $\eta_i(t)$, of length T_{DLG} constructed by the DLG to lead to the exposure-period-maximum of each surrogate process $z_i(t)$.

summed. The probability of the trimaran being in each heading is equal, as by the LR rules. Therefore, the probability of exceeding any of the load combinations given in Table 8.10 in the 7.71-hour exposure given the operational profile in Table 8.4 is:

$$\begin{aligned} p(N_{G_{overall,\ \text{7.71-hours}}}(T) \geq 1) &= p(N_{G_{head}}(T) \geq 1)p(\text{head seas}) + \cdots \\ &\quad p(N_{G_{beam}}(T) \geq 1)p(\text{beam seas}) + \cdots \\ &\quad p(N_{G_{oblique}}(T) \geq 1)p(\text{oblique seas}) \\ p(\text{head seas}) &= p(\text{beam seas}) = p(\text{oblique seas}) = 1/3 \\ p(N_{G_{overall,\ \text{7.71-hours}}}(T) \geq 1) &= 0.0029(1/3) + 0.0312(1/3) + 0.0003(1/3) = 0.0202 \end{aligned} \tag{8.5}$$

The probability in Eq.(8.5) is implicitly conditioned on the exposure defined in Table 8.4, that being a 7.71-hour exposure in the given sea state out of 20 years, associated with a $PNE = 0.9998$, or risk parameter $\alpha = 2.27\text{e-}4$. Therefore, the 20-year lifetime probability of exceeding any load combination case defined by Table 8.10 is:

$$\begin{aligned} p(N_{G_{overall,\ \text{20-years}}}(T) \geq 1) &= p(N_{G_{overall,\ \text{7.71-hours}}}(T) \geq 1 | \text{sea state} \cap \alpha)p(\text{sea state})\alpha \\ &= 0.0202 \times 4.4e-5 \times 2.27e-4 \\ &= 2.017e-10 \end{aligned} \tag{8.6}$$

where

$$\begin{aligned} p(\text{sea state}) &= \text{ 4.4e-5 from Table 8.4} \\ \alpha &= \text{ 2.27e-4 from Table 8.4} \end{aligned} \tag{8.7}$$

The design values for both the rule load and alternative load procedure are based on the criterion that the probability of experiencing any global load design value is 10^{-8} ("the operating life is generally to be taken as 20 years, which is assumed to

correspond to 10^8 wave encounters or a long-term probability level of 10^{-8}" (*Lloyd's Register*, 2017)). This appears to be the only explicit probabilistic basis associated with either the rule load or alternative load procedures. Recall that the risk parameter, α, was defined so that the most-probable global load value in the 7.71-hour exposure out of the 20-year service life has a 10^{-8} probability of exceedance, as by the LR rules. If this 10^{-8} probability of exceedance criterion is also meant to be applied to the load combinations, i.e. the probability of exceeding the load combinations over the exposure must be less than 10^{-8}, Eq.(8.6) indicates that the load combination cases defined by heading in Table 8.10 satisfy this overall probabilistic requirement. Given the risk parameter α applied to the loads with the operational profile in Table 8.4, to still satisfy the overall 10^{-8} probability of exceedance criterion, it is required that $p(N_{G_{overall,\ \text{7.71-hours}}}(T) \geq 1) \leq 1$.

Since the waves which lead to these load values in this chapter are so rare, all the load combination cases for Table 8.10 could be exceeded, and the overall 10^{-8} load probability of exceedance requirement would still be satisfied. Note that due to the rareness of the waves which excite these loads, *all* the load cases in this chapter, i.e. those from Table 8.3, 8.7, 8.9, and 8.10, satisfy the overall 10^{-8} probability of exceedance. However, not all of these cases realistically describe the lifetime combined loading experienced by this trimaran, and clearly some of the load case definitions are more conservative and exhaustive than others. As well, this 10^{-8} probability of exceedance bound did not equally affect all of the global loads. A similar result was also noted in Chapter 6.7.3, in which a high PNE bound applied to all loads acting on a system did not affect those loads equally or lead to a safe design. Therefore, it may be more useful to define a probability of exceedance based on the load combinations, and not individual load values. The NL-DLG process offers an efficient way to define load cases chosen for a desired lifetime probability of exceedance, while retaining the wave inputs which lead to extreme loading combinations. Then, it is clear where any built-in conservatism exists for a group of load combination cases.

8.12 Estimate of Most-Likely Load Exceedances in Head Seas

Based on the finalized cases from Table 8.10, directed by vessel heading, it is possible to visualize the most-likely exceedances of $G_{head/beam/oblique}$ by $\mathbf{LCF}(t)$ for each case, generated by the NL-DLG process. The head seas case is shown as an example, because its threshold surface, G_{head}, can be visualized in three dimensions. Figure 8.15

shows the load vector $(LCF_{M_{WH}/M_{WS}}(t),\ LCF_{M_{SPH}/M_{SPS}}(t), LCF_{M_{TT}}(t))$ along with some of the G_{head} threshold surface regions, particularly those where $\mathbf{LCF}(t)$ exceeds G_{head}. Each blue line is a single $(LCF_{M_{WH}/M_{WS}}(t), LCF_{M_{SPH}/M_{SPS}}(t), LCF_{M_{TT}}(t))$ load vector driven by an $\eta(t)$ time series chosen by the NL-DLG process for this most-likely exceedance estimate. The red stars are times when $\mathbf{LCF}(t)$ crosses G_{head}. The arrows indicate that the threshold regions are unbounded out from the specific corner origin, which marks the intersection of the LCF bounds from Table 8.10 for the global loads.

From this visualization of the load vector time series, it is clear that exceedances of G_{head} by $\mathbf{LCF}(t)$ only occur due to the simultaneous signs of the loads: $(LCF_{M_{WH}}(t),\ LCF_{M_{SPS}}(t), LCF_{M_{TT}}(t))$ or $(LCF_{M_{WS}}(t), LCF_{M_{SPH}}(t), LCF_{M_{TT}}(t))$. Note that these signs are opposite of the signs from the rule load Cases 1-2 in Table 8.3. In the LR rule load cases, the vertical wave and splitting bending moments are grouped together with the same sign (i.e. both are either hogging or sagging). The shape of the curve $\mathbf{LCF}(t)$ indicates the correlation between the different loads. Figures 8.16, 8.17, and 8.18 are projections of Figure 8.15 on the $(LCF_{M_{SPH}/M_{SPS}}, LCF_{M_{TT}})$, $(LCF_{M_{WH}/M_{WS}}, LCF_{M_{SPH}/M_{SPS}})$ and $(LCF_{M_{WH}/M_{WS}},\ LCF_{M_{TT}})$ planes, respectively.

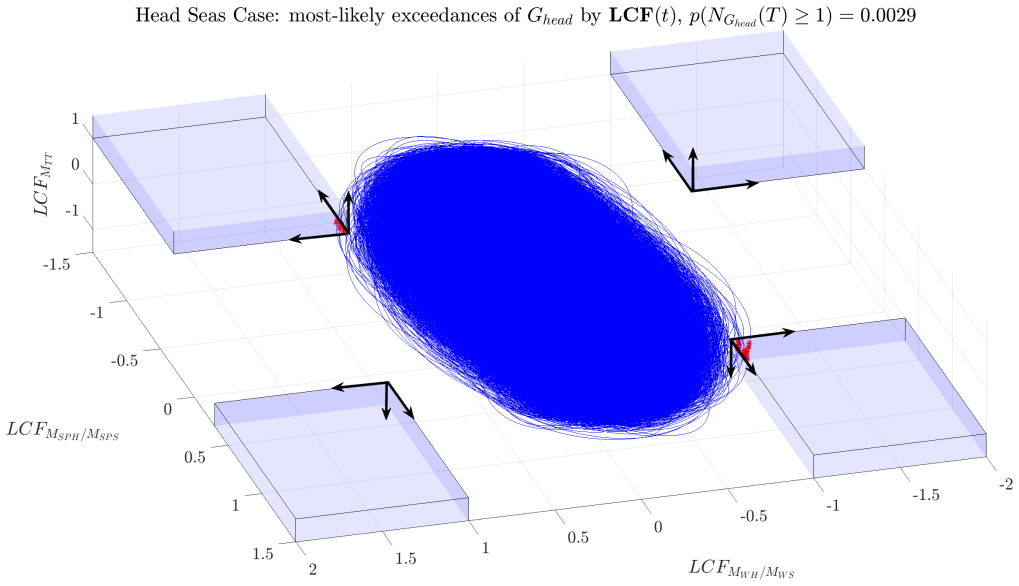

Figure 8.15: Vector of $(LCF_{M_{WH}/M_{WS}}(t),\ LCF_{M_{SPH}/M_{SPS}}(t), LCF_{M_{TT}}(t))$ and threshold regions where exceedances of G_{head} by $\mathbf{LCF}(t)$ occur. Some parts of G_{head} where no exceedances occur are not shown for clearer visualization.

8.12.1 Correlation between Transverse Torsional & Splitting Bending Moment

Figure 8.16 shows that positive lifetime extreme transverse torsional bending moment values are correlated with lifetime extreme sagging splitting bending moment values. This behavior is reinforced by the distributions in Figure 8.13, in which maximized M_{TT} values in head seas correspond to a distribution of M_{SPS} values. This correlation structure would be difficult to determine simply from the distributions in Figure 8.6, because those distributions are conditioned on maximized M_{WH}/M_{WS} in head seas. Additionally, in Figure 8.6 the simultaneous load values across the different distributions are not explicitly linked.

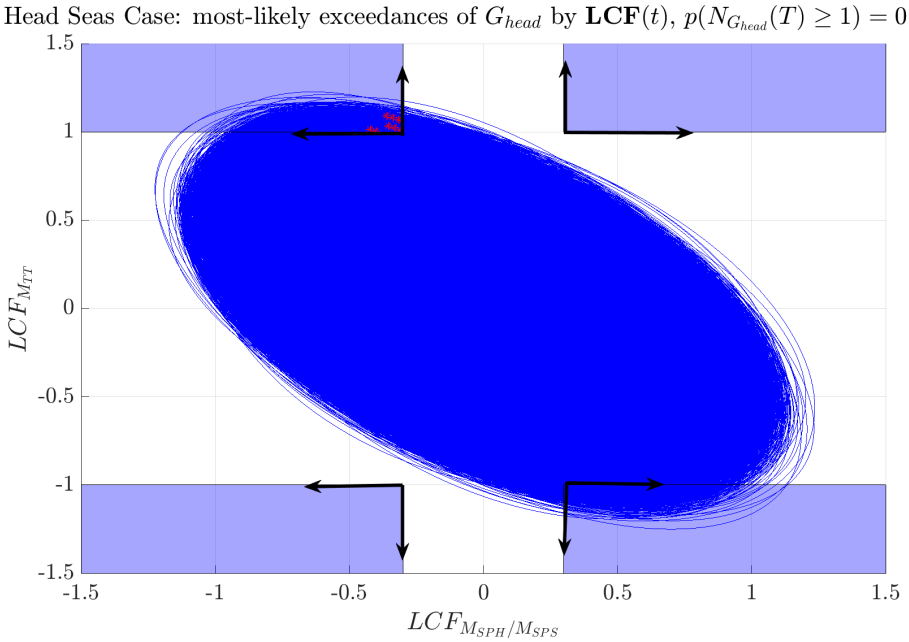

Figure 8.16: Projection of Figure 8.15 on the $(LCF_{M_{SPH}/M_{SPS}}, LCF_{M_{TT}})$ plane.

8.12.2 Correlation between Vertical Wave & Splitting Bending Moment

Figure 8.17 shows that there is little correlation, potentially implying independence, between the vertical wave bending and splitting moment based on the near-circular structure of the load vector curve. This is reinforced by the distributions shown in Figures 8.6, though the distributions in Figure 8.10 for oblique seas indicate that this is not a symmetric relationship, due to the different headings where M_{WH}/M_{WS} and M_{SPH}/M_{SPS} experience their respective design values. When M_{WH}/M_{WS}

is maximized in head seas (Figure 8.6), the corresponding M_{SPH}/M_{SPS} values are about uniformly distributed around zero, while when M_{SPH}/M_{SPS} is maximized in oblique seas (Figure 8.10), the M_{WH}/M_{WS} values take on rather significant negative values.

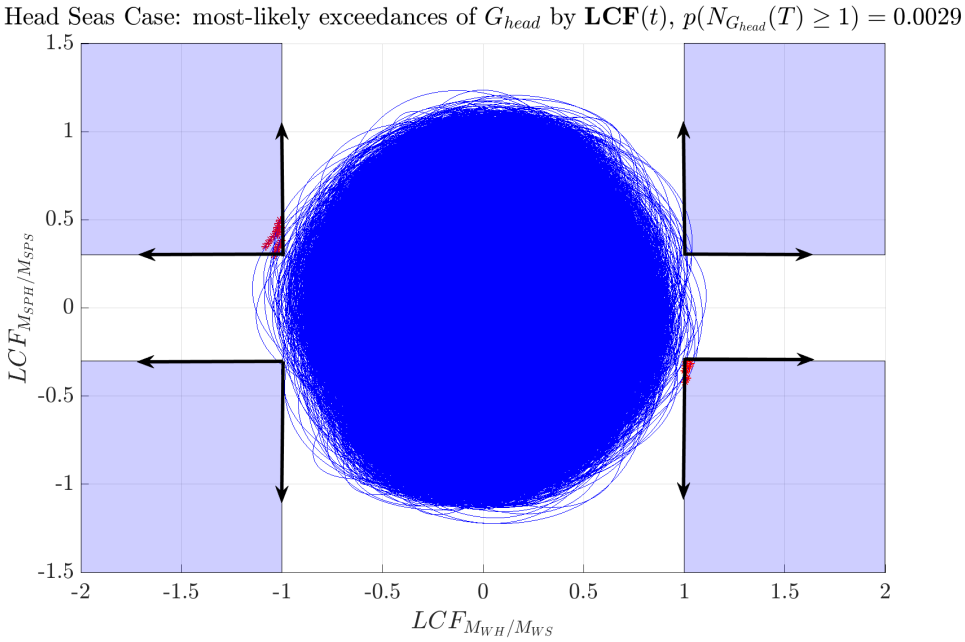

Figure 8.17: Projection of Figure 8.15 on the $(LCF_{M_{WH}/M_{WS}}, LCF_{M_{SPH}/M_{SPS}})$ plane.

8.12.3 Correlation between Vertical Wave & Transverse Torsional Bending Moment

Figure 8.18 shows a positive correlation between the vertical wave bending and the transverse torsional bending moments, as evidenced by Figure 8.6 in which large positive M_{TT} values are simultaneously recovered for maximized M_{WH}. In the load distributions for M_{TT} in head seas (where M_{TT} experiences its design value, Figure 8.13), there is also a strong connection between large positive M_{TT} values and M_{WH} values.

8.12.4 Events of Interest

Figures 8.15-8.18 show that in the head seas condition, this trimaran hull experiences large loading due to the vertical wave, splitting, and transverse torsional bending moments. Based on the threshold surface defined in Table 8.11, there is a

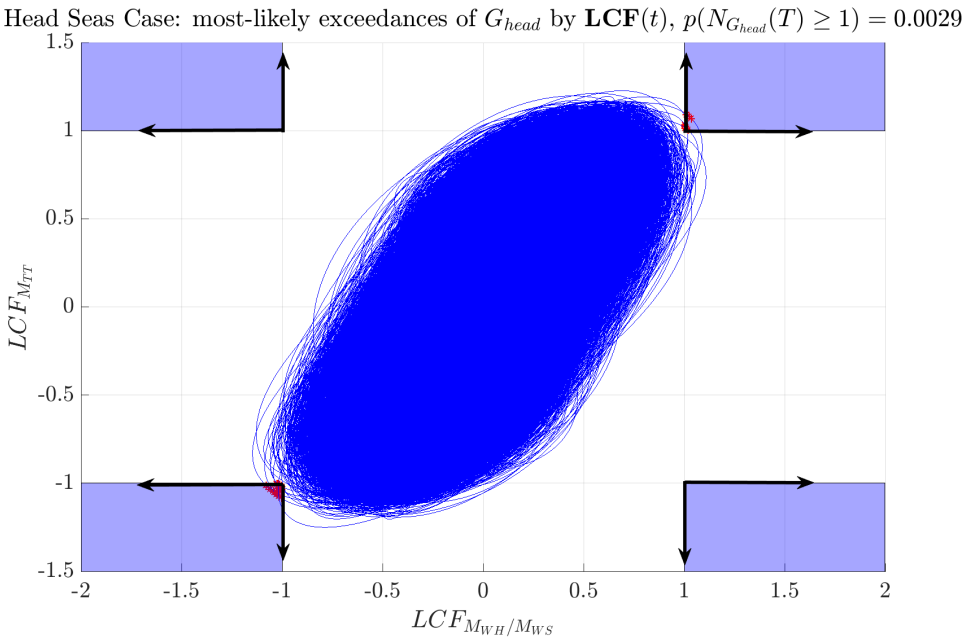

Figure 8.18: Projection of Figure 8.15 on the $(LCF_{M_{WH}/M_{WS}}, LCF_{M_{TT}})$ plane.

low probability that the load vector $\mathbf{LCF}(t)$ exceeds G_{head} over the given exposure, relating to times when all LCF bounds are simultaneously exceeded. However, there are many times when at least one load exceeds its individual LCF bound, again evidenced from Figures 8.15-8.18. Even the splitting moment, which experiences its largest values in oblique seas, still experiences 100% of its design value in the head seas condition. Any region that is not included in the blue threshold surfaces which make up G_{head} can be considered the 'safe' region. However, the safe region includes many load combinations which could also be severe conditions to test structural adequacy.

The value of the NL-DLG process is that lifetime load combinations can be visualized. Such visualizations immediately relay to designers what kind of loading the trimaran will experience, and at what levels. A discrete number of load combination cases may not fully or accurately describe the information that can be gleaned from Figures 8.15-8.18. The many different load combination cases offered in this chapter illustrate the difficulty of choosing the *right* set of load combination cases to exhaustively describe the lifetime combined loading experienced by a trimaran hull. In general, there may be no *right* set of load combination cases to accomplish this aim. But the NL-DLG process can clearly illustrate the lifetime loading experienced by a trimaran hull. The load visualizations from Figures 8.15-8.18 may be more useful to designers than any set of load combination cases, which are, in general, an attempt

to describe lifetime loading.

8.13 Relevance

Using the NL-DLG process to examine combined loading for a specific trimaran hull reveals key features of these combined loads, specifically how these loads interact in different headings during lifetime responses. The DLG assembled distributions of the simultaneous load combinations for seven global loads, conditioned on heading and a single load being maximized. These distributions indicate that combined loading on trimarans may be strongly affected by geometry and side-hull location. Neither the rule load approach (i.e. Table 8.3), nor the alternative loading procedure (i.e. Table 8.8) gave a realistic depiction of the lifetime combined loading experienced by the trimaran hull considered in this chapter.

The NL-DLG process was able to evaluate the probability of exceeding all LCF values for each case in a specific approach, which offered guidance on more appropriate load combination cases. The final recommended load combination cases were chosen to evaluate each global load in the heading where it experiences its design value. Additionally, these cases were designed for a low probability of exceeding all LCF values, to be exhaustive in terms of the seven global loads, and to be mutually exclusive. This allows a designer to constrain a testing profile with an allowable risk factor considering load combinations, rather than individual load values.

The NL-DLG process is useful for defining load combination cases with an explicit probabilistic basis. This gives clear information on the conservatism associated with loading combination cases. There are an infinite number of load combination cases which will lead to a given probability of simultaneously exceeding all load bounds. In a way, then, the final load cases from Table 8.10 are meant to illustrate the capability of the NL-DLG process when examining combined loading.

The visualization of load vector time series, like shown in Figures 8.15-8.18 shows the load relationships conditioned on lifetime extreme values. This may be helpful for a designer when considering the structural design of a trimaran hull, and how different structures may be vulnerable to certain loading combinations. The NL-DLG process determined conservative, exhaustive, and realistic load combination cases, associated with a given probability of exceedance, to test the structural integrity of the given trimaran. This is useful information for connecting allowable risk for a vessel design with load combination cases meant to evaluate structural integrity.

CHAPTER IX

Conclusions

9.1 Summary

For complex marine systems, the evaluation of lifetime extreme loads and responses is crucial for safe and well-performing designs. However, it is difficult to efficiently estimate these loads and responses without employing major system simplifications which limit the applicability to realistic physical scenarios, or lower-order methods which lose relevant physics. For complex systems in which the excitation is a vector of potentially correlated and non-Gaussian loading, it is a major challenge to analyze the interaction of that load vector with a non-linear, multi-dimension threshold definition, which defines allowable system responses, over a long exposure. To link a specific system response to an overall depiction of the system during a lifetime event requires profiles of the excitation input. But to maintain the excitation environment generally precludes most analytical methods which consider threshold-crossings of a vector of random processes.

This dissertation developed the non-linear Design Loads Generator process to utilize the capability of the DLG for systems governed by combined loading. The NL-DLG process is geared toward complex systems in which:

- Extreme system responses are defined by exceedances of a complex threshold surface.
- The multi-dimension threshold surface is a non-linear function of the combined non-linear loading.
- These loads may be correlated and non-Gaussian.

Given some threshold surface, the NL-DLG process can estimate the probability that a vector of non-Gaussian stochastic loads exceeds that threshold over a given exposure period. For marine systems, this can mean the probability of physical failure, or simply the probability of exceeding certain allowable combined load thresholds. Examples of these threshold exceedances were examined: structural collapse of a stiffened ship panel due to combined lateral and in-plane loading and combined loading on trimarans. Both examples included a vector of combined loads, long exposures in harsh environments, and a threshold definition. The NL-DLG process was able to estimate the probability of threshold exceedance and maintain an ensemble of short wave environments that lead to the most-likely threshold crossings.

9.2 Contributions

This dissertation makes contributions in the following specific areas. First, Chapter III showed that waves which lead to extremes of surrogate processes exist in physical oceanographic data (*Seyffert and Troesch*, 2016c). As an example, a maximum in the Gaussian derived process, which is similar to a moving average and samples a single random processes k times separated by τ seconds, identifies rare wave groups in a wave elevation record. Chapter III showed that the expected shape of a rare wave group matches physical wave profiles, both in an ensemble and individual sense (*Seyffert and Troesch*, 2016a; *Seyffert et al.*, 2016).

This is an important validation for the DLG method, which constructs wave profiles that lead to extreme values of surrogate processes. These surrogate processes describe some linear input/ output function and are a form of reduced-ordering modeling to indicate extreme behavior in a related non-linear system. Presumably, waves which lead to extreme values of these surrogate processes indicate extreme behavior of the non-linear system in question. For a surrogate process like the Gaussian derived process, extremes of the surrogate process indicate the onset of a rare wave group. It was shown that wave profiles which lead to these surrogate process maxima, i.e. wave records which contain wave groups of prescribed period and group index, can be identified in an irregular ocean environment. This strongly implies that the wave records constructed by the DLG to lead to extreme linear system responses are physically realizable.

Chapter V used the capability of the DLG to develop the NL-DLG process (*Seyffert and Troesch*, 2018). The NL-DLG process can consider a system in which extreme

responses are due to varying combinations of non-Gaussian combined loading, generalized by the exceedance of a complex threshold surface by a vector of non-Gaussian loads. The NL-DLG process estimates the probability that a vector of non-linear excitation exceeds a multi-dimension non-linear threshold over a long exposure. For the examples shown in Chapters VI and VII, in which the combined loading vector has different levels of non-linearity, the NL-DLG process accurately estimates threshold exceedance probabilities when compared to a full MCS analysis (*Seyffert et al.*, 2018a). The NL-DLG proved accurate with significant computational savings.

The NL-DLG process also considers a range of extreme responses, represented by a threshold surface, and assembles an ensemble of excitation inputs which lead to the most-likely exceedances. This allows an estimate of the probability of threshold exceedance given the operational profile, and not a probability conditioned on a single excitation input. The result reflects the information gained from brute-force MCS without the computational expense: excitation inputs that lead to a converged probability estimate of complex system threshold exceedance over a long exposure. This advancement indicates the potential for applying the NL-DLG process to determine short excitation inputs for use in non-linear structural and seakeeping models. Based on the formulation, the statistics of responses from these directed high-fidelity simulations should converge to the statistics collected from brute-force simulation.

These excitation inputs can also illustrate the correlation structures between the random processes considered in the excitation vector (*Seyffert et al.*, 2018b). This information directs the construction of allowable design thresholds, given an acceptable probability of non-exceedance. As shown in Chapter VIII, the NL-DLG process offers metrics on combined loading exceedances to construct load boundaries based on an allowable level of risk. These contributions, coupled with the low computational cost of the NL-DLG process, can efficiently evaluate specific design options, as shown in Chapter VII, or can evaluate lifetime loading scenarios, as in Chapter VIII.

9.3 Future Work

The development of this dissertation came from specific unexpected and curious results of intermediate analyses. Many of those unexpected results drove the growth of the NL-DLG process, but there were a few ideas that were not implemented, but should be considered in the future.

Within the NL-DLG process, it would be useful to consider more than four non-

linear load combination cases/ surrogate processes. For the examples considered, four surrogates accurately estimate performance statistics validated from full MCS. But for higher-dimension or more complicated threshold surfaces, more surrogate processes may be required for an accurate probabilistic assessment.

The combinatorial challenge of including more surrogate processes currently limits the maximum number of surrogate processes included in the NL-DLG process estimation to four. Many combinatorial problems utilize the same set partitioning associated with the Bell number as in the NL-DLG process, indicating the likelihood that methods and algorithms exist which could enable the efficient consideration of more surrogate processes within the NL-DLG process. The computational cost associated with additional surrogate processes is mainly associated with generating DLG realizations, which is not significant. Clearly, the computational advantages of the DLG and the NL-DLG process will diminish in the limit of a large number of surrogate processes. But, the ability to consider more than four surrogates would represent a major improvement of the NL-DLG process. This addition would improve the accuracy of the estimations and expand the applicability to more complex or high-dimension systems.

Further improvements to the NL-DLG process are related to relaxing assumptions required for the framework. For some dynamic responses, initial-conditions and cycle-counting may be significant drivers to threshold exceedances. The NL-DLG process assumes that the system threshold surface is time-invariant. For fatigue or dynamic responses heavily impacted by initial conditions, this assumption must be modified to utilize the capability of the NL-DLG process.

It is also of interest to consider what effects the non-linearity of a stochastic excitation has on the return period of an extreme response. Currently, the exposure period drives the DLG's construction of inputs which lead to the distribution of extreme responses for the linear surrogate processes. These inputs give a lower bound on the distribution of associated non-linear responses. In the example of Chapter VI, it was shown that with an accurate TEV estimate, the NL-DLG process gives a lower bound on the probability of exceeding the threshold definition. The probability estimate was within 1% error from the full MCS verification, but for systems with other types of non-linearities, the estimate from the NL-DLG process could lead to a significant under-prediction of the probability of threshold exceedances.

It may be possible to increase the exposure length so that the excitation inputs

constructed by the DLG more closely bound the non-linear response distributions. This would be a useful improvement, especially for systems with a given exposure and specified risk parameter or probability of non-exceedance. For linear systems, this explicitly relates to a longer exposure period, as explained in Chapter 2.2. But for non-linear functions, the addition of risk parameters to the linear response distribution may not translate to the same reliability for the non-linear distributions. It may be worthwhile to examine what sort of non-linearities require an increased exposure for the associated linear surrogate process to closely bound the non-linear responses. It would also be useful to know how this increased exposure relates to an imposed risk parameter on the non-linear system.

These areas of future work would improve the capability of the NL-DLG process, and expand its applicability to more complex and non-linear marine systems.

APPENDIX

APPENDIX A

Probability Space of Maxima Configurations for Related Surrogate Processes

A.1 Probability Space of Maxima Configurations

To determine the probability of experiencing the specific maxima configurations ci, like shown in Figure 5.5, the probability space is first defined. Three regions of the failure surface, G, are emphasized by three non-linear load combination cases. These cases are approximated using three surrogate processes, $z_i(t)$ $i = 1, 2, 3$, and for clarity here, $n = 3$ will be used for the definitions.

The NL-DLG process generates many $\eta_1(t)$, $\eta_2(t)$, and $\eta_3(t)$ for a threshold surface, G, with three regions emphasized by three non-linear load combination cases, approximated by three associated surrogate processes $z_1(t)$, $z_2(t)$, and $z_3(t)$. Using the notation from Chapter 5.4.1, consider that the $\eta_1(t)$ time series are constructed so that $z_{11}(t)$ has a maximum $\widehat{z_{11}} \in g(z_{1,T})$. These $\eta_1(t)$ time series also drive $z_{12}(t)$ and $z_{13}(t)$ time series, which may contain maxima $\widehat{z_{12}} \in g(z_{2,T})$ and $\widehat{z_{13}} \in g(z_{3,T})$, respectively. In this way, the maxima $\widehat{z_{11}}$ can be classified into disjoint and exhaustive groups depending on whether the $\eta_1(t)$ time series which leads to $\widehat{z_{11}} \in g(z_{1,T})$ also leads to $\widehat{z_{12}} \in g(z_{2,T})$ and/ or $\widehat{z_{13}} \in g(z_{3,T})$.

Using similar notation from Chapter 5.7.1, each $\eta_1(t)$ time series constructed from the DLG can be seen as an individual trial of an experiment with the possible outcomes: $\{\widehat{Z_1}, \widehat{Z_1 Z_2}, \widehat{Z_1 Z_3}, \widehat{Z_1 Z_2 Z_3}\}$. Here the order of the subscripts matters. The first subscript indicates which $\eta_i(t)$ time series are being examined. This means that the

event $\{\widehat{Z_1 Z_2}\}$ comes from a $\eta_1(t)$ time series, constructed to produce $\widehat{z_{11}} \in g(z_{1,T})$, that also contains $\widehat{z_{12}} \in g(z_{2,T})$, and $\widehat{z_{13}} \notin g(z_{3,T})$. Conversely, the event $\{\widehat{Z_2 Z_1}\}$ results from a $\eta_2(t)$ time series, constructed to produce $\widehat{z_{22}} \in g(z_{2,T})$, that also contains $\widehat{z_{21}} \in g(z_{1,T})$, and $\widehat{z_{23}} \notin g(z_{3,T})$. Note also that the event $\{\widehat{Z_1 Z_2 Z_3}\}$ comes from $\eta_1(t)$, whereas $\{\widehat{Z_2 Z_1 Z_3}\}$ comes from $\eta_2(t)$ and $\{\widehat{Z_3 Z_1 Z_2}\}$ comes from $\eta_3(t)$. A measurable probability space, $(\Omega_1, \mathcal{F}_1, P_1)$, for the possible event outcomes from the $\eta_1(t)$ time series is defined as:

$$
\begin{aligned}
\Omega_1 &= \{\widehat{Z_1}, \widehat{Z_1 Z_2}, \widehat{Z_1 Z_3}, \widehat{Z_1 Z_2 Z_3}\} \\
\mathcal{F}_1 &= \{\widehat{Z_1}, \widehat{Z_1 Z_2}, \widehat{Z_1 Z_3}, \widehat{Z_1 Z_2 Z_3}, \widehat{Z_1} \cup \widehat{Z_1 Z_2}, \widehat{Z_1} \cup \widehat{Z_1 Z_3}, \widehat{Z_1} \cup \widehat{Z_1 Z_2 Z_3}, \widehat{Z_1 Z_2} \cup \widehat{Z_1 Z_3}, \\
&\quad \widehat{Z_1 Z_2} \cup \widehat{Z_1 Z_2 Z_3}, \widehat{Z_1 Z_3} \cup \widehat{Z_1 Z_2 Z_3}, \widehat{Z_1} \cup \widehat{Z_1 Z_2} \cup \widehat{Z_1 Z_3}, \widehat{Z_1} \cup \widehat{Z_1 Z_2} \cup \widehat{Z_1 Z_2 Z_3}, \\
&\quad \widehat{Z_1} \cup \widehat{Z_1 Z_3} \cup \widehat{Z_1 Z_2 Z_3}, \widehat{Z_1 Z_2} \cup \widehat{Z_1 Z_3} \cup \widehat{Z_1 Z_2 Z_3}, \Omega_1, \emptyset\} \\
P_1 &= (p(\{\widehat{Z_1}\}), p(\{\widehat{Z_1 Z_2}\}), p(\{\widehat{Z_1 Z_3}\}), p(\{\widehat{Z_1} \cup \widehat{Z_1 Z_2}\}), \cdots)
\end{aligned}
\tag{A.1}
$$

where

$$
\begin{aligned}
&\Omega_1 = \text{sample space of all possible outcomes when considering a } \eta_1(t) \text{ time series} \\
&\mathcal{F}_1 = \text{event space, which is a } \sigma\text{-algebra} \\
&P_1 = \text{probability measure} \\
&p(\{\widehat{Z_1}\}) = \frac{\text{number of } \eta_1(t) \text{ time series which satisfy } \widehat{Z_1} \text{ condition}}{\text{number of } \eta_1(t) \text{ time series}} \\
&p(\{\widehat{Z_1 Z_j}\}) = \frac{\text{number of } \eta_1(t) \text{ time series which satisfy } \widehat{Z_1 Z_j} \ j = 2, 3 \text{ condition}}{\text{number of } \eta_1(t) \text{ time series}} \\
&p(\{\widehat{Z_1 Z_2 Z_3}\}) = \frac{\text{number of } \eta_1(t) \text{ time series which satisfy } \widehat{Z_1 Z_2 Z_3} \text{ condition}}{\text{number of } \eta_1(t) \text{ time series}} \\
&p(\{\widehat{Z_1}\}) + p(\{\widehat{Z_1 Z_2}\}) + p(\{\widehat{Z_1 Z_3}\}) + p(\{\widehat{Z_1 Z_2 Z_3}\}) = 1, \text{ by definition}
\end{aligned}
$$

The probability measure for any union of the events in the $(\Omega_1, \mathcal{F}_1, P_1)$ space is a simple sum because all of the events are by definition disjoint. Similarly, measurable probability spaces for the possible event outcomes from the DLG time series for $z_2(t)$ and $z_3(t)$ are defined as:

$$
(\Omega_2, \mathcal{F}_2, P_2) \tag{A.2}
$$

where

$$
\begin{aligned}
\Omega_2 &= \{\widehat{Z_2}, \widehat{Z_2 Z_1}, \widehat{Z_2 Z_3}, \widehat{Z_2 Z_1 Z_3}\} \\
\mathcal{F}_2 &= \{\widehat{Z_2}, \widehat{Z_2 Z_1}, \widehat{Z_2 Z_3}, \widehat{Z_2 Z_1 Z_3}, \widehat{Z_2} \cup \widehat{Z_2 Z_1}, \widehat{Z_2} \cup \widehat{Z_2 Z_3}, \widehat{Z_2} \cup \widehat{Z_2 Z_1 Z_3}, \widehat{Z_2 Z_1} \cup \widehat{Z_2 Z_3}, \\
&\quad \widehat{Z_2 Z_1} \cup \widehat{Z_2 Z_1 Z_3}, \widehat{Z_2 Z_3} \cup \widehat{Z_2 Z_1 Z_3}, \widehat{Z_2} \cup \widehat{Z_2 Z_1} \cup \widehat{Z_2 Z_3}, \widehat{Z_2} \cup \widehat{Z_2 Z_1} \cup \widehat{Z_2 Z_1 Z_3}, \\
&\quad \widehat{Z_2} \cup \widehat{Z_2 Z_3} \cup \widehat{Z_2 Z_1 Z_3}, \widehat{Z_2 Z_1} \cup \widehat{Z_2 Z_3} \cup \widehat{Z_2 Z_1 Z_3}, \Omega_2, \emptyset\} \\
P_2 &= (p(\{\widehat{Z_2}\}), p(\{\widehat{Z_2 Z_1}\}), p(\{\widehat{Z_2 Z_3}\}), p(\{\widehat{Z_2} \cup \widehat{Z_2 Z_1}\}), \cdots)
\end{aligned}
$$

$$(\Omega_3, \mathcal{F}_3, P_3) \tag{A.3}$$

where

$$\begin{aligned}
\Omega_3 &= \{\widehat{Z_3}, \widehat{Z_3Z_1}, \widehat{Z_3Z_2}, \widehat{Z_3Z_1Z_2}\} \\
\mathcal{F}_3 &= \{\widehat{Z_3}, \widehat{Z_3Z_1}, \widehat{Z_3Z_2}, \widehat{Z_3Z_1Z_2}, \widehat{Z_3} \cup \widehat{Z_3Z_1}, \widehat{Z_3} \cup \widehat{Z_3Z_2}, \widehat{Z_3} \cup \widehat{Z_3Z_1Z_2}, \widehat{Z_3Z_1} \cup \widehat{Z_3Z_2}, \\
&\quad \widehat{Z_3Z_1} \cup \widehat{Z_3Z_1Z_2}, \widehat{Z_3Z_2} \cup \widehat{Z_3Z_1Z_2}, \widehat{Z_3} \cup \widehat{Z_3Z_1} \cup \widehat{Z_3Z_2}, \widehat{Z_3} \cup \widehat{Z_3Z_1} \cup \widehat{Z_3Z_1Z_2}, \\
&\quad \widehat{Z_3} \cup \widehat{Z_3Z_2} \cup \widehat{Z_3Z_1Z_2}, \widehat{Z_3Z_1} \cup \widehat{Z_3Z_2} \cup \widehat{Z_3Z_1Z_2}, \Omega_3, \emptyset\} \\
P_3 &= (p(\{\widehat{Z_3}\}), p(\{\widehat{Z_3Z_1}\}), p(\{\widehat{Z_3Z_2}\}), p(\{\widehat{Z_3} \cup \widehat{Z_3Z_1}\}), \cdots)
\end{aligned}$$

The individual probability measures for the events in probability spaces $(\Omega_2, \mathcal{F}_2, P_2)$ and $(\Omega_3, \mathcal{F}_3, P_3)$ are calculated in the same way as for $(\Omega_1, \mathcal{F}_1, P_1)$. Note that the events in the $(\Omega_i, \mathcal{F}_i, P_i)$ spaces are equivalent to the sub-groups within the maxima configurations (i.e. $c3 : \{\widehat{Z_1}, \widehat{Z_2Z_3}\}$). What is of interest here is to find the probability of experiencing each maxima configuration $c1 - c5$ during an exposure.

This problem is similar to a 3-stage probability experiment of varying-length. A trial is drawn successively from each of the 3 stages and the experiment may prematurely terminate (may not include all three stages) and be labelled a 'success' if some criteria is satisfied during one of the three stages. A success may occur on the 1^{st}, 2^{nd}, or on the 3^{rd} stage. It is also possible that the three stages go by and no success occurs. For example, imagine the experiment is that a coin (heads {H} or tails {T}) is flipped up to three times. A success occurs, and the experiment ends, the 1^{st} time a heads is flipped. A success may occur on the 1^{st} flip: {H}, on the 2^{nd} flip: {T,H}, on the 3^{rd} flip: {T,T,H}, or not at all: {T,T,T}.

For the NL-DLG process, the criterion for success is the occurrence of a maxima configuration in which each surrogate process maximum occurs exactly once. This happens if each maximum occurs separately: $\{\widehat{Z_1}, \widehat{Z_2}, \widehat{Z_3}\}$, two maxima cluster together with the third separate: $\{\widehat{Z_1Z_2}, \widehat{Z_3}\}$, $\{\widehat{Z_1Z_3}, \widehat{Z_2}\}$, or $\{\widehat{Z_2Z_3}, \widehat{Z_1}\}$, or all maxima cluster together: $\{\widehat{Z_1Z_2Z_3}\}$. These are the five maxima configurations $c1 - c5$ possible that describe how the maxima of three surrogate processes may be clustered. Note these five configurations have different lengths and can occur with different orders (e.g. the maxima of surrogate processes $z_1(t)$ and $z_3(t)$ may be clustered, with the maximum of $z_2(t)$ occurring separately, and this event may come from different types and orderings of DLG simulations $\eta_i(t)$: $\{\widehat{Z_1Z_3}, \widehat{Z_2}\}$, $\{\widehat{Z_3Z_1}, \widehat{Z_2}\}$, $\{\widehat{Z_2}, \widehat{Z_1Z_3}\}$, or $\{\widehat{Z_2}, \widehat{Z_3Z_1}\}$). The aim of this appendix is to answer the questions:

- If a trial is drawn from each $(\Omega_i, \mathcal{F}_i, P_i)$ with $i = 1, 2, 3$, what is the probability of

experiencing a successful maxima configuration in which each maximum occurs exactly once during the 3-stage experiment?

- What is the probability of experiencing each specific successful maxima configuration $c1 - c5$?

To answer these questions, first dictate that the order of the three stages matters. For the overall probability of threshold exceedances, the ordering of the surrogate process maxima over an exposure does not matter, but the ordering assumption makes each configuration distinct, which simplifies the 3-stage experiment. With an ordering of the stages, there are six equally likely orders, corresponding to the six different ways that three surrogate process probability spaces can be ordered (order$\cdots = o123, o132, o213, o231, o312, o321$). The probability of experiencing each ordering is the same because each surrogate process maximum has the same return period (this is confirmed from MCS results in Chapter 7.7.1). Each probability space ordering represents another probability space *given* this ordering. As an example, the overall probability space for the ordering $o123$ is $(\Omega_{123}, \mathcal{F}_{123}, P_{123})$, defined as:

$$\begin{aligned}
\Omega_{123} &= \text{each possible triplet of events that takes a single draw from } (\Omega_1, \mathcal{F}_1, P_1), \\
&\quad \text{then } (\Omega_2, \mathcal{F}_2, P_2), \text{ and then } (\Omega_3, \mathcal{F}_3, P_3) \\
&= \{\Omega_{1i}, \Omega_{2j}, \Omega_{3k}\} \text{ with } i = 1,2,3,4,\ j = 1,2,3,4, \text{ and } k = 1,2,3,4 \\
\mathcal{F}_{123} &= 2^{\Omega_{123}} = \text{power set of } \Omega_{123} \\
P_{123} &= p(\{\Omega_{1i}\}) \times p(\{\Omega_{2j}\}) \times p(\{\Omega_{3k}\}) \text{ with } i = 1,2,3,4,\ j = 1,2,3,4, \text{ and } k = 1,2,3,4
\end{aligned} \tag{A.4}$$

where

$$\begin{aligned}
\{\Omega_{11}, \Omega_{12}, \Omega_{13}, \Omega_{14}\} &= \{\widehat{Z_1}, \widehat{Z_1 Z_2}, \widehat{Z_1 Z_3}, \widehat{Z_1 Z_2 Z_3}\} \\
\{\Omega_{21}, \Omega_{22}, \Omega_{23}, \Omega_{24}\} &= \{\widehat{Z_2}, \widehat{Z_2 Z_1}, \widehat{Z_2 Z_3}, \widehat{Z_2 Z_1 Z_3}\} \\
\{\Omega_{31}, \Omega_{32}, \Omega_{33}, \Omega_{34}\} &= \{\widehat{Z_3}, \widehat{Z_3 Z_1}, \widehat{Z_3 Z_2}, \widehat{Z_3 Z_1 Z_2}\} \\
\sum_{i=1}^{4} \sum_{j=1}^{4} \sum_{k=1}^{4} p(\{\Omega_{1i}\}) \times p(\{\Omega_{2j}\}) \times p(\{\Omega_{3k}\}) &= 1
\end{aligned}$$

This is a measurable probability space because the individual probability spaces

for each DLG time series $\eta_i(t)$, $(\Omega_i, \mathcal{F}_i, P_i)$, are measurable probability spaces:

$$\begin{aligned}
&\sum_{i=1}^{4} p(\{\Omega_{1i}\}) = \sum_{j=1}^{4} p(\{\Omega_{2j}\}) = \sum_{k=1}^{4} p(\{\Omega_{3k}\}) = 1 \\
&\sum_{i=1}^{4}\sum_{j=1}^{4}\sum_{k=1}^{4} p(\{\Omega_{1i}\}) \times p(\{\Omega_{2j}\}) \times p(\{\Omega_{3k}\}) \\
&= \sum_{i=1}^{4} p(\{\Omega_{1i}\}) \times \sum_{j=1}^{4} p(\{\Omega_{2j}\}) \times \sum_{k=1}^{4} p(\{\Omega_{3k}\}) = 1
\end{aligned} \tag{A.5}$$

The overall probability spaces for the other orderings are similarly defined. These distinct orderings imply that a successful maxima configuration can occur with different probability space orderings. For example, $\{\widehat{Z_1}, \widehat{Z_2Z_3}\}$, $\{\widehat{Z_2Z_3}, \widehat{Z_1}\}$, $\{\widehat{Z_3Z_2}, \widehat{Z_1}\}$, and $\{\widehat{Z_1}, \widehat{Z_3Z_2}\}$ are different events due to the distinct orderings. But these events all lead to the same successful maxima configuration $c\mathcal{3}$, in which the surrogate process maxima of $z_2(t)$ and $z_3(t)$ cluster together and the maximum of $z_1(t)$ occurs separately over the exposure. $\{\widehat{Z_1}, \widehat{Z_2Z_3}\}$ comes from drawing $\{\widehat{Z_1}\}$ from the $(\Omega_1, \mathcal{F}_1, P_1)$ space, and then $\{\widehat{Z_2Z_3}\}$ from the $(\Omega_2, \mathcal{F}_2, P_2)$ space. $\{\widehat{Z_2Z_3}, \widehat{Z_1}\}$ comes from drawing $\{\widehat{Z_2Z_3}\}$ from the $(\Omega_2, \mathcal{F}_2, P_2)$ space then $\{\widehat{Z_1}\}$ from the $(\Omega_1, \mathcal{F}_1, P_1)$ space. $\{\widehat{Z_3Z_2}, \widehat{Z_1}\}$ comes from drawing $\{\widehat{Z_3Z_2}\}$ from the $(\Omega_3, \mathcal{F}_3, P_3)$ space, then $\{\widehat{Z_1}\}$ from $(\Omega_1, \mathcal{F}_1, P_1)$ space. $\{\widehat{Z_1}, \widehat{Z_3Z_2}\}$ comes from drawing $\{\widehat{Z_1}\}$ from the $(\Omega_1, \mathcal{F}_1, P_1)$ space, then $\{\widehat{Z_3Z_2}\}$ from the $(\Omega_3, \mathcal{F}_3, P_3)$ space.

Similarly, the definitions of the five successful maxima configurations for $n = 3$ are expanded to consider all possible probability space orderings, as below. The uppercase and boldface **C** indicates the ordering distinction to distinguish the configurations from those referenced in Figure 5.5, which do not have an ordering distinction.

$$\begin{aligned}
\mathbf{C}\boldsymbol{1} &= \{\widehat{Z_1Z_2}, \widehat{Z_3}\}, \{\widehat{Z_2Z_1}, \widehat{Z_3}\}, \{\widehat{Z_3}, \widehat{Z_1Z_2}\}, \text{ or } \{\widehat{Z_3}, \widehat{Z_2Z_1}\} \\
\mathbf{C}\boldsymbol{2} &= \{\widehat{Z_1Z_3}, \widehat{Z_2}\}, \{\widehat{Z_3Z_1}, \widehat{Z_2}\}, \{\widehat{Z_2}, \widehat{Z_1Z_3}\}, \text{ or } \{\widehat{Z_2}, \widehat{Z_3Z_1}\} \\
\mathbf{C}\boldsymbol{3} &= \{\widehat{Z_2Z_3}, \widehat{Z_1}\}, \{\widehat{Z_3Z_2}, \widehat{Z_1}\}, \{\widehat{Z_1}, \widehat{Z_2Z_3}\}, \text{ or } \{\widehat{Z_1}, \widehat{Z_3Z_2}\} \\
\mathbf{C}\boldsymbol{4} &= \{\widehat{Z_1Z_2Z_3}\}, \{\widehat{Z_2Z_1Z_3}\}, \text{ or } \{\widehat{Z_3Z_1Z_2}\} \\
\mathbf{C}\boldsymbol{5} &= \{\widehat{Z_1}, \widehat{Z_2}, \widehat{Z_3}\}, \{\widehat{Z_1}, \widehat{Z_3}, \widehat{Z_2}\}, \{\widehat{Z_2}, \widehat{Z_1}, \widehat{Z_3}\}, \{\widehat{Z_2}, \widehat{Z_3}, \widehat{Z_1}\}, \{\widehat{Z_3}, \widehat{Z_1}, \widehat{Z_2}\}, \text{ or } \{\widehat{Z_3}, \widehat{Z_2}, \widehat{Z_1}\}
\end{aligned} \tag{A.6}$$

With the ordering distinction, next choose a surrogate process probability space ordering, say $o123$, which indicates the 1^{st} trial is drawn from $(\Omega_1, \mathcal{F}_1, P_1)$, the 2^{nd} from $(\Omega_2, \mathcal{F}_2, P_2)$, and the 3^{rd} from $(\Omega_3, \mathcal{F}_3, P_3)$. What is probability of experiencing one of the five successful maxima configurations with this ordering?

For the probability of experiencing a successful maxima configuration for $n = 3$, these configurations may be up to 3-stages long (i.e. $\{\widehat{Z_1 Z_2 Z_3}\}$, $\{\widehat{Z_1}, \widehat{Z_2 Z_3}\}$, $\{\widehat{Z_1}, \widehat{Z_2}, \widehat{Z_3}\}, \cdots$). For the probability space for specific orderings like $(\Omega_{123}, \mathcal{F}_{123}, P_{123})$, the experiment requires a trial be drawn from each individual probability space. $(\Omega_{123}, \mathcal{F}_{123}, P_{123})$ is only a valid probability space *because* each possible outcome is 3-stages long. The sum of the probabilities of each possible triplet is unity, i.e. Eq.(A.5). But, if a trial is less than 3-stages long, the sum of the probabilities of all possible trials is *not* unity.

With the order configuration $o123$, the only successful maxima configurations are $\{\widehat{Z_1}, \widehat{Z_2}, \widehat{Z_3}\}$, $\{\widehat{Z_1}, \widehat{Z_2 Z_3}\}$, $\{\widehat{Z_1 Z_3}, \widehat{Z_2}\}$, or $\{\widehat{Z_1 Z_2 Z_3}\}$. But, the outcomes for the $(\Omega_{123}, \mathcal{F}_{123}, P_{123})$ are all 3-stages long. Therefore, the definition of a successful sequence is altered include to all 3-trial sequences possible given that the experiment continues if a successful configuration occurs in less than three draws with the given ordering. The definitions of the successful combinations with the ordering $o123$ are expanded below:

$\{\widehat{Z_1}, \widehat{Z_2}, \widehat{Z_3}\}$: this sequence is already 3 draws long, so it is unchanged

$\{\widehat{Z_1}, \widehat{Z_2 Z_3}\}$: this sequence expands to include each possible draw from $(\Omega_3, \mathcal{F}_3, P_3)$

$$\begin{aligned}\{\widehat{Z_1}, \widehat{Z_2 Z_3}\} &\to \{\widehat{Z_1}, \widehat{Z_2 Z_3}, \widehat{Z_3}\} \\ &\to \{\widehat{Z_1}, \widehat{Z_2 Z_3}, \widehat{Z_3 Z_1}\} \\ &\to \{\widehat{Z_1}, \widehat{Z_2 Z_3}, \widehat{Z_3 Z_2}\} \\ &\to \{\widehat{Z_1}, \widehat{Z_2 Z_3}, \widehat{Z_3 Z_1 Z_2}\}\end{aligned}$$

$\{\widehat{Z_1 Z_3}, \widehat{Z_2}\}$: this sequence expands to include each possible draw from $(\Omega_3, \mathcal{F}_3, P_3)$

$$\begin{aligned}\{\widehat{Z_1 Z_3}, \widehat{Z_2}\} &\to \{\widehat{Z_1 Z_3}, \widehat{Z_2}, \widehat{Z_3}\} \\ &\to \{\widehat{Z_1 Z_3}, \widehat{Z_2}, \widehat{Z_3 Z_1}\} \\ &\to \{\widehat{Z_1 Z_3}, \widehat{Z_2}, \widehat{Z_3 Z_2}\} \\ &\to \{\widehat{Z_1 Z_3}, \widehat{Z_2}, \widehat{Z_3 Z_1 Z_2}\}\end{aligned}$$

$\{\widehat{Z_1 Z_2 Z_3}\}$: this sequence expands to include each possible draw from $(\Omega_2, \mathcal{F}_2, P_2)$ and $(\Omega_3, \mathcal{F}_3, P_3)$

$$\begin{aligned}\{\widehat{Z_1 Z_2 Z_3}\} &\to \{\widehat{Z_1 Z_2 Z_3}, \widehat{Z_2}, \widehat{Z_3}\} \\ &\to \{\widehat{Z_1 Z_2 Z_3}, \widehat{Z_2 Z_1}, \widehat{Z_3}\} \\ &\cdots \\ &\to \{\widehat{Z_1 Z_2 Z_3}, \widehat{Z_2 Z_1 Z_3}, \widehat{Z_3}\} \\ &\cdots \\ &\to \{\widehat{Z_1 Z_2 Z_3}, \widehat{Z_2 Z_1 Z_3}, \widehat{Z_3 Z_1 Z_2}\}\end{aligned}$$

This expansion defines the successful maxima configurations as members of the

64 possible triplet events from the $(\Omega_{o\cdots}, \mathcal{F}_{o\cdots}, P_{o\cdots})$ with the given probability space ordering $o\cdots$. This expansion, however, does not alter the probability of experiencing a successful maxima configuration within a given ordering. For example, with the ordering $o123$, the successful maxima configuration $\{\widehat{Z_1}, \widehat{Z_2Z_3}\}$ expands to include each possible draw from $(\Omega_3, \mathcal{F}_3, P_3)$. The probability of experiencing this successful configuration within the ordering $o123$ is the sum of the probabilities of experiencing the expanded group of sequences $\{\widehat{Z_1}, \widehat{Z_2Z_3}, \widehat{Z_3}\}$, $\{\widehat{Z_1}, \widehat{Z_2Z_3}, \widehat{Z_3Z_1}\}$, $\{\widehat{Z_1}, \widehat{Z_2Z_3}, \widehat{Z_3Z_2}\}$, and $\{\widehat{Z_1}, \widehat{Z_2Z_3}, \widehat{Z_3Z_1Z_2}\}$.

The probability of experiencing a specific outcome during a stage of the experiment is estimated from the DLG simulations, as in Eq.(A.1). Each stage in the 3-stage trial is assumed independent because each considers a different $\eta_i(t)$ time series, so the probabilities of experiencing specific sub-groups within the maxima configuration given a $\eta_i(t)$ trial are also independent. The validity of this assumption is an area of active research. With this assumption, the probability of experiencing the successful maxima configuration $\{\widehat{Z_1}, \widehat{Z_2Z_3}\}$ within the ordering $o123$ is:

$$\begin{aligned}
p(\{\widehat{Z_1}, \widehat{Z_2Z_3}\}|o123) &= p(\{\widehat{Z_1}, \widehat{Z_2Z_3}, \widehat{Z_3}\}) + p(\{\widehat{Z_1}, \widehat{Z_2Z_3}, \widehat{Z_3Z_1}\}) + \cdots \\
&\quad p(\{\widehat{Z_1}, \widehat{Z_2Z_3}, \widehat{Z_3Z_2}\}) + p(\{\widehat{Z_1}, \widehat{Z_2Z_3}, \widehat{Z_3Z_1Z_2}\}) \\
&= p(\{\widehat{Z_1}\})p(\{\widehat{Z_2Z_3}\})p(\{\widehat{Z_3}\}) + p(\{\widehat{Z_1}\})p(\{\widehat{Z_2Z_3}\})p(\{\widehat{Z_3Z_1}\}) + \cdots \\
&\quad p(\{\widehat{Z_1}\})p(\{\widehat{Z_2Z_3}\})p(\{\widehat{Z_3Z_2}\}) + p(\{\widehat{Z_1}\})p(\{\widehat{Z_2Z_3}\})p(\{\widehat{Z_3Z_1Z_2}\}) \\
&= p(\{\widehat{Z_1}\})p(\{\widehat{Z_2Z_3}\}) \left(p(\{\widehat{Z_3}\}) + p(\{\widehat{Z_3Z_1}\}) + p(\{\widehat{Z_3Z_2}\}) + p(\{\widehat{Z_3Z_1Z_2}\})\right) \\
&= p(\{\widehat{Z_1}\})p(\{\widehat{Z_2Z_3}\}) \times 1
\end{aligned} \tag{A.7}$$

The probability of experiencing the expanded definition of $\{\widehat{Z_1}, \widehat{Z_2Z_3}\}$ to include each possible draw from $(\Omega_3, \mathcal{F}_3, P_3)$ collapses back to the probability of experiencing simply $\{\widehat{Z_1}, \widehat{Z_2Z_3}\}$, because $\sum_{k=1}^{4} p(\{\Omega_{3k}\}) = 1$. Therefore, the expanded definitions are simplified for assessing the probability of experiencing a successful maxima configuration.

Finally, the probability of experiencing each maxima configuration requires the consideration of all successful maxima configurations with any possible orderings of draws ($o123$, $o132$, $\cdots$, $o321$). The successful maxima configurations, as referenced in the main paper, have been expanded to include all possible orderings of the maxima groups (meaning, e.g. $c5$, in which all surrogate process maxima occur separately includes the events from the orderings $o123 : \{\widehat{Z_1}, \widehat{Z_2}, \widehat{Z_3}\}$, $o132 : \{\widehat{Z_1}, \widehat{Z_3}, \widehat{Z_2}\}$, $o213 :$

$\{\widehat{Z_2}, \widehat{Z_1}, \widehat{Z_3}\}$, $o231 : \{\widehat{Z_2}, \widehat{Z_3}, \widehat{Z_1}\}$, $o312 : \{\widehat{Z_3}, \widehat{Z_1}, \widehat{Z_2}\}$, and $o321 : \{\widehat{Z_3}, \widehat{Z_2}, \widehat{Z_1}\}$).

This expansion estimates the probability of experiencing each maxima configuration, within the earlier confines of the independence of the non-failure events assumption, which means the order of events does not matter. However, not all maxima configurations are possible given a probability space ordering. The successful maxima configurations were also expanded to be 3-stages long, to be defined as possible events in the given probability space $(\Omega_{o\cdots}, \mathcal{F}_{o\cdots}, P_{o\cdots})$ for the ordering $o\cdots$. As shown in Eq.(A.7), the addition of the expansion is required only for relation to the 3-stage probability spaces, and this expansion simplifies in the probability calculation. The probability of experiencing each maximum configuration $\mathbf{C}\boldsymbol{i}$ with $i = \mathit{1}, \mathit{2}, \mathit{3}, \mathit{4}, \mathit{5}$ is given by Eq.(A.8)-(A.12):

$$\begin{aligned} p(\mathbf{C}\boldsymbol{1}) = p(\{\widehat{Z_1Z_2}, \widehat{Z_3}\}|o132)p(o132) + p(\{\widehat{Z_2Z_1}, \widehat{Z_3}\}|o231)p(o231) + \cdots \\ p(\{\widehat{Z_3}, \widehat{Z_1Z_2}\}|o312)p(o312) + p(\{\widehat{Z_3}, \widehat{Z_2Z_1}\}|o321)p(o321) \end{aligned} \tag{A.8}$$

where

$$\begin{aligned} p(\{\widehat{Z_1Z_2}, \widehat{Z_3}\}|o132) &= p(\{\widehat{Z_1Z_2}\})p(\{\widehat{Z_3}\}) \\ p(\{\widehat{Z_2Z_1}, \widehat{Z_3}\}|o231) &= p(\{\widehat{Z_2Z_1}\})p(\{\widehat{Z_3}\}) \\ p(\{\widehat{Z_3}, \widehat{Z_1Z_2}\}|o312) &= p(\{\widehat{Z_3}\})p(\{\widehat{Z_1Z_2}\}) \\ p(\{\widehat{Z_3}, \widehat{Z_2Z_1}\}|o321) &= p(\{\widehat{Z_3}\})p(\{\widehat{Z_2Z_1}\}) \\ p(\text{order}\cdots) \equiv p(o132) = p(o231) &= p(o312) = p(o321) = 1/6 \end{aligned}$$

$$\begin{aligned} p(\mathbf{C}\boldsymbol{2}) = p(\{\widehat{Z_1Z_3}, \widehat{Z_2}\}|o123)p(o123) + p(\{\widehat{Z_3Z_1}, \widehat{Z_2}\}|o321)p(o321) + \cdots \\ p(\{\widehat{Z_2}, \widehat{Z_1Z_3}\}|o213)p(o213) + p(\{\widehat{Z_2}, \widehat{Z_3Z_1}\}|o231)p(o231) \end{aligned} \tag{A.9}$$

where

$$\begin{aligned} p(\{\widehat{Z_1Z_3}, \widehat{Z_2}\}|o123) &= p(\{\widehat{Z_1Z_3}\})p(\{\widehat{Z_2}\}) \\ p(\{\widehat{Z_3Z_1}, \widehat{Z_2}\}|o321) &= p(\{\widehat{Z_3Z_1}\})p(\{\widehat{Z_2}\}) \\ p(\{\widehat{Z_2}, \widehat{Z_1Z_3}\}|o213) &= p(\{\widehat{Z_2}\})p(\{\widehat{Z_1Z_3}\}) \\ p(\{\widehat{Z_2}, \widehat{Z_3Z_1}\}|o231) &= p(\{\widehat{Z_2}\})p(\{\widehat{Z_3Z_1}\}) \\ p(\text{order}\cdots) \equiv p(o123) = p(o321) &= p(o213) = p(o231) = p(\text{order}\cdots) = 1/6 \end{aligned}$$

$$\begin{aligned} p(\mathbf{C}\boldsymbol{3}) = p(\{\widehat{Z_2Z_3}, \widehat{Z_1}\}|o213)p(o213) + p(\{\widehat{Z_3Z_2}, \widehat{Z_1}\}|o312)p(o312) + \cdots \\ p(\{\widehat{Z_1}, \widehat{Z_2Z_3}\}|o123)p(o123) + p(\{\widehat{Z_1}, \widehat{Z_3Z_2}\}|o132)p(o132) \end{aligned} \tag{A.10}$$

where

$$
\begin{aligned}
p(\{\widehat{Z_2Z_3},\widehat{Z_1}\}|o213) &= p(\{\widehat{Z_2Z_3}\})p(\{\widehat{Z_1}\}) \\
p(\{\widehat{Z_3Z_2},\widehat{Z_1}\}|o312) &= p(\{\widehat{Z_3Z_2}\})p(\{\widehat{Z_1}\}) \\
p(\{\widehat{Z_1},\widehat{Z_2Z_3}\}|o123) &= p(\{\widehat{Z_1}\})p(\{\widehat{Z_2Z_3}\}) \\
p(\{\widehat{Z_1},\widehat{Z_3Z_2}\}|o132) &= p(\{\widehat{Z_1}\})p(\{\widehat{Z_3Z_2}\}) \\
p(\text{order}\cdots) \equiv p(o213) &= p(o312) = p(o123) = p(o132) = 1/6
\end{aligned}
$$

$$
\begin{aligned}
p(\mathbf{C4}) = p(\{\widehat{Z_1Z_2Z_3}\}|o123)p(o123) + p(\{\widehat{Z_1Z_2Z_3}\}|o132)p(o132) + \cdots \\
p(\{\widehat{Z_2Z_1Z_3}\}|o213)p(o213) + p(\{\widehat{Z_2Z_1Z_3}\}|o231)p(o231) + \cdots \\
p(\{\widehat{Z_3Z_1Z_2}\}|o312)p(o312) + p(\{\widehat{Z_3Z_1Z_2}\}|o321)p(o321)
\end{aligned} \tag{A.11}
$$

where

$$
\begin{aligned}
p(\{\widehat{Z_1Z_2Z_3}\}|o123) &= p(\{\widehat{Z_1Z_2Z_3}\}) \\
p(\{\widehat{Z_1Z_2Z_3}\}|o132) &= p(\{\widehat{Z_1Z_2Z_3}\}) \\
p(\{\widehat{Z_2Z_1Z_3}\}|o213) &= p(\{\widehat{Z_2Z_1Z_3}\}) \\
p(\{\widehat{Z_2Z_1Z_3}\}|o231) &= p(\{\widehat{Z_2Z_1Z_3}\}) \\
p(\{\widehat{Z_3Z_1Z_2}\}|o312) &= p(\{\widehat{Z_3Z_1Z_2}\}) \\
p(\{\widehat{Z_3Z_1Z_2}\}|o321) &= p(\{\widehat{Z_3Z_1Z_2}\}) \\
p(o123) = p(o132) &= \cdots = p(o321) = p(\text{order}\cdots) = 1/6
\end{aligned}
$$

$$
\begin{aligned}
p(\mathbf{C5}) = p(\{\widehat{Z_1},\widehat{Z_2},\widehat{Z_3}\}|o123)p(o123) + p(\{\widehat{Z_1},\widehat{Z_3},\widehat{Z_2}\}|o132)p(o132) + \cdots \\
p(\{\widehat{Z_2},\widehat{Z_1},\widehat{Z_3}\}|o213)p(o213) + p(\{\widehat{Z_2},\widehat{Z_3},\widehat{Z_1}\}|o231)p(o231) + \cdots \\
p(\{\widehat{Z_3},\widehat{Z_1},\widehat{Z_2}\}|o312)p(o312) + p(\{\widehat{Z_3},\widehat{Z_2},\widehat{Z_1}\}|o321)p(o321)
\end{aligned} \tag{A.12}
$$

where

$$
\begin{aligned}
p(\{\widehat{Z_1},\widehat{Z_2},\widehat{Z_3}\}|o123) &= p(\{\widehat{Z_1},\widehat{Z_3},\widehat{Z_2}\}|o132) = \cdots \\
p(\{\widehat{Z_2},\widehat{Z_1},\widehat{Z_3}\}|o213) &= p(\{\widehat{Z_2},\widehat{Z_3},\widehat{Z_1}\}|o231) = \cdots \\
p(\{\widehat{Z_3},\widehat{Z_1},\widehat{Z_2}\}|o312) &= p(\{\widehat{Z_3},\widehat{Z_2},\widehat{Z_1}\}|o331) = p(\{\widehat{Z_1}\})p(\{\widehat{Z_2}\})p(\{\widehat{Z_3}\}) \\
p(\text{order}\cdots) \equiv p(o123) &= p(o132) = \cdots = p(o321) = 1/6
\end{aligned}
$$

The final step to finding the probability of experiencing each maxima configuration $c1 - c5$ as referenced in Eq.(5.6) is to condition all the above probabilities from Eq.(A.8)-(A.12) on being a successful configuration (that being each surrogate process maximum occurs exactly once). This is necessary because the only maxima configurations which have physical meaning as related to the NL-DLG process formulation in Chapter 5.8.2 are the successful configurations. For each 3-stage probability space, $(\Omega_{o\cdots}, \mathcal{F}_{o\cdots}, P_{o\cdots})$ with order $o\cdots$, there are many triplets of events which are

not successful maxima configurations. These non-successful maxima configurations are not physically realizable, because each surrogate process maxima can only be experienced once during an exposure.

Each exposure can be classified as exactly one of $c1 - c5$. These configurations express the only ways that 3 surrogate process maxima may be clustered over a full exposure. The 3-stage probability experiment shown here reflects the $p(c1) + \cdots + p(c5) = 1$ criterion when Eq.(A.8)-(A.12) are conditioned on a successful configuration being experienced (i.e., with $p(\mathbf{C1}|\text{success}) + p(\mathbf{C2}|\text{success}) + p(\mathbf{C3}|\text{success}) + p(\mathbf{C4}|\text{success}) + p(\mathbf{C5}|\text{success}) = 1$). This is adjusted as below in Eq.(A.13). Terms of the form $p(\mathbf{Ci} \cap \text{success})$ simplify to $p(\mathbf{Ci})$ because the configurations **C1**-**C5** are by definition successful configurations. The final expressions, $p(ci)$, are what is referenced in Eq.(5.6) in Chapter 5.8.2.

$$\begin{aligned} p(ci) = p(\mathbf{Ci}|\text{success}) &= \frac{p(\mathbf{Ci} \cap \text{success})}{p(\text{success})} = \frac{p(\mathbf{Ci})}{p(\text{success})} \\ p(\text{success}) &= p(\mathbf{C1}) + p(\mathbf{C2}) + p(\mathbf{C3}) + p(\mathbf{C4}) + p(\mathbf{C5}) \end{aligned} \tag{A.13}$$

This entire process generalizes to any number of surrogate processes, but more surrogate processes, n, require an analysis of more maxima configurations, defined by the Bell number, B_n, and more probability space orderings, which is of order $n!$. Adding more surrogate processes requires conducting more DLG simulations, but this is computationally cheap (about 3 minutes per surrogate process, to construct 2000 simulations). The difficulty of considering more surrogate processes is related to the organization of the probability space for the $n-$stage experiment, the increased number of possible probability space orderings, and the number of possible maxima configurations.

BIBLIOGRAPHY

BIBLIOGRAPHY

Alford, L. K. (2008), Estimating Extreme Responses Using a Non-Uniform Phase Distribution, Ph.D. thesis, The University of Michigan.

Ashe, G., et al. (2009), 17th International Ship and Offshore Structures Congress, Committee V.5 Naval Ship Design, *2*.

Au, S.-K., and J. L. Beck (2001), Estimation of Small Failure Probabilities in High Dimensions by Subset Simulation, *Probabilistic Engineering Mechanics*, *16*(4), 263 – 277, doi:https://doi.org/10.1016/S0266-8920(01)00019-4.

Bartoli, G., C. Mannini, and T. Massai (2011), Quasi-Static Combination of Wind Loads: A Copula-Based Approach, *Journal of Wind Engineering and Industrial Aerodynamics*, *99*(6-7), 672–681.

Bassler, C. C., V. Belenky, and M. J. Dipper (2010), Characteristics of Wave Groups for the Evaluation of Ship Response in Irregular Seas, in *International Conference on Offshore Mechanics and Arctic Engineering, 29th International Conference on Ocean, Offshore and Arctic Engineering*, vol. 2, pp. 227–237, Shanghai, China.

Bastian, K., M. Pahlow, Y. Hundecha, and A. Schumann (2009), Probability Analysis of Hydrological Loads for the Design of Flood Control Systems Using Copulas, *Journal of Hydrologic Engineering*, *15*(5), 360–369.

Beck, R., and A. W. Troesch (1990), Students' Documentation and Users' Manual for the Computer Program SHIPMO.BM, *University of Michigan, Ann Arbor*.

Bell, E. T. (1938), The Iterated Exponential Integers, *Annals of Mathematics*, *39*(3), 539–557.

Blanchard, T., and C. Ge (2007), Rules for the Classification of Trimarans, *Journal of Naval Engineering*, *44*(1).

Boccotti, P. (2015), *Wave Mechanics and Wave Loads on Marine Structures*, Elsevier; Butterworth-Heinemann.

CDIP (2018), Station 029 Pt. Reyes Buoy, *University of California San Diego, Coastal Data Information Program*.

Coles, S. (2001), *An Introduction to Statistical Modeling of Extreme Values*, Springer-Verlag.

de Waal, D. J., and P. H. A. J. M. van Gelder (2005), Modelling of Extreme Wave Heights and Periods Through Copulas, *Extremes*, *8*(4), 345–356.

Ewans, K., and P. Jonathan (2014), Evaluating Environmental Joint Extremes for the Offshore Industry Using the Conditional Extremes Model, *Journal of Marine Systems*, *130*, 124–130.

Ewing, J. A. (1973), Mean Length of Runs of High Waves, *Journal of Geophysical Research*, *78*(12), 1933–1936.

Faltinsen, O. M. (2005), *Hydrodynamics of High-Speed Marine Vessels*, Cambridge University Press.

Gong, J., Y. Li, L. Peng, and Q. Yao (2014), Estimation Of Extreme Quantiles For Functions Of Dependent Random Variables, *Royal Statistical Society B: Statistical Methodology*, *77*(5), 1001–1024.

Haslum, H. A., and O. M. Faltinsen (1999), Alternative Shape of Spar Platforms for use in Hostile Areas, *Offshore Technology Conference*.

Heffernan, J. E., and J. A. Tawn (2004), A Conditional Approach for Multivariate Extreme Values (With Discussion), *Journal of the Royal Statistical Society: Series B (Statistical Methodology)*, *66*(3), 497–546, doi:10.1111/j.1467-9868.2004.02050.x.

Hughes, O. F. (1988), *Ship Structural Design: A Rationally-Based, Computer-Aided Optimization Approach*, The Society of Naval Architects and Marine Engineers.

Hurtado, J. E. (2004), *Structural Reliability: Statistical Learning Perspectives*, Springer-Verlag.

IACS Rec. No. 34 (2001), Standard Wave Data.

Jensen, J. J. (1996), Second-Order Wave Kinematics Conditional on a Given Wave Crest, *Applied Ocean Research*, *18*, 119–128.

Jensen, J. J. (2005), Conditional Second-Order Short-Crested Water Waves Applied to Extreme Wave Episodes, *Journal of Fluid Mechanics*, *545*, 29–40.

Jensen, J. J. (2007), Efficient Estimation of Extreme Non-Linear Roll Motions using the First-Order Reliability Method (FORM), *Journal of Marine Science and Technology*, *12*(4), 191–202.

Jonathan, P., and P. H. Taylor (1995), Irregular, Non-Linear Waves in a Spread Sea, *Journal of Offshore Mechanics and Arctic Engineering*, *1-A*, 9–16.

Kim, D.-H. (2012), Design Loads Generator: Estimation of Extreme Environmental Loadings for Ship and Offshore Applications, Ph.D. thesis, The University of Michigan.

Kim, D.-H., and A. W. Troesch (2013), Statistical Estimation of Extreme Roll Response in Short Crested Irregular Seas, *Trans. SNAME 2013*.

Kim, D.-H., A. H. Engle, and A. W. Troesch (2011), Estimates of Long-Term Combined Wave Bending and Whipping for Two Alternative Hull Forms, *Trans. SNAME*, *Vol. 119*.

Kimura, A. (1980), Statistical Properties of Random Wave Groups, in *Proceedings 17th International Conference on Coastal Engineering*, vol. 3, pp. 2955–2973, ASCE, Sydney, Australia.

Kinsman, B. (1965), *Wind Waves: Their Generation and Propagation on the Ocean Surface*, Prentice-Hall, Inc.

Knight, J. T., M. Craig, and D. C. Kring (2017), Copula Functions for Prediction of Multivariate Extreme Loads, *International Conference on Fast Sea Transportation Nantes, France*.

Kring, D. C., W. M. Milewski, and N. E. Fine (2004), Validation of a NURBS-Based BEM for Multihull Ship Seakeeping, *25th Symposium on Naval Hydrodynamics St. John's, Newfoundland and Labrador, Canada*.

Kullback, S., and R. A. Leibler (1951), On Information and Sufficiency, *The Annals of Mathematical Statistics*, *22*, 79–86.

Lindgren, G. (1970), Some Properties of a Normal Process Near a Local Maximum, *Annals of Mathematical Statistics*, *41*(6), 1870–1883.

Lindgren, G. (1972a), Local Maxima of Gaussian Fields, *Archiv der Matematik*, *10*, 195–218.

Lindgren, G. (1972b), Wave-Length and Amplitude for a Stationary Gaussian Process after a High Maximum, *Z. Wahrscheinlichkeitstheorie verw. Gebiete*, *23*, 293–326.

Lloyd's Register (2017), Rules for the Classification of Trimarans.

Longuet-Higgins, M. S. (1957), The Statistical Analysis of a Random, Moving Surface, *Philosophical Transactions of the Royal Society of London: Mathematical and Physical Sciences*, *249*(966).

Madsen, H. O., S. Krenk, and N. C. Lind (2006), *Methods of Structural Safety*, Dover Publications.

Naess, A., and T. Moan (2014), *Stochastic Dynamics of Marine Structures*, Cambridge University Press.

Ochi, M. K. (1981), Principles of Extreme Value Statistics and their Application, *Trans. SNAME*.

Ochi, M. K. (1990), *Applied Probability and Stochastic Processes in Engineering and Physical Sciences*, John Wiley & Sons.

Papaioannou, I., W. Betz, K. Zwirglmaier, and D. Straub (2015), MCMC Algorithms for Subset Simulation, *Probabilistic Engineering Mechanics*, *41*, 89 – 103, doi:https://doi.org/10.1016/j.probengmech.2015.06.006.

Perryman, S., J. Chappell, I. Prisln, and Q. Xu (2009), Measurement, Hindcast and Prediction of Holstein Spar Motions in Extreme Seas, *Offshore Technology Conference*.

Phillips, O. M., D. Gu, and M. Donelan (1993), Expected Structure of Extreme Waves in a Gaussian Sea. Part I: Theory and SWADE Buoy Measurements, *Journal of Physical Oceanography*, *23*, 992–1000.

Renard, B., and M. Lang (2007), Use of a Gaussian Copula for Multivariate Extreme Value Analysis: Some Case Studies in Hydrology, *Advances in Water Resources*, *30*(4), 897 – 912, doi:https://doi.org/10.1016/j.advwatres.2006.08.001.

Rho, J. B., and H. S. Choi (2002), Heave and Pitch Motions of a Spar Platform with Damping Plate, *Proceedings of the Twelfth International Offshore and Polar Engineering Conference*.

Rho, J. B., and H. S. Choi (2005), A Study on Mathieu-type Instability of Conventional Spar Platform in Regular Waves, *International Journal of Offshore and Polar Engineering*, *15*(2), 104–108.

Rice, S. O. (1944), Mathematical Analysis of Random Noise, *The Bell System Technical Journal*, *23*(3), 282–332.

Rosenblatt, M. (1952), Remarks on a Multivariate Transformation, *The Annals of Mathematical Statistics*, *23*(3), 470–472.

Russo, V. L., and E. K. Sullivan (1953), Design of the MARINER-Type Ship, *Trans. SNAME*, *61*.

Seyffert, H. C., and A. W. Troesch (2016a), Large Wave Groups- Their Probability, Profiles, and Mean Offsets, *International Workshop on Water Waves and Floating Bodies*.

Seyffert, H. C., and A. W. Troesch (2016b), Spar Platform Response due to Rare Wave Groups, *Practical Design of Ships and Other Floating Structures*.

Seyffert, H. C., and A. W. Troesch (2016c), Data Mining Pt. Reyes Buoy for Rare Wave Groups, *Journal of Offshore Mechanics and Arctic Engineering*, *138*(1), 1–7, also doi: http://dx.doi.org/10.1115/1.4031,973.

Seyffert, H. C., and A. W. Troesch (2018), Estimation of Lifetime Failure Probability in Complex Systems due to Combined non-Gaussian Loading, *submitted to: Probabilistic Engineering Mechanics*.

Seyffert, H. C., D.-H. Kim, and A. W. Troesch (2016), Rare Wave Groups, *Journal of Ocean Engineering*, *122*(1), 241–252.

Seyffert, H. C., A. W. Troesch, and M. D. Collette (2018a), Combined Stochastic Lateral and In-Plane Loading of a Stiffened Panel Leading to Collapse, *in preparation: Journal of Marine Structures*.

Seyffert, H. C., A. W. Troesch, J. T. Knight, and D. C. Kring (2018b), Probabilistic Assessment of Combined Loads for Trimarans, *International Marine Design Conference, Helsinki, Finland*.

Taylor, P. H., P. Jonathan, and L. A. Harland (1997), Time Domain Simulation of Jack-up Dynamics With the Extremes of a Gaussian Process, *Journal of Vibration and Acoustics, Trans. of ASME*, *119*, 624–628.

Themelis, N., and K. Spyrou (2007), Probabilistic Assessment of Ship Stability, *Transactions - Society of Naval Architects and Marine Engineers*, *117*, 181–206.

Tromans, P. S., A. R. Anaturk, and P. Hagemeijer (1991), A New Model for the Kinematics of Large Ocean Waves - Application as a Design Wave, *Proceedings, 1st Internationl Offshore and Polar Engineering Conference (ISOPE)*, *Vol. III*, 64–71.

Winterstein, S. R., T. C. Ude, C. A. Cornell, P. Bjerager, and S. Haver (1993), Environmental Parameters for Extreme Response: Inverse FORM with Omission Factors, *Proc. 6th Int. Conf. on Structural Safety and Reliability*.

Wirsching, P. H., T. Paez, and K. Ortiz (2006), *Random Vibrations: Theory and Practice*, Dover Publications.